



HAL
open science

La₂NiO_{4+d}, a Mixed Ionic-Electronic Conductor for Interface-Type Valence Change Memories

Klaasjan Maas

► **To cite this version:**

Klaasjan Maas. La₂NiO_{4+d}, a Mixed Ionic-Electronic Conductor for Interface-Type Valence Change Memories. Electric power. Université Grenoble Alpes, 2019. English. NNT : 2019GREAI012 . tel-02160021

HAL Id: tel-02160021

<https://theses.hal.science/tel-02160021>

Submitted on 19 Jun 2019

HAL is a multi-disciplinary open access archive for the deposit and dissemination of scientific research documents, whether they are published or not. The documents may come from teaching and research institutions in France or abroad, or from public or private research centers.

L'archive ouverte pluridisciplinaire **HAL**, est destinée au dépôt et à la diffusion de documents scientifiques de niveau recherche, publiés ou non, émanant des établissements d'enseignement et de recherche français ou étrangers, des laboratoires publics ou privés.

THÈSE

Pour obtenir le grade de

DOCTEUR DE LA COMMUNAUTE UNIVERSITE GRENOBLE ALPES

Spécialité : 2MGE : Matériaux, Mécanique, Génie civil, Electrochimie

Arrêté ministériel : 25 mai 2016

Présentée par

Klaasjan MAAS

Thèse dirigée par **Michel BOUDARD**

Thèse codirigée par **Monica BURRIEL** et **Quentin RAFHAY**

préparée au sein du Laboratoire : **LMGP et IMEP-LaHC**

dans l'**École Doctorale I-MEP2 - Ingénierie - Matériaux,**

Mécanique, Environnement, Energétique, Procédés, Production

La₂NiO_{4+δ},
un Conducteur Mixte Ionique-Electronique
pour les Mémoires à Changement de Valence

La₂NiO_{4+δ},
a Mixed Ionic-Electronic Conductor for
Interface-Type Valence Change Memories

Thèse soutenue publiquement le **14 mars 2019**

devant le jury composé de :

Mr Christophe VALLEE

Professeur, Université Grenoble Alpes, Président du Jury et Examineur

Mme Regina DITTMANN

Professeur, Forschungszentrum Jülich GmbH, Rapporteur

Mme Graziella MALANDRINO

Professeur, Università degli Studi di Catania , Rapporteur

Mr José SANTISO

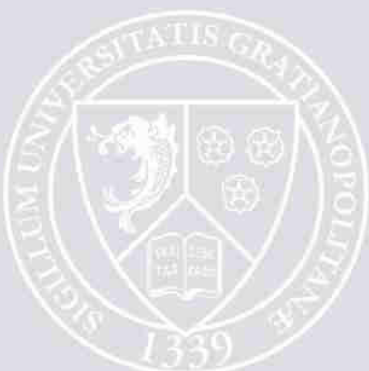
Chargé de Recherche, Institut Catalan de Nanociencia i Nanotecnologia,
Examineur

Mr Marc BOCQUET

Maître de Conférences, Ecole Polytech' Marseille, Examineur

Mr Michel BOUDARD

Chargé de Recherche, CNRS Délégation Alpes, Directeur de thèse



Contents

Contents	iii
List of Figures	vii
List of Tables	xiii
Acknowledgments	xix
Foreword	xxv
1 New memory and computation paradigms	1
1.1 Beyond the von Neumann computation architecture	1
1.2 Memristive systems: a new memory paradigm	4
1.2.1 The memristor	5
1.3 Valence-Change Memories	7
1.3.1 Interface-Type Valence-Change Memories	7
1.3.2 Triggering ion migration in oxides	9
1.3.3 Triggering memristivity through electroforming	12
1.4 Concluding Words	13
2 $\text{La}_2\text{NiO}_{4+\delta}$, a mixed ionic-electronic conductor for VCM applications	15
2.1 L2NO_4 : a layered structure with mixed conduction properties	16
2.1.1 Structural considerations and phase diagram	16
2.1.2 Mechanism for the incorporation of excess oxygen in L2NO_4	19
2.1.3 Oxygen-ion diffusion in L2NO_4	20
2.1.4 Hole self-doping and electronic conductivity in L2NO_4	23
2.2 Motivation to use L2NO_4 as a memristive material for VCM applications	26
2.3 Growth of L2NO_4 thin films by PiMOCVD	28
2.3.1 Materials characterization aspects of the as-prepared thin films	29

2.3.2	Tuning the oxygen content through post-annealing treatments	36
2.4	Summary	38
3	Functionality through interface: role of the electrodes	41
3.1	The Metal/Oxide heterojunction	42
3.1.1	Conduction mechanisms	42
3.1.2	Ohmic and Schottky contacts	43
3.1.3	Oxygen affinity of the electrode and formation of interlayers	47
3.2	Metal/L2NO4 heterojunction properties	49
3.2.1	Choice of the electrode material	49
3.2.2	Effect of the oxygen content in L2NO4 on the Pt/L2NO4 junction properties.	51
3.2.3	Pt/L2NO4 and Ti/L2NO4 MS heterojunctions	54
3.2.4	Evidence of a TiO _x interlayer	56
3.2.5	Temperature-dependent measurements and transport mechanisms	58
3.3	Summary	61
4	Pt/L2NO4/Ti, a prototypical memristive device for VCMs	65
4.1	Memristivity in Pt/L2NO4/Ti using the ‘top-top’ planar electrode configuration	66
4.1.1	The initialisation step	67
4.1.2	Analog I(V) characteristics and memory storage	69
4.1.3	Role of the oxygen content in L2NO4	72
4.2	Spontaneous relaxation behaviour	78
4.3	Neuromorphic aspects	81
4.4	Discussion	85
4.4.1	Analog-type change in resistance in metal/oxide/metal heterostructures	85
4.4.2	Proposed mechanism for the memristive behaviour in Pt/L2NO4/Ti devices	88
4.5	Summary	91
5	The top-bottom L2NO4/LNO3 heterostructure	95
5.1	The need for a functional electrode for the growth of oriented L2NO4	96
5.2	The bottom electrode layer: LNO3 films deposited by PiMOCVD	98
5.2.1	Optimization of the growth of LNO3 thin films on STO and LAO	98
5.2.2	Role of the impurities on the growth of LNO3 films on STO	103
5.3	Lanthanum-nickelate thin films deposited by PLD	106
5.3.1	Structural properties of LNO3 films deposited by PLD	107

5.3.2	Structural properties of L2NO4 films deposited by PLD	108
5.4	Comparison of LNO3 and L2NO4 single layers deposited by PiMOCVD and PLD	109
5.5	L2NO4/LNO3 bilayers	112
5.5.1	L2NO4/LNO3 bilayers deposited by PiMOCVD	112
5.5.2	L2NO4/LNO3 bilayers deposited by PLD	116
5.6	Resistance-change in Pt/LNO3/L2NO4/Pt heterostructures grown by PLD . .	117
5.6.1	The initialisation step	117
5.6.2	Analog-type bipolar resistance change in Pt/LNO3/L2NO4/Pt	119
5.6.3	Resistance relaxation	121
5.7	Summary	123
Concluding summary & perspectives		127
References		133
A Lanthanum-nickelate thin film deposition and optimization using PiMOCVD		151
A.1	PiMOCVD: a chemical vapour deposition technique	151
A.1.1	Metal-Organic Chemical Vapour Deposition (MOCVD)	152
A.1.2	The particularities of PiMOCVD	155
A.1.3	Details on the substrate preparation and deposition procedure	155
A.1.4	Post annealing treatments	158
A.2	Role of the solvent on the structural properties of L2NO4 thin films deposited by PiMOCVD	158
A.3	The La/Ni ratio in the precursor solution	159
B LaNiO₃ thin film deposition and optimization by PiMOCVD		163
B.1	Experimental	163
B.1.1	Thin film deposition by PiMOCVD	163
B.1.2	Thin film characterization	165
B.2	LNO3 deposition optimization using PiMOCVD	166
B.2.1	La and Ni atomic concentration in the injected solution	166
B.2.2	Temperature study	167
B.3	Film characterization	167
B.3.1	Electrical properties of the films	167
B.3.2	Strain effect in the epitaxial LNO3/LAO and LNO3/STO films	169
B.3.3	Microscopic Characterization of the microstructure: a TEM study . .	173

B.4	L2NO4/LNO3 bilayers prepared by PiMOCVD	177
B.5	Conclusions	180
C	Methods	183
C.1	Cleanroom microfabrication	183
C.2	Thin film characterization	185
C.2.1	X-Ray Diffraction	185
C.2.2	Reciprocal Space Maps of La ₂ NiO ₄	185
C.2.3	Transmission Electron Microscopy	187
C.2.4	X-ray Photoemission Electron Microscopy (XPEEM)	188
C.2.5	Electron-Probe Micro-Analysis	189
C.2.6	Atomic-Probe Microscopy	190
C.2.7	Electrical Characterization	190
C.2.8	Raman Spectroscopy	190
C.3	Details on the Transmission Line Measurements (TLM) measurements	190
C.4	Conduction mechanisms in a metal/oxide/metal heterostructure	192
D	Synchrotron-based experiments	195
D.1	X-Ray Absorption Near-Edge Spectroscopy (XANES)	195
D.2	Device in operation: microscopic aspects behind the resistance-change mechanism (in Pt/L2NO4/Ti)	198
D.2.1	Sample preparation	198
D.2.2	XRD in selected micro-patterned regions of the device	198
D.2.3	<i>Operando</i> Hard X-Ray Photoemission Spectroscopy (HAXPES)	200
E	Résumé de la thèse en Français	205

List of Figures

1	Structuration of the thesis.	xxvi
1.1	Comparison of conventional von Neumann and neuromorphic computer architectures.	2
1.2	Memristor crossbar arrays and memristivity.	5
1.3	Illustration of several resistance-change mechanisms which can be present in memristive devices.	8
1.4	Interface-type VCM mechanism.	9
1.5	Schematic illustration of the forces that can trigger oxygen-anion motion.	11
2.1	Schematic representations of the tetragonal $\text{La}_2\text{NiO}_{4.00}$ structure.	17
2.2	Location and local environment of the interstitial oxygen ion in $\text{La}_2\text{NiO}_{4+\delta}$	18
2.3	Phase diagram of $\text{La}_2\text{NiO}_{4+\delta}$ as a function of temperature and oxygen overstoichiometry.	19
2.4	Tracer-diffusion and surface exchange coefficients of L2NO_4 reported in literature.	21
2.5	Oxygen diffusion pathways and molecular dynamics calculations	24
2.6	Comparison of the oxygen-tracer diffusion coefficient D^* for several oxide materials.	27
2.7	XRD pattern and HRTEM image of a L2NO_4 thin film deposited on $\text{STO}(100)$ at $650\text{ }^\circ\text{C}$ by PiMOCVD with $\text{La/Ni} = 5.00$ in the precursor solution.	31
2.8	HRTEM (HAADF) image of an $\text{L2NO}_4/\text{STO}$ sample.	32
2.9	TEM and HRTEM images of L2NO_4 thin films deposited on LAO, NGO and STO single crystal substrates.	34
2.10	ASTAR images of a $\text{L2NO}_4/\text{STO}$ sample.	35
2.11	Evolution of the out-of-plane c lattice parameter and film resistivity of $\text{L2NO}_4/\text{STO}$ as a function of oxygen off-stoichiometry.	37

3.1	Illustration of the electron conduction paths through a metal/oxide/metal heterostructure.	43
3.2	Potential energy for isolated metal surface and semiconductor surface plotted on the same energy scale.	45
3.3	Ohmic and Schottky contact between a metal and a p-type semiconductor.	46
3.4	Ellingham diagrams.	48
3.5	I-V characteristics of different metal/L2NO4/metal heterojunctions.	50
3.6	Transmission-line measurements carried out on L2NO4 films with different oxygen contents.	52
3.7	Resistance as a function of the inverse of the pad side for a symmetrical M/L2NO4/M device (M = Pt or Ti).	55
3.8	HAADF TEM images of a pristine Pt/L2NO4/Ti device cross-section taken beneath a Pt and a Ti electrode.	57
3.9	Evolution of the electrical I-V characteristics of a Pt/L2NO4/Pt and a Pt/L2NO4/Ti device as a function of temperature.	59
4.1	initialisation of a Pt/L2NO4/Ti device.	68
4.2	I-V characteristics of the same Pt/L2NO4/Ti device after initialisation	70
4.3	Stabilized I-V characteristics of a Pt/L2NO4/Ti device.	70
4.4	R-V characteristics of a Pt/L2NO4/Ti device showing highly reproducible HRS and LRS.	71
4.5	Initialisation of a Pt/L2NO4/Ti device annealed in H ₂ (6%)/Ar, Ar and O ₂ , respectively.	73
4.6	Relative contribution of the L2NO4 film, the Pt/L2NO4 contact and the Ti/L2NO4 contact to the total resistance R _T of the oxygen, argon and hydrogen annealed samples before and after initialisation.	74
4.7	Possible band diagram illustrating the Schottky contact between Ti and L2NO4 with varying oxygen content.	75
4.8	Dynamic resistance changes of a pristine Pt/L2NO4/Ti device after a pulsed initialization.	79
4.9	Controlled and progressive resistance-change in Pt/L2NO4/Ti achieved through the application of voltage pulse.	82
4.10	Variation of the relative resistance of an oxygen-annealed Pt/L2NO4/Ti device as a function of time after having been initialised and intensively programmed during a few hours.	84
4.11	Band-diagram based model for the interface-type resistance-change mechanism in a Pt/L2NO4/Ti device.	89

5.1	XRD patterns of LNO3 thin films deposited on STO and LAO single crystals with La/Ni = 2.38 in the precursor solution and increasing deposition temperatures.	99
5.2	Evolution of the LNO3 film resistivity as a function of the deposition temperature and the substrate.	99
5.3	TEM cross-section of LNO3/STO obtained at 550 °C with La/Ni = 2.38 in the precursor solution and showing the [0 0 1] _{NiO} domains.	101
5.4	TEM cross-section of LNO3/LAO obtained at 550 °C with La/Ni = 2.38 in the precursor solution and showing the [0 0 1] _{NiO} domains.	102
5.5	Correlated evolution of the integrated relative peak intensities of 1 1 0 _{LNO3} with 2 0 0 _{NiO}	104
5.6	Electron diffraction and TEM cross section image of a thin LNO3/STO sample deposited at 650 °C using 1000 pulses of a precursor solution with La/Ni=2.38.	105
5.7	HRTEM image of LNO3/STO taken around a NiO defect.	105
5.8	XRD patterns of LNO3 thin films with increasing thickness deposited on STO by PLD at T = 600 °C and p = 70 mTorr.	108
5.9	XRD patterns of L2NO4 thin films with increasing thickness deposited on STO by PLD at T = 700 °C and p = 70 mTorr.	109
5.10	Reciprocal space maps of L2NO4/STO samples with increasing L2NO4 film thickness prepared by PLD.	110
5.11	Resistivity as a function of film thickness for L2NO4/STO and LNO3/STO samples deposited both by PiMOCVD and PLD.	111
5.12	XRD patterns L2NO4/LNO3/STO and L2NO4/LNO3/LAO bilayer samples.	114
5.13	HRTEM images of a L2NO4/LNO3/STO bilayer deposited by PiMOCVD.	115
5.14	Picture and sketch of the measuring configuration of a Pt/LNO3/L2NO4/Pt sample.	117
5.15	I-V characteristics showing the initialisation of a Pt/LNO3/L2NO4/Pt memristive device prepared by PLD.	118
5.16	Electrical characteristics of an initialised Pt/LNO3/L2NO4/Pt memristive device.	120
5.17	Evolution of the resistance over time of a Pt/LNO3/L2NO4/Pt memristive device from its IRS to its initialised HRS, followed by the relaxation of the HRS and the relaxation of several programmed resistance states achieved by stressing the device with increasing and alternating positive and negative voltages.	122
A.1	Detailed illustration of the PiMOCVD process.	153
A.2	Metalorganic precursors used for the deposition of LNO3 and L2NO4 thin films by PiMOCVD.	157

A.3	Pictures of the « Bâti D11 », the PiMOCVD reactor used for the deposition of lanthanum-nickelate thin films.	157
A.4	Picture of the tubular furnaces used for the post-annealing treatments.	158
A.5	Role of the solvent on the quality of L2NO4 thin films.	160
A.6	Composition analysis (EPMA) of LNO3 and L2NO4 thin films deposited on STO.	161
A.7	θ -2 θ XRD patterns of lanthanum-nickelate thin films deposited on STO substrates with increasing La/Ni precursor ratio.	162
B.1	Deposition optimization LNO3 - XRD diagrams	168
B.2	Correlation between the LNO3 film thickness and the deposition temperature.	169
B.3	Optimization of the LNO3 film resistivity.	170
B.4	XRD diagrams of LNO3/STO and LNO3/LAO samples with increasing LNO3 film thickness.	171
B.5	Raman spectra of LNO3 films of different thicknesses (14, 38 and 85 nm).	172
B.6	Resistivity of LNO3 as a function of film thickness for films deposited on STO and LAO.	174
B.7	Measured and fitted XRR curves of LNO3 films obtained at 650 °C and with La/Ni = 2.38 in the precursor solution.	175
B.8	STEM and HRTEM images of LNO3/STO obtained at 650 °C with La/Ni=2.38 in the precursor solution.	176
B.9	HRTEM images of a LNO3/LAO film deposited at 650 °C with La/Ni = 2.38 in the precursor solution.	178
B.10	XRD patterns of L2NO4/LNO3 bilayers and LNO3 single layers deposited on STO and LAO single-crystal substrates.	179
B.11	HRTEM images of a L2NO4/LNO3/STO bilayer deposited by PiMOCVD.	180
C.1	Process flow followed during the cleanroom microfabrication of metallic top electrodes.	184
C.2	Generated reciprocal space map of L2NO4/STO.	186
C.3	Schematic representation of the crystal orientation of multi domain L2NO4 on STO.	187
C.4	PEEM measurements carried out on two L2NO4/STO samples with different oxygen contents.	189
D.1	XANES calibration curves	197
D.2	Electrical characteristics of a Pt/L2NO4/Ti/Pt device before and after RTA.	199
D.3	Picture of a sample prepared for synchrotron measurements.	199

D.4	Measurement setup for the HAXPES <i>in-situ</i> biasing experiment.	201
D.5	<i>Operando</i> HAXPES measurements of the Ti1s core level for different resistance states of the device.	202
D.6	<i>Operando</i> HAXPES and XRD experiment carried out at the ESRF	204
E.1	Caractéristiques électriques d'un composant Pt/L2NO4/Ti.	207

List of Tables

2.1	Optimized deposition conditions used for the growth of L2NO4 thin films by PiMOCVD.	29
2.2	Lattice-mismatch values between the basal plane of tetragonal L2NO4 and STO, NGO and LAO single crystal substrates.	33
5.1	Lattice parameters for rhombohedral LNO3 reported in literature.	97
5.2	Deposition conditions used for the growth of LNO3 and L2NO4 single layers by PLD.	107
5.3	Deposition conditions used for the growth of LNO3 and L2NO4 single layers by PiMOCVD.	111
5.4	Deposition conditions used for the growth of L2NO4/LNO3 bilayers by PiMOCVD	113
5.5	Deposition conditions used for the growth of L2NO4/LNO3 bilayers by PLD.	116
B.1	Deposition conditions used for the growth of LNO3 thin film by PiMOCVD .	164
B.2	Out of plane lattice parameters of LNO3 films from Son et al. are compared with our data on STO and LAO.	170
C.1	Equations expressing the field and temperature dependence of the conduction mechanisms presented in Figure 3.1.	193

Nomenclature

Acronyms / Abbreviations

AFM Atomic Force Microscopy

ALU Arithmetic and Logic Unit

CMOS Complementary Metal-Oxide Semiconductor

CPU Control and Processing Unit

ECM ElectroChemical Metallization, a type of resistive memory mechanism

EELS Electron-Energy Loss Spectroscopy

EPMA Electron Probe Microanalysis

ESRF European Synchrotron Radiation Facility

FET Field-Effect Transistor

FIB Focused-Ion Beam

FTO Fluorine-doped Tin Oxide, a transparent conducting oxide material widely used in optoelectronic devices

FWHM Full-Width at Half Maximum

HAADF High-Angle Anular Dark Field, a particular type of TEM measurement sensible to the atomic number Z of elements

HAXPES Hard X-ray Photoelectron Spectroscopy (carried out at the ESRF)

HRS High Resistance State

HRTEM High-Resolution TEM

- IRS** Initial Resistance State
- L2NO4** La_2NiO_4 , first member ($n=1$) of the Ruddlesden Popper series $\text{La}_{n+1}\text{Ni}_n\text{O}_{2n+1}$. p-type semiconductor exhibiting MIEC properties. This material is central to this thesis.
- LAO** LaAlO_3 , a perovskite used as substrate for the growth of oriented films
- LNO3** LaNiO_3 a metallic perovskite used as template electrode for the growth of oriented L2NO4
- LRS** Low Resistance State
- MIEC** Mixed Ionic-Electronic Conductor
- MIS** Metal/Insulator/Semiconductor heterojunction
- MOM** Metal/Oxide/Metal capacitor-like heterostructure
- MS** metal/semiconductor heterojunction
- MU** Memory Unit
- NDR** Negative Differential Resistance
- NGO** NdGaO_3 , a perovskite used as substrate for the growth of oriented films
- PEEM** Photoemission Electron microscopy
- PiMOCVD** Pulsed-injection Metal-Organic Chemical Vapour Deposition
- PLD** Pulsed-Laser Deposition
- ReRAM** Resistive (or Redox) Random-Access Memory
- ROI** Region Of Interest
- RS** Resistive Switching
- RSM** Reciprocal Space Maps
- RTA** Rapid Thermal Annealing
- SBH** Schottky Barrier Height
- SOFC** Solid-Oxide Fuel Cell

SpLine Spanish Beamline at the ESRF

STO SrTiO₃, a perovskite used as substrate for the growth of oriented films

TAT Trap-Assisted-Tunnelling

TEM Transmission Electron Microscope

TLM Transmission-Line measurements

VCM Valence-Change Mechanism/Memory

XANES X-ray Absorption Near-Edge Structure (carried out at the ESRF)

XAS X-Ray Absorption Spectroscopy (carried out at the ESRF)

XRD X-Ray Diffraction

Acknowledgments

Choosing the way of the PhD is as much a professional choice as it is a personal adventure, and as in every aspect of your life, a PhD has its beautiful moments and its disastrous ones... except that you are oscillating between these two states more often and more dramatically, and it just gets worse with time. Keeping a healthy work-life balance is in itself already a demanding task, as you're soon confronted with your own limitations in a never ending pool of knowledge that made me feel like I knew less every time I learned more. You will eventually also have to deal with the inevitable problems that come your way as much as with the people that might help you solve them.

Even though the field of Research and its never failing *Scientific Method* is supposed to be as objective as it is robust, allowing us to deepen our understanding of the world we live in by carrying out these well designed experiments resulting in those trustworthy measurements, it also remains profoundly human. As in any other collaborative work, you get to spend time with other people which have more or less big egos against whom you can confront your own. This results in the development of sometimes conflicting, sometimes symbiotic relationships.

I like the idea that even though your past lies behind you, it is not immutable. That in a certain way both your future and the memories of your past are a result of your present, evolving constantly depending on your current mood and on the people you meet and interact with, day after day. The following acknowledgments are bound to be engraved in a never ending present, a still photograph of an otherwise constantly evolving mind and mindset, witnessed by you as the reader. Today it is time to shape tomorrow and remember all the good that happened during this adventure and to thank all the people that helped me along the way.

First I would like to express my gratitude to all the members of the jury, in all their diversity of specializations for having accepted to assess my work and without whom this entire acknowledgments section would have lost some of its sense.

Thank you Franz, for being the director of LMGP during my entire stay. I had the chance to realize that, even though occupying this position is a highly demanding task, you still managed to be deeply concerned by the well being of the entire staff in an unobtrusively subtle way. Carmen, how could the lab survive without you?! Being part of the non-permanent staff, I

wholeheartedly support your well deserved title of '*Mother of the lab*'!

Michel, I'm grateful that you endorsed the role of PhD director during my time as a PhD student. Thank you also for having shared your knowledge about X-Rays and how they diffract, and for your never ending skepticism about my experimental results.

Quentin, thank you for your wise advice, for being fair and square, and for all the good mood you sent my way during this thesis. I'm happy having had the chance to enjoy your pedagogy as a teacher and your unrivaled eccentricity.

Mónica... thank you.

Raquel, I'm happy you joined our team, it is priceless to have a colleague with whom you share the same ways of working. It makes communication so much easier that I sometimes even felt communicating was overrated... and it's even better if that colleague is also a very good friend! Carlos, as I'm writing these acknowledgments you are our latest recruit to the group and I already know you will take over the 'ways of the work' with great dexterity. Valentin, the tall intern I once had: it has been a pleasure working with you! Dolors, I've very much enjoyed your dynamism and fierce personality during our meetups. I wish you the best for wherever the future will be taking all of you.

Thank you Laetitia, Odette, Xavier, Etienne, David and Edouard for your precious help with the characterization of my samples and all your diverse personalities. I'm very grateful also to you Hervé. On top of taking care of the XRD experiments you are also a backbone in the functioning of LMGP. In the backstage you make things seem transparent, you are one of the upright persons I could meet in the lab.

Still concerning the people I want to acknowledge from LMGP, Céline I'm glad I could share an office with you during my last year as a PhD student, thank you for being a great office mate!

Daniel, I've enjoyed very much those late-night writing sessions of our respective PhD theses where you provided the necessary fuel to keep on going!

Michèle, un grand merci pour ta bonne humeur quotidienne ! A l'image d'un engrenage ne fonctionnant que s'il est bien huilé, tu permet au laboratoire de fonctionner pendant que nous autres chercheurs avons le nez dans nos recherches. Tu assures autant sur les problèmes administratifs (qui peuvent être au combien frustrants) que sur le contact humain, et ça ce n'est pas donné à tout le monde. Merci à toi aussi Virginie pour la gestion des missions que j'ai faites à l'étranger.

Viet, we started and finished our PhD together and I'm glad we could share this period of our lives. All these insightful discussions about science and the world, on how from a child living in the remote countryside you can become a full-grown scientist at the other side of the Earth! I wish you all the best for your future projects back in Vietnam.

Cesar, thank you for all the great discussions about society, artificial intelligence and greater dimensions around the coffee table... I started programming in Python thanks to you, undoubtedly one of my better decisions!

I really want to thank the entirety of the LMGP staff, both permanent and non-permanent for its diversity and for making it a very pleasant and lively place to work.

Outside of LMGP: German and Juan, thank you for your skills and knowledge, and for being our hosts at the SpLine ESRF beamline, 2018 has been ‘the year of the beamtime’ (at least for me).

During my time as a PhD student, I had the chance to collaborate with other humans abroad:

At ICN2 in Barcelona: thank you Santi for your warm welcoming in your team, Sensei Roque, for being a great host and making me feel comfortable in the lab from the first day of my arrival, Laura and Jessica for your help with the experiments and your friendliness.

At Imperial: thank you Ainara for your invitation, Richard for sharing your knowledge about SIMS, Federico and Andrea as representatives of the local Italian mafia and finally Fidel for our decision to carry out an internship in the same place at the same time.

At UCL: thank you Tony for allowing me in, and then there is also Mark... I won't forget our late night cAFM experiments you so kindly proposed to do.

Finally, Mónica (second round!)... the most difficult acknowledgments I've had to write yet. Of course ‘thank you’, doesn't even begin to say how grateful I am for everything you've done. Without your motivation and never failing perfectionism, this thesis would only have been the shade of what it has become. You've offered me the chance to go abroad and to give me a taste of how international Research really is, and I willingly took them. I know now that your support and dedication during some of the difficult moments of my PhD is in itself already something special and that not every student gets that chance. I received some general directions, a lot of positive feedback, an immense freedom and a few intense brainstorming sessions, coupled with major revisions of the final manuscript, and now I'm a Dr!... well that escalated quickly! Again: thank you.

I want to open the friends-acknowledgments-section with you João as you have proven to be much more than a work colleague, over the years you have become a trustworthy friend and a big part of my ‘Grenoble experience’. This is also where I want to thank everybody in the select #LouvreInGrenoble group, I'm not naming you on purpose so you can remain special.

Rata, je suis vraiment heureux de t'avoir comme amie, à ton amour pour les choses bien faites... et ton salon de thé! A la magnifique Elsa qui a vu le jour pendant ma tumultueuse période de pré-soutenance, on m'a dit que tu n'y étais pas pour rien Claude (HéHé). Merci pour cette amitié partagée.

Gracias KiKe, Marin, Camille et Simon mes collocs d'un temps, Cindy ma colloc d'un autre temps.

Thomas, Thibault, Maxime, Simon et Joan je vous transporte avec moi depuis de nombreuses années, vous me procurez cette bouffée d'air frais qui sent bon les Cévennes.

À ma jeunesse passée en haut d'une montagne, à la sensibilité qui m'y a été transmis. Ik ben geen familie mens, maar... paps en mams ik hou zielsveel van jullie, ik draag jullie mee waar ik ook ga. Aan mijn zussen, nichtjes en andere familie in het buitenland, aan Loïs, het broertjes dat toch nog kwam.

Pour finir, merci à toi ma Madam des petits matins aux café crème.

This thesis is now finished.

To all the people I have met, and the ones I still have to meet.
To Life and its Diversity.

Foreword

Structuration of the thesis - storyline

This thesis is focused on the optimization and understanding of the valence-change memory (VCM) mechanism in memristive devices. Even though each chapter has been written with the intention of being self-contained, this dissertation should be read linearly as every new chapter prepares the field for the next one. This project turned out to be highly multidisciplinary, from the deposition optimization of complex oxides, the cleanroom fabrication of microelectronic devices, the device characterization and finally the comprehension of the physical mechanism behind the measured device properties, this thesis has been written in a way that better conveys the logical steps giving rise to the story behind this PhD project.

The storyline is the following. The first chapter situates the work carried out during this thesis in the rapidly evolving field of microelectronics, and more particularly in the emergent memory technologies and new computing paradigms within the field. The materials characteristics required to build these new memories with interface-type memristance are emphasized, in this case the need for mobile oxygen ions in the solid state. The material properties of $\text{La}_2\text{NiO}_{4+\delta}$, an oxide with very interesting oxygen-ion conduction properties, when used as building block for VCMs are presented in Chapter 2. Chapter 3 offers a transition between material science and device design, showing how a material such as $\text{La}_2\text{NiO}_{4+\delta}$ can evolve into a functional device when evaporating electrical contacts on top of it. Chapter 4 is mostly an experimental chapter where the electrical characteristics of a previously optimized Pt/ La_2NiO_4 /Ti memristive device are assessed. Finally, Chapter 5 opens up new perspectives of using a functional electrode such as LaNiO_3 to grow complex-oxide epitaxial heterostructures such as $\text{La}_2\text{NiO}_{4+\delta}/\text{LaNiO}_3$. Each chapter has its own summary to facilitate the reading. The manuscript ends with a general summary and perspectives for this PhD project. All the results which did not fit into this storyline have been transferred to the (rather large) appendix section of the thesis, in view of keeping the main message as clear as possible. Figure 1 illustrates the structure of the thesis and the links between the main chapters and the appendixes.

I wish you a pleasant reading!

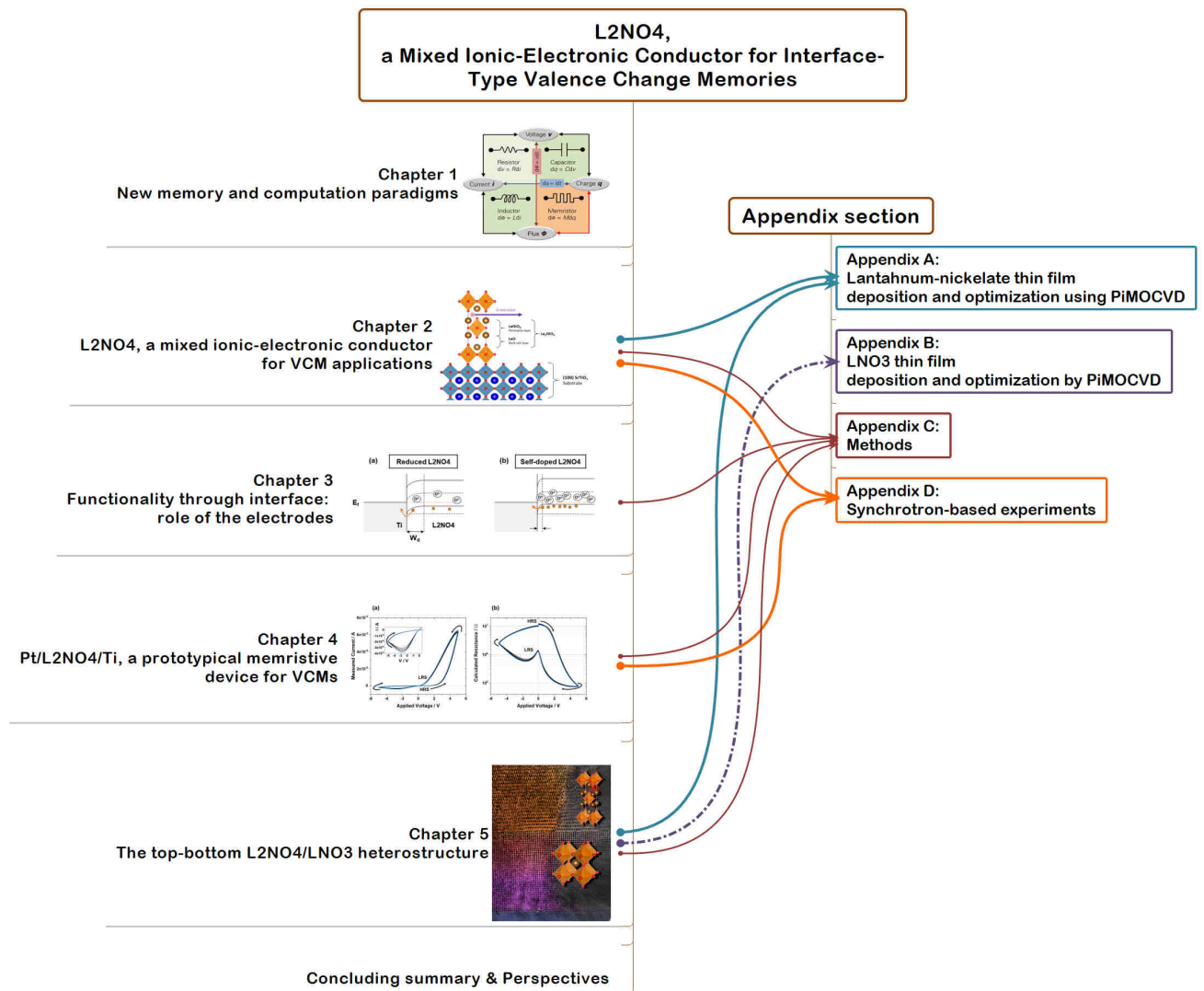


Figure 1 – Structuration of the thesis.

Chapter 1

New memory and computation paradigms

Contents

1.1	Beyond the von Neumann computation architecture	1
1.2	Memristive systems: a new memory paradigm	4
1.2.1	The memristor	5
1.3	Valence-Change Memories	7
1.3.1	Interface-Type Valence-Change Memories	7
1.3.2	Triggering ion migration in oxides	9
1.3.3	Triggering memristivity through electroforming	12
1.4	Concluding Words	13

1.1 Beyond the von Neumann computation architecture

Traditional computation relies on the von Neumann architecture where the functional units are both physically separated and rigid, meaning that they can only execute the task which they were built for. These units comprise: the memory unit (MU), the control/processing unit (the CPU, which encompasses both the control unit and the arithmetic/logic unit, or ALU) and all of them are linked by the data paths (Figure 1.1). The spatial separation of the different units leads to a physical limitation in the maximum speed the information can travel between memory and CPU, which is referred-to as the ‘von Neumann bottleneck’. Multi-core processors were able to increase the computing performances artificially by multiplying the amount of data being processed in parallel in different ‘cores’. Nevertheless, these processors are still limited by the von Neumann bottleneck as the fundamental computing elements remain unchanged [114]. By way of illustration, the Watson supercomputer is a very good

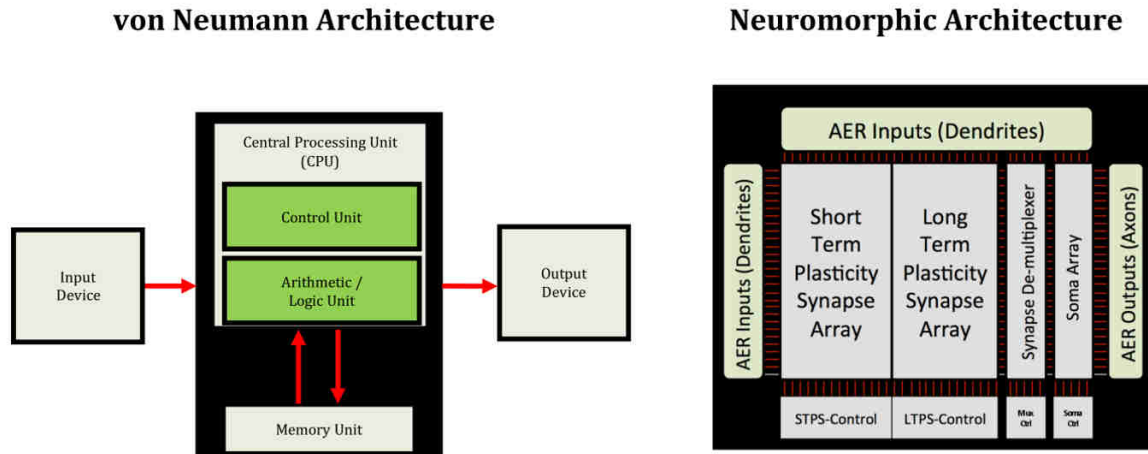


Figure 1.1 – Comparison of high-level conventional (von Neumann) and neuromorphic computer architectures. The so-called “von Neumann bottleneck” is the data path between the CPU and the memory unit. In contrast, a neural network based architecture combines synapses and neurons into a fine grain distributed structure that scales both memory (synapse) and compute (soma) elements as the systems increase in scale and capability, thus avoiding the bottleneck between computing and memory. Reprinted with permission from [114]

example of the technological prowesses that were enabled by the von Neumann architecture. Watson was initially built by IBM to be able to understand natural - thus context dependent - human language. As many as 2880 massively parallelized processors are providing its computational power. The total weight of IBM’s Watson is close to 100 000 kg, for an energy consumption of several megawatts . One of its key achievements already back in 2011 was winning against two of the greatest champions at Jeopardy, a famous American television game where three contestants are competing to be the first to figure out the question after having heard a series of clues that are part of the answer. This is a very complex and highly context-dependent task. Understanding the individual meaning of words is not enough to win this game, but understanding the meaning of a word in the *context* of a sentence is at least as important. Although the prowesses of this supercomputer are staggering, it is even more impressive that our brain provides us with the same contextual understanding of natural language, but with the major difference that it weighs just a little more than a kilogram, and consumes as little as 20 W of energy, the equivalent of a low-power incandescent light-bulb [134]. Furthermore, our brain makes us outstanding at performing a wide variety of highly diverse tasks such as reading, speaking, driving, and abstract reasoning to name a few. The large interconnectivity of our brain, provided by the 10^{11} neurons and 10^{15} synapses [73] is certainly one of the key factors that allows for this flexibility. This is where the neuromorphic architecture finds its inspiration.

The neuromorphic computing architecture goes beyond the classical von Neumann architecture as all the computational elements are mixed together (Figure 1.1). Their strength lie in the fact that they can evolve and adapt to changes in a dynamical way by “rewiring their circuits” so to speak. This makes them perfect for learning processes. A neuromorphic circuit is also inherently fault and noise-tolerant, able to discriminate signal from noise in real time. While non-volatile memories are also desired in this type of computational architectures, memory volatility is a key aspect to implement learning processes. *In fine* neuromorphic systems should enable near real-time analysis of large amounts of data, have an embedded learning process and approach human-brain power efficiencies [114].

Software-based machine learning, and in particular ‘deep learning’, which is based on multilayered neural networks will benefit highly from a hardware implementation of deep neural networks. Neuromorphic computing systems are designed to support dynamic learning of complex and unstructured data [114]. They are able to find patterns and classify data which would otherwise be impossible to classify using explicitly-written rules. A concrete example is the rising likelihood of having completely autonomous cars in the nearby future. Indeed, it is impossible to ‘hard-code’ every action a self-driving car should take so not to crash into another car, or a truck, a tree, a person or any other obstacle that has not been invented yet. Nevertheless, the autonomous car should still understand that the object it is driving behind is another car to adapt its speed if it wants to overtake it, or that a person standing next to a pedestrian crossing might start crossing the street at some point, but that a tree certainly will not. As human beings we are very efficient at making decisions based on this diverse and unstructured continuous flow of data thanks to the ability of our brain to learn, improving our decision-making capabilities by making it faster every time we discover or repeat a given task.

Today, the hardware of already commercialized neural networks are still mostly running on CMOS-based von Neumann architecture. The ‘neural’ part is actually only a software layer [73]. Already back in 2015, it was agreed during a roundtable about the needs for basic research in the field of neuromorphic computing that ‘*conventional approaches to computation will hit a wall in the next 10 years*’ [114]. The biggest challenge in the field is to be able to implement machine-learning on the hardware level, without requiring the additional software layer. An entirely new architecture with a completely new flexible interconnectivity is therefore needed, but above all, new components which inherently show neuron-like programming capabilities are required as the fundamental building pieces of this type of architecture. New components means new materials and/or engineered combinations of materials to show the desired neuromorphic memory properties.

1.2 Memristive systems: a new memory paradigm

It was already in the early 60's that Gordon Moore understood the immense influence integrated electronics would have on our relation to technology, in fields such as communication, transportation, data processing and many more. It would lead to a digital era where wonders such as personal computers and portable communication equipment would be rendered possible. In his paper "Cramming More Components onto Integrated Circuits" from 1965 [87], he first predicted empirically that the number of transistors on a chip would double roughly every year (it was refined to every two years in 1975). This prediction has been unexpectedly accurate over the past 50 years, and has led to very cheap integrated electronic systems. Gordon Moore foresaw that reducing the cost of integrated electronics would naturally decrease the manufacturing costs and lead to the technological bloom we have been experiencing over the last decades. In 1971, Intel released the first microprocessor that counted roughly 2300 transistors [59]. Today, the newly released processors count several billions of them and have increased calculation speeds, less leakage currents and overall better performances. There is no comparable technology that has seen such a drastic performance improvement within such a short timespan.

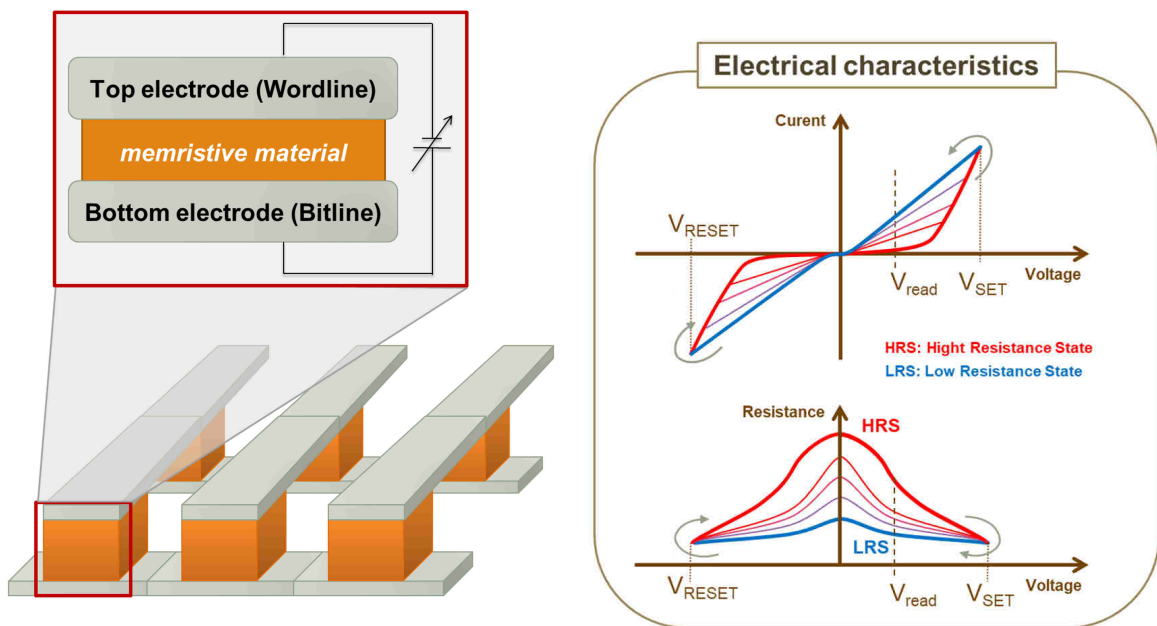
Nevertheless, as elementary components such as transistors continue shrinking to the nanometre scale, fundamental scaling limits are being reached [114]. They are indeed *fundamental* scaling limits as even if manufacturing technologies were to improve, they would not be able to increase the performance of our CPUs or memory chips any further. The increase in integration density is already leading to increased fabrication costs and power consumption, and more importantly to reliability issues. The complementary metal-oxide semiconductor, or 'CMOS' technology, with in particular the archetypal *field-effect transistor* (FET) is suffering from tunnelling current issues, loss of effective gate control and threshold fluctuations upon miniaturization [72]. It is thus the entire transistor architecture that needs to be rethought to keep on improving the computational power of our integrated electronic circuits. Two paths have been wandered to reach this goal. On the one hand new, but still transistor-based architectures (such as FinFETs or 'gate all around' FETs), which still rely on conventional CMOS technology are being developed, together with new 3D stacking technologies, allowing for an substantial increase in integration density. On the other hand, academia and industry are also considering new non-FET architectures to replace or complement the transistor-based memory and computation hardware still ubiquitous in our electronic devices as of today.

This thesis is focused on the further understanding and development of novel materials and heterostructures to be applied in Two-Terminal Memristive Elements, widely used in resistive random-access memories (ReRAM). ReRAM is an emerging non-volatile memory technology using a two terminal capacitor-like structure as its fundamental building block. This building

block is called a *memristor*. The characteristics of a memristor are discussed in the following section.

1.2.1 The memristor

The crossbar array architecture offers the most densely packed memory or computational architecture possible with a minimal device size¹ of $4F^2$, offering a large interconnectivity between electrode lines (wordlines and bitlines) such that each memory unit can be programmed individually. This interconnectivity enables the random access of the stored information instead of the sequential access leading to rather slow read/write delays experienced for example in magnetic hard drives. Figure 1.2a is an illustration of a crossbar array constructed from individual memristors.



(a) Sketch of a crossbar memory array with a magnification on an individual memristive unit cell showing the top-bottom electrode configuration.

(b) Simplified illustration of the I-V (top) and R-V (bottom) characteristics of a multilevel memristive cell.

Figure 1.2 – Memristor crossbar arrays and memristivity.

The memristor itself was first theorized by Leon Chua in 1971 as the missing circuit element [30], an element as fundamental as the resistor, the capacitor or the inductor. Controversy

¹the 'F' in $4F^2$ represents the smallest feature size possible at a given technology node. For example, ASML the worldwide provider of lithography tools for chip manufacturers announced their "TWINSCAN NXE:3400B", to be commercialized in late 2018 or early 2019 which would reach the 7 and 5 nm technology nodes! [5]

about finding the memristor [40, 123, 132] has led to the appearance of a more general term being used. Instead of memristor - which corresponds to a fundamental circuit element with well defined *theoretical* properties - the term ‘memristive device’ is often used instead to refer to devices showing hysteretic current-voltage characteristics with a so-called ‘pinched hysteresis’ at the origin (*i.e.* when $V = 0$ V, $i = 0$ A).

A memristive device has a very simple architecture: it has a capacitor-like structure where an insulating or semiconducting material is sandwiched between two electrodes. The application of an external bias, for example in the form of a current or a voltage pulse enables a reversible change in resistance of the device. Figure 1.2b illustrates how the current-voltage (I-V) characteristics of a memristive device evolve under a bipolar voltage sweep. The device can be programmed into two different resistance states, the high resistance state (HRS) and the low resistance state (LRS). At a positive threshold voltage (V_{SET}), the device is switched from LRS to HRS while at a negative threshold voltage (V_{RESET}) the device can be switched back from HRS to LRS. Furthermore, intermediate resistance states can also be programmed as illustrated by the additional resistance levels in the R-V characteristics at the bottom of Figure 1.2b. These intermediate resistance states can for example be attained when changing the voltage sweep rate or the current compliance, or the pulse duration/amplitude in the case of a pulse-controlled programming of the device (which is the final goal when implementing it into the final ReRAM crossbar memory arrays). Finally, the programmed resistance-state of the device can then be accessed in a non-destructive way using a lower readout voltage (V_{read}).

This resistance-change phenomenon was first reported in 1962 by T.W. Hickmott [54] in a Al/Al₂O₃/Au stack and many other works have documented this memristive behaviour ever since, usually by using the terms ‘resistive switching’ (RS) although, electronic pulse induced resistance (EPIR) or ‘memristivity’ have also been used.

In literature, the electrical response leading to RS can be categorized mainly into two types: unipolar or bipolar, referring to the bias polarity that should be applied to switch the device reversibly between HRS and LRS. Furthermore, subcategories such as *filamentary switching* or *interface-type switching* have been made to get a better insight on the switching mechanism and its location. Indeed, in filamentary switching, the phenomenon takes place locally (in the form of filaments) within the bulk of the sandwiched material while in interface-type switching it takes places throughout the entire electrode/insulator (or semiconductor) interface. Experimentally, the two types of switching can be differentiated by the fact that only the interface-type switching should scale with the electrode area while the localized filamentary pathways should not be affected by a change in pad size (Figure 1.3.a and b). Nevertheless, other intermediate situations can also occur, such as the formation of multiple filaments or large but incomplete switching regions beneath the electrode. Furthermore, a scenario where the two

idealized switching mechanisms are present in the same device is also very likely [90, 108]. The reader is redirected to the review written by Bagdzevicius *et al.* for more details about interface-type switching in perovskite materials in particular [10].

The switching mechanisms can be narrowed down even further to the physical origin of the measured memristivity. Figure 1.3.c illustrates the main resistive switching mechanisms present at the microscopic level which have been reported in literature. The understanding of the microscopic mechanisms behind memristivity is ultimately the goal of research carried out at the academic level in hopes of better understanding, modelling and finally proposing a rational design of material stacks for their implementation in reliable memory technologies.

The valence-change memory mechanism (VCM) will be detailed in the following section as it is central to the work presented in this thesis.

1.3 Valence-Change Memories

A subcategory of bipolar memristive devices is referred-to as ‘Valence-Change Memories’ in which internal redox reactions govern the resistance-change mechanism. More particularly, in oxide materials, the motion of oxygen ions is held responsible for the local valence-change (redox-reaction) in the cation sublattice [135], with as consequence a more or less important change in the electronic conductivity depending on the structure of the device and the materials composing it. Both filamentary and interface-type switching can exhibit a VCM mechanism (Figure 1.3.c). Nevertheless, it should be noted that once memristive devices are manufactured at the nanometer scale, there comes a point where only interface-type switching can be present due to the finite, nanometer-size of the filaments. When reaching that point, the exact composition and structure (or lack thereof) of the filaments should be known in hopes of being able to engineer them². Currently there is little control over the filament properties as they are most usually obtained after a so-called ‘forming process’, which is usually compared to a soft dielectric breakdown of the sandwiched material.

1.3.1 Interface-Type Valence-Change Memories

In this section the functioning of oxide-based interface-type valence-change memories will be described.

In interface-type VCMs, the resistance-change is usually attributed to a field-induced change of a Schottky barrier at the metal/oxide heterojunction [135]. The externally-applied

²This understanding of the structure and composition of the material at the nanoscale is of course only interesting from the academic point of view, in industry the priorities lie elsewhere (it does not really matter how it works, as long as it does work!)

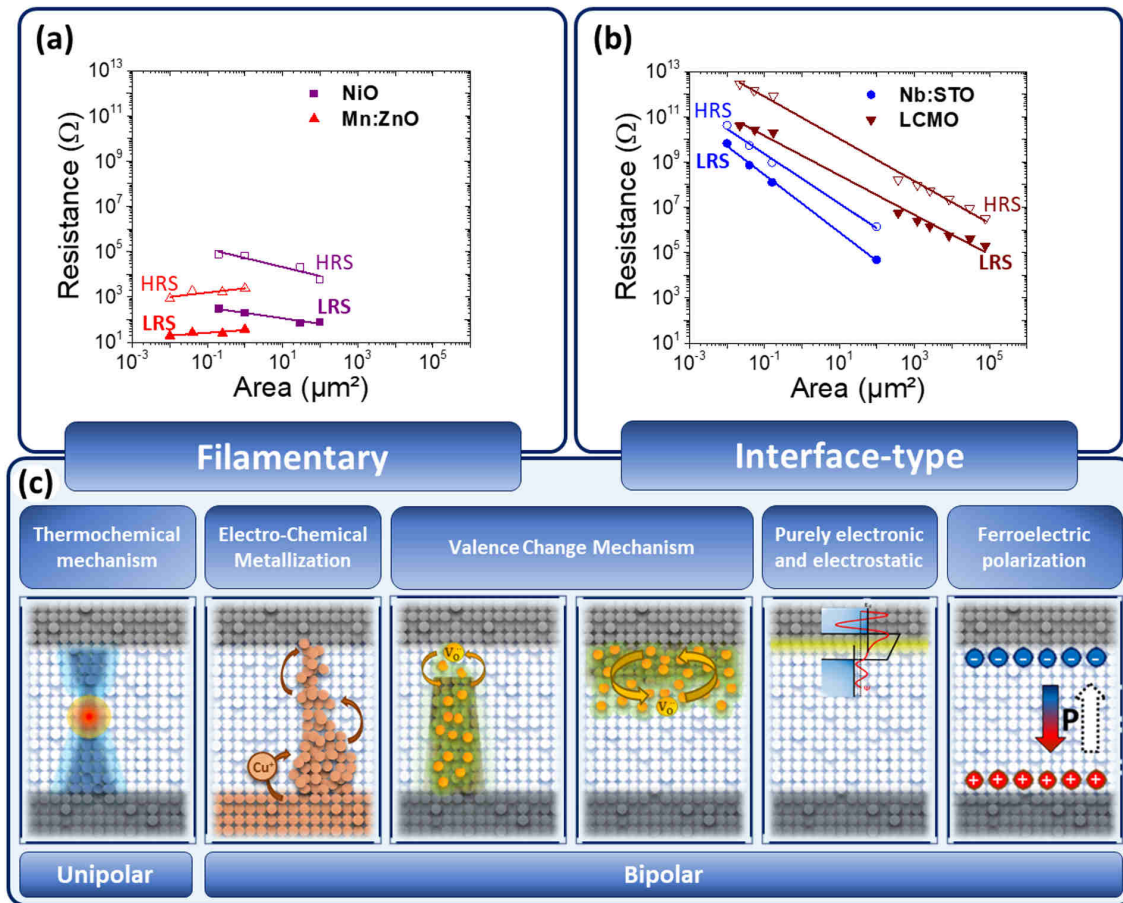


Figure 1.3 – Area dependence of the high- and low-resistance state (HRS and LRS) values for (a) filamentary and (b) interface-type RS. Data for each oxide-based memristive device extracted from references: NiO [7], Mn:ZnO [97], Nb:STO [118] and LCMO [51]. (c) Classification and illustrations of the reported RS mechanisms for filamentary and interface-type switching. From left to right: thermochemical mechanism (TCM), electro-chemical metallization (ECM), filamentary valence change mechanism (VCM), interface VCM, purely electronic and electrostatic effects and ferroelectric polarization mechanism. For the ECM mechanisms, the arrows depict migration of the electrode material in the form of cations (eg Cu^+ or Ag^+) while in VCM-type switching, the arrows show the migration of oxygen vacancies under device operation. Reprinted with permission from [10].

electric field induces a drift of oxygen ions which accumulate at the positive electrode, locally changing the metal/oxide junction properties, such as for example the depletion width (W_d) of the majority carriers. This process is illustrated in Figure 1.4.

Besides changing the characteristics of the Schottky contact, the accumulation of oxygen ions near the electrode can also lead to the generation of interlayers. The supply of oxygen ions from the oxide layer (or from the atmosphere) into the metallic electrode can result in

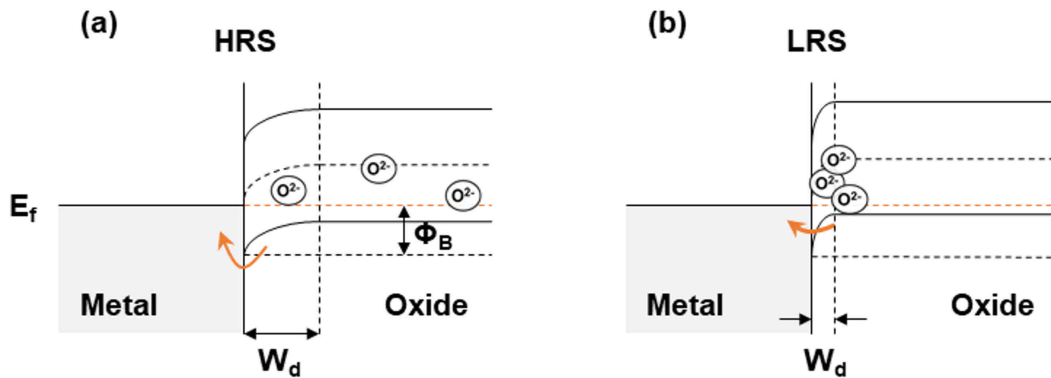


Figure 1.4 – (a) Schottky junction between a metal and an p -type oxide semiconductor with homogeneously distributed oxygen ions. (b) The same junction after having applied a positive voltage on the metal electrode, causing the drift of the oxygen anions towards the metal/oxide junction and changing the characteristics of the memristive device from HRS to LRS. W_d is the depletion width and Φ_B is the Schottky barrier height.

the formation of these oxide interlayers. This process is mostly dependent on the Gibbs free energy for the formation of the metal-oxide phase (from the electrode material) and will be further discussed in Chapter 3, in the Section: **Oxygen affinity of the electrode and formation of interlayers**. The additional oxide interlayer then adds a series resistance to the device, increasing its resistance-state and (in some cases) can trigger a memristive behaviour.

Finally, an homogeneous bulk valence-change mechanism where internal redox reactions change the electronic-conduction properties of the entire sandwiched oxide layer can also take place, and was for example reported in [3]. Nevertheless, an oxygen reservoir (being it a solid layer added to the stack or the atmosphere) is still required to store and restore the oxygen content exchanged by the oxide film.

R. Waser pointed out that ‘*The limiting factor of the switching process in VCM cells is supposed to be the mobility of oxygen vacancies due to its low value at room temperature and at low electric field*’ [135]. Therefore, the different ways to trigger or improve oxygen migration in mixed ionic-electronic conducting materials will be discussed briefly in the following section.

1.3.2 Triggering ion migration in oxides

There are multiple ways to trigger oxygen-ion migration in solid ionic conductors. In this section we will describe how a chemical gradient, an electric-field or a temperature gradient can trigger these migration dynamics.

Electric Field When considering the oxygen atoms as negatively-charged point defects (or similarly oxygen vacancies as their positively-charged counterparts), they become sensible to coulombic interactions and thus to externally-applied electric fields. In a crystalline matrix, oxygen-ion migration can be thought of as a hopping process in a periodic potential [77] (Figure 1.5.a). Nevertheless, an electrical field can only modulate the oxygen distribution in a nanoscale distance, as the expected field required to move oxygen ions is around the order of 10^6 V/cm [8, 33]. Luckily this field strength becomes technologically viable at the nanoscale, representing for example 10 V applied on a 100 nm-thick film. The more localized the voltage drop (at the metal/oxide interface for example), the higher the electric field and the more likely a field-induced drift of oxygen becomes.

On another side, a local temperature increase in the form of Joule heating could dramatically increase oxygen mobility. The local heating is however difficult to assess at the nanoscale. Important atomic displacements can happen when combining these two effects: high electric fields and subsequent Joule-induced temperature increase [8, 68]. In these conditions, hopping rates can attain $\sim 10^7$ s⁻¹ [77], consistent with some reports of nanosecond switching speeds in filamentary systems [26].

Soret diffusion A temperature gradient ∇T can result in an isotropic hopping of oxygen atoms. The additional thermal energy an atom possesses makes it easier for it to hop to another site until it finds itself trapped again in another potential well in a cooler region of the material. The microscopic force leading to this net oxygen motion from hotter to cooler regions in the sample is termed the *Soret force* [77] and is represented in Figure 1.5.b. The Joule heating generated when applying an external electric field can generate these temperature gradients within the material, particularly in the presence of highly conducting filamentary pathways [77]. In the case of interface-type switching, the metallic electrode could also play the role of a heat sink (depending on the electrode material), generating more homogeneous temperature gradients within the oxide material in a perpendicular direction to the contact, effectively attracting oxygen atoms towards it.

Fick diffusion A chemical composition gradient will tend to re-equilibrate to maximize entropy. Practically speaking, oxygen atoms present in oxygen-rich regions will tend to diffuse towards oxygen poor regions until a flat oxygen profile within the material is achieved [77]. This process is illustrated in Figure 1.5.c. An oxide in its pristine (unprogrammed) state should initially have a uniform³ distribution of oxygen atoms, making the Fick diffusion process

³The term ‘uniform’ might be a bit of a stretch here as space-charge regions usually exist at the surface of a material and/or at grain boundaries or other extended defects. Nevertheless, there should initially exist a *stable* oxygen distribution taking into account all these chemical and electrical fluctuations within the material.

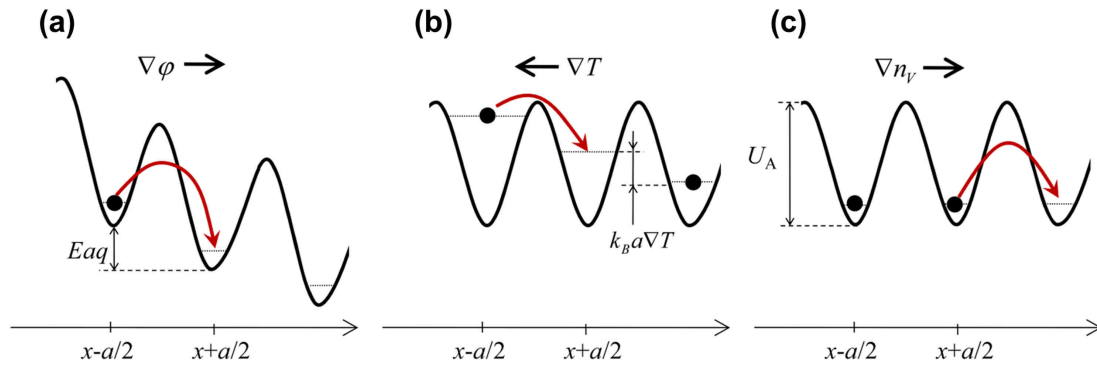


Figure 1.5 – Schematic illustration of the forces that influence oxygen anion motion for (a) drift (electrical potential gradient), (b) thermophoresis (temperature gradient) and (c) Fick diffusion (concentration gradient). Adapted with permission from [122].

negligible.

Nevertheless, once an external field is applied, assuming that no solid state reactions take place at the interface and that the oxide material allows for a wide range of oxygen stoichiometries (*e.g.* perovskites), then oxygen ions would start accumulating at the positive electrode interface (see for example Figure 1.4), the oxygen concentration profile is then no longer uniform, and, once the field is removed, it would be expected to relax back to a state that resembles the initial resistance state (IRS)⁴. This equilibration process should have a duration which is characteristic to the oxide used as ionic conductor (related to its oxygen diffusion coefficient), keeping in mind that some metastable states of a material can have very long time constants.

The fickian diffusion process should be of key importance in the volatility-rate of VCMs. Oxide-ion conductors with different oxygen-diffusion coefficients would then enable tuning the retention time of memristive systems. This is particularly interesting for neuromorphic applications as both volatile *and* non-volatile memories are of interest in the construction of neuromorphic computing architectures, in the *short-term plasticity* and the *long-term plasticity* synapse arrays, respectively (see Figure 1.1). The three forces described above can be present simultaneously with different magnitudes depending on the biasing conditions and the material systems. They are also intricately connected: applying an external electric field induces a current which can lead to a subsequent temperature increase through Joule heating, triggering Soret and Fickian diffusion processes. Temperature increase and concentration gradients can then favour chemical redox processes and new chemical gradients... the complex

⁴only if the biasing did not lead to important and irreversible changes in the structure/composition of the oxide material, as would be the case during an electroforming step.

interplay between all these forces will determine whether or not the new state of the material is thermodynamically stable, and if not how fast this new kinetically stable state will return to equilibrium.

Interestingly, the important non-linearities in the oxygen mass transport activation provided by temperature or electric-field, in conjunction with the chemical activity of oxygen are key to solving the ‘voltage-time dilemma’. This dilemma was pointed out by Schroeder *et al.* [113] to illustrate how, in purely electronic systems, very fast memory operation speeds (preferably in the nanosecond-range) are not compatible with long-term memory retention capabilities (which should be ~10 years for non-volatile memory applications). Additional mechanisms such as redox reactions and mass transfer should also be present to render these contradictory memory requirements possible.

Enhancing oxygen mobility in oxides Materials exhibiting slow ion migration can benefit from a large amount of grain boundaries or amorphous phases while ionic conductors benefit from a highly ordered single-crystalline micro structure [33]. Tensile or compressive chemical stresses can - in theory - alter the oxygen mobility in a material by several orders of magnitude when compared to its bulk values by modifying the activation barrier for migration [33]. In particular, a tensile strain of the crystal lattice will favour the generation of oxygen vacancies to relax stress, enhancing the overall oxygen mobility in an oxide material [75].

Other ways of increasing oxygen mobility in the particular case of filamentary resistive switching is through a ‘forming step’, as will be discussed in the following section.

1.3.3 Triggering memristivity through electroforming

The electroforming step is typically a one-time application of a high voltage (or current) triggering a large and usually irreversible change in resistance of the (pristine) memristive device. After being formed, the device can normally be programmed using lower voltages than the one required for electroforming.

In the final ReRAM devices, the implementation of a forming step leads to complications such as current overshoots and/or a non-uniform forming bias distribution inherent to the architecture of the memory [63]. The current overshoots can lead to a deterioration of any one of the components present on the chip, or even to the hard breakdown of the formed memory cell to a non-switchable resistance state. In the case of a voltage-controlled electroforming (as opposed to current-controlled), the use of a current compliance is usually crucial to avoid a hard breakdown of the device, setting it in an irreversible LRS [64]. On top of being a hassle for technological implementation, an electroformed device is subject to highly variable electrical properties [68]. Furthermore, the need for a forming step highly complicates the

comprehension of the mechanism behind the change in resistance. While a chemical resemblance might still exist, the formed device has no need to show any physical similarity to the pristine material. The forming step is likely to create new phases, or dope the material locally by generating new charge carriers through redox processes and/or point defects [129].

The forming step is usually needed when using an insulating material as switching medium, generating the LRS state. The current overshoot during electroforming was shown to be directly proportional to the pristine resistance of a HfO_2 -based memristive device [63]. The pristine insulating material then defines the highest resistance state possible, which usually cannot be retrieved after forming. The issue that arises when starting with a highly insulating material is that the control over the forming step is highly non trivial and usually leads to a stochastic switching process by nature. The forming step being analogous to a soft dielectric breakdown of the insulating medium, it will therefore likely nucleate at defects present within the bulk of the material. These defects come in the form of grain boundaries, regions with a higher concentration of point defects (such as oxygen vacancies) or even film roughness creating localized current hotspots upon device operation. These types of defects have already received a lot of attention and are now engineered in order to have a better control over the forming step and thus on the location of the filaments (roughness engineering in SiO_x [91], electrode shape engineering in Ti/STO/Pt [98]).

In general, defective oxides (deposited for example in reducing conditions such that oxygen vacancies are readily present in the material) can help getting rid of the forming step [41, 68]. This indirectly proves that the forming step is a destructive method, needed to generate defects and/or new phases that will trigger the functionality in memristive devices.

We will show in Chapter 4, Section: **The initialisation step** that an electroforming step is not required to trigger a memristive behaviour in Pt/ La_2NiO_4 /Ti heterostructure. Instead, what we will refer to as an ‘initialisation step’ (carried out at the same voltage as the one used for further programming of the memory), was needed to set the device in a HRS. It could be argued that MIECs in general, which are already good electronic conductors in their pristine state, allow eliminating the electroforming step and facilitate interface-type resistance-change mechanisms.

1.4 Concluding Words

Valence-change memories (VCMs) are in essence electrochemical systems based on a metal oxide capacitor-like structure where migrating defects give rise to the memory properties. Their implementation in micro/nanoelectronic solid state devices relies on an electronic readout to measure the state of the device and to operate them, but their functionality is highly depend-

ent on the electrochemical properties of the materials constituting the final device. Ion motion and its subsequent oxidation/reduction reactions is a key parameter that needs to be controlled in order to improve the properties of these types of memories.

In the following chapter we will present how the mixed ionic-electronic conducting properties of $\text{La}_2\text{NiO}_{4+\delta}$ offer a perfect playground for valence-change memory applications and how we could successfully prepare the material in the form of thin films using pulsed-injection chemical vapour deposition.

Chapter 2

La₂NiO_{4+δ}, a mixed ionic-electronic conductor for VCM applications

Contents

2.1	L2NO4: a layered structure with mixed conduction properties	16
2.1.1	Structural considerations and phase diagram	16
2.1.2	Mechanism for the incorporation of excess oxygen in L2NO4	19
2.1.3	Oxygen-ion diffusion in L2NO4	20
2.1.4	Hole self-doping and electronic conductivity in L2NO4	23
2.2	Motivation to use L2NO4 as a memristive material for VCM applications	26
2.3	Growth of L2NO4 thin films by PiMOCVD	28
2.3.1	Materials characterization aspects of the as-prepared thin films	29
2.3.2	Tuning the oxygen content through post-annealing treatments	36
2.4	Summary	38

“L2NO4” will be used throughout the thesis to refer to La₂NiO₄ when the exact oxygen stoichiometry is either not known or of little importance in the discussion. The exact composition will be detailed explicitly when needed (for example “La₂NiO_{4.00}” means that there is no over-stoichiometric oxygen in the lattice, in which case “La₂NiO_{4+δ}” would be used instead)

This chapter is divided into four main sections. The first section is a literature review on the structural, oxygen diffusion and electronic conduction properties of L2NO4. The second section then discusses the motivation that led to the consideration of L2NO4 as active material in a memristive device and how it can be of interest for VCM applications. The third section condenses the experimental results and material properties of L2NO4 prepared in the form of

highly oriented thin films using Pulsed-injection Metal-Organic Chemical Vapour Deposition (PiMOCVD). The chapter ends with a summary of the most important points exposed in each section.

2.1 L2NO4: a layered structure with mixed conduction properties

This section details the structural properties of L2NO4 and how the crystal is affected by the oxygen stoichiometry present in the sample. The mechanism for the incorporation of over-stoichiometric oxygen as interstitial point defect will be explained, followed by the presentation of the most relevant oxygen diffusion mechanisms reported in literature obtained from atomistic simulations. The origin of the *p*-type electrical conductivity in L2NO4 will end this section.

2.1.1 Structural considerations and phase diagram

L2NO4 is a member of the Ruddlesden-Popper series with general formula La_{n+1}Ni_nO_{3n+1}, which electronic conduction properties evolves from semiconducting for $n = 1$ (La₂NiO₄, K₂NiF₄ structure) to metallic for $n = \infty$ (LaNiO₃, perovskite structure) [20]. L2NO4 is best described as an alternation along the *c* crystallographic direction of LaNiO₃ perovskite blocks and LaO rock salt layers rotated by 45° in the basal plane of the parent tetragonal structure¹. Another description of the structure when considering only the shortest bond distances, would be a succession of NiO₂ and rock salt type La₂O₂ double layers. The two schematic descriptions are depicted in Figure 2.1. An additional Jahn-Teller distortion mechanism induces the elongation of the NiO₆ octahedra along the *c* crystallographic direction. The mismatch between these heterogeneous layers resulting from different Ni-O or La-O bond lengths is the reason for a variety of structural lattice instabilities described next.

Several stable but temperature-dependent structures have been refined using X-ray or neutron based diffraction techniques [52, 67, 102, 103, 119] on stoichiometric La₂NiO_{4.00} samples². A tetragonal *I4/mmm* structure is stable at high temperature ($T > 700$ K [52]). At lower temperatures ($80 \text{ K} < T < 700 \text{ K}$), a phase transition to an orthorhombic *Bmab* structure has obtained general consensus. This symmetry lowering is the result of a strain-induced tilt-

¹La₂NiO₄: ICDD : 00-034-0314; *SG* : *I4/mmm* (139); $a = b = 3.8617 \text{ \AA}$; $c = 12.683 \text{ \AA}$; $\alpha = \beta = \gamma = 90^\circ$

²stoichiometric samples could only be obtained using reducing treatments as La₂NiO_{4.00} was reported to already incorporate over-stoichiometric interstitial oxygen ions when simply exposed to air in ambient conditions [100, 101]

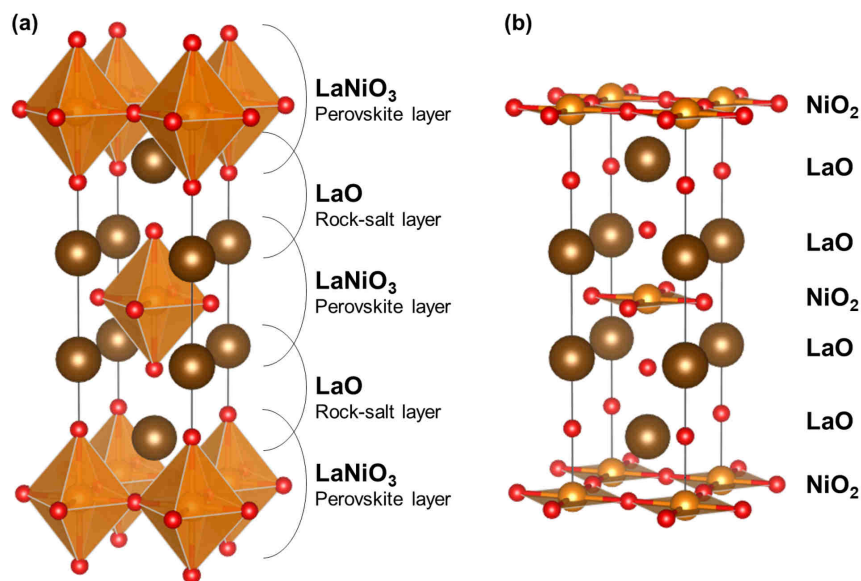


Figure 2.1 – Two schematic representations of the tetragonal $\text{La}_2\text{NiO}_{4.00}$ structure based on the NiO_6 perovskite-type octahedra (left) and closest bonds square-planar NiO_2 entities (right).

ing of the NiO_6 octahedra to release the internal stresses between compressed NiO_2 planes and stretched LaO layers. At even lower temperatures, a new tetragonal $P4_2/nm$ phase appears but there is no general agreement on this phase transition as an orthorhombic $Pccn$ structure has also been reported. All these temperature-dependent structures are referred to in literature as: HTT (High Temperature Tetragonal), LTO (Low Temperature Orthorhombic), LTT (Low Temperature Tetragonal) and LTLO (Low Temperature Less Orthorhombic). These are the main phases reported in literature for the indexing of stoichiometric L2NO_4 , but the possibility of monoclinic unit cells have also been evoked, showing the complexity to reach a general consensus and a simple description of the crystallographic structure for this compound. One of the reasons for this can be attributed to varying oxygen stoichiometry, meaning that different synthesis methods (and thus for example differences in the oxygen partial pressure) can result in the growth of different L2NO_4 phases. The K_2NiF_4 structure indeed offers a flexible playground for variable oxygen stoichiometry, with a preference for oxygen over-stoichiometry, which is referred to in literature as the Greek letter ‘ δ ’. In $\text{La}_2\text{NiO}_{4+\delta}$, this δ overstoichiometry is induced by oxygen ions localized in interstitial sites within the LaO rock salt blocks. As depicted in Figure 2.2, the additional oxygen which, when indexed in the tetragonal $I4/mmm$ space group is located at $(\frac{1}{2}; 0; z \approx \frac{1}{4})$ where it finds itself tetrahedrally coordinated by four La^{3+} ions and four O^{2-} ions, has an important influence on the lattice parameters and even the crystallographic symmetry of the L2NO_4 phase. High oxygen concentrations tend to prevent the NiO_6 octahedra from tilting (which lowers the symmetry), leading to a better stabilization

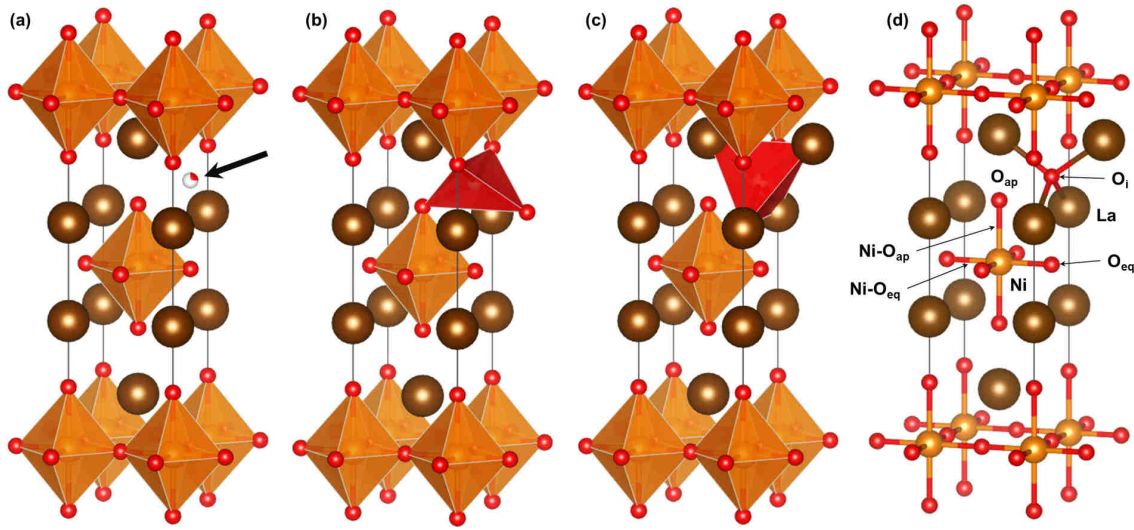


Figure 2.2 – (a) Location and local environment of the interstitial oxygen ion (arrow) in La₂NiO_{4+δ}. The interstitial oxygen is tetrahedrally coordinated by (b) four La³⁺ atoms and (c) four O²⁻ atoms (the resulting tetrahedrons are displayed in red). The naming convention used in the text for the different atoms and their bounds composing the structure is better evidenced in (d). O_{ap} stands for “apical oxygen atom”, O_{eq} for “equatorial oxygen atom”, O_i for “interstitial oxygen atom”, Ni-O_{ap} for “nickel-apical oxygen bond” and Ni-O_{eq} for “nickel-equatorial oxygen bond”. L2NO4 is represented in the space group *I4/mmm* (SG n°139).

of the HTT phase when $T < 700$ K [103].

While there is some level of discrepancy between the proposed phase diagrams in literature, Figure 2.3 proposes the phase diagram of La₂NiO_{4+δ} as a function of δ and temperature. A monoclinic unit cell has been reported at room temperature for stoichiometric La₂NiO_{4.00} samples [100, 101] although the *Bmab* LTO structure has been favoured in the more recent studies [57, 67, 102, 128]. Jorgensen *et al.* stated that the *Bmab* phase has a finite solubility for excess oxygen where $0.01 \leq \delta \leq 0.05$ [67]. Above this solubility limit the phase transforms into the *F/mmm* structure allowing it to better release the additional strain induced by the presence of the interstitial oxygen atom. Nevertheless, this finite solubility is believed to be the reason for a miscibility gap where the two orthorhombic structures coexist as a result of the interstitial oxide ions segregating into oxygen rich domains (with *F/mmm* symmetry) and oxygen poor domains (with *Bmab* symmetry) when $\delta > 0.05$. According to Rice *et al.* [102], the tetragonal *F4/mmm* structure is present at room temperature over a large range of oxygen over-stoichiometry, from $\delta \sim 0.06$ to $\delta \sim 0.15$ beyond which La₂NiO_{4+δ} adopts the orthorhombic *F/mmm* structure.

The appearance of miscibility gaps is explained by the strong correlation effects between these anionic defects. 1D ordering of the interstitials was reported for moderate oxygen con-

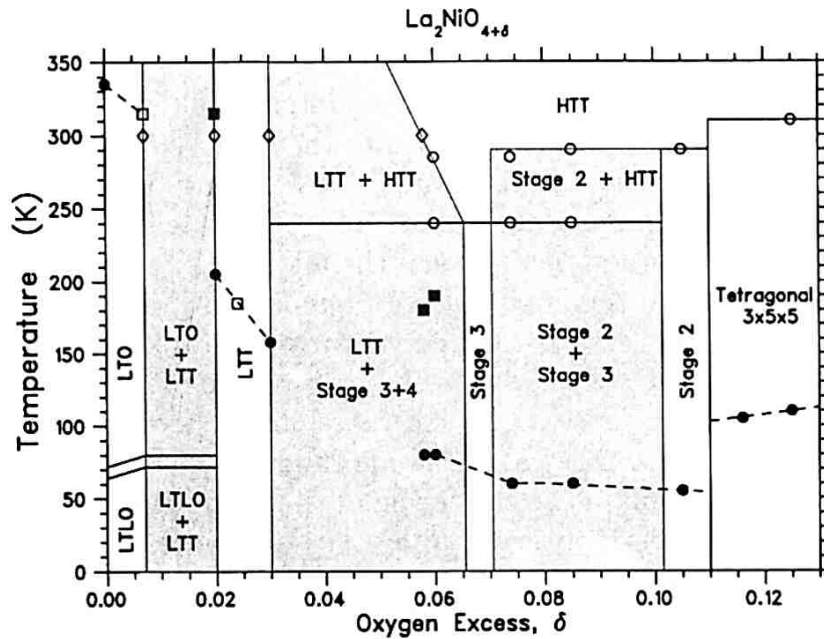


Figure 2.3 – Phase diagram for $\text{La}_2\text{NiO}_{4+\delta}$. Open circles (diamonds) indicate phase boundaries determined by neutron single-crystal (x-ray powder) diffraction. Solid circles denote Néel temperatures of primary phase, solid squares indicate Néel temperatures of secondary phases, and open squares indicate these transitions translated to the appropriate values of δ . The stage-3 phase region is an estimate that pure phase has not yet been observed. For $0.11 \lesssim \delta \lesssim 0.13$, the interstitial oxygens are ordered three dimensionally, and the incommensurate magnetic ordering involves a simultaneous ordering of holes. Reproduced with permission from [128].

centrations while very high oxygen overstoichiometry can lead to 3D interstitial ordering [57]. More details on how a structure, which at first glance seems to be densely packed, can accommodate an extra oxygen atom is given in the following section.

2.1.2 Mechanism for the incorporation of excess oxygen in L2NO4

The oxidation of $\text{La}_2\text{NiO}_{4.00}$ being an exothermic process is widely accepted [86, 93]. This can be explained when considering that the charge separation between the $\text{La}_2\text{O}_2^{2+}$ and the NiO_2^{2-} layers is reduced upon incorporation of the negatively-charged interstitial oxygen defects in the $\text{La}_2\text{O}_2^{2+}$ layer and the charge compensating holes in the NiO_2^{2-} layer [102]. This being said, the incorporation of an additional oxygen atom in a structure composed of two densely packed substructures (rock-salt and perovskite) is in itself a surprising phenomenon. Skinner showed that this process is possible thanks to an important synergy between the different atoms (and their bonds) composing the K_2NiF_4 structure [119]. Through neutron diffraction experiments, he has showed that the apical Ni-O_{app} bond-length undergoes a dramatic length-

ening with the loss of interstitial oxygen. What is more, he also showed that the Ni-O and La-O bonds are continuously compensating the loss of interstitial oxygen by adapting their bond length, keeping changes in the lattice volume minimal. The Ni-O_{app} bond shortening in the presence of an interstitial oxygen atom was also confirmed in the work of Jorgensen *et al.* who refined the L2NO4 structure either in *Bmab* or *Fmmm* depending on the oxygen content [67]. In their work, the interstitial oxygen defect occupies the $(\frac{1}{4}, \frac{1}{4}, z \approx 0.23)$ position in the orthorhombic *Fmmm* lattice where it is coordinated to four neighboring La atoms and triggers the displacement of four neighboring apical oxygen atoms (of nearly 0.5 Å) from their original sites to take its position. Regardless of the structure, the Ni-O_{app} bond is more affected by the presence of O_i than Ni-O_{eq}. According to Bassat *et al.*, an additional anti-phase boundary arising from the tilting of the NiO₆ octahedra is needed to provide sufficient space for the accommodation of O_i [11]. This cooperative effect of octahedra tilting can then help the formation of other interstitial oxygen ions and act like an extended defect. A one dimensional ordering of the interstitials induced by (and inducing) NiO₆ octahedra tilts has been well described by Tranquada *et al.* where the ordering has been measured through the presence of superlattice peaks in their XRD diffraction patterns [127, 128], or by Hiroi *et al.* through electron diffraction techniques [55].

First-principle calculations carried out by Akbay *et al.* have shown that L2NO4 exhibits catalytic properties towards the reduction of oxygen [2]. Indeed, the presence of an electron in the 5d orbital of La ([La] = [Xe]5d¹6s²) polarizes the 6s valence orbitals, facilitating the chemisorption and dissociation of molecular oxygen due to the charge transfer between O₂ and the LaO surface of L2NO4. Furthermore, the presence of vacant oxygen sites in the NiO₆ octahedra significantly lowers the activation energy required for the dissociation of O₂ (0.28 eV instead of 1.095 eV in the case of a defect-free LaO terminated surface). Frayret *et al.* calculated that the formation energy of a Frenkel-type defect where O_{eq} takes the place of O_i, leaving behind an oxygen vacancy in the equatorial position ($O_{O,eq}^x \leftrightarrow V_{O,eq}^{\cdot\cdot} + O_i^{\cdot\cdot}$) is around 1.59 eV [39]. The presence of such a defect, as was shown by Akbay *et al.*, is then beneficial for the oxygen uptake and further explains why over-stoichiometric La₂NiO_{4+δ} is a stable compound, at least in ambient conditions.

Frayret *et al.* also evoke the possibility that these $V_{O,eq}^{\cdot\cdot} - O_i^{\cdot\cdot}$ Frenkel pairs are a prerequisite for the oxygen bulk conduction in L2NO4. This aspect will be developed further in the next section.

2.1.3 Oxygen-ion diffusion in L2NO4

The structural anisotropy of L2NO4 is the origin of the important anisotropy in its oxygen migration properties. Kharton *et al.* stated that the oxygen transport through nickelate ceram-

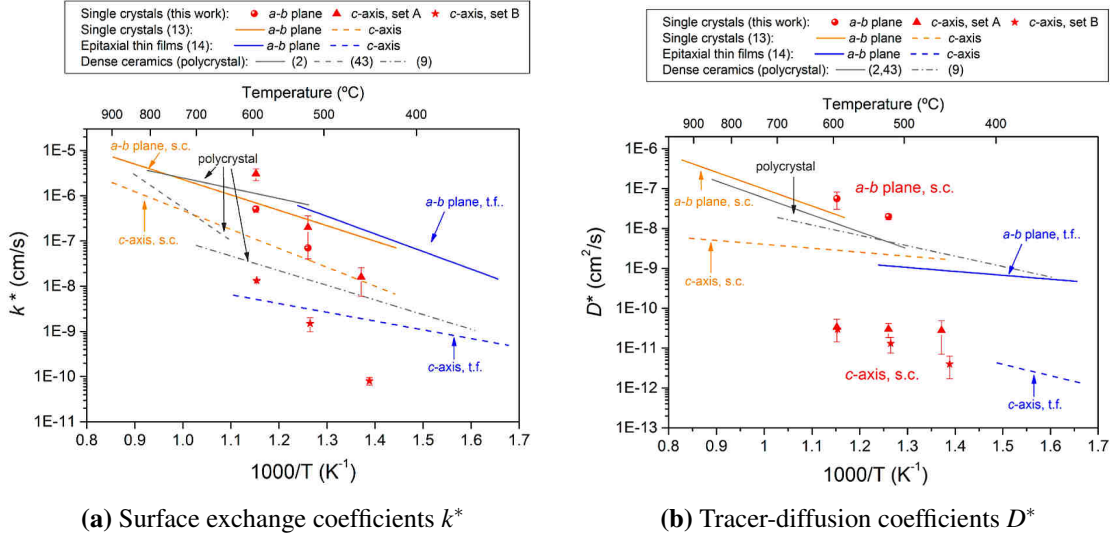
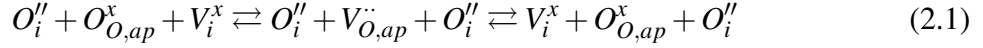


Figure 2.4 – Tracer-diffusion and surface exchange coefficients obtained for L2NO4 in literature. Reproduced with permission from [22]. Correspondence between references: (2)=[18]; (9)=[110]; (13)=[11]; (14)=[21]; (43)=[120];

ics is limited by both the bulk tracer diffusion coefficient D^* and surface exchange coefficient k^* [70]. An important discrepancy exists between reported values for k^* , which is attributed to an evolution of the surface of complex oxides during high temperature annealing treatments and/or possible contamination during the handling of the samples, making cross-comparison between different studies difficult [22]. Studies on the effect of the crystal orientation on the values of D^* and k^* have been carried out primarily by Bassat *et al.* and Burriel *et al.* using bulk single crystals or epitaxial thin films of L2NO4, respectively. They measured faster diffusion and surface-exchange coefficients along the a - b plane than in the perpendicular c direction using a tracer diffusion coupled with a SIMS profiling experiment [11, 21, 22]. As the two perpendicular oxygen diffusion pathways are different by several orders of magnitude ($D_{a,b}^* \gg D_c^*$, at least for temperatures in the ~ 300 - 900°C range), it is expected for polycrystalline samples to exhibit average D^* values closer to $D_{a,b}^*$ than to D_c^* . This being said, at lower temperatures the contribution of D_c^* to the total ionic conductivity could be larger. Figure 2.4 reports the values for D^* and k^* reported in literature for L2NO4 with different microstructures and different crystal orientations.

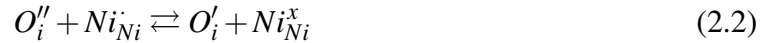
As far as bulk diffusion is concerned, computational evidence has showed that an interstitialcy diffusion mechanism is the preferred pathway for a fast diffusion along the a - b plane [29]. This particular diffusion mechanism involves a doubly negatively-charged oxygen interstitial (O_i^{2-}), an apical oxygen from a nearby NiO_6 octahedron ($O_{O,ap}^x$) and an available interstitial site (V_i^x) as follows. First the apical oxygen site is freed when the oxygen at $O_{O,ap}^x$

moves to V_i^x , leaving behind an oxygen vacancy $V_{O,ap}^{\cdot\cdot}$. This vacancy is then filled with the nearest interstitial oxygen O_i'' . The transfer is usually referred to in literature as a “push-pull” mechanism and can be expressed as follows (using the Kröger-Vink notation):



Minervini *et al.* have calculated an activation energy of $E_a = 0.88$ eV [86] for this interstitialcy diffusion mechanism, equal to the one measured experimentally by Bassat *et al.* [11].

An additional mechanism should also exist as Equation 2.1 cannot directly explain the very low activation energy measured experimentally for oxygen diffusion along $[0\ 0\ 1]_{L2NO4}$ [11]. This pathway is more complex as it requires an oxygen atom to cross the LaNiO₃ perovskite block, finding a path through the NiO₂ layer where the Ni and O_{eq} atoms are closely bound together when compared to the less energetic Ni-O_{ap} bounds. The following mechanism (largely inspired from the two step reaction proposed by Bassat *et al.* [11]) is therefore proposed next. First an electronic transfer from a doubly negatively-charged interstitial oxygen to a positively-charged Ni atom³ in his octahedral site allows reducing the Ni-O_{eq} bound strength:



The reduced Ni-O_{eq} bond strength facilitates the generation of an anionic Frenkel defect where an equatorial oxygen takes the place of a vacant interstitial site:



Finally, an anionic transfer between the singly negatively-charged oxygen interstitial O_i' (Equation equation (2.2)) and the newly generated oxygen vacancy $V_{O,eq}^{\cdot\cdot}$ (Equation equation (2.3)) can now occur:



The additional step described by Equation 2.3 has been introduced here (when compared to the diffusion mechanism proposed by Bassat *et al.* [11]) to explain the presence of the $V_{O,eq}^{\cdot\cdot}$ site in Equation 2.4.

An important effect of Equation 2.2 is that it diminishes the size and the charge of the interstitial oxygen O_i (by loosing an electron from its outer shell). This makes the ionic transfer described in Equation 2.4 much less energetic, hence possibly explaining the low activation energy measured for this diffusion pathway. Nevertheless, as this mechanism requires addi-

³The positive charge is the results of a charge compensation to balance the presence of the negatively-charged oxygen defect

tional steps, its probability decreases which would explain why higher oxygen diffusivity is being measured along the a - b plane than in the perpendicular c -direction. It should also be said that in their more recent joint work Bassat and Burriel [22] concluded that the very low activation energy (0.22 eV [11]) measured by Bassat *et al.* for the oxygen diffusion along the c -direction could be due to a limitation in the experimental method.

The different pathways (in the a - b plane and along the c -direction) are described schematically in Figure 2.5a.

Atomistic simulations carried out by Cleave *et al.* on perfectly stoichiometric $\text{La}_2\text{NiO}_{4.00}$ showed that the oxygen follows a vacancy-mediated diffusion, where the most likely pathway is between equatorial sites in the a - b plane, with an activation energy as low as 0.55 eV [31]. These vacancy mechanisms rely on the intrinsic anion Frenkel disorder present in the material to provide equatorial vacancy sites for the diffusion of oxygen⁴.

Antiphase boundaries generated by the cooperative tilting of the oxygen octahedra through interstitial ordering effects will locally increase the available space for oxygen atoms to self-diffuse inside the lattice, and could be at the origin of higher oxygen diffusion coefficients measured for increasing δ values. Additional phonon modes are likely a key parameter to take into account as they could generate the necessary lattice dynamics allowing for the room temperature diffusion of oxygen ions [99].

While the mass transport of O_i'' takes place mainly in the La_2O_2 layer, the electronic conduction occurs within the NiO_2 layer. The electronic conductivity in L2NO4 mediated by hole carriers generated through a self-doping mechanism will be discussed in the following section.

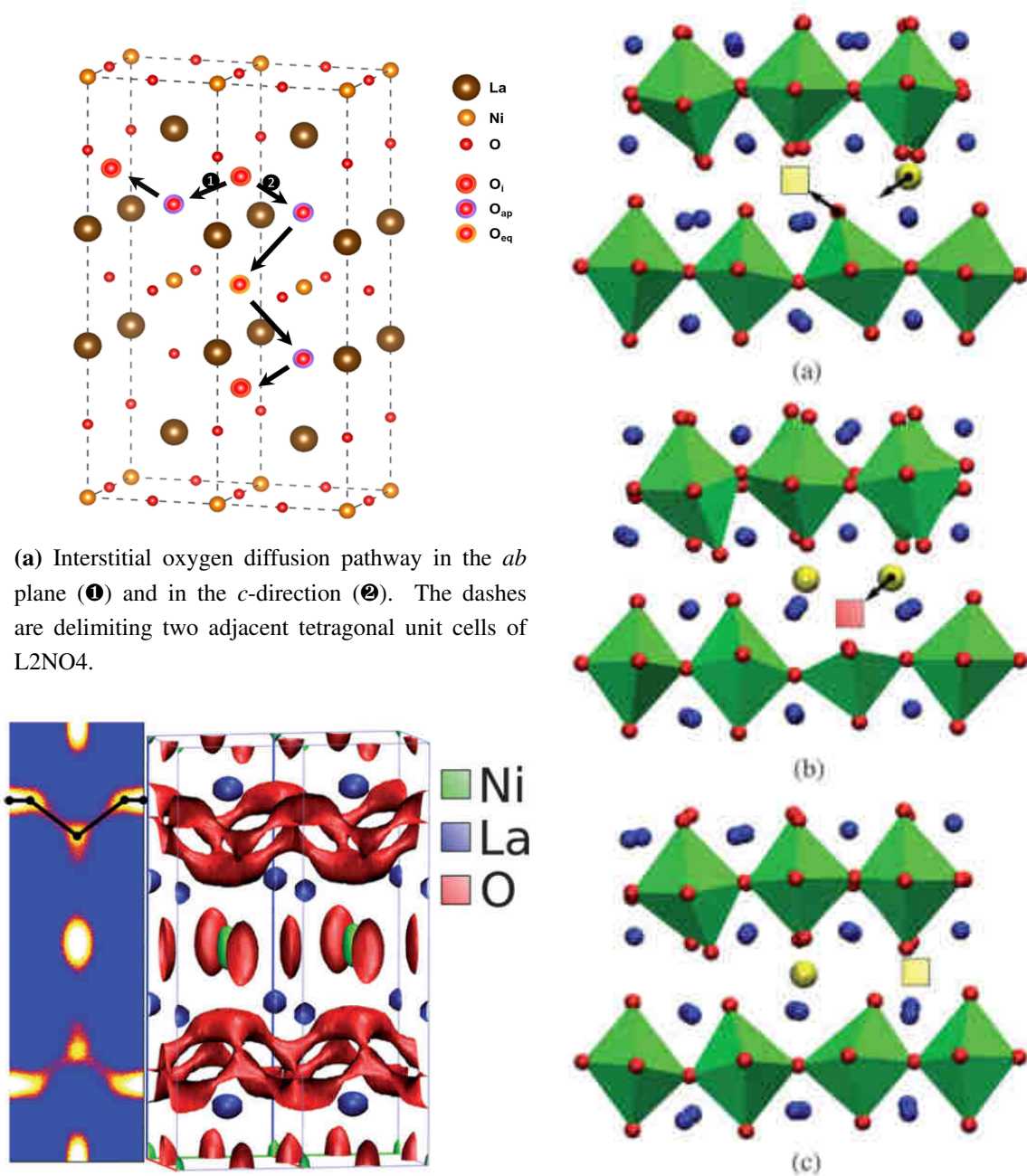
2.1.4 Hole self-doping and electronic conductivity in L2NO4

In the $\text{La}_2\text{NiO}_{4+\delta}$ structure the negatively-charged defect O_i'' has to be electrically compensated by positive holes to keep the overall charge-neutrality within the lattice, as shown in the following equation:

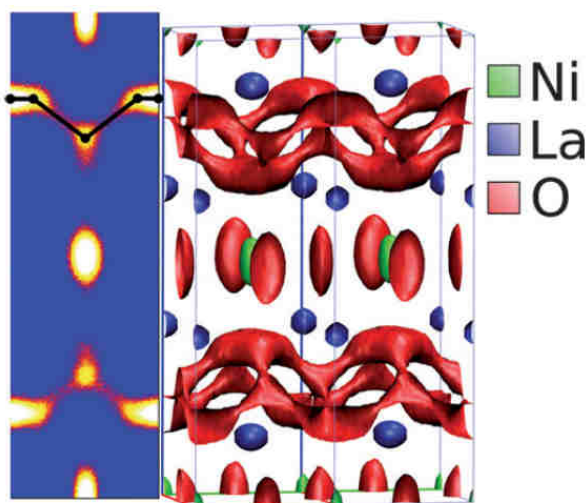


This means that the more O_i'' are present in L2NO4, the higher the charge carrier concentration. It is in this sense that O_i'' can be considered as acceptor dopants, giving rise to the p -type conductivity measured in this material [12]. While impurity doping is achieved through the addition of a very small percentage of impurity atoms in the material, this particular doping

⁴Both Minervini *et al.* and Cleave *et al.* agree that the formation of an oxygen vacancy in the equatorial site is more favourable than in the apical position (1.98 eV against 2.27 eV, respectively) upon generation of an intrinsic O_i'' Frenkel defect [31, 86].



(a) Interstitial oxygen diffusion pathway in the *ab* plane (1) and in the *c*-direction (2). The dashes are delimiting two adjacent tetragonal unit cells of L2NiO4.



(b) Oxygen ion density in the (010) plane (left) and the isosurface connecting the oxygen conduction sites (right) from a simulation at 900 K and a delta value of 0.09. Highlighted on the left is the proposed interstitial conduction mechanism. Also note the highly anisotropic liberation of the equatorial oxygen ions along the *c*-axis in agreement with the neutron diffraction data of Skinner [119]. Reproduced with permission from [29]

(c) (a–c): Snapshots of a typical diffusion process occurring during a molecular dynamics simulation of La₂NiO_{4+δ} at 900 K and *d* = 0.09. Only a small subset of ions is plotted to aid visualization. Lanthanum ions are represented by blue spheres, nickel–oxygen polyhedra are plotted in green and individual oxygen ions represented by red spheres, or yellow in the case of interstitial ions. Vacant sites relevant to the diffusion process are indicated by red and yellow squares, see text for details. Reproduced with permission from [29]

Figure 2.5 – Oxygen diffusion pathways and molecular dynamics calculations

mechanism in which oxygen point defects are generating additional charge carriers is usually referred-to as “self-doping”.

Kharton *et al.* evoked hopping of p -type carriers between mixed valence Ni cations as the electronic conduction mechanism for L2NO4 [70]. This hopping conduction has an activation energy in the 50-100 meV range [13, 34]. More particularly, a *polaronic* hopping conduction has been reported in several works [69, 95].

When incorporating interstitial oxygen into the structure, a Ni valence as large as +2.48 was measured for $\delta = 0.24$ [120]. The shortening of the Ni-O_{ap} bonds is believed to be at the origin of the charge transfer from the interstitial oxygen defect to the NiO₂ layer. However Jorgensen *et al.* [67] showed that the Ni-O_{ap} bond length was only affected by the interstitial defect in the highly doped ($0.13 \leq \delta \leq 0.18$) *Fmmm* phase, while showing negligibly small changes for the *Bmab* phase ($0.00 \leq \delta \leq 0.02$). This important result suggests that a charge transfer between the interstitial oxygen and the NiO₂ conducting layer is not always necessary, and that a charge-neutral defect could be formed in the *Bmab* phase. In the case of very low doping (oxygen overstoichiometry) concentrations, the presence of oxygen vacancies in the NiO₂ layers could hinder the charge transfer between Ni and O_{eq}, drastically increasing the resistivity of the material and explaining why stoichiometric La₂NiO_{4.00} has been reported an insulator [103]. Conversely, oxygen interstitial doping makes the material semiconducting. Although initial works reported metallic behaviour at higher temperatures ($T > 400$ -500 K) [60, 103], this apparent metallicity was challenged by at least two groups as being due to a carrier loss concomitant to the loss of oxygen occurring around these temperatures [13, 95]. This fact has been proven and is now widely accepted. Anisotropy in the thermally-activated electronic conduction was also measured by Bassat *et al.*, conduction facilitated in the *ab* basal plane when compared to the *c*-direction [12]. Nevertheless, the overall carrier mobility remains low ($0.3 \text{ cm}^2 \cdot \text{V}^{-1} \cdot \text{s}^{-1}$ at $T = 650 \text{ K}$) [14].

Gopalan *et al.* evoke a “near-localization” of the holes [46] when trying to explain the persistence of magnetic ordering with increasing oxygen overstoichiometry. This would suggest that, even though O_i'' and h are residing in two different layers within L2NO4, the holes remain somewhat “attached” to the interstitial point defects that generated them and could move along with them. This hole localization has also been mentioned by Tranquada *et al.* [128] and Bassat *et al.* [14]. This is of high importance in our study of L2NO4 as memristive material as our aim is to use this material as a medium for the transportation of oxygen. The fact that the holes generated by this mobile O_i'' are not itinerant suggests that there is a possibility to dope the material only locally where the mobile dopant is residing. This aspect will be developed further in Chapter 4.

2.2 Motivation to use L2NO4 as a memristive material for VCM applications

A better control over the ionic conductivity in a material can be achieved through a careful engineering of the material's composition and/or micro structure, favouring for example a high concentration of grain boundaries [104] and defects or at the contrary single crystal samples, depending on which one of the two "pathways" shows the highest ion mobility. Grain boundary pathways can highly improve the oxygen mobility in oxide materials showing initially poor bulk conduction [85]. Nevertheless, these localized pathways are prone to lead to concomitant highly localized electric current flows, which in turn lead to Joule heating and ultimately to a filamentary-like resistive switching mechanism. When thriving for a more homogeneous interface-type resistance-change mechanism, a bulk ionic conduction becomes the pathway of choice. Highly electrically insulating materials should also be avoided as they will likely suffer from a dielectric breakdown upon device operation.

As detailed in the previous section, L2NO4 is a mixed ionic-electronic conductor (MIEC), combining electronic conductivity and high oxygen exchange/diffusion coefficients. In addition L2NO4 presents anisotropic conduction properties when grown for example in the form of epitaxial thin films or single crystals [11, 21]. Furthermore, it has the particularity - when compared to other complex oxides - to accommodate interstitial oxygen anions within its lattice. This additional oxygen is key to the bulk oxygen conduction present in the material. A large range of oxygen over-stoichiometry can be stabilized in L2NO4, which is also a key property when aiming for a better control over the oxygen supply/intake needed to operate a VCM-based memristive device.

From a historical point of view, L2NO4 first received attention after the report of superconducting properties in its cuprate homologue: La₂CuO₄ [66]. In their work Jorgensen *et al.* reached the remarkable conclusion that a significant oxygen diffusion was occurring near room temperature. Some years later Chou *et al.* were able to measure diffusivity values for La₂CuO₄ at even lower temperatures, obtaining a diffusion length of 60 μm at 200 K and 90 Å at 150 K on a 1 h time scale [28]. Furthermore, in their structural study of L2NO4 [67] and due to the large similarities between both isostructural compounds Jorgensen *et al.* evoked the possibility of "significant oxygen diffusion near room temperature" for L2NO4. As no low temperature data are available, we have extrapolated the oxygen diffusion coefficients at room temperature from the literature values measured down to 340 °C.

When comparing with literature values extrapolated for other binary and ternary oxides used in the memristor community, L2NO4 shows a significantly higher oxygen diffusion, and thus a longer characteristic diffusion length at room temperature, as evidenced in Figure 2.6.

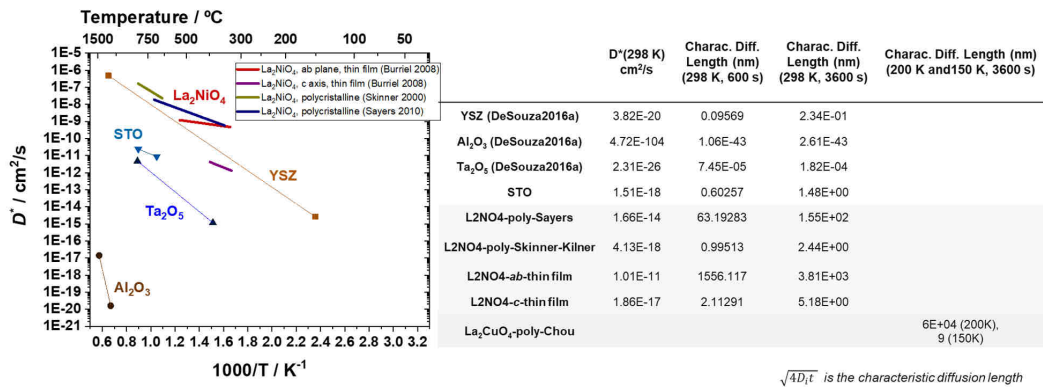


Figure 2.6 – Comparison of the oxygen-tracer diffusion coefficient D^* for several oxide materials already used in the resistive switching community and known for their VCM-type resistance-change mechanism (such as SrTiO_3 , Ta_2O_5 and Al_2O_3). Yttria-stabilized zirconia (YSZ, with the general formula $\text{Zr}_{1-x}\text{Y}_x\text{O}_{2-\delta}$), which enables oxygen ion conduction while blocking electronic conduction, is the most common electrolyte material used in SOFCs. L2NO4 has - to date - not received much attention in the memristor community. This is surprising when considering its potential oxygen conduction capabilities all the way down to room temperature.

While other compounds such as YSZ show excellent oxygen conduction properties at high temperature, their high activation energies lead to rapidly decreasing diffusion lengths at lower temperatures, and usually become negligible at room temperature. L2NO4 is an exception in this matter. It shows potentially orders of magnitude higher diffusion coefficients at room temperature compared to all other oxides presented in Figure 2.6 (YSZ, Al_2O_3 , Ta_2O_5 and SrTiO_3). Furthermore, it also exhibits highly anisotropic diffusion properties depending on the diffusion direction which is another interesting aspect from a materials point of view when aiming to engineer the oxygen conduction properties in oxide-based memristive systems. The inherent oxygen storage and conduction capabilities of L2NO4 makes it a material of choice for a rational design of VCM-based memories.

In addition to the high diffusivity of the oxygen interstitial ions, L2NO4 also possesses good electrocatalytic properties at intermediate temperatures (500-700 °C) and a relatively low thermal expansion coefficient that results in a good match with the common electrolyte materials, reasons why it became a material of interest as a cathode in the SOFCs community⁵ [71].

A multitude of materials, from high-k dielectrics such as HfO_2 [116] or TiO_2 [78], band insulators such as SrTiO_3 [9], both *p* and *n*-type semiconductors such as $(\text{Pr,Ca})\text{MnO}_3$ [107] or ZnO [97] and even electric conductors such as LaNiO_3 [126] have shown VCM memory properties, where the changes in resistance are ascribed to the movement of oxygen ions (also often described as the movement of oxygen vacancies in opposite direction for the materials

⁵SOFC: Solid-Oxide Fuel Cell

which present oxygen vacancy-type diffusion) and the concomitant redox processes in the cation sublattice they induce on their passage. The electronic conduction properties of the active material (it being for example a semiconductor or an insulator) does not seem to be determinant for the appearance of resistance-change properties, as shown by the profusion of different materials that have been used in the field.

Conversely, as VCM cells rely on the motion of oxygen ions, the ionic conductivity of the material would be expected to be a *key* factor in the choice of RS medium. This is obviously not the case as important advancements in the memristor field have been carried out on rather poor ionic conductors, that is when considering these materials in their pure, stoichiometric and defect-free form. Poor ionic conductors in their pristine state share a common characteristic: they need to be doped to exhibit ionic conduction and VCM properties. The doping can be controlled and implemented in the processing steps, through the incorporation of donor or acceptor impurity atoms in the sample or by post annealing them in controlled atmospheres and relying on a self-doping mechanism where the sample equilibrates with the atmosphere through the generation of point defects (such as oxygen or cation vacancies or interstitials). Doping can also arise during the device operation, and in particular during the forming step as discussed in Section section 1.3.3. Nevertheless, these are all somewhat artificial or harsh (for the electroforming) ways to trigger oxygen mobility, which remains rather low in most homogeneously-doped materials. When the oxygen mobility is important, as can be the case in extended defects such as grain boundaries or in the conducting filaments resulting from a soft dielectric breakdown, it becomes difficult to relate the observed mobility to a given material (what material composes a grain boundary or a filament?). Not being able to define the material responsible for the ionic conduction then becomes an important handicap when trying to reproduce the resistance-change and to model and validate its mechanism.

These considerations, combined with the material properties described in Section 2.1, make an oxide with bulk ionic conductivity such as L2NO4 an appropriate material to build memristive devices, an edge case to evidence and corroborate the role of oxygen mobility in the valence-change memory mechanism.

2.3 Growth of L2NO4 thin films by PiMOCVD

Pulsed injection Metal Organic Vapour Deposition (PiMOCVD) was used as depositon technique as it allows the growth of thin films on wafer level, facilitating the technology transfer between academic research and industry. This technique needs to operate at relatively high temperatures ($T > 500$ °C) in order to allow the decomposition of the metal-organic precursors and the combustion of the organic ligands. If used at lower temperatures, carbon impurities can

contaminate the prepared films although a rational precursor design can facilitate the combustion reaction process. Thermodynamically stable phases can be obtained and depend mainly on the stoichiometry of the reactants, the operating pressure and the deposition temperature. A more detailed description of this technique as well as the optimization procedure followed for the deposition of lanthanum-nickelate thin films is given in Appendix A and B.

2.3.1 Materials characterization aspects of the as-prepared thin films

In order to obtain stoichiometric L2NO4 thin films the La/Ni ratio of the precursor solution, the deposition temperature and number of pulses were first optimized. The optimal growth conditions for L2NO4 thin films are summarized in Table 2.1. Using these conditions, it was possible to grow highly oriented films on [1 0 0]-oriented SrTiO₃ (STO) single crystals. The best temperature for the growth of L2NO4 is 750 °C, offering the highest peak intensity and crystallinity (smaller FWHM) with no visible secondary phases in the diffraction pattern. However, the deposition temperature was lowered to 650 °C to prevent the decomposition of LaNiO₃ (LNO3) as a compromise in view of the preparation of L2NO4/LNO3 bilayers (see Chapter 5 for more details about this). Furthermore, by adjusting the La/Ni precursor solution ratio to 2.38, it was also possible to grow the LNO3 perovskite phase (the optimization procedure for the growth of LNO3 using PiMOCVD is described in Appendix B).

In this section, only the optimized L2NO4 thin films, which have been subsequently used to build memristive devices (Chapter 4 and Chapter 5), will be described.

Table 2.1 – Optimized deposition conditions used for the growth of L2NO4 thin films by PiMOCVD.

Parameter	Value
Precursors	La(TMHD) ₃ and Ni(TMHD) ₂
Solution concentration	0.02 mol/L (solvent = m-xylene)
Injection frequency	1 Hz
Opening time	2 ms
Number of injected droplets	4000
Evaporation temperature	220 °C - 280 °C (several heating stages)
Substrate temperature	650 °C
Carrier gas	34% Ar (218 sccm) + 66% O ₂ (418 sccm)
Total pressure inside the reactor	5 Torr

The composition of the films was measured by Electron Probe Microanalysis (EPMA) and EDX as explained in Appendix A.

The crystal quality of these films can be observed in Figure 2.7.a and b where the θ -2 θ X-ray diffraction (XRD) patterns show only 0 0 1_{L2NO4} (1 even) reflections of a highly oriented L2NO4 phase in addition to the h 0 0_{STO} substrate peaks. No crystalline impurity phases were observed in the XRD patterns.

The Transmission Electron Microscopy (TEM) cross-section image in Figure 2.7.c shows a continuous, homogeneous and dense film with a thickness of roughly 50 nm. The Root Mean Square (RMS) roughness of the film measured by Atomic Force Microscopy (AFM) is below 2 nm. The large magnification High Resolution TEM (HRTEM) image taken at the L2NO4/STO interface (Figure 2.7.d) shows the high crystal quality of the L2NO4 film having well defined and regularly-spaced lattice fringes growing perpendicular to the substrate, coherent with a [0 0 1]_{L2NO4}//[0 0 1]_{STO}, [0 1 0]_{L2NO4}//[0 1 0]_{STO} orientation relationship. This orientation relationship will be referred to as “ $c_{L2NO4,\perp}$ ” (c -axis of L2NO4 pointing out of plane, perpendicular to the substrates surface).

Nevertheless, while the growth of L2NO4 is $c_{L2NO4,\perp}$ close to the interface with STO, another orientation of the grains where the c -axis of L2NO4 “falls in plane” is observed above a certain film thickness (\gtrsim 30 nm). This orientation corresponds to a [0 1 0]_{L2NO4}//[0 0 1]_{STO}, [0 0 1]_{L2NO4}//[0 1 0]_{STO} orientation relationship and will be referred to as “ $c_{L2NO4,\parallel}$ ” (c -axis of L2NO4 in plane, parallel to the surface of the substrate). The two orientations of L2NO4 are better highlighted in the HRTEM image presented in Figure 2.8. This image was acquired using a High-Angle Anular-Dark-Field (HAADF) detector, which offers a “Z-contrast” (the contrast is highly sensitive to the atomic number Z of the probed elements, the heavier the element, the brighter the contrast). The magnified region ‘A’ in Figure 2.8 shows the epitaxial quality of $c_{L2NO4,\perp}$ at the interface with STO (similar to Figure 2.7.d). It also puts in evidence the presence of a few unit cells of LNO3 (4 to 7 u.c. depending on the region, \approx 1.5-2.5 nm). We found that this interfacial layer is present in all the L2NO4/STO sample we have deposited (it is also there in Figure 2.7.d). Bach *et al.* [6] have made the same observation for L2NO4/STO samples prepared by PLD, although the interlayer was attributed to “ a -domains” of L2NO4 (having the c -axis parallel to the film surface) instead of LNO3. The authors claim that the change in growth direction depends on the oxygen partial pressure used during the growth of the film (higher oxygen partial pressures being favourable for the presence of the interlayer). The relatively high oxygen partial pressure used in our PiMOCVD system (approx. 3.3 Torr) to grow the L2NO4 films is consistent with the p_{O_2} -dependence of the presence of this interfacial layer. Nevertheless, additional evidence (discussed hereafter) also shows that the presence or absence of this layer is substrate-dependent (and thus very likely corresponds to a substrate-induced strain relaxation mechanism in epitaxial thin films of L2NO4). The magnified HRTEM images presented in Figure 2.8 ‘B’ show a twinning between two crystals

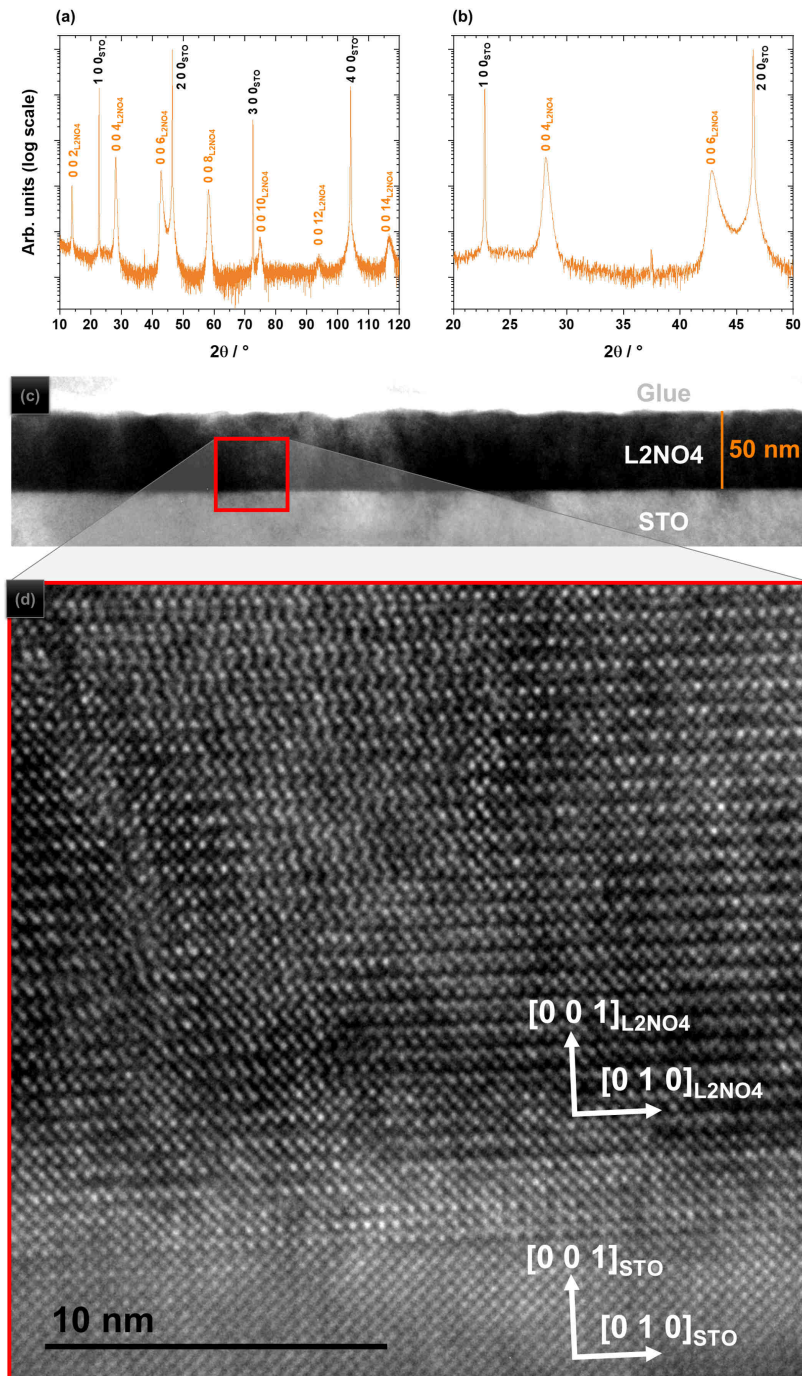


Figure 2.7 – (a) Typical XRD pattern of a L2NO4 thin film deposited on STO(100) at 650 °C by PiMOCVD with La/Ni = 5.00 in the precursor solution. The diffractogram was calibrated to the 2 0 0 peak of STO. (b) Magnification of (a). (c) TEM cross-section image showing a wide angle view of the L2NO4 film. (d) magnification of (c) showing the epitaxial quality of the sample in the L2NO4/STO interfacial region.

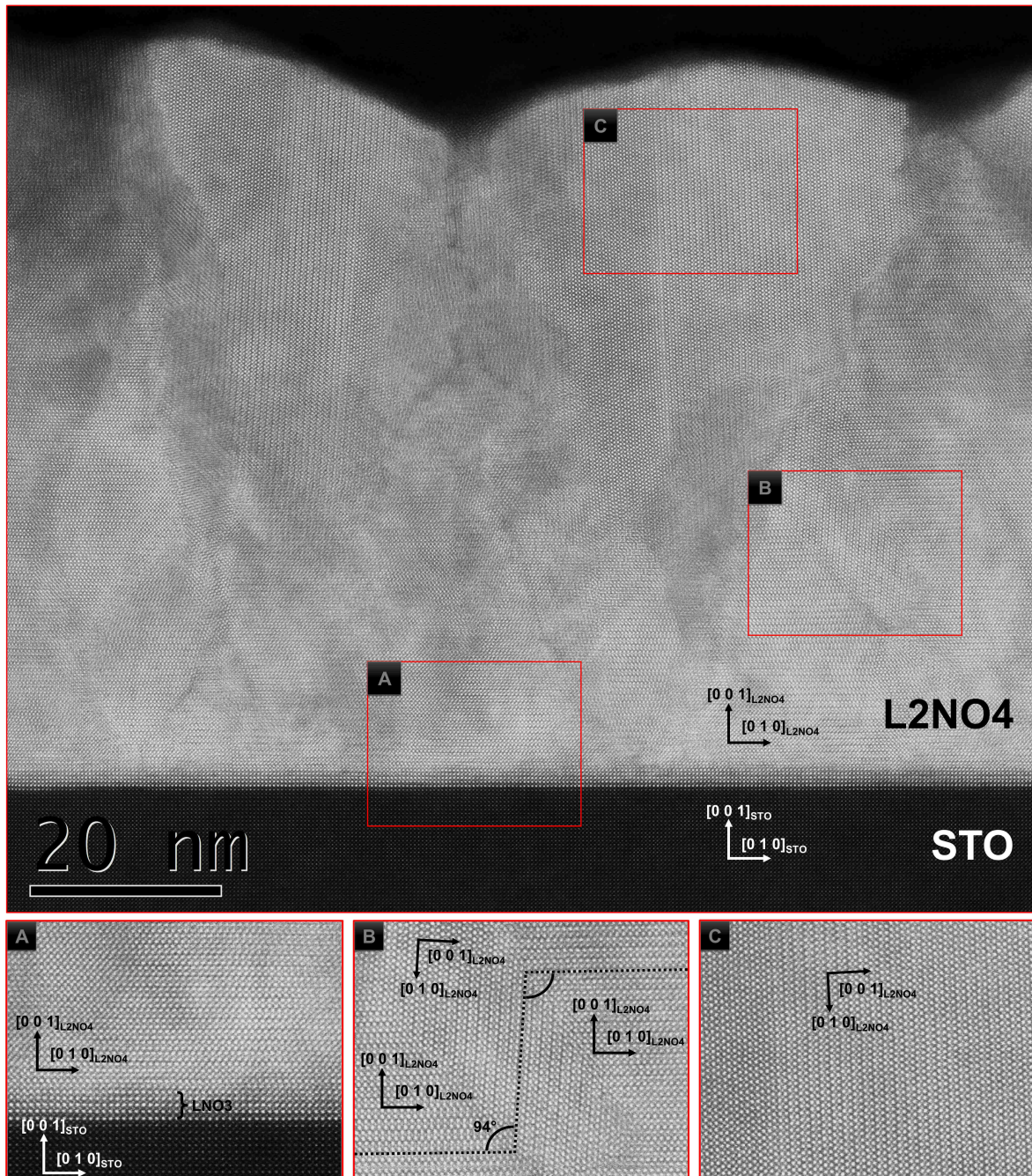


Figure 2.8 – HRTEM image of an L2NO4/STO sample. The three images in the bottom correspond to magnifications of the main image (red rectangles). ‘A’ is a magnification of the L2NO4/STO interface showing the epitaxial quality of the film around this region, ‘B’ is a magnification of the central region of the L2NO4 film showing two twin boundaries and ‘C’ is a magnification of a grain of L2NO4 with a different orientation close to the top of the film. The images were acquired with a HAADF detector (sensitive to the atomic number Z of the elements).

Table 2.2 – Lattice-mismatch values between the basal plane of tetragonal L2NO4 and three different substrates used for the deposition of highly-oriented L2NO4 thin films (STO, NGO and LAO).

Substrate	a lattice parameter (bulk, nm)	Lattice mismatch with La ₂ NiO ₄ ($(a_{\text{Substrate}} - a_{\text{L2NO4,bulk}}) / a_{\text{Substrate}}$ (%))	Reference (ICDD)
SrTiO ₃ (STO)	0.391	1.28	00-035-1734
NdGaO ₃ (NGO)	0.385	-0.26	01-089-4799
LaAlO ₃ (LAO)	0.379	-1.85	01-070-4106
La ₂ NiO ₄ (L2NO4)	0.386	0.00	00-034-0314

of the L2NO4 film where two $c_{L2NO4,\perp}$ and $c_{L2NO4,\parallel}$ domains meet. The measured angle of $\sim 94^\circ$ between two twin boundaries shows that the $c_{L2NO4,\parallel}$ domains are not exactly parallel to the growth direction, but slightly rotated of 4° . We did not go deeper into finding the reason for the presence of twined domains, but they seem very easy to obtain in this material. The final magnification (Figure 2.8 'C') shows a completely $c_{L2NO4,\parallel}$ -oriented domain that grew in the upper part of the film at the end of the deposition. The occurrence of a domain-reorientation (from $c_{L2NO4,\perp}$ to $c_{L2NO4,\parallel}$) was also reported by Telesca *et al.* [124] for L2NO4 films grown by PLD, although it only happened for a critical film thickness > 450 nm which is much larger than our critical thickness of ~ 30 nm. We will show later in section 5.3.2 (Chapter 5) that this change of orientation during the PLD growth of L2NO4/STO samples with increasing L2NO4 film thickness also happened after a critical thickness between $30 \text{ nm} < t < 80 \text{ nm}$.

In order to understand if the presence of the few unit cells of what we attribute to LNO3 at the L2NO4/STO interface is due to strain effects, a batch of three samples (grown simultaneously) was prepared on three different substrates: SrTiO₃ (STO), NdGaO₃ (NGO) and LaAlO₃ (LAO) which each have a different lattice mismatch with respect to L2NO4 (see Table 2.2).

The TEM and HRTEM cross-section images of the three samples is shown in Figure 2.9. Interestingly, the presence of the thin epitaxial interlayer is only present in the L2NO4/STO sample (Figure 2.9.c). Films deposited on either one of the two other substrates (NGO or LAO) show a direct growth of $c_{L2NO4,\perp}$ domains without the presence of an additional “buffer layer”. We propose that the tensile strain exerted by the clamping of L2NO4 on STO is the reason for the presence of the additional ~ 2 nm of LNO3 as a stress-relaxation mechanism. It should be noted that the L2NO4 film grown on STO is highly defective. Indeed, a large number of dislocations can be seen in the HRTEM image in Figure 2.9.c, giving the impression that the film is somewhat wavy. This is not the case for the compressed L2NO4 film grown on LAO (Figure 2.9.a), although a small amount of reoriented grains corresponding to $c_{L2NO4,\parallel}$

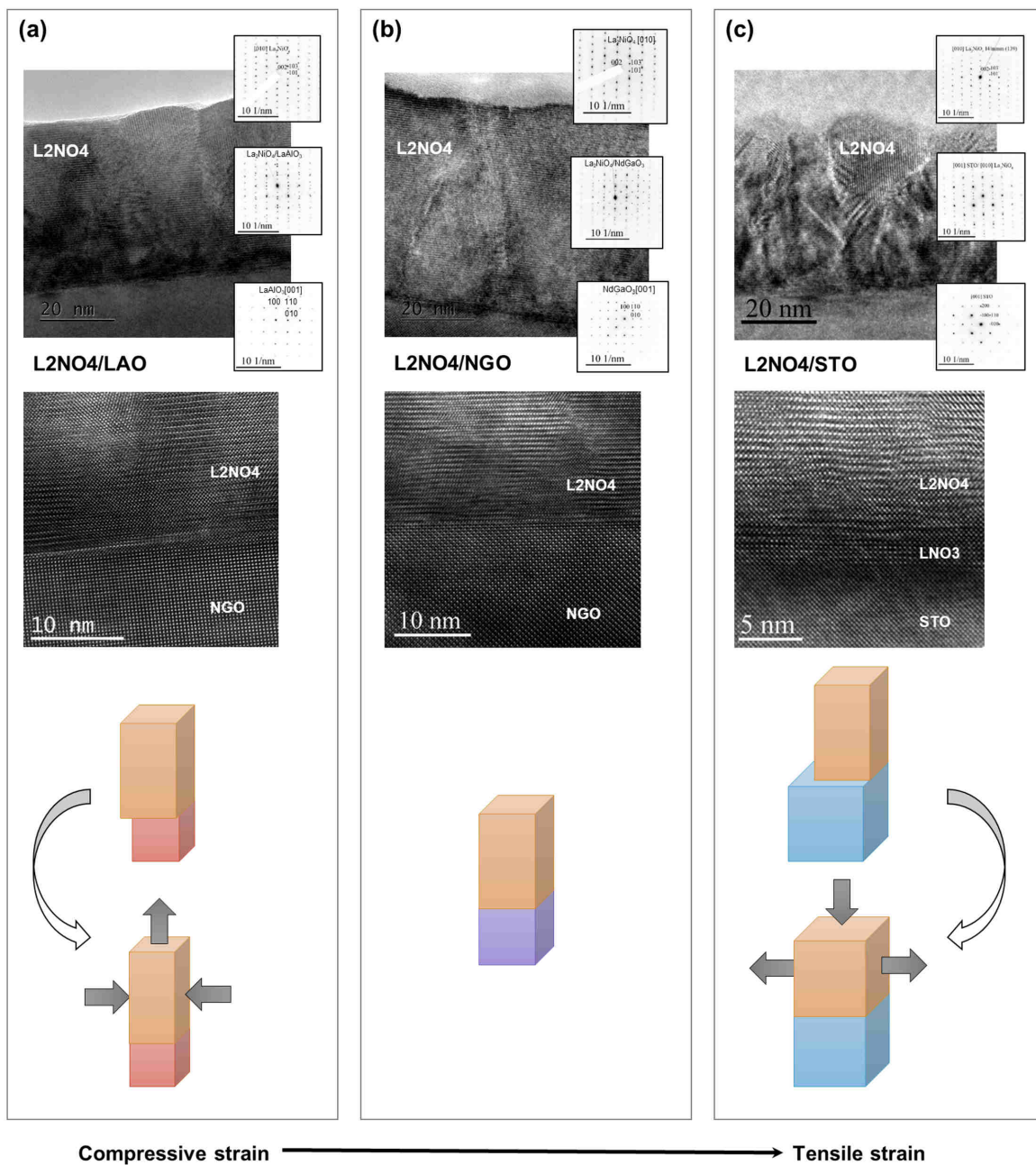


Figure 2.9 – TEM (top) and HRTEM (bottom) images of (a) L2NO4/LAO, (b) L2NO4/NGO and (c) L2NO4/STO samples. Three electron-diffraction images are included on the side of the TEM image for each sample and correspond to the L2NO4-only, the L2NO4/substrate and substrate-only regions (from top to bottom, respectively). Illustrations at the bottom of each panel are provided to illustrate the lattice distortions undergone by L2NO4 due to clamping on the different substrates (evolving from compressive strain on LAO to tensile strain on STO).

domains are also present in the sample. The highest epitaxial quality of L2NO4 is achieved when grown on NGO (which has the lowest lattice mismatch of -0.26%).

The LNO3 interlayer present in the L2NO4/STO samples could be further confirmed using the ASTAR technique. This particular technique couples electron-diffraction with a scanning electron probe (of ~2 nm). The obtained diffraction pattern, when compared to several reference patterns, allows the indexation of the different phases present in the imaged region of the sample and/or the domains-orientation, which in turn allows the delimitation of the different grain boundaries composing the material (only boundaries between grains with different orientations are visible). Figure 2.10.a shows the different phases that could be indexed, clearly showing the presence of a very thin layer of LNO3 (in red) at the surface of STO (green) and just before L2NO4 (blue). Furthermore, the grain-boundary image presented below (Figure 2.10.b) confirms the highly oriented growth of L2NO4, as most of the film grows coherently from the bottom to the top of the film showing a single orientation. A few grain boundaries can be seen at the top of the film and likely correspond to the $c_{L2NO4, \parallel}$ -oriented domains.

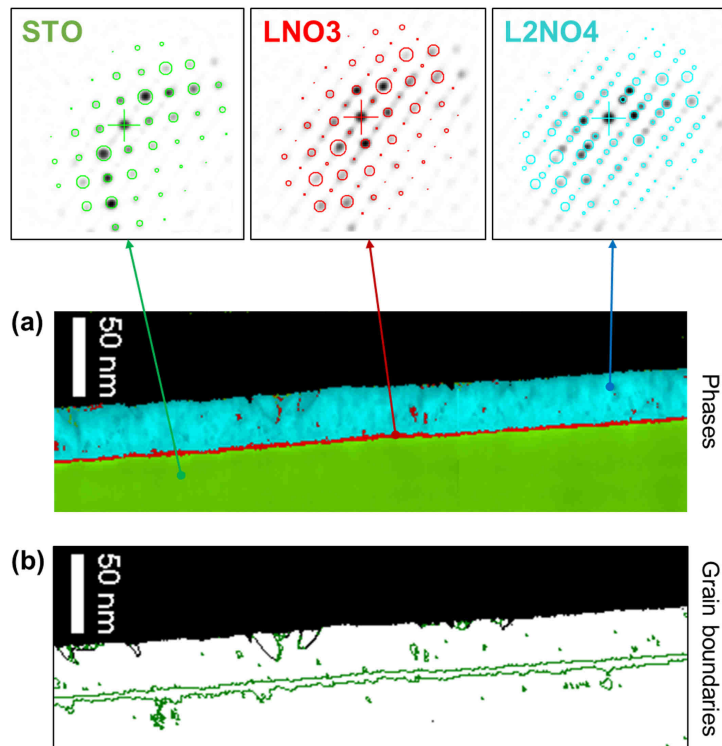


Figure 2.10 – ASTAR reconstructed images of (a) the different phases (STO in green, LNO3 in red and L2NO4 in blue) composing the L2NO4/STO sample and (b) the grain boundaries present in the sample (boundaries either with grains from different phases or with different orientations).

The $c_{L2NO4,\perp}$ regions are expected to exhibit a high oxygen mobility in plane, parallel to the surface of the substrate while the $c_{L2NO4,\parallel}$ domains should show a higher mobility in the out of plane direction, perpendicular to the substrate (see Section [Oxygen-ion diffusion in L2NO4](#) for more details). The reorientation from $c_{L2NO4,\perp}$ close to the STO substrate to $c_{L2NO4,\parallel}$ when reaching the top of the film is in itself a very interesting and potentially very useful phenomenon in memristive devices having a planar electrode configuration (also called the “top-top” electrode configuration). Indeed, these different domains would allow for the fastest oxygen transfer possible from one electrode to the other one, bypassing the slower oxygen-diffusion along the c -axis of L2NO4 (path ② in Figure 2.5a). Although the oxygen transfer at the twin boundaries linking the two $c_{L2NO4,\perp}$ and $c_{L2NO4,\parallel}$ domains together is yet unknown and could be slow, the engineering of such “mixed oxygen-diffusion pathways” in L2NO4 was unexpected and could be of interest for the further optimization and control over the oxygen supply from one location of the memristive device to the other. Metaphorically speaking, L2NO4 could potentially play the role of an “oxygen pipeline”, ensuring the mass transport of oxygen ions between two regions interconnected by L2NO4.

2.3.2 Tuning the oxygen content through post-annealing treatments

In order to evaluate how the oxygen stoichiometry of L2NO4 affects its conduction properties, first a batch of four identical L2NO4/STO samples was prepared during a single deposition. One of the samples was kept as deposited (which will be referred to as pristine) while the other three were annealed in O₂, Ar or a highly reducing H₂ (6%)/Ar gas mixture at 500 °C for 1 h. The diffractogram in Figure 2.11.b shows a clear displacement of the 0 0 6_{L2NO4} peak to higher 2θ angles (lower interplanar spacing along the c crystallographic direction of L2NO4) when the samples are subjected to reducing conditions⁶. This is coherent with a loss of oxygen, and more particularly of interstitial oxygen as the generation of vacancies should at the contrary lead to a lattice expansion, although the two defects might coexist. The c lattice expansion was calculated and is reported in Figure 2.11.d as a function of the oxygen off-stoichiometry. This δ value was determined from X-ray Absorption Near-Edge Structure (XANES) experiments carried out on the SpLine beamline (BM25) at the European Synchrotron Radiation Facility (ESRF), measuring the displacement of the Ni-K edge, from which the Ni oxidation state was calibrated. Figure 2.11.c shows the shift of the Ni K-edge towards higher energies when the samples are treated in increasingly oxidizing atmospheres. The oxidation state of Ni then allows the calculation of the oxygen off-stoichiometry by charge-balance (see Appendix D.1 for more details). A linear relationship is observed between the c lattice parameter and the

⁶the peak position was determined by fitting the 0 0 4_{L2NO4} peak with a pseudo-voigt function. The interplanar spacing was then obtained with the Bragg formula: $d_{hkl} = \frac{n\lambda}{2\sin(\theta)}$

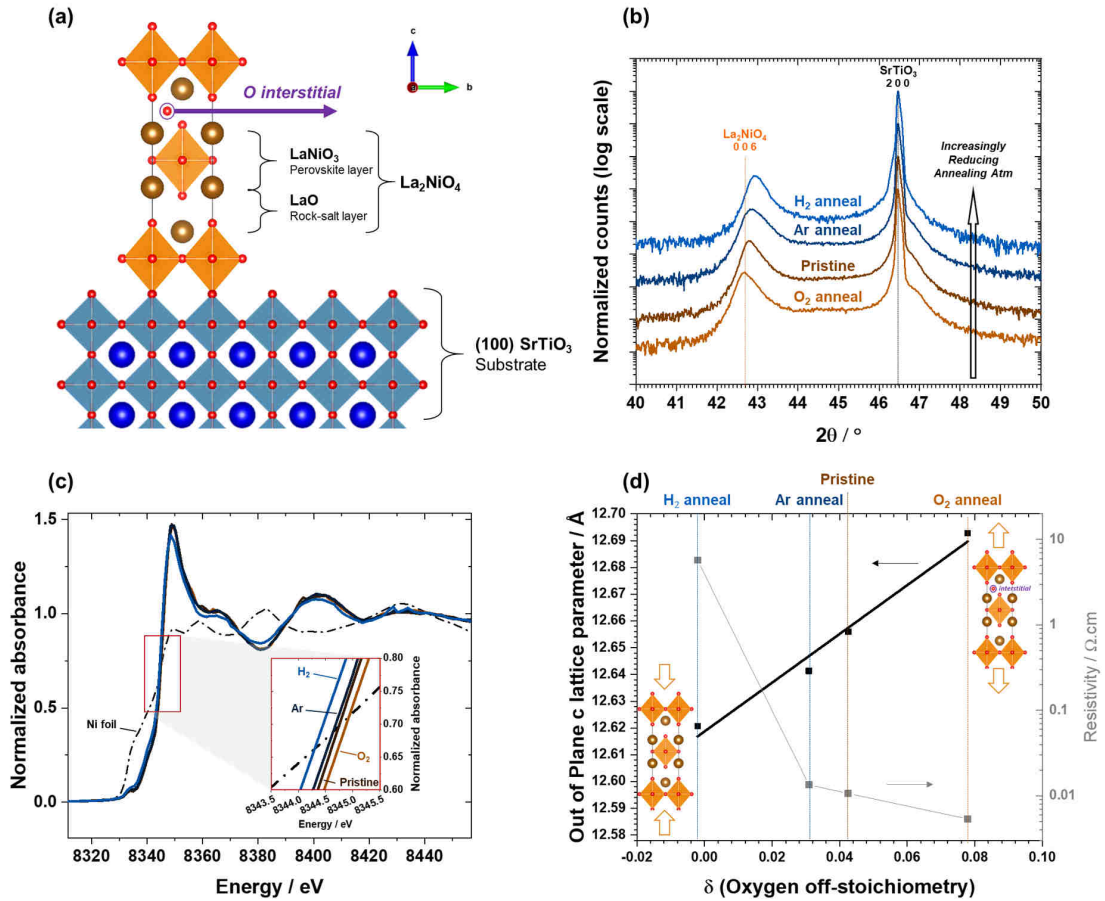


Figure 2.11 – (a) Schematic of the L2NO4/STO epitaxial heterostructure and location of the mobile interstitial oxygen site in the LaO rock-salt layer. (b) Out of plane θ - 2θ XRD pattern of L2NO4/STO samples with different gas anneals (500 °C/1 h). A clear displacement of the out of plane 0 0 6 Bragg peak to higher 2θ values (lower interplanar spacing) is observed. The out-of-plane c parameter equals 12.62 Å, 12.64 Å, 12.66 Å and 12.69 Å for the H₂, Ar, pristine and O₂ anneal, respectively. This behaviour is expected when removing interstitial oxygen ions from the lattice. (c) XANES spectra at the Ni K-edge obtained for L2NO4 with different gas anneals. The inset shows a magnification of the edge area, better showing the shift of the Ni K-edge towards higher energies when the samples are treated in increasingly oxidizing atmospheres. A solid Ni foil was used as reference for the calibration of the curves (dashed-dotted line). The edge position was obtained using the first/second derivative method. (d) Evolution of the c lattice parameter and film resistivity of L2NO4 (measured with a 4 probe setup) with oxygen off-stoichiometry δ (δ equals 0.00, 0.03, 0.04 and 0.08, respectively). The δ value was determined by XANES, measuring the displacement of the Ni K-edge (as shown in (c)). All the films are 75 ± 5 nm thick as measured by XRR and are part of the same batch.

oxygen off-stoichiometry, at least in the $0 \leq \delta \leq 0.08$ range, (black line in Figure 2.11.d). The out of plane lattice parameter increases from $c = 12.62 \text{ \AA}$ to $c = 12.69 \text{ \AA}$ when the estimated oxygen over-stoichiometry varies from $\delta = 0.00$ to $\delta = 0.08$. The range of lattice parameters for the highest δ values are coherent with the results obtained by Bach *et al.* who also prepared L2NO4 thin films on STO but using pulsed-laser deposition (PLD) with two different oxygen partial pressures (10 mTorr and 200 mTorr) [6]. They measured an out of plane c lattice parameter of $\sim 12.66 \text{ \AA}$ and $\sim 12.68 \text{ \AA}$ for approximately 72-77 nm thick films grown with $p_{O_2} = 10 \text{ mTorr}$ and 200 mTorr , respectively.

The resistivity of the films is also reported in Figure 2.11.d and shows a steady increase in resistivity from $5.3 \times 10^{-3} \text{ \Omega.cm}$ to $1.3 \times 10^{-2} \text{ \Omega.cm}$ when decreasing δ from 0.08 to 0.03. Interestingly, the film annealed in a highly reducing H₂/Ar atm corresponds to close to stoichiometric L2NO4 (estimated $\delta = 0$) and shows a jump in resistivity of over two orders of magnitude to 5.7 \Omega.cm . Similar values of resistivity ($\sim 5 \text{ \Omega.cm}$ at 300 K) have been reported by Sayer *et al.* [109] for samples annealed in a highly reducing CO/CO₂ atmosphere. If we consider the thermodynamic stability diagram of L2NO4, it can decompose into La₂O₃ + Ni in very reducing conditions (both high temperatures and low oxygen partial pressure, for example $T = 1373 \text{ K}$ and $p_{O_2} < 10^{-10} \text{ bar}$ was reported in [147]). Nevertheless, when comparing the integrated intensity of the diffraction peaks relative to the L2NO4 phase before and after annealing the films, we could not measure a significant difference suggesting no phase decomposition for any of the samples.

These results confirm that the oxygen content has an important influence on the electrical properties of L2NO4 and that changes in its value are directly related to the changes in the c lattice parameter in L2NO4/STO samples.

Photoemission Electron Microscopy (PEEM) measurements confirmed the p -type semiconducting properties of L2NO4. Indeed, the work function of two different L2NO4 films, one pristine and one annealed in oxygen, were measured using PEEM. The oxidizing treatment lead to an increase of 200 meV in the work function of L2NO4 (from 4.1 eV to 4.3 eV for the pristine and the oxygen-annealed films, respectively - see Section C.2.4 in Appendix C for more details). This is consistent with the supposition that the interstitial oxygen ions act as acceptor dopants through a self-doping process, as described in subsection: 2.1.4, giving rise to the p -type conductivity in this material.

2.4 Summary

The main points tackled in this chapter are summarized hereafter.

- Material properties of L2NO4 (literature review):

- Stoichiometric $\text{La}_2\text{NiO}_{4.00}$ has a complex phase diagram. Its archetypal K_2NiF_4 tetragonal structure undergoes an orthorhombic distortion to accommodate the internal stresses induced by the stacking of compressed electronegative NiO_2^{2-} planes and stretched electropositive $\text{La}_2\text{O}_2^{2+}$ double layers;
- This distortion is reduced when increasing the temperature (due to different thermal expansion coefficients of the two layers) or by the presence of an additional interstitial oxygen located in the LaO rock-salt blocks;
- The incorporation of a negatively-charged O_i'' point defect into the electropositive $\text{La}_2\text{O}_2^{2+}$ double-layer, together with the charge compensating holes it generates injected into the electronegative NiO_2^{2-} planes reduces the charge separation between the layers and explains the stability of the oxygen over-stoichiometric $\text{La}_2\text{NiO}_{4+\delta}$ compound;
- A cooperative tilting of the NiO_6 octahedra is beneficial both for the oxygen incorporation and the oxygen diffusion in $\text{La}_2\text{NiO}_{4+\delta}$, creating extended defects such as antiphase boundaries;
- The presence of an electron in the 5d orbital of La ($[\text{La}] = [\text{Xe}]5d^1 6s^2$) polarizes the 6s valence orbitals, facilitating the chemisorption and dissociation of molecular oxygen due to the charge transfer between O_2 and the LaO. This can explain the high oxygen-exchange coefficient k^* of L2NO4;
- The oxygen diffusion in $\text{La}_2\text{NiO}_{4+\delta}$ is amongst the highest in the MIEC field. Furthermore, the diffusion is highly anisotropic due to its also anisotropic structural properties. A fast diffusion path in the basal plane of L2NO4 was both measured experimentally and confirmed by atomistic simulations. The low activation energies required for this diffusion process potentially leads to fast diffusion kinetics when extrapolated to room temperature (relative to other materials used in the memristor community);
- The incorporation of O_i'' point triggers a self-doping mechanism, where O_i'' can be regarded as an acceptor dopant. The generated holes give rise to the p-type semiconducting properties of $\text{La}_2\text{NiO}_{4+\delta}$;
- The combination of a high bulk oxygen-diffusion coefficient and good electronic conduction properties makes the material less likely to suffer from a dielectric breakdown when applying an external bias, while still showing high oxygen drift capabilities. These two aspects are essential when aiming to achieve a mild, controlled and homogeneous redox-induced change in resistance in an oxide-based

memristive device. In other words, L2NO4 is a promising candidate to be used as memristive medium in VCM cells.

- Experimental results on the preparation of L2NO4 thin films by PiMOCVD:
 - Highly oriented L2NO4 films deposited on STO, LAO and NGO were successfully deposited using PiMOCVD;
 - A domain reorientation from $c_{L2NO4,\perp}$ to $c_{L2NO4,\parallel}$ was observed when L2NO4 grows on STO and after a critical film thickness of ~ 30 nm by analysing HRTEM images of L2NO4/STO samples. The domain reorientation seems to be very favourable from an epitaxial point of view as they generate seemingly defect-free twin boundaries;
 - The presence of 4 to 7 unit cells of LNO3 at the L2NO4/STO interface could be observed in HRTEM images and by using the ASTAR phase-indexation technique. The presence of this interlayer was attributed to a relaxation mechanism of the tensile strain induced by the clamping of L2NO4 on STO. The interlayer is absent when L2NO4 is grown on NGO or LAO substrates which have lower lattice parameters than STO;
 - The oxygen content in L2NO4 thin films was successfully tuned using post annealing treatments, both in oxidizing and reducing atmospheres. Important effects on the the out-of-plane c lattice parameter, Ni oxidation state (and thus on the oxygen content) and the resistivity of the films were measured (increasing the oxygen content in L2NO4 increases c and decreases the resistivity);
 - The increase in hole carriers through a self-doping mechanism was confirmed by measuring the work function of two L2NO4 films, one of which was annealed in an oxidizing atmosphere. This supports the idea that the over-stoichiometric interstitial oxygen ions also play the role of acceptor dopants in L2NO4, thus affecting its semiconducting properties.

The optimized L2NO4 thin films obtained by PiMOCVD are the basis for the following step: the microfabrication of the metal/oxide/metal (MOM) memristive devices. The role of the metal/oxide junction on the overall device properties will be discussed in the following chapter.

Chapter 3

Functionality through interface: role of the electrodes

Contents

3.1	The Metal/Oxide heterojunction	42
3.1.1	Conduction mechanisms	42
3.1.2	Ohmic and Schottky contacts	43
3.1.3	Oxygen affinity of the electrode and formation of interlayers	47
3.2	Metal/L2NO4 heterojunction properties	49
3.2.1	Choice of the electrode material	49
3.2.2	Effect of the oxygen content in L2NO4 on the Pt/L2NO4 junction properties.	51
3.2.3	Pt/L2NO4 and Ti/L2NO4 MS heterojunctions	54
3.2.4	Evidence of a TiO _x interlayer	56
3.2.5	Temperature-dependent measurements and transport mechanisms	58
3.3	Summary	61

While the oxygen stoichiometry of L2NO4 is an important aspect from a materials point of view¹, the functionality of a memristive device also highly depends on its electrical contacts. The intent of this chapter is to offer a transition between the material aspects of L2NO4 discussed in the previous chapter, and the following chapter that will tackle the device properties of L2NO4-based memristive heterostructures. The chapter is divided into two main sections.

¹the reader is redirected to the previous Chapter: [La₂NiO_{4+δ}](#), a mixed ionic-electronic conductor for VCM applications for more information about this

The first section, entitled ‘*The Metal/Oxide heterojunction*’ presents the fundamental aspects necessary to better understand the experimental section that follows: ‘*Metal/L2NO4 heterojunction properties*’. The important points discussed in this chapter are summarized in the final section.

3.1 The Metal/Oxide heterojunction

This section provides a brief insight on the formalism developed by semiconductor physics and used to characterize electric transport properties across metal/semiconductor heterojunctions.

3.1.1 Conduction mechanisms

The charge transport mechanism in a material (or a heterostructure) is an indirect but important indicator of the nanoscale mechanisms responsible for the macroscopic changes in resistance measured in memristive devices. Several conduction mechanisms can be present in a given material, but usually only one of them prevails at a given electric field, temperature and location (the bulk, a grain boundary, at an interface...). Bulk-limited conduction mechanisms include: Poole-Frenkel (PF); hopping conduction, Ohmic conduction, Space-charge-limited conduction (SCLC), ionic conduction and grain-boundary-limited conduction [27]. These charge transport mechanisms depend on the intrinsic properties of the material used as resistive switching medium. This being said, a device is often composed of multiple materials forming an heterostructure and the combination of these different materials gives rise to the functionality of the final device. When working with heterostructures, additional conduction mechanisms have to be considered as the material junctions and interfaces themselves can govern the electrical properties of the entire device. In fact, the presence of these interface-limited conduction mechanisms are key when trying to achieve an homogeneous change in resistance across an entire heterojunction (such as the metal/oxide interface), a phenomenon referred to in literature as *interface-type resistive switching* [10]. Interface-limited conduction mechanisms include: thermionic or Schottky (Sch) emission, Fowler-Nordheim (FN) tunnelling, direct tunnelling, trap assisted tunnelling (TAT) and thermionic-field emission [27].

The charge-transport mechanism in memristive devices can be easily probed using electrical measurements. In particular I-V (applying a voltage and measuring the resulting current) or I-t (measuring the evolution of the current over time while applying a constant voltage) measurements are amongst the most widely used in thin-film characterization techniques to extract and help modelling its conduction properties.

A schematic representation of all the previously mentioned conduction mechanisms is

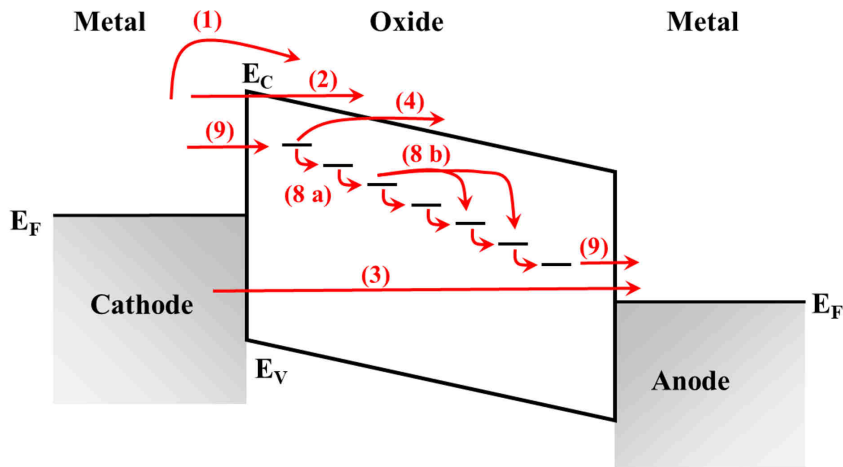


Figure 3.1 – Illustration of the electron conduction paths through a metal/oxide/metal heterostructure. (1) Schottky emission (Sch); (2) Fowler-Nordheim (FN) tunnelling; (3) direct tunnelling; (4) Poole-Frenkel (PF) emission; (5) ohmic conduction (not shown); (6) space-charge limited conduction (SCLC) (not shown); (7) ionic conduction (not shown); (8) hopping conduction: 8a Nearest Neighbour Hopping (NNH), 8b Variable-range Hopping (VRH); and (9) trap-assisted tunnelling (TAT). The sandwiched oxide material is represented as a dielectric for simplification. It should be kept in mind that oxides are often semiconductors and sometimes even show metallic properties. Adapted from [10].

given in Figure 3.1 in the case of a metal/oxide/metal MIM heterostructure (the oxide material is represented as an insulator for simplification). In addition, Table C.1 (in Appendix C.4) summarizes the expressions for each of them, showing the electric field and/or temperature dependence of the current density through a dielectric film.

In the following section we will focus our attention on a metal/semiconductor (MS) interface and how different electrode materials can form MS junctions with very different conduction properties.

3.1.2 Ohmic and Schottky contacts

This section is inspired from the review article from R. Tung: the *The Physics and Chemistry of the Schottky Barrier Height* [130].

The Metal/Semiconductor (MS) contact is a crucial aspect in most of the microelectronic devices we use or study, and is in fact still not fully understood. The complexity in the description of the heterogeneous MS junction arises from the fact that it depends on many parameters such as the atomic structure and chemistry of the interfaces brought in contact, as well as the usually uncontrolled defects and impurities that arise during the processing of these interfaces.

As a full (and thus complex) description falls out of the scope of this thesis, only a sim-

plified understanding of the MS junction will be exposed in this section, enough to gain some insight and a general understanding of the electrical characteristics described in the rest of the thesis.

The Shottky-Mott rule describes the MS interfaces before any charge or atomic relaxation/exchange happens and gives a first hint on the magnitude of the Schottky Barrier Height (SBH) $\Phi_{B,n}^0$ which is an indicator of how easy it will be for charges to be injected from the metal into the semiconductor (and from the semiconductor into the metal):

$$\Phi_{B,n}^0 = \phi_M - \chi_{SC} \quad (3.1)$$

where ϕ_M is the metal work function (energy difference between the vacuum level and the Fermi level of the isolated metal) and χ_{SC} is the electron affinity of the semiconductor (energy difference between the vacuum level and the conduction band minimum). While Equation (3.1) describes a n -type SBH (resulting from the contact between a metal and a n -type semiconductor), a p -type SBH is better described as follows:

$$\Phi_{B,p}^0 = I_{SC} - \phi_M = \chi_{SC} + E_{gap} - \phi_M \quad (3.2)$$

where $\Phi_{B,p}^0$ is the p -type SBH, I_{SC} is the ionization potential of the semiconductor (energy difference between the vacuum level and the valence band maximum), E_{gap} is the energy gap between the conduction band minimum and the valence band maximum, ϕ_M and χ_{SC} are the metal work function and the electron affinity of the semiconductor like previously.

As is shown in Figure 3.2, the Schottky-Mott rule considers that the periodic electrostatic potentials within the metal and the semiconductor superimpose at the interface, leading to a band bending in the semiconductor to ensure that there is no discontinuity in the work function of the two materials at the MS interface (*i.e.* that the Fermi levels are aligned throughout the entire heterojunction).

In particular, Figure 3.3.a shows what happens when contacting a high work function metal with a p -type semiconductor such as L2NO4. We are in the case where $\phi_M > \phi_{SC}$, *i.e.* the work function of the metal is higher than the one of the semiconductor. Before contact both materials are considered free, at this point surface states can already exist and lead to a slight band bending due to a charge reorganization at the semiconductor's surface, but this additional complexity will not be considered here. When bringing the two materials in contact, as is for example the case when evaporating metallic contacts on the surface of the semiconductor, the energy difference between the Fermi level of the semiconductor and the Fermi level of the metal will be the driving force for a charge re-equilibration at the MS junction. Electrons

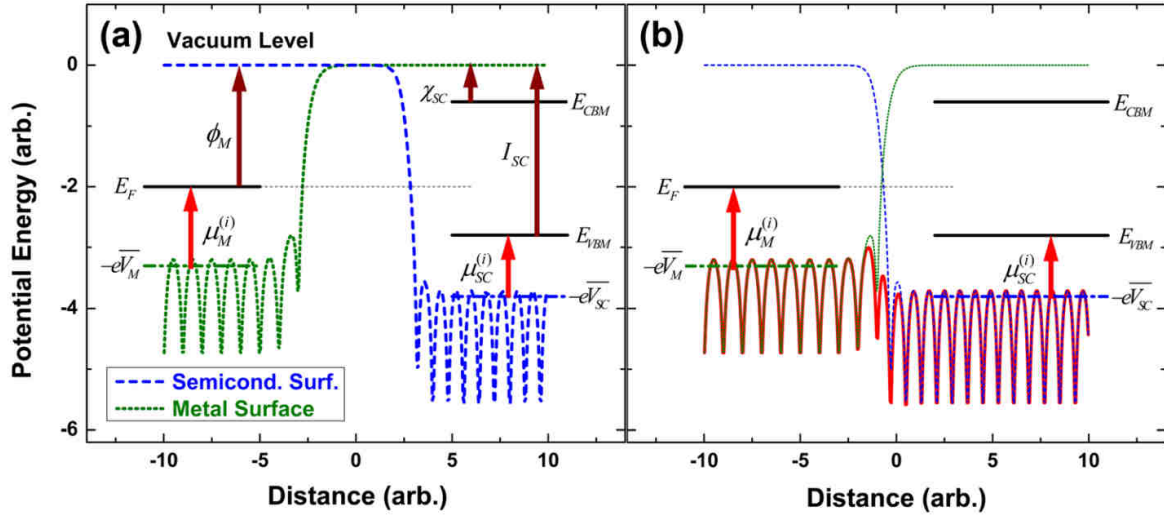
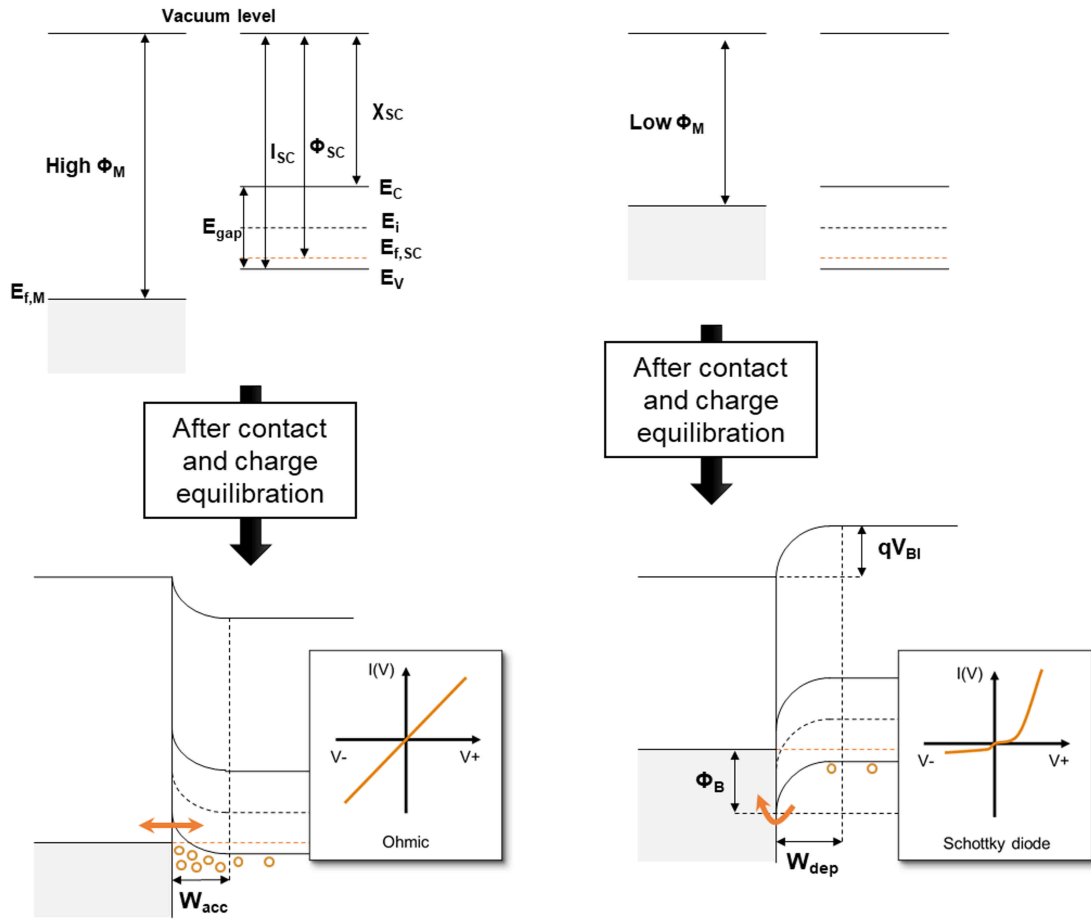


Figure 3.2 – Potential energy for isolated metal surface (dotted) and semiconductor surface (dashed) plotted on the same energy scale. (a) When the two crystals are far apart. (b) When the two crystals are next to each other but without allowing charge redistribution as would be the case for a non-interacting MS interface described by the Schottky-Mott rule. The solid line is the sum of the two individual potential energies. Note the relative position of the semiconductor potential to the metal potential remains unchanged, independent of the distance separating the two crystals. ϕ_M is the metal work function χ_{SC} is the semiconductor electron affinity, E_F is the Fermi energy level of the metal, E_{CBM} is the conduction band minimum energy level of the semiconductor, E_{VBM} is the valence band maximum energy level of the semiconductor, I_{SC} is the ionization potential of the semiconductor, $\mu_{M,SC}^i$ are the internal chemical potentials of the metal or the semiconductor in their bulk form, $-e\bar{V}_{M,SC}$ are the average electrostatic potential energies per unit cell of metal (M) or semiconductor (SC). Reprinted from [130]

will flow from the semiconductor into the metal until the two Fermi levels are aligned and the MS junction reaches a thermodynamic equilibrium. This equilibrium is represented in the bottom of Figure 3.3.a where an upwards band bending is present at the MS junction (on the semiconductor side) and is the result of the depletion of electron carriers at this location. Conversely, if electron *holes* are the majority carriers as is the case in a *p*-type semiconductor, this region is actually enriched in free carriers and forms an accumulation zone with a very small width of W_{acc} into the semiconductor. The accumulation of free carriers at the MS junction results in an ohmic I-V characteristic. Furthermore the increased amount of carriers also ensures that there is very little to no voltage drop at this location, ensuring a good contact, (generally with a negligible contact resistance).

In the opposite case where $\phi_{SC} > \phi_M$, the MS junction properties are very different as illustrated in Figure 3.3.b. Before contact the Fermi level of the metal lies above the Fermi level of the semiconductor. This results in an electron diffusion from the metal to the semiconductor when the two materials are put in contact with each other until charge equilibration is reached



(a) high work function metal (ex: Pt, Au, ...)

(b) low work function metal (ex:Ti, Ag, Al, ...)

Figure 3.3 – (a) Shows how a high work function metal when brought into contact with a *p*-type oxide semiconductor (L2NO4 in our case) can form an ohmic contact. Conversely, (b) shows that when contacting a low work function metal to the same semiconducting material, a Schottky contact is more likely to form. $\Phi_M = q \cdot \phi_M$ is the energy needed to extract a charge from the metal (ϕ_M is the metal work function), likewise $\Phi_{SC} = q \cdot \phi_{SC}$ is the energy needed to extract a charge from the semiconductor (ϕ_{SC} is the semiconductor work function), χ_{SC} is the electron affinity of the semiconductor, I_{SC} is the ionization potential of the semiconductor, E_{gap} is the energy difference between the conduction and the valence band of the semiconductor, $E_{f,M/SC}$ is the Fermi energy of the metal or the semiconductor, E_i is the intrinsic energy level of the otherwise undoped semiconductor, E_C is the conduction band maximum, E_V is the valence band minimum, $\Phi_B = q \cdot \phi_B$ is the Schottky barrier height, V_{BI} is the built-in voltage, W_{dep} and W_{acc} are the depletion width and the accumulation width, respectively. The insets show the $I(V)$ characteristics for an Ohmic or a Schottky contact (in the case where the semiconductor is being polarized).

and the Fermi levels are aligned. In the case of a *p*-type semiconductor, the additional electrons that are now present lead to a charge compensation and the formation of a zone that is depleted of majority carriers. This depletion zone extends of a width W_{dep} away from the MS interface and into the bulk of the semiconductor. The I-V characteristics of such a junction are highly nonlinear and rectifying as a negative bias applied to the semiconductor will further increase the band bending and the potential barrier (V_{BI}) that a hole has to overcome before it can drift into the metal while a positive voltage will have the opposite effect of decreasing V_{BI} . The low amount of carriers ensures that the voltage drop is located at this junction. This additional highly localized electric field can be of assistance in interface-controlled resistance-change mechanisms.

It should be noted that the Schottky-Mott rule is usually a simplified model of what occurs when bringing a metal and a semiconductor in close contact to each other. Indeed if we would look at this problem at the sub-nano scale, when putting the two materials in very close proximity, the interface will start to “blur out” and new hybrid molecular orbitals and thus chemical bounds can form, possibly leading to a completely new electrostatic potential distribution coupled with a charge redistribution at the MS interface. The surface states of the two isolated crystals are then replaced with new interface states localized at the MS interface and these states will depend solely on the atomic structure and chemistry of the two constituents and can therefore be very different for each new MS couple. This phenomenon is usually referred to in literature as ‘Fermi level pinning’. The chemistry behind the electronic (or sometimes even atomic) restructuring of the MS interface is the reason why the final charge distribution can sometimes be very different from a simple linear superposition of the charge distribution present on the initial surfaces.

This illustrates well that the electrode material and its work function should be chosen carefully when aiming to prepare interface-controlled memristive devices, but that in the particular case where the semiconductor is also an oxide material, and even more so an oxygen ion conductor, an additional characteristic of the electrode material needs to be considered: its affinity towards oxygen.

3.1.3 Oxygen affinity of the electrode and formation of interlayers

The MS junction discussed previously can be highly affected by the oxygen ‘affinity’ of the electrode material. A material with a good “affinity for oxygen” is also referred to in literature as being an “oxygen sink” or an “oxygen getter”, and while all these terms are good metaphors, their more scientific and quantifiable equivalent is the value of the Gibbs free energy of oxidation (ΔG_{ox} , in kJ/mol) of the electrode material used as electrical contact. Figure 3.4.a shows the free energy of oxidation for some noble and transition metals as a function of tem-

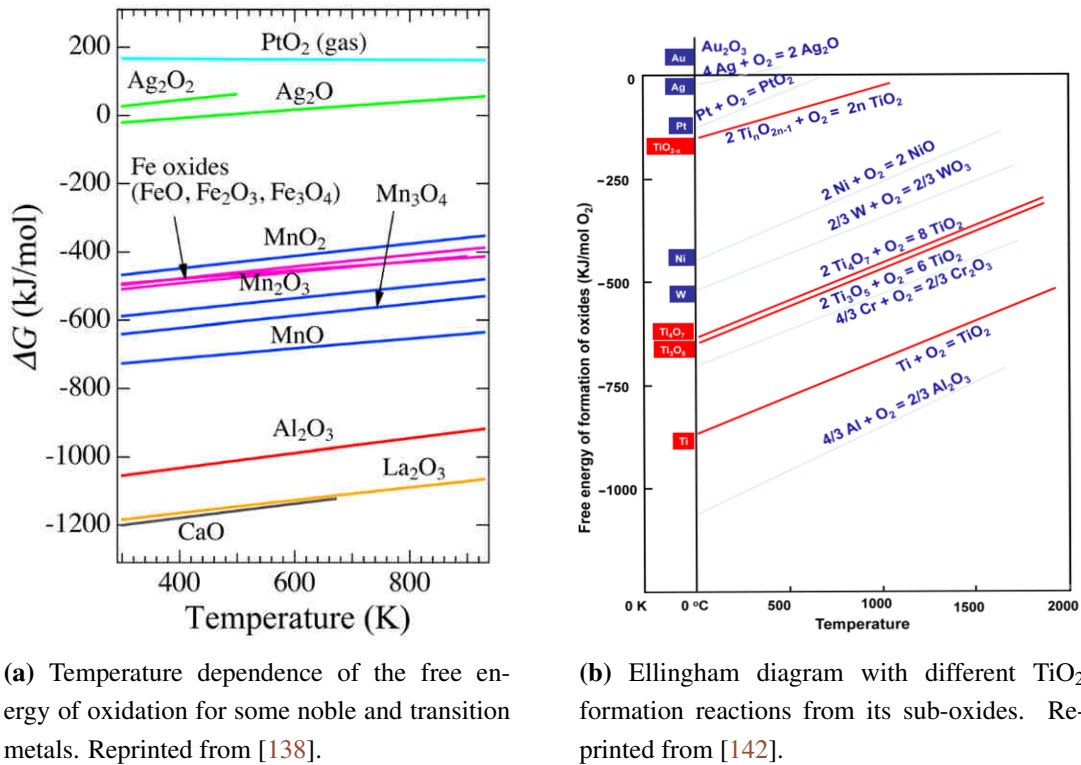


Figure 3.4 – Ellingham diagrams.

perature. The lower the free energy of oxidation, the more stable the oxide compound is. For example high and sometimes even positive (depending on the temperature) ΔG_{ox} of metals such as Pt or Ag means that their corresponding oxides (PtO_2 or Ag_2O_2) need energy to be formed and are expected not to be stable over time. At the contrary, metals such as Al or Ti have a very low ΔG_{ox} , meaning that they form very stable oxides. Figure 3.4.b details the free energy of formation of TiO_2 both from metallic Ti and from its wide range of available oxygen-deficient sub-oxides Ti_xO_y . The very low free energy of oxidation of stoichiometric TiO_2 (around -800 kJ/mol at 300 K) means that, in the presence of oxygen, the forward oxidation reaction $\text{Ti} + \text{O}_2 \rightleftharpoons \text{TiO}_2$ is very favourable from a thermodynamic point of view while the backwards reduction reaction (leading to oxygen evolution) requires additional energy. Nevertheless, another metal with an even lower free energy of oxidation can spontaneously reduce TiO_2 . This would for example be the case if Al was to be deposited on top of TiO_2 , the following reaction would then be thermodynamically favoured: $\frac{4}{3}\text{Al} + \text{TiO}_2 \rightarrow \frac{2}{3}\text{Al}_2\text{O}_3 + \text{Ti}$.

The oxygen affinity of the electrode material needs to be considered when preparing oxide-based memristive devices, as an additional interlayer can potentially form during the evaporation of the metallic electrodes or during device operation. This interlayer will then likely have a critical effect on the transport properties at the MS junction. For example, an insulating bar-

rier can be formed, effectively turning the MS junction into an MIS (Metal/Insulator/Semiconductor) heterojunction which will hinder the charge injection and can trigger new conduction mechanisms such as direct tunnelling or Poole-Frenkel emission if the insulating layer is thin enough ($\lesssim 3\text{ nm}$) or if traps are present in the band gap of the insulator, respectively. A more complex situation can also arise if the interlayer has semiconducting properties. This is for example the case for oxygen deficient TiO_{2-x} , a material in which the oxygen vacancies act as donor dopants effectively turning it into an n-type semiconductor.

This illustrates how what started as a relatively simple junction between a metal and a *p*-type semiconductor can quickly turn into a more complex MIS or even a metal/*p*-n heterojunction. Using a mixed ionic-electronic conductor with mobile interstitial oxygen ions such as L2NO4 in conjunction with a metallic electrode having a high oxygen affinity such as Ti means that the formation of an interlayer is a very likely scenario. This is however an interesting aspect that will be discussed further in the following experimental section, where several electrode materials were evaporated on top of the optimized L2NO4 thin films (discussed in the previous Chapter, Section 2.3) in order to investigate their electrical properties and choose the most promising contact materials for the preparation of M/L2NO4/M memristive devices.

3.2 Metal/L2NO4 heterojunction properties

This section presents the electrical characteristics of different metal/L2NO4 heterojunctions. The effect of the metal work function will be discussed briefly in the first subsection. The last two subsections will focus mainly on the spontaneous generation of TiO_x interlayers when using Ti electrodes, and their effect on the electrical conduction properties of a L2NO4-based memristive device.

3.2.1 Choice of the electrode material

In order to investigate the transport properties across a M/L2NO4 heterojunction, several noble metals with decreasing work function such as Pt (5.65 eV) and Ag (4.26 eV) were evaporated on top of a pristine (non annealed) L2NO4/STO sample to study the role of the electrode material on the final device characteristics. The resulting current-voltage (I-V) characteristics for the different pairs of electrodes (Pt-Pt, Pt-Ag and Ag-Ag) are displayed in Figure 3.5.a and clearly show an evolution from an ohmic contact with Pt to a more nonlinear and slightly rectifying (not visible in the I-V characteristics presented in Figure 3.5.a) Schottky-like contact with Ag. These results are coherent with the creation of a *p*-type SBH for L2NO4 given the work function of these metals and the contact evolution (as illustrated in Figure 3.3). Ti

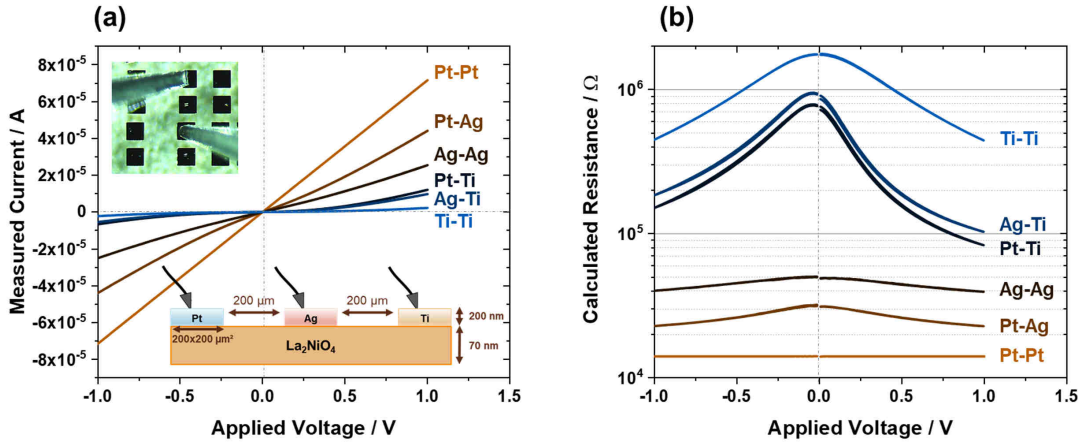


Figure 3.5 – (a) I-V characteristics between ± 1 V for different metal/L2NO4/metal heterojunctions. The top inset is a top-view picture taken during the measurements, showing the two probes and the rows of square pads composed of different electrode materials (either Pt, Ag or Ti). The bottom inset is a sketch of the sample’s cross-section (b) R-V characteristics for the different junctions presented in (a) from which the resistance was calculated. The L2NO4 film is 70 ± 3 nm thick.

electrodes were also evaporated on the same sample to test the possibility of forming a metal-oxide interlayers. Ti is known for having a very low enthalpy of oxidation (as discussed in Section 3.1.3), leading to the formation of TiO_x interlayers when put in contact with oxide materials [142]. Many research groups in the memristor community have already reported using this material as active electrode, or so-called “oxygen reservoir” [1, 4, 19, 53, 84, 107, 117]. The mechanism behind the oxygen storage is nevertheless completely different from the one discussed earlier concerning L2NO4 as a new and likely amorphous TiO_x phase has to be created in order to store the oxygen, while in L2NO4 the oxygen can occupy well-defined interstitial sites within the rock-salt planes (see subsection 2.1.1 in Chapter 2). The important increase in resistance shown in the R-V characteristics for electrode pairs containing at least one Ti electrode (Figure 3.5.b) suggest that a TiO_x interlayer was indeed formed at the Ti/L2NO4 interface. Since Ag and Ti have similar work functions (4.26 eV and 4.33 eV, respectively), a conventional metal/semiconductor Schottky contact cannot explain the observed increase in resistance. Instead, this result is attributed to the presence of an additional series resistance from TiO_x , effectively turning the initial Ti/L2NO4 into a Ti/ TiO_x /L2NO4 junction. A *n-p* junction cannot be ruled out at this point as oxygen vacancies are known donor dopants and are able to turn stoichiometric and insulating TiO_2 into a *n*-type semiconducting TiO_{2-y} (here ‘y’ represents the amount of oxygen vacancies V_O^\bullet present in the material).

Only asymmetric devices with exactly one Ti electrode exhibited a reproducible change in

resistance when applying an external electric field as will be discussed in detail in Chapter 4. The other electrode could be either Pt or Ag. This is an important result that allows narrowing down the active region responsible for the change in resistance at the Ti/L2NO4 junction of the memristive device. A Pt/L2NO4/Ti device with a top-top electrode configuration was selected to further test the electrical properties of L2NO4-based memories. Pt was preferred over Ag since it exhibits the highest Gibbs free energy and lowest contact resistance with ohmic characteristics, effectively locating the voltage drop across the rest of the device and particularly at the opposite L2NO4/Ti junction since L2NO4 is a relatively good electronic conductor (depending on its oxygen stoichiometry, Figure 2.11). This is expected to yield electrical fields high enough to locally trigger the drift of oxygen ions near the L2NO4/Ti interface.

3.2.2 Effect of the oxygen content in L2NO4 on the Pt/L2NO4 junction properties.

A new batch of four L2NO4/STO samples with different oxygen contents was prepared in the same conditions as previously described in subsection 2.3.2 (Chapter 2). Bar-shaped platinum electrodes were evaporated on the samples to carry out transmission-line measurements (TLM). This particular measurement technique allows the calculation of the contact resistance, the film resistivity and the transmission length through the following relationships:

$$R_T = \frac{R_S}{l}L + 2R_C \quad (3.3)$$

$$R_T = \frac{R_S}{l}(L + 2L_T) \quad (3.4)$$

where R_T is the total (measured) resistance of the Pt/L2NO4/Pt device, R_S is the sheet resistance of L2NO4 ($R_S = \frac{\rho_{L2NO4}}{e}$, with ρ_{L2NO4} and e the film resistivity and film thickness of L2NO4, respectively), l is the lateral length of two electrodes facing each other, L is the distance separating the two electrodes, R_C is the contact resistance (in the case of a symmetric M/L2NO4/M device where the two M/L2NO4 junctions are equivalent) and L_T is the transfer length, or the average distance a charge travels in the semiconductor beneath the contact before being injected in it (L_T was defined as the distance at which 63% of the current has been injected into the electrode [105]). More details on the derivation of Equations 3.3 and 3.4 are given in Appendix C, section C.3. The sample geometries used for the TLM measurements are shown at the top of Figure 3.6.

From the TLM fitting results presented in Figure 3.6.a-d, it appears that the Pt/L2NO4 con-

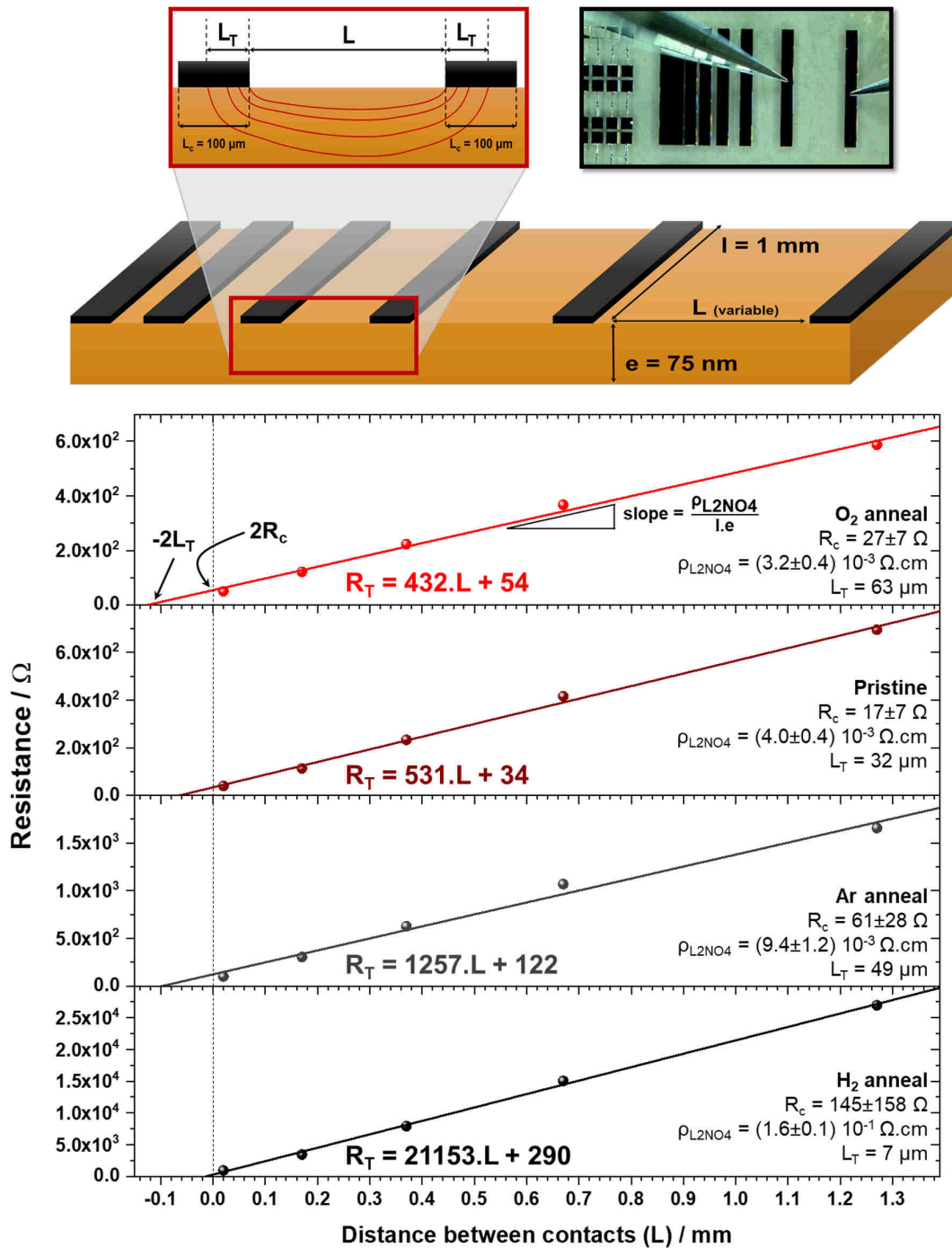


Figure 3.6 – The top part of the figure is an illustration of the TLM test pattern (bar shaped contacts in black). L is the distance between two electrodes, e is the thickness of the L2NO4 thin film, l is the length of the electrode and L_T is the transfer length. A picture of the TLM test pattern deposited on the different L2NO4 films is also shown in the top-right corner of the figure. (a-d) shows the TLM results carried out for the different L2NO4 films: the oxygen, pristine, Argon and H₂(6%)/Ar annealed samples, respectively. A linear fit of the data allowed calculating the contact resistance (R_c), the L2NO4 film resistivity (ρ_{L2NO4}) and the transfer length (L_T).

tact resistance (R_C) is not largely affected by the oxygen content in L2NO4. The values of R_C are all similar within the uncertainty, and lies somewhere around 20-30 Ω . A contact resistivity of Pt/L2NO4 can be calculated ($\rho_C = R_C \cdot L_T \cdot l$) and yields $1.7 \cdot 10^{-2} \Omega \cdot \text{cm}^2$, $5.4 \cdot 10^{-3} \Omega \cdot \text{cm}^2$, $3.0 \cdot 10^{-2} \Omega \cdot \text{cm}^2$ for the oxygen, pristine and argon-annealed samples, respectively. The contact resistance of the hydrogen-annealed sample is undefined (the uncertainty is larger than the value), meaning that its contribution should be negligible with respect to the resistance of the L2NO4 film itself. A value for the contact resistivity of the hydrogen annealed sample can therefore not be calculated, but it should remain low due to the small transfer length ($L_T = 7 \mu\text{m}$) extracted from the TLM plot for this particular sample.

The different annealing treatments have a clear effect on the film resistivity of L2NO4 (ρ_{L2NO4}). The resistivity varies from 3.2×10^{-3} to $1.6 \times 10^{-1} \Omega \cdot \text{cm}$ depending if the sample has been annealed in an oxygen or a hydrogen atmosphere, respectively. The large difference in resistivity of the samples was also measured by a 4-probe technique, yielding 7.9×10^{-3} and $1.2 \Omega \cdot \text{cm}$ for the same two samples (oxygen and hydrogen annealed, respectively). The different resistivity values measured for different measurements techniques remains unexplained for now and could be due to a problem of homogeneity of the sample or to our TLM measurement which can contain some error as the pads have a finite length². Nevertheless, the overall trend is the same: the sample annealed in oxygen shows orders two orders of magnitude lower resistivity values than the sample annealed in a highly reducing $\text{H}_2(6\%)/\text{Ar}$ atmosphere, confirmed both by 4-probe or TLM measurement techniques, with the additional information now from TLM that the contact resistance of Pt with L2NO4 is very low (a few tens of Ohms). Another information which could be extracted from the TLM measurements in Figure 3.6.a-d is the transfer length L_T . It decreases from $L_T = 63 \mu\text{m}$ to $49 \mu\text{m}$ and finally $7 \mu\text{m}$ for the sample annealed in oxygen, argon and $\text{H}_2(6\%)/\text{Ar}$, respectively. The transfer length of the pristine sample ($L_T = 32 \mu\text{m}$) is of the same magnitude but does not fit exactly the trend shown by the other three post-annealed samples. The reason for this might be a temperature-induced change in the samples microstructure upon annealing, also influencing the Pt/L2NO4 contact properties. As far as the post-annealed samples are concerned, the evolution of the transfer length is consistent with an increasingly resistive L2NO4. By choosing the path of lowest resistance, and as it becomes more difficult for the current to flow in L2NO4 the current will be injected sooner into the Pt electrode (resulting in a decrease of L_T). In the case of the sample annealed in oxygen, the transfer length represents is exactly 63% of the total pad width, which means that the total current is likely being injected throughout the entire Pt electrode. The situation is very different for the sample annealed in hydrogen where 63% of the total current is being

²to carry out rigorous TLM measurement the rectangular contacts should cross the entire width of the sample, else additional current can be measured on the lateral sides which is not taken into account in the geometry we used to calculate the film resistivity.

injected in the first 7 μm of the pad. The larger transfer length obtained for oxygen-enriched (thus self-doped) L2NO4 samples is an important result as it means that the current injection will be more homogeneously distributed throughout the surface of the Pt electrodes instead of only along the pad edges, leading to local current hotspots and possible pad degradation. This also means that if the contact resistance is increased, keeping the L2NO4 film resistivity low, the transfer length could eventually be equal or even be limited by the pad size, ensuring a more homogeneous current injection throughout the entire metal/L2NO4 junction which is interesting for a homogeneous interface-type resistance-change mechanism.

This aspect is investigated in the following section where it will be shown that the M/L2NO4 junction properties are drastically different when replacing the Pt contacts with Ti contacts.

3.2.3 Pt/L2NO4 and Ti/L2NO4 MS heterojunctions

The pristine sample prepared for the study on the effect of the oxygen content in L2NO4 on the Pt/L2NO4 junction properties (discussed in the previous subsection) was used to study the effect of the pad size on the electrical characteristics of symmetric Pt/L2NO4/Pt and Ti/L2NO4/Ti devices. Figure 3.7.a and b presents the total resistance of these two types of devices as a function of the inverse pad-side (defined as ' l ')³. The resistance of the device was calculated at two different voltages (0.1 V and 1.0 V, represented in the figures by squares and triangles, respectively) to detect possible nonlinearities in the electrical properties as a function of the pad size.

The total resistance evolves linearly with the inverse pad side for the Pt/L2NO4/Pt device (Figure 3.7.a), suggesting that the current flows homogeneously through the entire cross-section of the device. This means that there are no filamentary pathways through the bulk of the material locally short-circuiting the device. The resistivity of L2NO4 (ρ_{L2NO4}) could be calculated using the slope of the linear regression line (following Equation 3.4) and the transfer length determined from the previous TLM experiment for the pristine sample (Figure 3.6.b). Similar L2NO4 film resistivity values could be calculated for the pristine sample using the two measurement techniques ($4.0 \pm 0.4 \times 10^{-3} \Omega \cdot \text{cm}$ against $3.2 \pm 0.5 \times 10^{-3} \Omega \cdot \text{cm}$ for the TLM experiment and the varying pad size measurement, respectively). An interesting observation is that the applied voltage does not affect the slope of the curve (and thus ρ_{L2NO4}) in Figure 3.7.a, which is consistent with the already established ohmic characteristics of the Pt/L2NO4 junction in Figure 3.5.a and confirms the good Pt/L2NO4 contact properties (regardless of the pad size).

³as the electrodes are in a "top-top" planar configuration, the current is, at least in a first approximation, limited by the film's cross-section with a width defined by the pad side. See inset in Figure 3.7 for a better understanding of the device geometries.

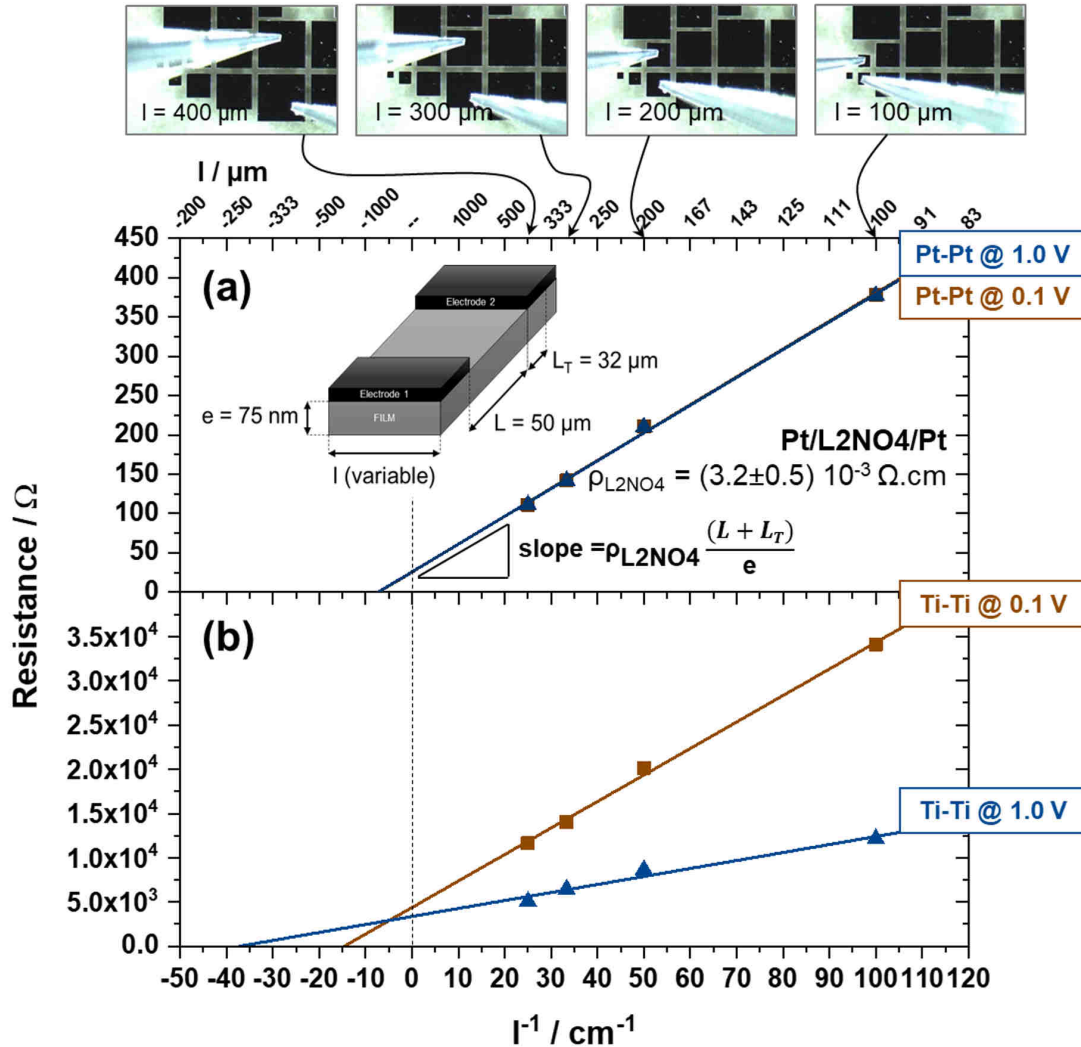


Figure 3.7 – (a) Resistance as a function of the inverse of the pad side for a symmetrical Pt/L2NO4/Pt device. The inset shows the geometry of the sample (e = L2NO4 film thickness; l = pad side; L = distance between two facing pad edges, L_T = transfer length determined in the previous TLM experiment). (b) Similar measurements carried out on a Ti/L2NO4/Ti heterojunction. Each data point corresponds to a different pad size as shown by the pictures at the top of the figure. The resistance was measured at two different voltages (0.1 V and 1.0 V) for the two different types of devices (the data points are superimposed in the case of the Pt/L2NO4/Pt device). The continuous lines correspond to linear regression fits for the four sets of data points. The pristine L2NO4 film is 70 ± 5 nm thick.

This is not the case for the Ti/L2NO4 junction. As can be seen in Figure 3.7.b, increasing the voltage from 0.1 to 1.0 V changes the slope of the linear regression line, which would imply that the resistivity of L2NO4 is voltage-dependent. Even though this could be true at higher electrical fields, as this behaviour was not measured with the Pt/L2NO4/Pt device (where the same electrical field has been used), this implies that Equation 3.4 is certainly no longer valid. The Schottky-like characteristics of the Ti/L2NO4 junction are certainly the reason for the measured voltage-dependence as the contact resistance of a Schottky junction is itself highly voltage-dependent. Since the transfer length depends on the contact resistance ($R_C = \frac{\rho_c}{L_T \cdot l}$), the decreasing contact resistance resulting from the application of a higher voltage means increasing the transfer length, which leads to an *apparent* decrease of the film resistivity (the measured change of slope in Figure 3.7.b). Nevertheless, linearity is conserved at a fixed voltage when changing the pad size, meaning that the current is still flowing homogeneously throughout the entire cross-section of the device and that there are no filamentary pathways, and even more importantly that the Schottky contact characteristics are preserved across the entire Ti/L2NO4 interface.

The increased resistance of the Ti/L2NO4/Ti devices when compared to Pt/L2NO4/Pt devices is understandable if we consider that an additional TiO_x insulating interlayer adds an additional series resistance to the stack.

3.2.4 Evidence of a TiO_x interlayer

The spontaneous oxidation of Ti (or similarly Al) electrodes during the processing steps has been mentioned in several research articles and is always attributed to the high affinity for oxygen of the material [19, 82, 117, 138]. Therefore, the presence or not of a TiO_x interlayer in the L2NO4-based memristive devices containing at least one Ti electrode has been further investigated using transmission electron microscopy (TEM). Cross-section specimens were prepared using a focused-ion beam (FIB) milling technique, allowing to very precisely select a region of interest below a given electrode material. Figures 3.8.a and b show the TEM image of a Pt/L2NO4/STO stack and a Ti/L2NO4/STO stack, respectively. The two specimens were analysed using a high-angle annular dark-field (HAADF) detector, highly sensitive to a change in the atomic number *Z* of a given chemical element, or the average *Z* for a compound material⁴. The HAADF image of the Pt/L2NO4/STO half device (Figure 3.8.a) clearly shows the presence of the three expected layers, being the STO substrate at the bottom followed by the L2NO4 thin film and finally the Pt electrode that had been evaporated on top. In the case of

⁴the higher *Z*, the brighter the contrast. For example Pt with an atomic number of *Z*=78 will turn out much brighter than Ti which has an atomic number almost four times lower (*Z*=22).

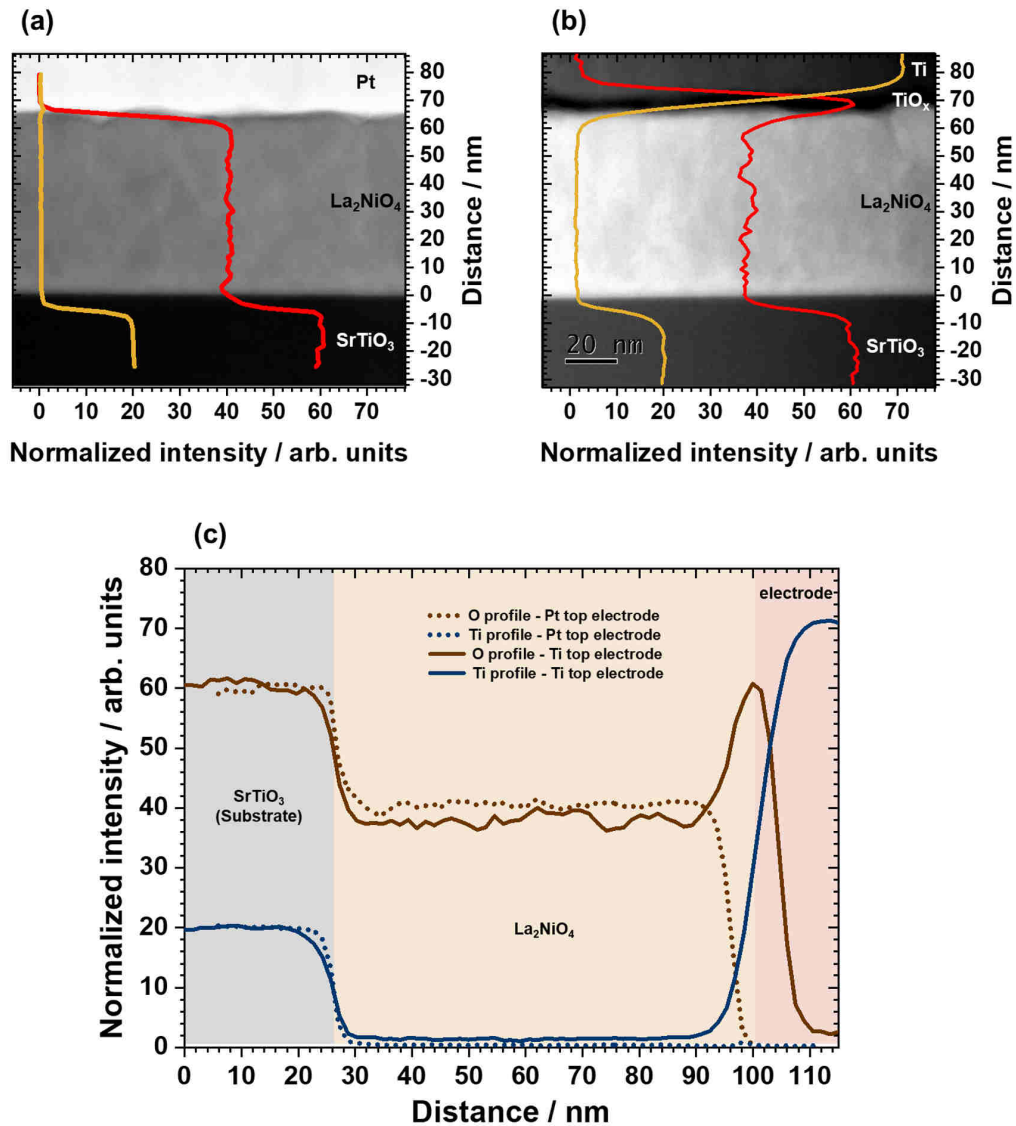


Figure 3.8 – HAADF TEM images of a pristine Pt/L2NO4/Ti device cross-section taken beneath a Pt electrode (a) and a Ti electrode (b) showing the presence of a darker contrast (lower density) interlayer beneath the Ti electrode which is not present on the Pt side. Chemical profiles for oxygen (red) and titanium (yellow) are superimposed to the images. These profiles were measured by EELS and have been normalized in intensity to the STO substrate. They are also plotted together in (c) to ease the comparison between the two heterostructures. A clear oxygen peak is present at the L2NO4/Ti interface and extends about 8 nm into the Ti electrode, suggesting a TiO_x interlayer has formed at this location.

the Ti/L2NO4/STO half device, these three layers (electrode/film/substrate) are also present, but an additional darker contrast can be observed between Ti and L2NO4. In HAADF, this darker contrast suggests the presence of a low density (low Z) and likely amorphous material. In order to obtain the composition of this interlayer, electron-energy loss spectroscopy (EELS) has also been carried out on the two TEM specimens. The chemical profiles for O (red curve) and Ti (yellow curve) are superimposed to the TEM cross-section images, clearly showing the presence of an oxygen-rich interlayer at the Ti/L2NO4 interface which is otherwise absent at the Pt/L2NO4 interface. Figure 3.8.c shows the same chemical profiles but this time altogether on the same graph to better distinguish possible differences in the intensity of the two chemical elements measured: O and Ti. These intensities are normalized to the STO substrate which contains both O and Ti in a 1:3 ratio. It is interesting to see that the overall amount of oxygen present in the L2NO4 film seems lower below Ti than below Pt, indeed suggesting that Ti has scavenged oxygen from L2NO4. Furthermore, the oxygen peak present at the Ti/L2NO4 interface coexists with a high intensity of Ti. When considering the normalized intensities at a distance of $d \simeq 100$ nm, a Ti/O ratio of 1.75/3 can be calculated, which corresponds roughly to the composition $\text{TiO}_{1.70}$ (or TiO_{2-y} with $y \simeq 0.29$ the number of oxygen vacancies per unit cell of TiO_2). This calculation is of course a simplification as other elements that were not considered could also be present in the interlayer. In addition, this interlayer is probably amorphous, meaning that the composition can largely vary depending on the location and could for example take the form of a chemical gradient between the Ti electrode and the L2NO4 film (as Ti is being oxidized by L2NO4). The presence of a highly oxygen deficient TiO_{2-y} is plausible, meaning that the interlayer would rather be an n -type semiconductor than an insulator.

3.2.5 Temperature-dependent measurements and transport mechanisms

Temperature-dependent electrical measurements have been carried out for an oxygen-annealed L2NO4/STO sample to investigate the transport mechanisms in M/L2NO4 ($M = \text{Pt}, \text{Ti}$) heterojunctions where L2NO4 plays the role of a highly acceptor-doped p -type semiconductor. Figure 3.9.a shows the evolution of the I-V characteristics between ± 1 V of a Pt/L2NO4/Pt device with decreasing temperature ($180\text{ K} \leq T \leq 300\text{ K}$, measured in vacuum). The slope of unity extracted from the $\log(I)$ - $\log(V)$ plot (inset in Figure 3.9.a) and the area dependence of Figure 3.7 demonstrates an ohmic conduction mechanism which is valid for the whole temperature range.

It is surprising to see that the temperature has very little effect on the measured current as the number of carriers in a semiconductor depends exponentially on the temperature (equation (5) in Table C.1). A reason for this might be that the Fermi level is very close to the the

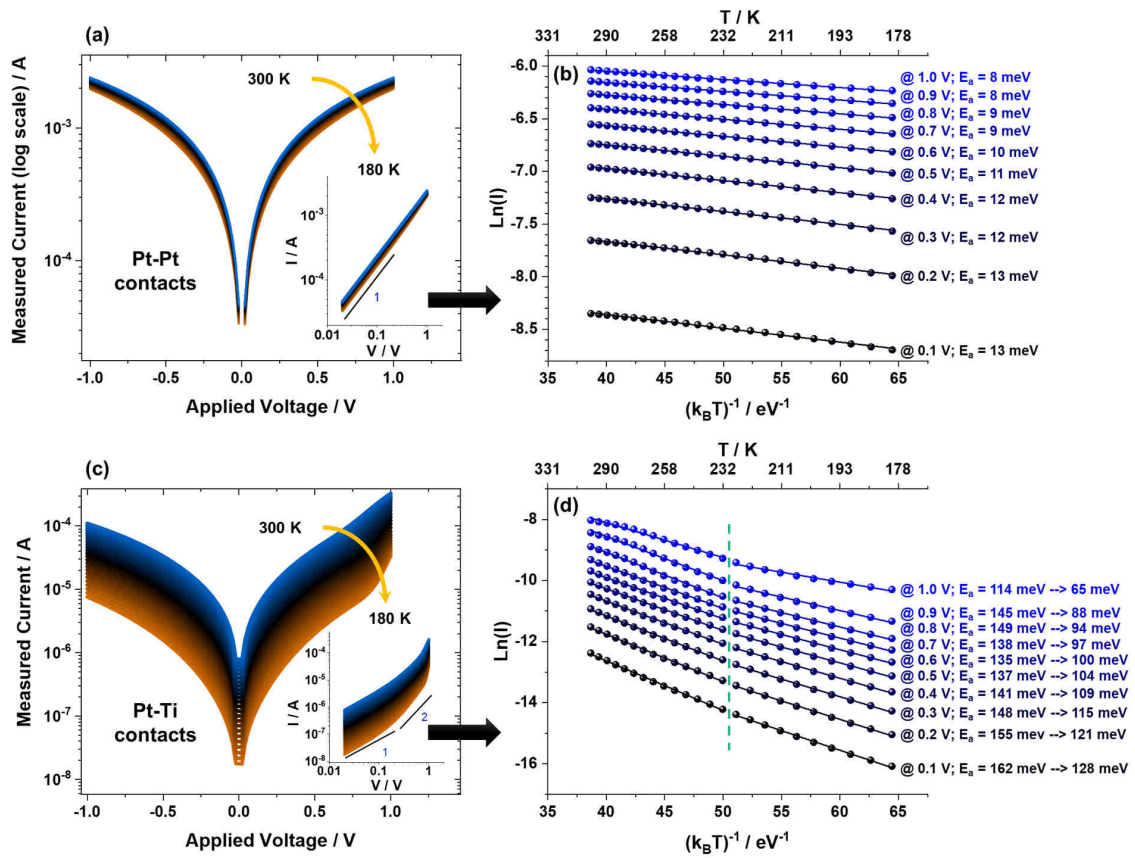


Figure 3.9 – Evolution of the electrical I-V characteristics for (a) Pt/L2NO4/Pt and (b) Pt/L2NO4/Ti as a function of temperature. The corresponding activation energies for different measurement voltages were obtained by fitting the data considering a conventional thermally activated process: $I = I_0 \exp\left(\frac{-E_a}{k_B T}\right)$ as is shown in (b) and (d) for the data presented in (a) and (c), respectively. The data in (d) presented two different regions: $300 \text{ K} < T < 230 \text{ K}$ and $230 \text{ K} < T < 180 \text{ K}$ which were fit independently using two linear regressions, yielding two temperature-dependent activation energies.

valence band edge of L2NO₄. Goodenough *et al.* have reported the possible degeneracy of this material in the presence of a sufficient amount of Ni³⁺ [45]. The oxygen-interstitial doping could thus be the reason for an almost degenerate L2NO₄. The activation energies were extracted from the measured I(V) curves and are displayed in Figure 3.9.b. Activation energies (E_A) as low as 8 meV are obtained, which is $\frac{1}{2}k_B T$ at 180 K (the lowest measurement temperature). E_A also has a (weak) field-dependence, which means that there should also be a small but measurable field-activated drift process involved in the conduction mechanism. The small temperature dependence of the I(V) data can be interpreted if the assumption is made that the Fermi level is degenerate and resides in the valence band of L2NO₄. At this point, grain-boundary scattering likely becomes one of the limiting conduction mechanisms. The very low activation energies are then coherent with a quantum tunnelling conduction mechanism, which in the case of direct tunnelling for example (equation (3) in Table C.1) is not affected by temperature but only by the thickness of the tunnelling barrier. The grain boundaries themselves would then play the role of the tunnelling barriers, a phenomenon well described by Nguyen *et al.* to explain the charge-scattering mechanisms happening in Al:ZnO thin films, a degenerate *n*-type semiconductor [94]. Even though we cannot conclude on the degeneracy or non degeneracy of the Fermi level, the hole-doped L2NO₄ is likely the main contributor to the overall device resistance in Pt/L2NO₄/Pt, while the contribution of the ohmic Pt/L2NO₄ junctions is very small.

The transport properties are different when using Ti electrodes. The same temperature measurements as previously with Pt have been carried out for an asymmetric Pt/L2NO₄/Ti device (Figure 3.9.c). First, the conduction is no longer ohmic in the entire voltage range as can be concluded by the slope > 1 in the $\log(I)$ - $\log(V)$ plot presented in the inset. The ohmic conduction only holds at low voltages, typically < 0.1 V, above which other nonlinear ($1 < slope \leq 2$) transport mechanisms have to be considered to account for the extra current. In this case the temperature has a visible effect on the measured I-V characteristics, but this effect is still low compared with the temperature range used to carry out these measurements, suggesting that the Fermi level of L2NO₄ is still close to the valence band edge as was the case for Pt/L2NO₄/Pt. A 'de-doping' effect due to the oxygen scavenging of Ti, reducing the amount of hole carriers in L2NO₄ remains a very likely situation as that would have the effect of increasing the Fermi level away from the valence band edge, removing the possible degeneracy discussed earlier. The activation energies extracted from this temperature data are presented in Figure 3.9.d. These low activation energies are ($65 \text{ meV} < E_A < 162 \text{ meV}$) are suggesting a tunnelling mechanism. However, a grain boundary-limited conduction mechanism is less likely here as the degeneracy should be removed and the activation energy values are ten-fold the ones obtained for Pt/L2NO₄/Pt. Here a thermally-assisted tunnelling mechanism

through a thin insulating barrier is more likely, and is in good agreement with the presence of as TiO_x interlayer. Interestingly, the activation energy of the conduction mechanism decreases with temperature (change of slope around 230 K). This could be explained by the presence of temperature-activated trap sites - such as oxygen vacancies - present for example in the TiO_x interlayer. Reducing the temperature could decrease the thermalization of carriers into these trap sites, restoring the direct tunnelling current to its maximum values. In other words, around 230 K the conduction mechanism could change from trap-assisted-tunnelling (TAT) to direct tunnelling.

3.3 Summary

The main points tackled in this chapter are summarized hereafter.

- The metal/oxide heterojunction (theoretical aspects):
 - Multiple conduction mechanisms can be present in a memristive device, performing electrical measurements varying the electrical field, the measurement temperature and the materials composing the final memristive heterostructure can help elucidate and separate them;
 - Both bulk and interface-limited conduction mechanisms need to be considered, keeping in mind that interface-limited mechanisms are key to an homogeneous interface-type resistance-change mechanism;
 - The work function of the metal used as electrical contact material can play a decisive role on the metal/oxide junction, providing either an ohmic or a Schottky contact. The combination of the two types of contacts is interesting to build memristive devices as it allows a certain control over location of the voltage drop within the device;
 - It is often the case that so-called ‘Fermi-level pinning’ renders the contact insensitive to the metal work function. Surface states or chemical reactivity of the oxide material with the electrode material needs to be considered;
 - Electrode materials having a low Gibbs free energy of oxidation (eg: Ti, Al,...) can easily form metal-oxide interlayers when brought in contact with an oxide material, giving rise to new conduction mechanisms.
- The metal/ L_2NO_4 heterojunction (experimental results):

- An ohmic contact could be obtained when evaporating Pt (high work function) on L2NO₄ while a slightly more resistive Schottky-like contact could be obtained with Ag (low work function), confirming the *p*-type semiconducting properties of L2NO₄. Devices built with at least one Ti electrode also showed Schottky-like characteristics with an important increase in resistance;
- TLM carried out on Pt/L2NO₄/Pt devices with varying oxygen contents (and thus a varying amount of hole carriers through the self-doping effect of L2NO₄) confirmed the larger conductivity of L2NO₄ when increasing its oxygen content. The TLM also provided a relatively small (~20-30 Ω) value for the Pt/L2NO₄ contact resistance, which is almost independent on the electrical properties of L2NO₄ (whether it is more or less resistive);
- The transfer length has also been extracted from the TLM, showing that lower resistivity values of L2NO₄ are beneficial for a more homogeneous current injection throughout the entire Pt/L2NO₄ interface instead of generating current hotspots along the facing edges of the contacts (as would be the case for the film annealed in a highly reducing H₂(6%)/Ar atmosphere);
- An homogeneous current flow has been shown both for the symmetric Pt/L2NO₄/Pt and Ti/L2NO₄/Ti devices by changing the pad size used for electrical measurements. This has confirmed the absence of current short-circuits, as well as the presence of an homogeneous Ti/L2NO₄ Schottky contact, regardless of the pad size;
- The presence of an amorphous and likely oxygen-deficient TiO_x interlayer has been observed at the Ti/L2NO₄ interface by HRTEM. This interlayer formed spontaneously when evaporating the Ti electrodes. Substoichiometric TiO_x effectively acts as a *n*-type semiconductor, meaning that the initial Ti/L2NO₄ *p*-type Schottky junction should rather be considered a Ti/TiO_x/L2NO₄ metal/*p-n* heterojunction;
- Temperature measurements (in the 300 K-180 K) were carried out on a symmetric Pt/L2NO₄/Pt device. The ohmic characteristics were maintained throughout the entire temperature range, with very low activation energies (~10 meV) suggesting a direct-tunnelling mechanism, possibly through grain-boundaries of L2NO₄;
- Similar temperature measurements carried out on an asymmetric Pt/L2NO₄/Ti device have shown that the conduction mechanisms are drastically affected by the presence of a Ti contact as the temperature dependence of the current is more important. The conduction mechanism shows a higher activation energy (~150 meV) which is still compatible with tunnelling mechanisms. In this case, the TiO_x in-

terlayer can act as the tunnelling barrier. A change of slope in the Arrhenius plot around 230 K could be explained by a change in the conduction mechanism from trap-assisted tunnelling (between 300 K and 230 K) to direct tunnelling at lower temperatures (at least down to 180 K).

In this chapter we have discussed the critical role of the electrode material on the electrical properties of an oxide-based memristive device, in particular when trying to obtain a homogeneous interface-type change in resistance. After having investigated the electrical properties of several M/L2NO4/M heterostructures, an asymmetric Pt/L2NO4/Ti was selected for further experiments aimed at assessing the memory capabilities of this L2NO4-based memristive device. These experiments are described and discussed in the following chapter.

Chapter 4

Pt/L2NO4/Ti, a prototypical memristive device for VCMs

Contents

4.1 Memristivity in Pt/L2NO4/Ti using the ‘top-top’ planar electrode configuration	66
4.1.1 The initialisation step	67
4.1.2 Analog I(V) characteristics and memory storage	69
4.1.3 Role of the oxygen content in L2NO4	72
4.2 Spontaneous relaxation behaviour	78
4.3 Neuromorphic aspects	81
4.4 Discussion	85
4.4.1 Analog-type change in resistance in metal/oxide/metal heterostructures	85
4.4.2 Proposed mechanism for the memristive behaviour in Pt/L2NO4/Ti devices	88
4.5 Summary	91

This chapter is mainly experimental dedicated to the in depth characterization of the Pt/L2NO4/Ti device, focusing on its memristive properties. The first section will explain the reasons for choosing the asymmetric ‘top-top’ electrode configuration, with the use of a Pt and a Ti electrode. The three subsections it contains will detail the device operation in chronological order, starting with the need of an initialisation step to trigger the memristive behaviour, followed by a continuous analog-type resistance-change achieved through bipolar voltage sweeps, and finally the role of the oxygen content of L2NO4 (which has been

varied through post annealing treatments) on the electrical characteristics of a Pt/L2NO4/Ti memristive device. The second main section puts in the spotlight intriguing resistance relaxation characteristics of the device which have been first observed after the initialisation step. The third section is dedicated to the highly multilevel neuromorphic programming capabilities with synaptic functions achieved through the application of voltage pulses. The fourth section is a discussion divided into two subsections. The first subsection is a brief literature review on other MOM heterostructures having shown memristive properties with a ‘Gradual Resistance-Change’ behaviour. A band diagram-based model is then proposed on the basis of this literature review to explain the similar gradual resistance-change properties obtained with the Pt/La₂NiO₄/Ti heterostructure in the second subsection. The important points discussed in this chapter are summarized in the final section.

4.1 Memristivity in Pt/L2NO4/Ti using the ‘top-top’ planar electrode configuration

A top-top configuration with macroscopic distances (a few hundreds of microns) between electrodes was preferred to the more common top-bottom configuration with a narrow spacing between electrodes. The reason behind this choice was to avoid the formation of conductive filaments and have a better control of the interface-type resistance changes in the memristive devices. In the conventional top-bottom configuration the low series resistance of tens of nm-thick L2NO4 is expected to lead to high currents, subsequent Joule heating and can ultimately induce an important degradation of the electrode material. At this point, other undesired resistance-change mechanisms such as electrochemical metallization (ECM) thermochemical or even phase change memory mechanisms become more likely. While Cu or Ag-based ECM cells have already been studied for their filamentary resistive switching mechanism, the formation of Pt filament in a Pt/TiO₂/Pt memristive device has also been reported [62], suggesting that the majority of electrode materials can end up migrating through the cell and short circuit the device if exposed to harsh programming conditions. The formation of filaments (being either metallic or formed within the oxide e.g. oxygen vacancies) is an undesired resistance-change mechanism here as we are aiming for a more homogeneous and highly multilevel change in resistance induced by the movement and accumulation of oxygen ions at the metal/L2NO4 interface instead.

Furthermore, and as has been discussed in the previous chapter, the electrode materials have been chosen carefully. Platinum was selected as it forms an ohmic contact with L2NO4, meaning that the Pt/L2NO4 junction offers little resistance to the passage of current, but also,

and maybe more importantly, that this same junction should be chemically inactive. The chemical inertness is an important aspect here as it allows narrowing down the materials (and their junctions) that are responsible for the memristive properties of the final device. Titanium at the contrary was selected for its high oxygen affinity, making it a chemically active electrode that can easily form a TiO_x interlayer at the Ti/L2NO4 junction. This oxygen defective interlayer may then play the role of an oxygen storage/release medium. The exchange of oxygen between the two materials, which could also be put in terms of reversible redox reactions, provides an effective playground for VCMs as some of the constituent elements composing the materials (for example Ni and Ti for L2NO4 and TiO_x , respectively) will increase (decrease) their oxidation state to compensate for the gain (loss) of atomic oxygen.

It is in these terms that the Pt/L2NO4/Ti - with a focus on the L2NO4/Ti heterojunction - is proposed as a prototypical device for VCM as it represents an experimental playground to investigate and understand how oxygen motion and subsequent redox reactions (which are key aspects of the VCM mechanism) are translated into the macroscopic electrical characteristics of this particular type of resistance-change mechanism.

4.1.1 The initialisation step

First we have tested the supposition that L2NO4 can as an “oxygen dispenser” by applying an increasing negative voltage to Pt (while grounding Ti). This leads to an external electric field pointing towards the Pt electrode and thus to the movement of negatively-charged species - such as O_i'' - in the opposite direction towards the L2NO4/Ti interface. An increase in the total resistance of the device would be consistent with a further oxidation of the TiO_x interlayer which formed spontaneously when evaporating Ti on pristine L2NO4 (read section 3.2.4 for more details) and is an indirect and partial proof that L2NO4 acts as an oxygen dispenser.

The results of such a biasing experiment are shown in Figure 4.1. The inset therein shows the resistance-voltage (R-V) characteristics of the device at different stages of the experiment. Initially the device shows non-linear and slightly rectifying electrical properties, with a resistance of 878 k Ω (calculated from the current measured at +10 mV). This resistance state is stable as shown by the 200 s sampling measurement carried out at a low read voltage of +10 mV. The device is then stressed electrically by applying successive 100 s long voltage levels with increasing negative voltage amplitude (*i.e.* -1 V, -2 V, -3 V, -4 V and -5 V). It is only after the stress at -3 V that the device starts to show a significant increase in resistance and ohmicity. It should be noted that the apparent increase in ohmicity is in fact more likely to be due to an increase in the built-in potential. This translates into an increase of the threshold voltage, under which the thermally-generated carriers ensure an ohmic-like conduction. It still remains an open question if the built-in potential is due to a MIS or to a *p-n* heterojunc-

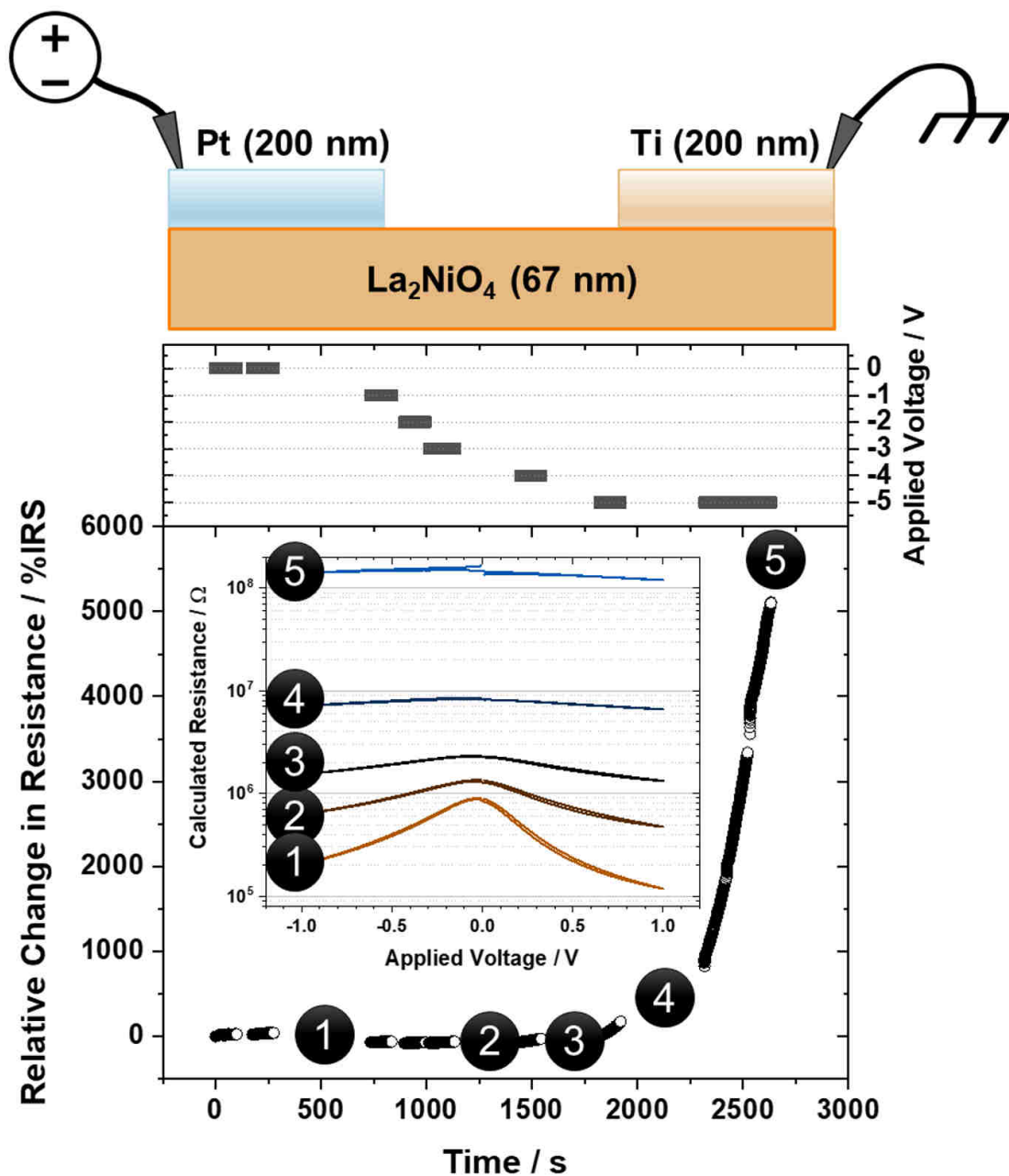


Figure 4.1 – (a) Response of a Pt/L2NO4/Ti device to an increasing voltage level. The upper panel shows the applied voltage over time (2x100 s at +10 mV followed by 100 s at -1 V, -2 V, -3 V, -4 V, -5 V and finally 2x100 s at -5 V again) while the lower panel shows the relative change in resistance as a percentage of the initial resistance over time ($R(t)$) and for each of these biasing conditions. The inset in the lower panel shows the evolution of the R-V characteristics (log scale) of the device at different stages of the experiment, these stages are indicated by the numerals in the $R(t)$ sampling curve.

tion between Ti, TiO_x and L2NO4. At the end of the experiment the resistance of the device increased over more than two orders of magnitude up to 145 MΩ.

We will refer to this experiment (the resistance-increase when applying a negative voltage to Pt) as an “initialisation step” as it does not strictly correspond to the typical “electroforming step”. The classical electroforming step is comparable to a soft dielectric breakdown which occurs at high voltage (higher than the cycling/operating voltage), creating locally conducting pathways in an initially insulating medium and gives rise to the memristive properties of the device. The operation carried out here increased the resistance of a more conducting IRS, ruling out the possibility of a soft dielectric breakdown and the formation of conducting filamentary pathways. Also, as will be shown later, the amplitude of the forming voltages does not need to be higher than the actual programming voltage, which is another major difference with the dielectric-breakdown type of forming.

4.1.2 Analog I(V) characteristics and memory storage

The newly initialized high resistance state (HRS) of the Pt/L2NO4/Ti device is then submitted to bipolar voltage sweeps ($0\text{ V} \rightarrow +V_{\text{max}} \rightarrow 0\text{ V} \rightarrow -V_{\text{max}} \rightarrow 0\text{ V}$), increasing the maximum voltage amplitude (V_{max}) every five cycles as displayed in Figure 4.2.a-c. The first five sweeps between $\pm 1\text{ V}$ show ohmic-like I-V characteristics with almost no rectification, suggesting that we are still in the sub-threshold voltage region of the I(V) curve. Already at $\pm 2\text{ V}$ hysteretic and rectifying I-V characteristics start to appear. Interestingly, the current levels and rectification of the device increases with the number of cycles without needing to increase the maximum voltage amplitude nor the dwell time at each voltage step. This suggests that an additional dynamic relaxation in which both the HRS and the LRS are decreasing over time is superimposed to each I(V) cycle. This effect is very clear when cycling at $\pm 3\text{ V}$ where an hysteresis is now visible on both sides of the I(V) curve. At $\pm 4\text{ V}$, the relaxation is still present, but when cycling $\pm 5\text{ V}$ the device shows two stable and highly reproducible resistance states separated by roughly one order of magnitude.

Figure 4.3.a and b respectively detail the highly reproducible I-V and R-V characteristics of the formed Pt/L2NO4/Ti devices and their memristive behaviour when cycling them between $\pm 5\text{ V}$. The device shows very little variability upon cycling and the transition from one resistance state to the other occurs gradually in a continuous analog way. The HRS and the LRS are both rectifying, suggesting that the underlying carrier transport mechanism might not have changed between the two states. The HRS features a large built-in potential (or threshold voltage) that decreases when programming the device to the LRS, which is achieved here after a $0\text{ V} \rightarrow +5\text{ V}$ voltage sweep.

Once the device is in its LRS and the voltage is swept in the reverse bias, the modulus

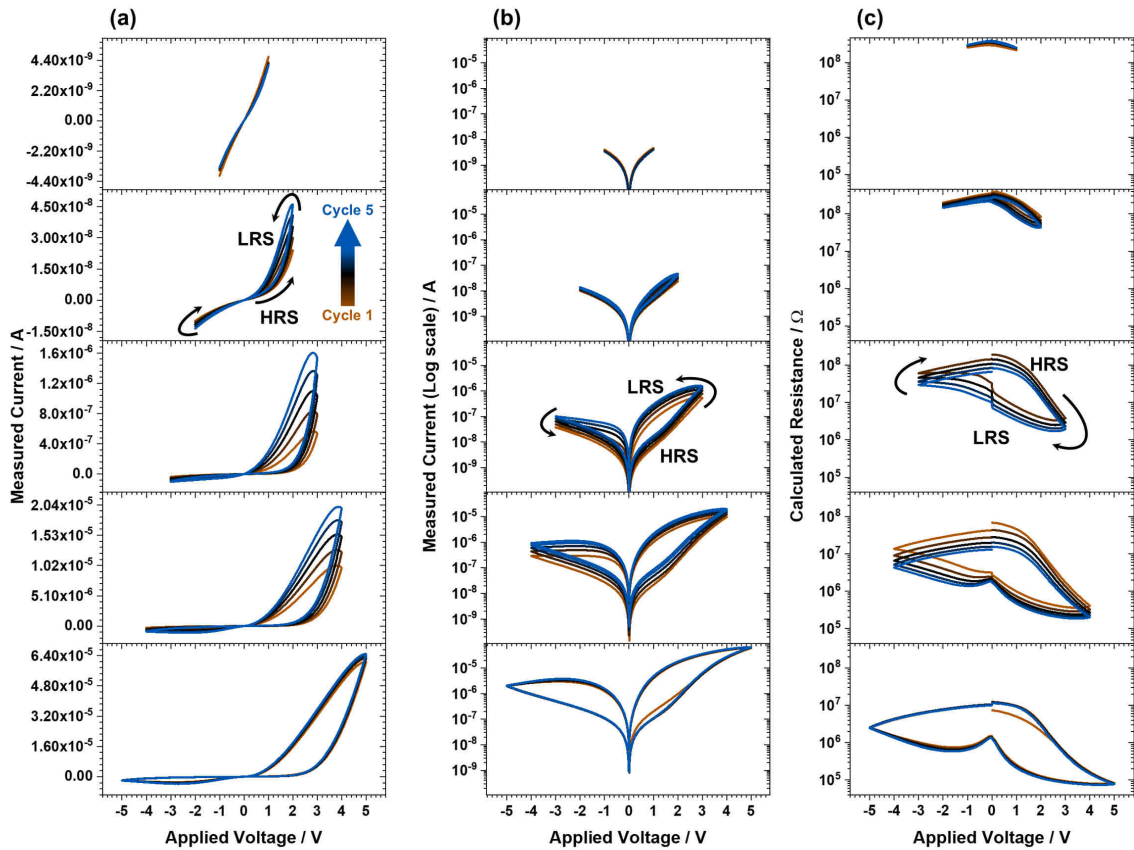


Figure 4.2 – (a) I-V characteristics of the same Pt/L2NO4/Ti device after the initialisation experiment described in Figure 4.1. Each panel shows five consecutive bipolar I(V) sweeps executed in the same biasing conditions ($0\text{ V} \rightarrow +V_{\text{max}} \rightarrow 0\text{ V} \rightarrow -V_{\text{max}} \rightarrow 0\text{ V}$). The maximum voltage amplitude (V_{max}) is increased from 1 V to 5 V with a step of 1 V in each new panel. (b) is the same as (a) but in semilogY scale and (c) is the same as (b) but described in terms of R-V characteristics. The Pt electrode was biased while Ti remained grounded throughout the experiment.

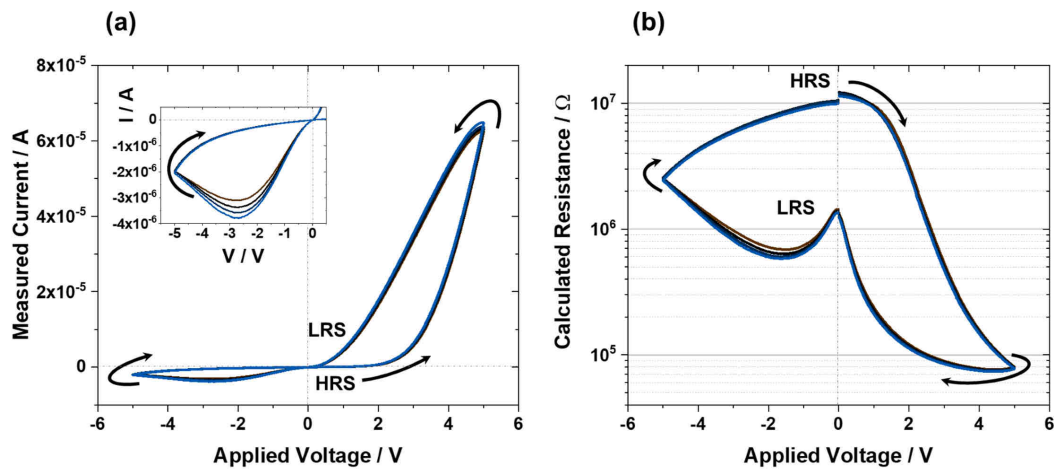


Figure 4.3 – (a) Stabilized I-V characteristics of a Pt/L2NO4/Ti device. As depicted by the arrows, the cycle starts at 0 V in the HRS, is set in its LRS applying a positive bias of +5 V and reset to HRS by applying a negative bias of -5 V. (b) R-V curve calculated from the measured current in (a). The Pt electrode was biased while Ti remained grounded in all the biasing experiments. The L2NO4 film is 67 nm thick.

of the current increases until it reaches a maximum around -2.75 V (see inset in figure 4.3.a), after which the current gradually decreases with the voltage modulus. This is often referred to in the literature as negative differential resistance (NDR), meaning that locally $\frac{dV}{dI} < 0$. This behaviour is in fact causing the change in resistance or ‘switching’ of the device and the possibility of returning to its HRS after the negative voltage sweep. The fact that this decrease in current occurs in a gradual manner within the timescale of the measurement (*e.g.* here a sweeping rate of ~ 350 mV/s), offers the opportunity of controlling the exact value of the HRS in a very precise manner. On the contrary this gradual ‘analog-type’ control of the resistance change is not easy to achieve in filamentary-type switching, in which the changes between resistance states are very abrupt, in a very short period of time and occur in a narrow voltage range. This $\frac{dV}{dI} < 0$ region present between -2.75 V and all the way down to -5 V disappears when the device is subjected to a series of negative unipolar sweeps as shown in Figure 4.4. Each new 0 V \rightarrow -5 V \rightarrow 0 V cycle gradually sets the device in a higher resistance state, but the maximum resistance that can be achieved in these biasing conditions seems to saturate around 50 M Ω .

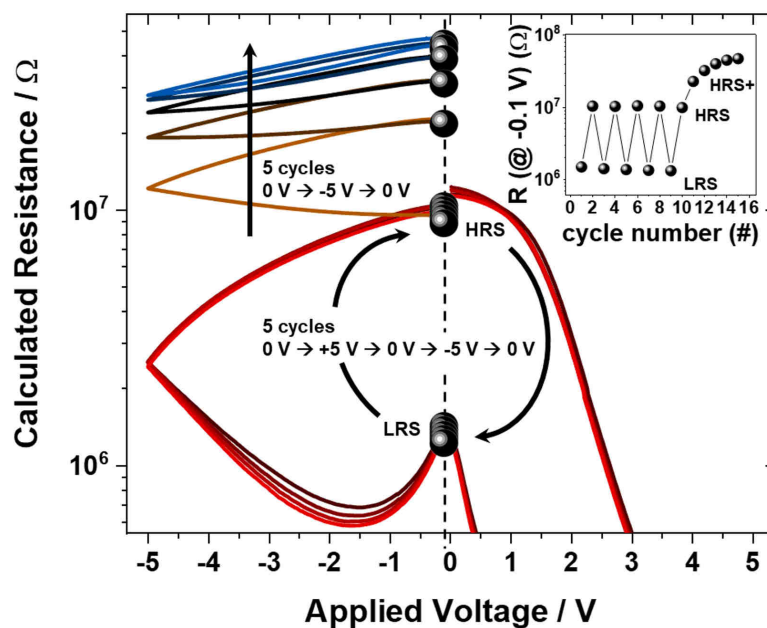


Figure 4.4 – R-V characteristics of a Pt/L2NO4/Ti device showing highly reproducible HRS and LRS over five consecutive ± 5 V cycles. The device is then gradually programmed to an even higher resistance state (HRS+) when carrying out five unipolar 0 V \rightarrow -5 V \rightarrow 0 V voltage sweeps. The inset shows the resistance state of the device (read out at -100 mV) after each cycle.

4.1.3 Role of the oxygen content in L2NO4

To illustrate the key role of oxygen on the electrical characteristics of L2NO4-based memristive devices, several pristine L2NO4 films received an annealing treatment prior to the evaporation of the Pt and Ti contacts. Similar treatments have been used as for the samples described in Section 2.3.2: one sample was annealed in a pure oxygen atmosphere while the two others were exposed to an increasingly reducing Ar or H₂(6%)/Ar gas mixture to lower its bulk oxygen content. The samples were all annealed at 500 °C for 1 h. After the preparation of the top electrodes in cleanroom facilities (see Appendix C.1), three Pt/L2NO4/Ti devices (one for each sample) were programmed from their IRS to a HRS following the standardized initialisation procedure described in Figure 4.5.a and which goes as follows. First the IRS is readout at +10 mV during 100 s to test its stability over time, followed by a train of 100 write/read ([-10 V; 1500 ms]/[+10 mV; 250 ms]) pulses and, finally, another 100 s long readout at +10 mV is carried out to probe the new resistance state of and measure its stability over time. The results of this initialisation for the three Pt/L2NO4/Ti samples with different oxygen contents are displayed in Figure 4.5.b-d. It can be noted that the three devices all have a different initialisation behaviour. First of all the IRS is different for the three samples and larger for the samples annealed in a more reducing atmosphere. We can consider in a first approximation that the total resistance equals:

$$R_T = R_{C,Pt} + R_{L2NO4} + R_{C,Ti} \quad (4.1)$$

where R_T is the total resistance of the Pt/L2NO4/Ti device, $R_{C,Pt}$ is the contact resistance between Pt and L2NO4, R_{L2NO4} is the resistance of the L2NO4 film and $R_{C,Ti}$ is the contact resistance between Ti and L2NO4. Figure 4.6 shows the relative contribution of R_{L2NO4} , $R_{C,Pt}$, $R_{C,Ti}$ to the total resistance of each of the three devices. R_{L2NO4} ($= \rho_{L2NO4} \cdot \frac{L}{e_i}$) has been estimated using the measured 4-probe resistivity of each L2NO4 film (yielding $8.0 \cdot 10^{-3} \Omega \cdot \text{cm}$, $1.4 \cdot 10^{-2} \Omega \cdot \text{cm}$ and $1.2 \Omega \cdot \text{cm}$ for the O₂, Ar and H₂-annealed samples, respectively) and the device geometry¹ (see sketch at the top of Figure 4.5). $R_{C,Pt}$ ($= \frac{\rho_{C,L2NO4}}{L_T \cdot l}$) has been estimated using the Pt/L2NO4 contact resistivity $\rho_{C,L2NO4}$ and transfer length L_T extracted from the TLM experiment carried out in the previous chapter (see section 3.2.2). The remaining resistance has been attributed to the contact resistance between Ti and L2NO4 and thus includes the possible series resistance of the TiO_x interlayer: $R_{C,Ti} = R_T - (R_{C,Pt} + R_{L2NO4})$.

The relative contribution of the Pt/L2NO4 contact resistance ($R_{C,Pt}$) is either small (*e.g.* ~12 % for the highly conducting oxygen-annealed sample in its IRS) or negligible (< 2 %

¹A correction has been made to take into account the presence of the small Pt contact between the measured electrodes, as previous measurements have demonstrated that the current will flow through the Pt electrode instead of the L2NO4 film whenever allowed to do so.

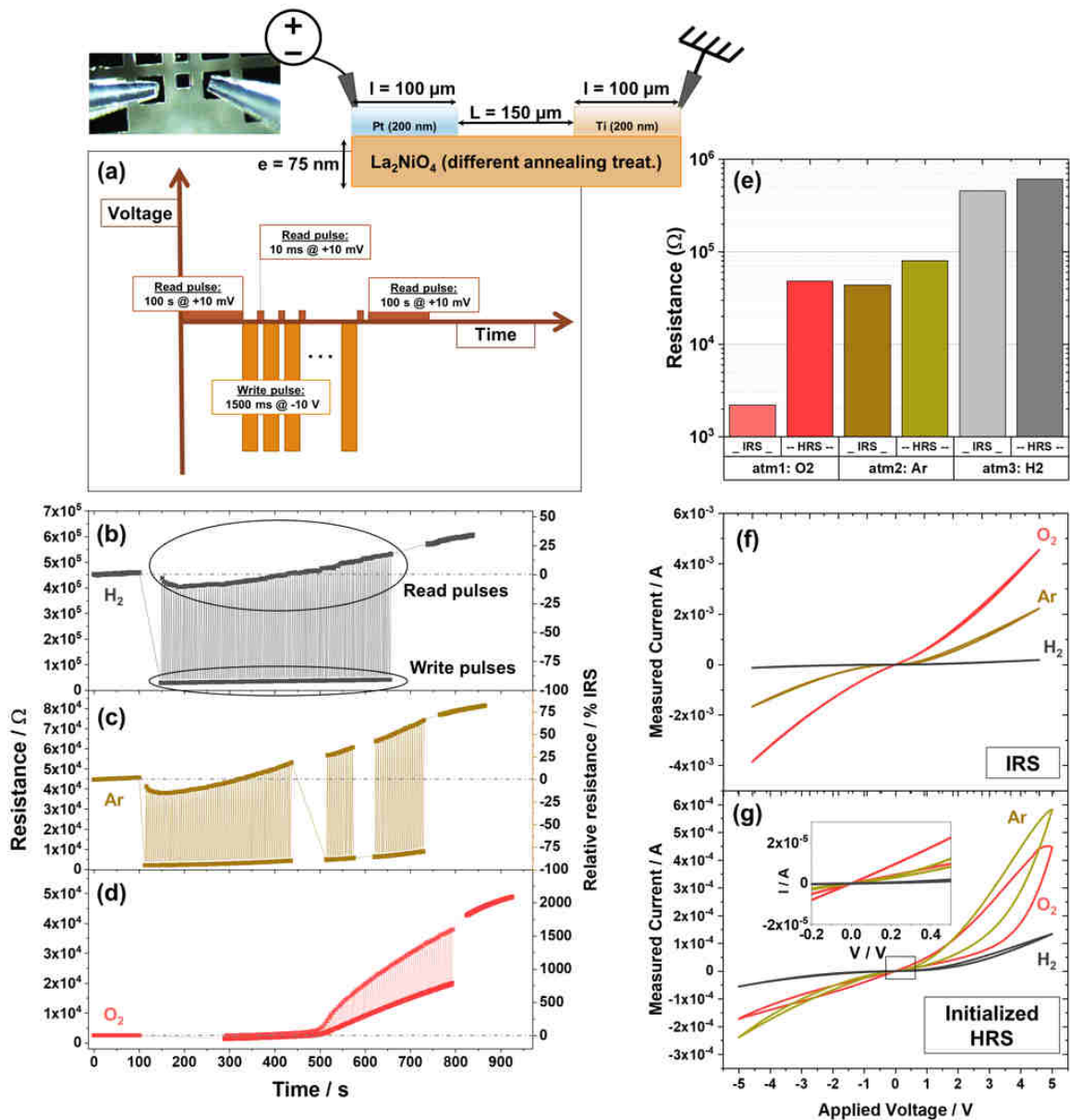


Figure 4.5 – (a) Illustration of the voltage-time initialisation sequence for the curves displayed in (b)-(d). The sequence starts with a 100 s readout of the resistance state at +10 mV, followed by 100 write/read pulses [-10 V; 1500 ms] and ends with another readout at +10 mV during 100 s. (b)-(d) Initialisation of a Pt/L₂NO₄/Ti device annealed in H_2 (6%)/Ar, Ar and O_2 , respectively. (e) Bar diagram summarizing the response to the initialisation procedure for the three different samples. (f)-(g) I-V characteristics of the Pt/L₂NO₄/Ti devices annealed in O_2 , Ar or H_2/Ar in their IRS and after being initialized to a HRS, respectively. The inset in (g) is a magnification of the I-V curve between -0.2 V and +0.5 V. A picture and a sketch of the sample and the biasing conditions is shown at the top of the figure.

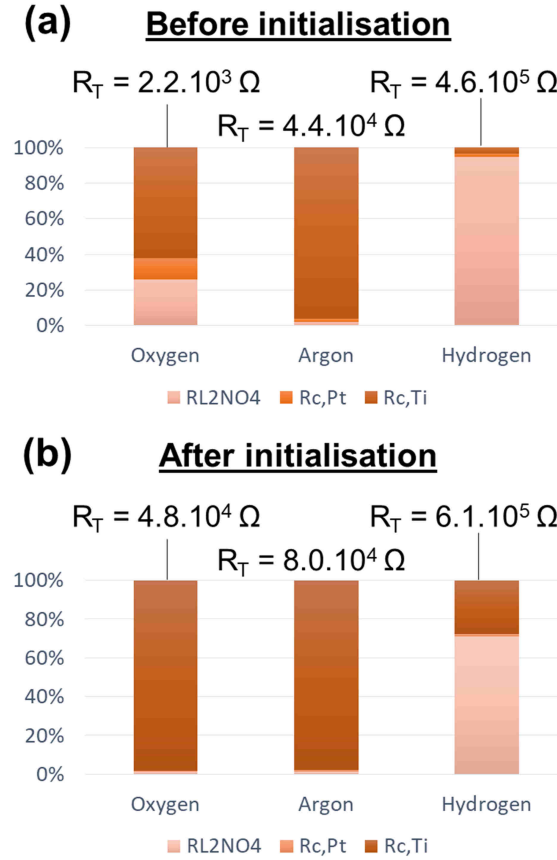


Figure 4.6 – (a) Relative contribution of the L2NO4 film (RL2NO4), the Pt/L2NO4 contact ($R_{C,Pt}$) and the Ti/L2NO4 contact ($R_{C,Ti}$) to the total resistance R_T of the oxygen, argon and hydrogen annealed samples in their IRS (before the initialisation step). (b) Same as (a) but after the initialisation step.

in all the other cases). The total resistance of the Pt/L2NO4/Ti device can thus be attributed mainly to R_{L2NO4} and $R_{C,Ti}$. When considering the three samples in their IRS (Figure 4.6.a), the L2NO4 film initially has the highest contribution to the total resistance of the device for both the hydrogen-annealed sample (contribution of ~95 %), while its contribution is ~26 % for the oxygen-annealed sample and only ~2 % in the case of the argon-annealed sample. Thus the increase in the L2NO4 film resistivity with decreasing oxygen cannot explain alone the larger IRS when decreasing the oxygen content of the device. $R_{C,Ti}$ represents ~96 % and ~3 % of the total resistance for the argon and hydrogen annealed samples, respectively, while $R_{C,Ti}$ represents ~62 % of the total resistance in the case of the oxygen-annealed sample accounting for the spontaneously-formed TiO_x interlayer.

In the case of the hydrogen-annealed sample, the important increase in the L2NO4 film resistivity (of nearly two orders of magnitude) reduces considerably the relative importance

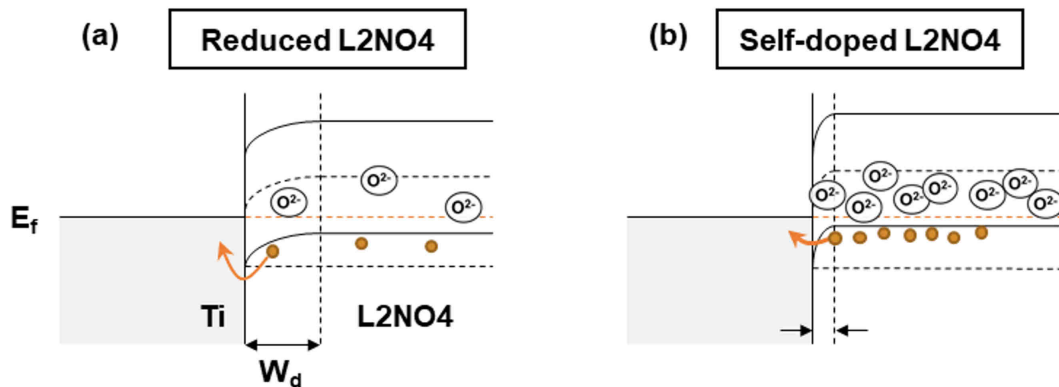


Figure 4.7 – Possible band diagram illustrating the Schottky contact between (a) Ti and reduced L2NO4, (b) Ti and oxidized L2NO4. The oxidized sample contains a higher amount of interstitial oxygen ions (represented here by O^{2-}), resulting in additional hole carriers (yellow discs) through a self-doping mechanism. The increasing amount of hole carriers reduces the depletion width W_d at the Ti/L2NO4 junction, reducing the contact resistance $R_{C,Ti}$.

of $R_{C,Ti}$, its contribution remains however similar than for the argon-annealed sample ($R_{C,Ti} = 1.5 \cdot 10^4 \Omega$ against $4.2 \cdot 10^4 \Omega$ for the hydrogen and the argon-annealed samples, respectively), meaning that the Schottky contact properties might also be similar. The much lower $R_{C,Ti}$ contact resistance for the oxygen-annealed sample ($R_{C,Ti} \sim 1.4 \cdot 10^3 \Omega$) implies very different Ti/L2NO4 contact properties and likely also different conduction mechanisms. Nevertheless, these differences remain coherent with a Schottky contact model as illustrated in Figure 4.7. Indeed, when L2NO4 is post-annealed in an oxidizing atmosphere, the higher amount of hole carriers obtained through a self-doping mechanism not only decreases the resistivity of L2NO4, but it also decreases the depletion width in the case where a Schottky junction exists between Ti and L2NO4. The decreased depletion width then allows new transport mechanisms to take place (such as direct tunnelling for example).

Coming back to the initialization procedure of the three devices (Figure 4.5.b-d), it can be noticed first that the IRS is stable during the first 100 s long readout at +10 mV, with a value of $4.6 \cdot 10^5 \Omega$, $4.4 \cdot 10^4 \Omega$ and $2.2 \cdot 10^3 \Omega$ for the hydrogen, argon and oxygen-annealed sample, respectively. When applying the write pulses (-10 V; 1500 ms), the samples follow two different behaviours depending on them having received a reducing or an oxidizing annealing treatment. The resistance of the two reduced samples (Figure 4.5.b and c) first decreases during the first ten write pulses before increasing again. The hydrogen-annealed sample needs the first 55 pulses to retrieve its IRS value of $4.6 \cdot 10^5 \Omega$, while the argon-annealed samples needs slightly less (42 pulses) to climb back to its initial $4.4 \cdot 10^4 \Omega$. The oxygen annealed sample (Figure 4.5.d) does not show the initial decrease in resistance and is directly programmed to a

higher resistance state after each new write pulse. Interestingly, this last device initially shows a slow increase in resistance during the first 40 pulses, followed by a steeper increase afterwards. The initial resistance drop for the two reduced samples could find its origin in the field-induced drift of the interstitial oxygen ions still present in the sample towards the Ti/L2NO4 interface. This would reduce the contact resistance $R_{C,Ti}$ in the same way as is illustrated in Figure 4.7, but instead of doping the entire L2NO4 film there would only be a local doping increase at the Ti/L2NO4 interface. At a certain threshold concentration (achieved after the first ten write pulses), the oxygen ions could continue oxidizing the Ti electrode and increase the resistance of the device by increasing the thickness and/or the oxidation of the (thin) TiO_x interlayer.

In the case of the oxygen-annealed sample, the oxygen concentration at the Ti/L2NO4 interface is already high initially, meaning that oxygen ions could start drifting into the Ti electrode and oxidizing it as soon as the first write pulse is applied.

At the end of the initialisation procedure, the resistance continues increasing spontaneously (*i.e.* without the application of an external electric field) during the second 100 s long readout step. The increase is very subtle for the two reduced samples, and more substantial for the oxidized sample. This effect could be explained by the diffusion of the oxygen ions away from the Ti/L2NO4 interface to restore an homogeneous chemical gradient across the sample. This Fickian diffusion process would lower the doping concentration, increase the depletion width and would thus increase $R_{C,Ti}$ and the total resistance of the device. This effect is more important for the oxygen-annealed sample as a higher gradient of interstitial oxygen ions has to re-equilibrate. Figure 4.6.b shows the relative contribution of R_{L2NO4} , $R_{C,Pt}$, $R_{C,Ti}$ to the total resistance of each one of the three devices after being initialized. The assumption has been made that only $R_{C,Ti}$ (which also contains the series resistance of TiO_x) changes during the initialisation procedure. This is surely a simplification as R_{L2NO4} is also expected to change (increase) when losing part of its oxygen during the oxidation process of Ti. Nevertheless, the volume of L2NO4 affected by this oxygen loss is likely concentrated in close proximity to the Ti electrode and should only represent a fraction of the total volume of L2NO4 traversed by the current. An effect on R_{L2NO4} can be expected when reducing the size of the device to such dimensions where the ‘active volume’ of L2NO4 (*i.e.* the volume that exchanges oxygen with Ti) becomes an important fraction of the total volume. Similarly, the assumption has been made that $R_{C,Pt}$ remains constant throughout the initialisation procedure. This hypothesis has been verified with the help of a third (non biased) Pt electrode serving as a reference to test whether the resistance-change occurred beneath the Pt or the Ti electrode in the biased device. This experiment revealed that only the region around the biased Ti electrode changed while the electrical characteristics of the biased Pt electrode are unaltered after the initialisation experi-

ment. The assumption that only $R_{C,Ti}$ changes during the biasing of the device seems therefore reasonable as a first approximation. What is clear from Figure 4.6.b is that the three devices all exhibited a resistance-increase, regardless of their annealing treatment. This increase is due (following the approximation discussed before) to the increase of the relative contribution of $R_{C,Ti}$ to the total resistance. Indeed, the Ti/L2NO4 contact resistance now represents ~98 % of the oxygen and the argon-annealed devices and ~28 % of the highly H₂-reduced device.

The bar chart in Figure 4.5.e summarizes the initialisation results, the bar height shows the resistance value before and after the initialisation step for each one the three samples annealed in increasingly reducing atmospheres. The oxygen-annealed sample stands out in the relative resistance change it experienced after initialisation. This sample shows a more than twenty-fold increase in resistance while the argon and hydrogen-annealed samples only show a factor 1.8 and 1.4, respectively. A likely explanation of this result would be the presence of a thicker or more oxidized (thus more resistive) TiO_x interlayer in this sample that formed with the field-induced drift of oxygen from L2NO4 into the Ti electrode. Furthermore, the larger resistivity of the reduced L2NO4 samples leads to a larger voltage drop across the film, while this voltage drop should be concentrated mostly at the Ti/L2NO4 junction in the case of the more conducting oxygen-annealed sample, even more so in the presence of a continuous TiO_x interlayer. The lower amount of oxygen ions available in L2NO4 combined with a smaller electric field at the Ti/L2NO4 junction makes the drift of these oxygen ions and the oxidation of the Ti electrode more difficult. This then explains why the magnitude of the resistance-change during device operation is lower for the reduced samples.

The I-V characteristics of the devices in their IRS are displayed in Figure 4.5.f in which a non-linear behaviour with little rectification for the two reduced samples to almost no rectification for the oxidized sample can be observed. The absence of rectification is an important marker of an inhomogeneous Schottky barrier height [130]. The I-V characteristics of the initialized samples are shown in Figure 4.5.g where the inset (corresponding to a magnification of the electrical characteristics at low voltage) puts in evidence that only the oxygen-annealed sample has a significant difference in the HRS and LRS when cycling the devices between ±5 V. The argon-annealed sample has an hysteretic behaviour when $V > 300$ mV but the opening vanishes at lower voltages. The hydrogen-annealed sample has a very small opening when $V > 1$ V. The presence or absence of two well differentiated resistance states all the way down to 0 V is certainly a marker of the potential retention capabilities of the device. This means that only the oxygen-annealed sample has memory retention while the changes induced in the two other reduced samples are volatile, at least in these biasing conditions. The oxidation (reduction) of Ti (TiO_x) might explain the varying retention characteristics. Redox reactions are likely present in the oxygen-annealed case, while in the reduced samples the hysteresis could

be due to a temporary variation in the hole-doping concentration at the Ti/L2NO4 interface, changing its electrical characteristics in a reversible and volatile way.

This section on the role of the oxygen content on the memristive properties of a L2NO4-based memristive devices has shown that the additional oxygen ions present in the form of interstitial point defects in L2NO4 are beneficial, and even necessary to give rise to the memristive properties of the device. A precise interplay between the TiO_x interlayer thickness, stoichiometry and homogeneity and the oxygen content of L2NO4 are certainly crucial parameters that need to be controlled to be able to tune the resistance-change and the retention characteristics of the memristive device.

4.2 Spontaneous relaxation behaviour

To further investigate the previously observed dynamic resistance changes, a new pristine device has been initialised. The voltage was applied in a pulsed mode with two different pulse durations. The results of this new experiment are shown in Figure 4.8. First the IRS of the device was readout at +10 mV during 1000 s showing a stable resistance of 1.4 M Ω . Then a train of 200 write/read ([-10 V; 300 ms]/[+10 mV; 300 ms]) pulses was used to program the device to a HRS. However, this led to a very small increase in the overall device resistance. The device first decreased its IRS by 21 % after the first 5 write pulses, but then slowly increased to an intermediate HRS lying 12 % above its initial IRS during the next 195 write pulses. The write pulse duration was then increased fivefold (to 1500 ms) to obtain a larger increase in resistance. Another pulse train consisting in 200 write/read ([-10 V; 1500 ms]/[+10 mV; 300 ms]) was launched, this time leading to a very substantial and continuous increase in resistance, reaching almost 2400 % of the devices IRS. The dependence of the resistance increase rate as a function of the duration of the write pulse, or in other words, the fact that the resistance increases faster when applying a high voltage during a longer period of time suggests that the temperature could have an important influence on the resistance-change process. Indeed, increasing the duration of the voltage pulse means that the device is submitted to a current flow for a longer period of time, generating more Joule heating. Decreasing the pulse duration allows the device to release some heat between each new voltage pulse, decreasing the temperature-activated ionic motion and thus the oxygen drift towards the Ti electrode.

When sampling the resistance at a read voltage of +10 mV to probe the relaxation dynamics of the device, the resistance continued increasing over more than one order of magnitude during the first ten minutes that followed the stressing ('Relax #1' in Figure 4.8). The device then decays back to a lower resistance state during the next twenty sampling minutes ('Relax

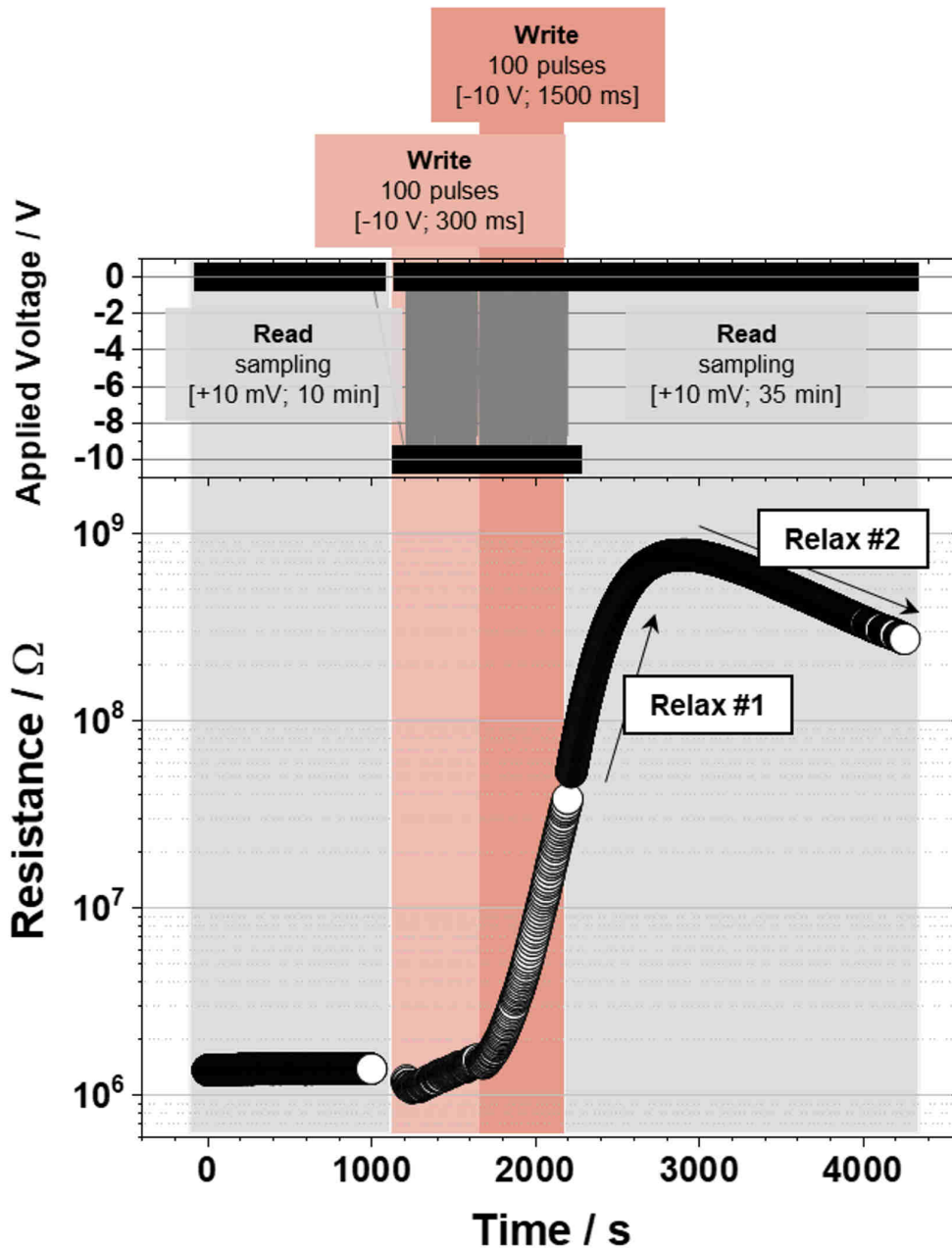


Figure 4.8 – Evolution of the resistance of a pristine Pt/L2NO4/Ti device over time. A stable IRS is measured during the initial readout at $V = +10$ mV during $t = 1000$ s. The initialisation step consisting in the application of 200 write[-10 V; 300 ms]/read[$+10$ mV; 300 ms], followed by another 200 write[-10 V; 1500 ms]/read[$+10$ mV; 300 ms] voltage pulses (orange regions, only the resistance readout at $+10$ mV is shown) shows a gradual increase of the resistance of the device over approximately two orders of magnitude. The new HRS of the device is finally readout again at $+10$ mV, showing a continuation in the resistance increase over the first ten read minutes, followed by a relaxation to a lower resistance state until the experiment is stopped.

#2'). The resistance increase has been attributed earlier (see previous section) to a Fickian diffusion process, allowing the oxygen ions accumulated at the Ti/L2NO4 junction during the initialization procedure to relax back into the bulk of L2NO4, restoring a more homogeneous chemical gradient throughout the material. This de-doping process of the Ti/L2NO4 junction increases the Schottky barrier width, hence increasing the total resistance of the device. Nevertheless, this cannot explain the spontaneous resistance decrease that follows (when $t > 3000$ s). A plausible explanation for this second relaxation phenomenon would be that the reduction of the TiO_x interlayer which thickness (and stoichiometry) is directly influencing the total resistance of the device. Since the free energy of oxidation of Ti is very low (the reaction $Ti + O_2 \rightarrow TiO_2$ has $\Delta G_{ox}(300K) \simeq -800$ kJ/mol, see Figure 3.4.b), there are only few materials capable of spontaneously reducing the very stable TiO_2 compound (in close to room-temperature conditions). Nevertheless, the free energy of oxidation of partially oxidized TiO_{2-y} into stoichiometric TiO_2 is drastically larger, i.e. -200 kJ/mol (Figure 3.4.b), meaning that the energy required to partially reduce TiO_x only (without having to completely regenerate the metallic Ti electrode) could be much lower. Furthermore, even though the value of ΔG_{ox} for the oxidation of L2NO4 (i.e. $La_2NiO_{4.00} + O_2 \rightarrow La_2NiO_{4+\delta}$) is unknown, it is clear that the stoichiometric $La_2NiO_{4.00}$ compound is highly unstable and can only be obtained in highly reducing conditions [109], which is confirmed by the value of its enthalpy of formation close to zero (2.2 ± 5 kJ/mole) reported by Navrotsky *et al.* [93]. In the case where a hole-depletion region exists at the L2NO4 side of the Ti/L2NO4 junction, there should locally be a concomitant absence of interstitial oxygen dopants in this same region. This 'highly reduced' $La_2NiO_{4.00}$ interfacial region could then partially reduce TiO_{2-y} in the regions where the two materials are in contact with each other. Another possibility is that some of the oxygen that drifted into the Ti electrode during the initialization step has not reacted chemically with it. Instead of participating to the formation of the TiO_x interlayer the oxygen might be adsorbed at the surface or in the grain boundaries of the Ti electrode. This adsorbed atomic (or maybe even molecular) oxygen could then easily be incorporated back again into L2NO4. Even though the possibility of having adsorbed oxygen at the surface of a Ti electrode has already been proposed in memristive devices based on graphene-oxide [92], it seems unlikely that the oxygen would not react with metallic Ti and spontaneously reincorporate L2NO4 instead. An additional stoichiometric TiO_2 layer only present after the initialization step could play the role of a oxygen-saturated and thus ion blocking layer and is therefore more likely to spontaneously restore adsorbed oxygen from its surface back into L2NO4. Nevertheless, the two aforementioned cases - i.e. the spontaneous reduction of TiO_{2-y} by the presence of a thin layer of stoichiometric $La_2NiO_{4.00}$ or the reincorporation into L2NO4 of adsorbed oxygen atoms from a thin insulating TiO_2 interlayer (or present in the grain boundaries of the Ti

electrode) - have similar outcomes. In both cases the TiO_x interlayer (here TiO_x can be either TiO_{2-y} or TiO_2) loses oxygen atoms which are likely playing the role of electron traps at the $\text{TiO}_x/\text{L2NO}_4$ interface. When these oxygen ions diffuse back into L2NO_4 , they release the trapped electrons and can restore additional conduction paths (such as TAT) through the TiO_x interlayer, increasing the total current and thus gradually lowering the resistance state of the device (*i.e.* ‘Relax #2’).

4.3 Neuromorphic aspects

A new pristine sample was prepared to investigate the neuromorphic programming capabilities of L2NO_4 -based memristive devices. The nonlinearities in the electrical characteristics of the $\text{Pt}/\text{L2NO}_4/\text{Ti}$ device were studied in order to optimize the pulse characteristics and the programming sequence. The aim was to find the optimal pulse characteristics that would ultimately lead to an enhanced control over the resistance, being able to increase or decrease the resistance gradually or, on the contrary, operate a hard RESET to the system when increasing for example the pulse amplitude. Figure 4.9 shows an example of the programming capabilities and large flexibility offered by the $\text{Pt}/\text{L2NO}_4/\text{Ti}$ memristive system. The device is first initialized by applying two trains of ten pulses [-20 V; 750 μs] (Figure 4.9a and b) after which it exhibits the usual resistance dynamics: first a fast increase followed by a slower decrease of the resistance during the readout at +10 mV (only the read pulses are shown in the figure for clarity). After having optimized the pulse characteristics (not shown), the device is then subjected to a hard RESET using a single [+20 V; 100 μs] pulse (“2” in Figure 4.9.c). It can be noticed that this hard RESET changes the resistance of the device to a resistance state that lies 68% lower than its IRS. As the resistance of the L2NO_4 -based memristive system can be changed to higher or lower values relative to the IRS, this shows that the IRS is not a threshold that imposes a limit to the programmable resistance (as is usually the case in pure filamentary memristive systems where the IRS is a HRS that cannot be retrieved after forming). This could be attributed to the inherent oxygen storage/release capabilities of L2NO_4 and its capacity to accommodate a wide range of oxygen stoichiometry without decomposing. A single [-20 V; 750 μs] pulse is then able to program the device back to a HRS that lies approximately 10% above the IRS (“3” in the inset in Figure 4.9.c). The corresponding electrical characteristics presented in Figure 4.9.e and f show an important rectification of the device when programmed to a HRS (“3”). The IRS (“1”), while showing highly nonlinear electrical characteristics, presents very little rectification. This HRS is then gradually lowered of a few percent when applying [+5 V; 24 ms] pulses (“4” and “5” in Figure 4.9.c). This is accompanied with a change of shape of the electrical characteristics with a slight decrease

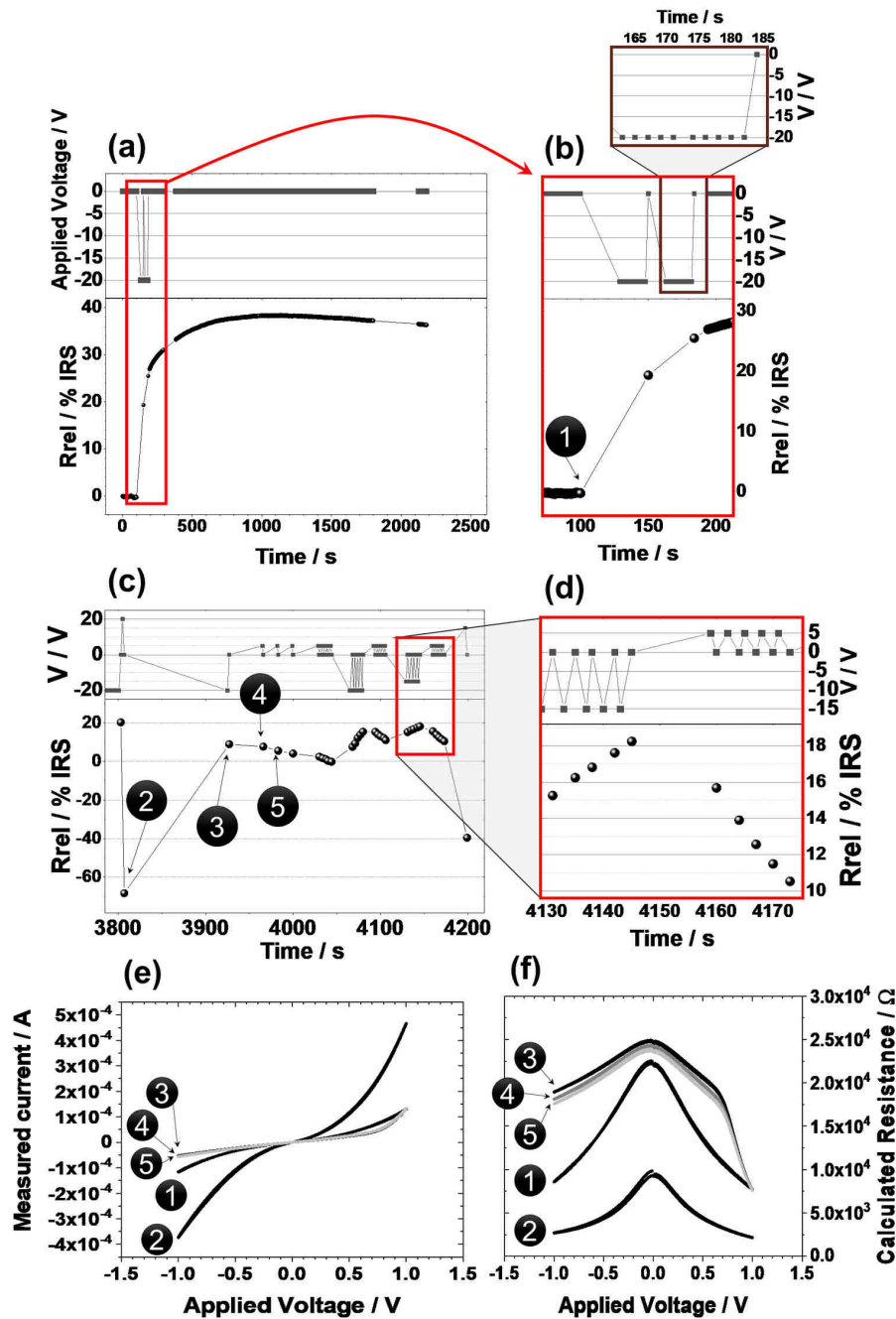


Figure 4.9 – (a) Relative resistance change over time of a pristine Pt/L2NO4/Ti device after applying two trains of 10 pulses [-20 V; 750 μ s] as presented in the top panel. (b) Magnifications of (a) around the initialisation step. (c) Programming sequence of the device where an optimized pulse amplitude and width can either operate a hard reset of the device to a LRS when applying a strong positive voltage (e.g +15 V or +20 V) or at the contrary change the resistance progressively as shown in (d). Only the readouts at +10 mV of the devices resistance state is shown in all the sampling measurements for clarity. (e-f) I-V and R-V characteristics of the Pt/L2NO4/Ti device in different resistance states. In chronological order, ‘1’ corresponds to the R-V characteristics of the device in its IRS, ‘2’ corresponds to a hard reset of the device in a LRS (after a [+20 V; 100 μ s] pulse), ‘3’ is the resistance state after a hard set to HRS [-20 V pulse; 750 μ s], ‘4’ and ‘5’ is the resistance state of the device after two “gentle” resets to a slightly lower resistance [+5 V; 24 ms].

in rectification as can be observed in the corresponding I-V and R-V characteristics in Figure 4.9.e and f. This rectification loss is mainly due to an increase in the reverse bias current at -1 V while the current at +1 V (forward bias) remains constant. The resistance of the device can then be decreased further or instead be increased back again with rates that depend on the pulse polarity, amplitude, duration and the biasing history (Figure 4.9.c and d).

New programming experiments carried out on an oxygen-annealed Pt/L2NO4/Ti device confirm that the resistance dynamics of the device are highly dependent on the programming history. This new device showed an IRS of $\sim 4 \text{ k}\Omega$ before being programmed to a HRS of $35 \text{ k}\Omega$ after an initialization step consisting in the application of roughly 1000 [-15 V; 1 ms] pulses (not shown here). The device was then intensively programmed during the next four hours in order to find the optimal operating conditions of this new device. Indeed, as the IRS of this oxygen-annealed device is different than that of the previously operated pristine device (Figure 4.9), the pulse characteristics had to be adapted. This time the choice was made to fix the pulse duration to 1 ms and to adapt the pulse amplitude accordingly to be able to increase or decrease the resistance state of the device gradually, taking advantage of the highly multilevel programming capabilities of these L2NO4-based memristive systems. Figure 4.10 shows the interesting short-term memory characteristics the device acquired after having been intensively programmed. First, it should be noticed that the resistance dynamics of the device occurring after being programmed to a HRS (Figure 4.10.a) are different to those measured after the first initialization step (see for example Figure 4.5.d or Figure 4.8). The relative resistance increase is smaller during the programming step and saturates faster, but more importantly, the first relaxation mechanism consisting in a spontaneous increase in resistance ('Relax #1' in Figure 4.8) is no longer present. The device now directly relaxes to a lower resistance state ('Relax #2' in Figure 4.10). The volatility of the memory is now evident. During the first 6 h, the device loses almost half of its resistance (it decreases from $\sim 14\,400 \Omega$ to $\sim 7\,300 \Omega$). Nevertheless, after $\sim 14 \text{ h}$ of relaxation (during which the device lost 54% of its previously programmed HRS), the device can still be programmed reliably and gradually to another HRS by applying twenty [-15 V; 1 ms] pulses (Figure 4.10.b). The newly programmed resistance state seems stable during the 60 s long readout that follows, although a very slight positive slope (reminding 'Relax #1') is visible. The resistance can then be lowered (also gradually) by applying another twenty [+7 V; 1 ms] pulses with the opposite voltage polarity and a lower amplitude. These pulse characteristics were determined from the pulse optimization procedure for this device. A negative slope (meaning a decrease of resistance with time) is now visible during the 60 s readout that follows this 'erase' step.

The device is then left unbiased during the next 34 h, after which a similar write/erase experiment is reiterated (Figure 4.10.c), showing that the device is still responsive with a very

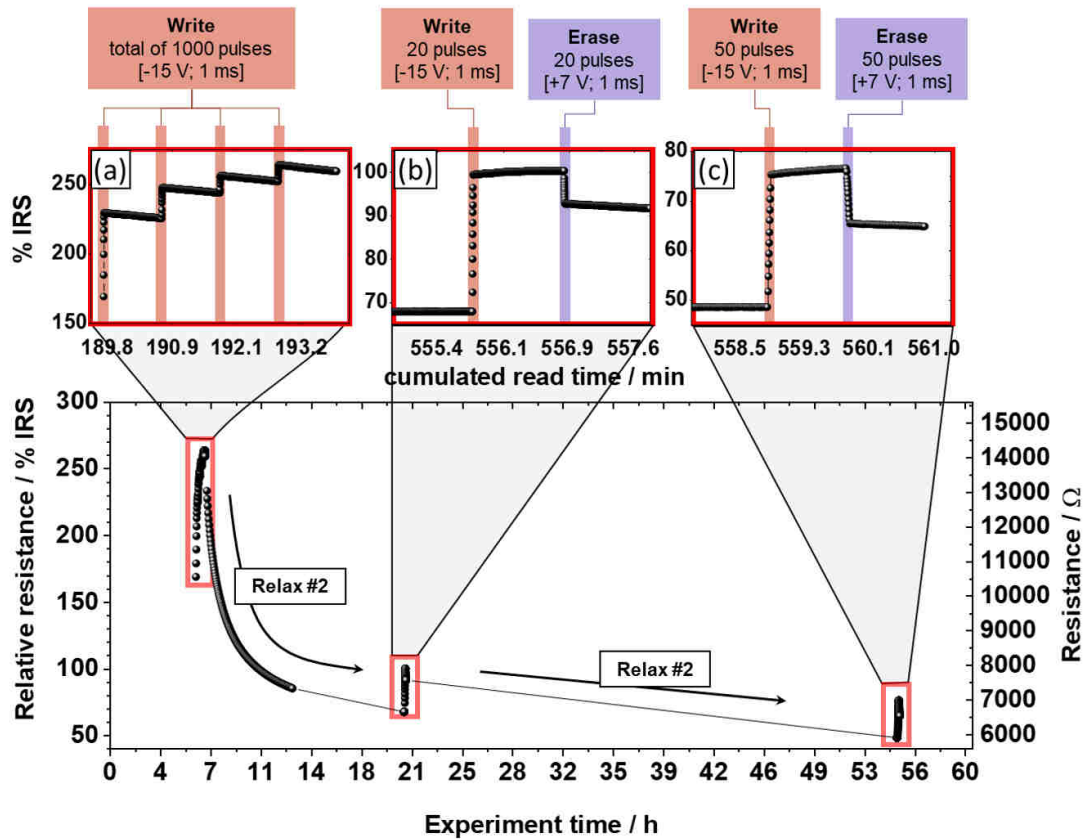


Figure 4.10 – Variation of the relative resistance of an oxygen-annealed Pt/L2NO4/Ti device as a function of time after having been initialised and intensively programmed during a few hours (not shown). (a) The device is programmed to HRS again using 1000 [-15 V; 1 ms] pulses divided into 4 pulse trains each separated by a 60 s readout. (b) After letting the device relax back spontaneously to a lower resistance state during 6 h, it is programmed again to a HRS using 20 [-15 V; 1 ms] pulses, followed by a 60 s long readout of the new resistance state and a partial erase of the memory after applying 20 [+7 V; 1 ms] pulses. (c) After having relaxed again to a lower resistance state during 34 h, a similar write/erase experiment is reiterated.

reproducible resistance change response and preserving its highly multilevel programming capabilities.

Although the programmed HRS is volatile, the resistance does not seem to relax back completely to the IRS of the device. A new and higher resistance state with a value $\sim 45\%$ above the IRS of the device seems to be the new stable resistance state. This higher resistance could be explained by the formation of a stable TiO_x interlayer during device operation.

The memory relaxation dynamics of this device are very interesting for neural applications. This short-term memory characteristic, or ‘forgetting behaviour’, is important in synaptic fil-

tering functions for real-time and on-chip information processing [16, 35, 73, 133].

4.4 Discussion

A model is proposed in this section to shine light on the possible mechanisms responsible for the complex memristive behaviour measured for the Pt/L2NO4/Ti system. A literature research opens the section, focusing on other works having reported a similar analog-type memristive behaviour. As we believe that a *gradual* change in resistance is key in the valence-change mechanism due to the self-limiting nature of Ti oxidation, we will focus mainly on other studies having reported this “resistance anomaly” (usually put in terms of *Negative Differential Resistance*, or ‘NDR’, in the resistive switching community).

To our knowledge, there are only two other studies which have used L2NO4 as memristive medium [56, 125]. However those studies were not performed using thin films of LNO4 with Ti contacts; instead the authors used bulk $\text{La}_2\text{NiO}_{4+\delta}$ ceramic pellets to build symmetric Ag/ $\text{La}_2\text{NiO}_{4+\delta}$ /Ag heterostructures with memristive properties.

4.4.1 Analog-type change in resistance in metal/oxide/metal heterostructures

This subsection is a short literature review on different metal/oxide/metal (MOM) heterostructures that have been reported to present an analog-type change in resistance associated with a particular region of the I-V characteristic that fulfils $\frac{dV}{dI} < 0$, in the same way as has been previously shown for the Pt/ La_2NiO_4 /Ti devices (see inset of Figure 4.4.a). This behaviour is quite counter intuitive as it means that an increase in the applied voltage leads at some point to a decrease in the measured current. Tunnel diodes have been designed around this characteristic and the advent of number of emerging applications, such as threshold switches, periodic and chaotic oscillators, and small signal amplifiers working on the same principle, have been proposed as key components enabling threshold logic and neuromorphic computing [44]. It should be noted that although the term NDR is often used in the literature within the resistive switching community, within the semiconductor physics community this term is normally used only if $\frac{dV}{dI} < 0$ in the particular case of a *static measurement* and regardless of the biasing history of the device. In order to avoid using the same term (NDR) for different formal definitions, we have preferred here to use the term GRC standing for ‘Gradual Resistance Change’, when referring to the decrease in resistance that occurs only in one sweep direction and only when coming from a different resistance state (from LRS to HRS), as is the case of memristive devices.

Au/BaTiO₃/FTO [139] Yang *et al.* prepared Au/BaTiO₃(BTO)/FTO top-bottom devices with an analog-type memristive behaviour. According to them, the BTO/FTO interface can be regarded as a *n-n* junction which contribution to the total resistance of the device is negligible. The Au/BTO Schottky junction on the other hand dominates the transport properties of the entire heterostructure and is responsible for the measured GRC behaviour observed in their devices. Although BTO is a well known ferroelectric material, they showed that the resistance switching and GRC are independent on ferroelectric polarization effects. Interestingly, they also showed that a large positive voltage (> 4 V) was first needed for the device to exhibit a GRC behaviour when swept in the opposite negative bias region (GRC starting around -3 V), as is the case in our Pt/L2NO4/Ti system. Yang *et al.* attributed this behaviour to the need to store a sufficient amount of charges (electrons) in interface states. In this case the memristive behaviour is attributed to a trapping/de-trapping process of electrons from ‘donor-like’ interface states present at the Au/BTO junction.

Pt/TiO₂/Pt [64] Jeong *et al.* showed that several electroforming steps with different voltage polarities and with increasing current compliance could activate the LRS in a Pt/TiO₂/Pt device and trigger a stable bipolar switching behaviour. They confirmed the completion of the electroforming step with the observation of a gradual increase in resistance often accompanied with a GRC behaviour. The evolution of oxygen gas during electroforming was confirmed by TOF-SIMS (time-of-flight secondary ion mass spectroscopy) measurements and suggests the reduction of TiO₂, possibly explaining this GCR behaviour.

TiN/TiO₂/Pt [38] Du *et al.* used an oxygen blocking electrode (TiN) to obtain reproducible and symmetrical GRC characteristics with TiO₂ as sandwiched material. They claim that a thin (~1.84 nm) insulating layer at the TiN/TiO₂ interface acts as a charge-trapping layer and is at the origin of the GRC. The insulating layer is actually also TiO₂, but depleted of the conducting filaments that populate the bulk of the film (filaments that have formed during a prior electroforming step). Interestingly, they consider that molecular oxygen, when introduced into the TiO₂ lattice can act as the trapping sites, fixing the electrons at the defect sites of the insulator layer.

Pt/Ga:Cr₂O₃/Pt [17] Bhowmik *et al.* prepared thin pellets of polycrystalline Ga doped Cr₂O₃ (GCO) to investigate the electrical properties of a Pt/GCO/Pt heterostructure. They measured a GRC behaviour when applying a large positive voltage (+50 V) and attribute it to charge-trapping at defect sites.

Ti/TiO_x/La_{0.7}Ca_{0.3}MnO₃/Pt [84] Liu *et al.* prepared two samples: one simple Ti/LCMO/Pt

stack and another similar stack with an additional ~20 nm-thick TiO_x interlayer at the Ti/LCMO junction to improve the memristive properties of a Ti/LCMO/Pt device (larger HRS/LRS ratio and endurance). A substantial GRC behaviour was measured only for the first positive voltage sweep (positive with respect to the Ti electrode) in the sample with no engineered TiO_x layer and was attributed to the further oxidation of a spontaneously-formed TiO_x interlayer with oxygen ions coming from the LCMO film. When TiO_x is further oxidized, the depletion width of the TiO_x /LCMO *n-p* heterojunction increases and prevents electron-tunnelling mechanisms, setting the device in HRS. The device can be programmed to a LRS when applying an opposite negative voltage to the Ti electrode, leading to a reduction of TiO_x and the subsequent oxygen electromigration towards the LCMO layer.

Au/ZnO/Nb:SrTiO₃ [65] Jia *et al.* reported on the memristive behaviour of a Au/ZnO/NSTO device. While Au forms an ohmic contact with ZnO, the ZnO/NSTO junction can be described in terms of a Schottky junction between a (degenerate) n-type semiconductor and a metal. The GRC behaviour is present when a negative voltage is applied to NSTO and is more prominent when the device is first swept with a large ($V \geq +4$ V) opposite positive polarity. Bipolar RS and GRC were attributed to a change in the space-charge region in ZnO and the trapping/detrapping of electrons at acceptor-like interface states located at the NSTO/ZnO Schottky junction, respectively.

W/ α -Fe₂O₃/FTO [24] Cai *et al.* claimed that the co-existence of memristivity and GRC is possibly caused by defects such as oxygen vacancies and interstitial iron ions present in their amorphous Fe₂O₃ nanorod film. They consider that the rupture of conducting filaments (formed from oxygen vacancies) leads to a drop in the total conductivity and explains the current-drop in the GRC region of the I-V characteristics.

Other I-V characteristics showing both memristivity and an GRC behaviour have also been reported in several other works but without being discussed (for example in: [41, 81, 82, 96, 107, 138]). The GRC always corresponds to the change from LRS to HRS of the memristive device.

The mechanisms described in the aforementioned examples can be roughly divided into ‘electrochemical mechanisms’ and ‘charge trapping/detrapping mechanisms’. The traps are located at the metal/oxide interface and are generally considered fixed (read for example [65]). It should be pointed out that the trapping/detrapping of charge carriers can also be considered a redox reaction process, which means that in the particular case in which the trap sites are mobile oxygen ions/vacancies, the oxidation and reduction of these trap sites is compatible with both the electrochemical and the trapping/detrapping mechanisms. In the following sub-

section we propose a mechanism where the trap states are not fixed but are instead generated and removed in a dynamical way, together with the charge trapping/detrapping and electrochemical processes they can induce. Our model resembles most the one from Du *et al.* [38], with the particularity of also explaining the dynamical behaviour we have measured such as the resistance relaxation over time.

4.4.2 Proposed mechanism for the memristive behaviour in Pt/L2NO4/Ti devices

As previously explained it is very likely that a n - p junction between an amorphous oxygen-deficient TiO_{2-y} phase (n -type) and an oxygen hyperstoichiometric $\text{La}_2\text{NiO}_{4+\delta}$ phase (p -type semiconductor) readily forms upon evaporation of the Ti top electrode material. A sketch of the $\text{Ti}/\text{TiO}_{2-y}/\text{La}_2\text{NiO}_{4+\delta}$ junction in terms of band alignment is presented in Figure 4.11. The $\text{Ti}/\text{TiO}_{2-y}$ contact has been reported ohmic [141], allowing us to focus mainly on the $\text{TiO}_{2-y}/\text{La}_2\text{NiO}_{4+\delta}$ n - p junction. In thermal equilibrium (Figure 4.11.a) the alignment of the different Fermi levels across the entire M/n -SC/ p -SC stack results in an upwards and downwards band-bending of n - TiO_{2-y} and p - $\text{La}_2\text{NiO}_{4+\delta}$, respectively. The resulting majority carrier depletion regions in both materials concentrate most of the voltage drop across the junction. Upon application of an optimized negative voltage pulse (or a train of pulses) on the L2NO4 side, the negatively charged oxygen ions (O_i'') gain sufficient energy to drift from the bulk of L2NO4 towards the grounded Ti electrode (Figure 4.11.b). When the pulse ends and the bias is removed, the system finds itself in a non-equilibrium state (Figure 4.11.c) where an important dopant gradient exists on the L2NO4 side. Indeed, the O_i'' point defects act as mobile acceptor dopants, locally generating hole carriers to ensure charge neutrality within the $\text{La}_2\text{NiO}_{4+\delta}$ matrix. The opposite is true for TiO_{2-y} , where positively-charged oxygen vacancies V_o^\bullet act as donor defects. The increase in hole carriers at the surface of $\text{La}_2\text{NiO}_{4+\delta}$ due to the external field-induced accumulation of O_i'' decreases its Fermi energy and shrinks the depletion width. This has the double effect of increasing the built-in potential at the $\text{TiO}_{2-y}/\text{La}_2\text{NiO}_{4+\delta}$ junction and to localize the voltage drop on a shorter distance (effectively increasing the electric field across the n - p junction). Two scenarios are then possible. In the first scenario (Figure 4.11.d) the device remains unstressed (at least for a characteristic amount of time), resulting in an interdiffusion of the O_i'' species away from the $\text{TiO}_{2-y}/\text{La}_2\text{NiO}_{4+\delta}$ interface and back into the bulk of $\text{La}_2\text{NiO}_{4+\delta}$. This interdiffusion is triggered by the re-equilibration of the O_i'' concentration gradient within L2NO4 through a Fickian diffusion process, leading to a relaxation of the device to the previous equilibrium state (Figure 4.11.a). In the second scenario, a new negative voltage pulse is applied on the $\text{La}_2\text{NiO}_{4+\delta}$ side (Figure 4.11.e). If the oxygen ions

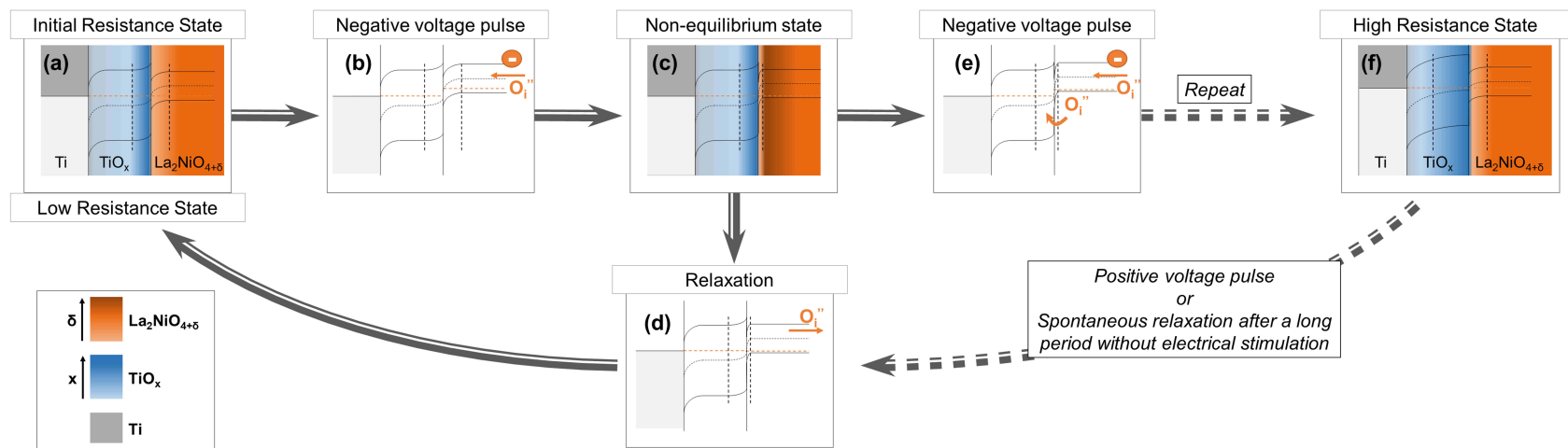
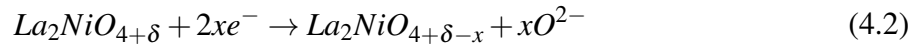


Figure 4.11 – Band-diagram based phenomenological model for the interface-type resistance-change mechanism in a Pt/L2NO4/Ti device (only the active Ti/TiO_x/L2NO4 junction is represented here). (a) IRS of the device, the assumption is made that a continuous (and homogeneous) TiO_x interlayer is present at the surface of L2NO4 resulting from the spontaneous oxidation of the Ti electrode during its evaporation. A depletion region (dashed vertical lines) is present on both sides of the *n-p* junction formed by TiO_x and L2NO4. (b) Application of a negative voltage pulse (or a train of pulses) on the L2NO4 side, triggering the drift of negatively-charged oxygen interstitials towards the TiO_x/L2NO4 interface. (c) A metastable state is created where an important chemical gradient of oxygen is present in L2NO4. The internal electric field is increased due to the reduced depletion width induced by the acceptor-dopant nature of the interstitial oxygen ions that accumulated at the TiO_x/L2NO4 interface. (d) If no other voltage stress is applied after (c), the chemical gradient is re-equilibrated through a Fickian diffusion process and the resistance remains in a low resistance state. (e) If another (or several other) negative voltage pulses are applied after (c), the strong internal fields and high oxygen concentration present at the TiO_x/L2NO4 interface trigger the drift of an oxygen ion from the L2NO4 side to the TiO_x side (redox process). (f) After a certain amount of iterations of step (e), TiO_x gets more and more oxidized (higher series resistance) and the amount of charge carriers (both in TiO_x and in L2NO4) is reduced, effectively setting the device in HRS. The entire process is reversible upon application of a positive voltage pulse on the L2NO4 side or by waiting a certain amount of time after which the device spontaneously relaxes back to a lower resistance state. See text for more details.

did not have the time to re-equilibrate, the interfacial region is doped further, and the previous process (decreasing Fermi level and depletion width) is reiterated, further increasing the built-in potential and the electric field across the n - p junction. At a certain threshold oxygen ion concentration, the applied voltage now strongly assisted by the large internal electric fields is able to trigger the drift of oxygen ions from the p - $\text{La}_2\text{NiO}_{4+\delta}$ side to the n - TiO_{2-y} side (Figure 4.11.e). This process is best described from the materials point of view as a reduction of $\text{La}_2\text{NiO}_{4+\delta}$ followed by an oxidation of TiO_{2-y} following the two half reactions:

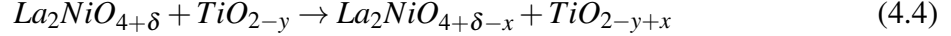
Reduction reaction (occurring on the negatively biased L2NO4 side):



Oxidation reaction (occurring on the TiO_{2-y} side):



When combining the two half reactions together, assuring that the complete system remains electro-neutral ($z = x$), we obtain the following equilibrated redox reaction:



Both mass transport (movement of an oxygen ion from $\text{La}_2\text{NiO}_{4+\delta}$ to TiO_{2-y}) and charge transfer (from Ni to Ti, although several sub-transfer steps can exist) govern this reaction and can be rate-limiting. There are at least two interesting conclusions to Equation 4.4. First, the reaction appears self-limiting in the sense that in the particular cases where $x = \delta$ or $x = y$, or in other words, if there are no more oxygen interstitials in $\text{La}_2\text{NiO}_{4+\delta}$ or available/accessible vacancy sites for them to occupy in TiO_{2-y} the redox reaction should terminate. Furthermore, for the formation of thin films of oxides which are predominantly insulating (such as TiO_2), the growth will take place until the electric field generated by the driving force is compensated by the resistance drop in the oxide [131]. This can explain the apparent saturation behaviour described in Figure 4.4 when carrying-out unipolar $0 \text{ V} \rightarrow -5 \text{ V} \rightarrow 0 \text{ V}$ sweeps. The other interesting aspect of Equation 4.4 is that this particular redox reaction annihilated two point defects together with their charge-compensating electric carriers ($2h^+$ for O_i'' and $2e^-$ for $\text{V}_\text{O}^\bullet$). From the semiconductor point of view, a “de-doping” process happens simultaneously in both materials composing the n - p junction when the oxygen ion drifts from the $\text{La}_2\text{NiO}_{4+\delta}$ side into TiO_{2-y} . This can explain the GRC effect discussed earlier (Figure 4.3.a) where an increase in electric field in the reverse bias region would lead to a decrease in current due to the simultaneous loss of n and p charge carriers assuring the electrical conduction at the $\text{TiO}_{2-y}/\text{La}_2\text{NiO}_{4+\delta}$ junction.

The annihilation of oxygen vacancies in TiO_{2-y} leading to a larger resistance in a Pt/ TiO_2 /Pt memristive device has also been evoked in [64].

Finally, after this voltage-pulse-induced redox process, the device finds itself in a higher resistance state (Figure 4.11.f). The resistance can nevertheless return to a lower resistance state when applying a positive voltage pulse or if the device is not stimulated for a long period of time, due to the reduction of TiO_x and the release of oxygen ions which will diffuse back into L2NO4 (dotted arrow from Figure 4.11.f to d) and the increase in the carrier concentration (both in TiO_x and L2NO4). As said earlier, the oxygen loss experienced by TiO_x can, on top of releasing trapped electrons and increasing the overall carrier density, also restore other conduction mechanisms through the TiO_x interlayer (such as TAT or direct tunnelling if the layer is thin enough) which effectively also decreases the resistance of the device.

The ion drift process is certainly temperature activated, meaning that increasing the pulse duration, amplitude or number will assist the entire resistance change mechanism through Joule heating. Furthermore, the presence of electrochemical redox reactions can explain the polarity-dependant memristive properties of the device as changing the voltage polarity changes the role of the electrodes (the cathode becomes the anode and vice-versa), effectively inverting reaction 4.4 (and thus triggering the drift of an oxygen ion from the TiO_x side to the L2NO4 side).

4.5 Summary

The main points tackled in this chapter are summarized hereafter.

- Memristivity in Pt/L2NO4/Ti using the ‘top-top’ planar electrode configuration:
 - An initialisation step, consisting in the application of a negative voltage on the Pt side of the Pt/L2NO4/Ti device, leading to an increase in the total resistance of the device is required to trigger reproducible memristive characteristics. This initialisation step is however different to the more classical electroforming step as the applied voltage does not need to be higher than the operation voltage. When voltage pulses are used to program the device, the memory behaviour can arise directly after applying the first pulse (for example at -20 V or -15 V). The lower the pulse amplitude the more pulses are required to trigger a change in resistance of the device;
 - Highly reproducible analog-type I(V) characteristics are obtained after initialisation when cycling the device between ± 5 V. The LRS and HRS are separated by roughly one order of magnitude in resistance ($\sim 1 \text{ M}\Omega$ and $\sim 10 \text{ M}\Omega$, respectively).

Successive unipolar voltage sweeps ($0\text{ V} \rightarrow -5\text{ V} \rightarrow 0\text{ V}$) can gradually increase the resistance state above the HRS until saturation (around $50\text{ M}\Omega$). This progressive saturation of the resistance might be the fingerprint of a self-limiting redox reaction;

- The evolution of the IRS of a Pt/L2NO4/Ti device with decreasing oxygen content is consistent with a *p*-type Schottky contact model between Ti and L2NO4. The hole-doping induced by annealing L2NO4 in an oxidizing atmosphere results in a narrowing of the depletion width at the Ti/L2NO4 junction and thus in an overall decrease in resistance of the device;
 - The presence of interstitial oxygen ions in L2NO4 are beneficial, and even necessary to give rise to the memristive properties. A precise interplay between the TiO_x interlayer thickness, as well as its stoichiometry and homogeneity and the oxygen content of L2NO4 are certainly crucial parameters that need to be controlled to be able to tune the resistance-change and the retention characteristics of a Pt/L2NO4/Ti memristive device;
 - An intriguing spontaneous relaxation behaviour of a device after initialisation has been measured, showing first a fast increase of the resistance before decaying back to a low resistance state (without the application of an external electric field). The increase in resistance has been attributed to a Fickian diffusion process re-equilibrating the oxygen gradient that was built-up after the initialisation process, leading to a de-doping and an increase of the depletion width of the *p*-type Schottky contact at the Ti/ TiO_x /L2NO4 heterojunction. The second relaxation behaviour has been attributed to a spontaneous reduction of the TiO_x interlayer, possibly restoring new conduction mechanisms through this thin insulating (or *n*-type semiconducting) layer.
- Neuromorphic aspects
 - Highly multilevel and bipolar memory characteristics can be obtained when operating the device in pulsed-mode, which is a prerequisite for neuromorphic programming;
 - A controlled and still highly multilevel resistance change can be achieved with optimized voltage pulses of 1 ms when increasing the voltage amplitude to -15 V to initialise/set the device in a higher resistance state (or $+7\text{ V}$ to reset it to a lower resistance state). Even lower power consumptions of these L2NO4-based memristive devices are expected when taking the architecture to the micro or even nano scale;

- The spontaneous relaxation (decrease of the resistance to LRS) mechanisms which are measured when programming the device to a HRS are very interesting for neuromorphic applications. Indeed, a dynamic change in resistance allows the implementation of memory loss or at the contrary memory strengthening and mimics brain-inspired computation capabilities in which both long and short-term memory are of importance. Short-term memory is important in dynamic-filtering applications, enabling the discrimination between signal and noise;
 - The neuromorphic characteristics of the memory are conserved even after harsh programming conditions. There is however a possibility that a stable TiO_2 interlayer forms after long periods of electrical stimulation, which could ultimately lead to the failure of the memory.
- Proposed mechanism for the memristive behaviour in $\text{La}_2\text{NiO}_4/\text{Ti}$ devices:
 - Literature reports having observed a ‘gradual resistance-change’ (GRC) in memristive devices (instead of a fast, almost binary resistance ‘switch’) explain this behaviour using mechanisms which can be roughly divided into two categories: ‘electrochemical’ and charge trapping/detrapping’;
 - We propose that these two mechanisms coexist, that the accumulation of oxygen ions at the $\text{Ti}/\text{TiO}_x/\text{L2NO}_4$ junction play the role of the charge traps, trapping or releasing electrons through redox reactions occurring between TiO_x and L2NO_4 .
 - The GRC behaviour and self-limiting nature of the memory properties in L2NO_4 -based memristive devices could be explained by mass-transport (of oxygen ions) being the kinetically limiting process of the redox reaction;
 - Our current understanding of the memory properties of L2NO_4 -based memristive devices is mainly based on experimental evidence. The further demonstration and completion of the model requires an important simulation work. This task is however complex as it requires the coupling of Poisson’s equation to solve the coupled continuity drift-diffusion equations for electron, holes and oxygen ions (where the oxygen ions also act as mobile dopants).

The fact that a stable TiO_2 interlayer could eventually lead to the failure of the device, putting the device in an irreversible HRS shows that this $\text{Pt}/\text{L2NO}_4/\text{Ti}$ prototype has its limits. Different material stacks with a comparable chemistry could be of interest to increase the control over the meta-stability of the programmed resistance states. In the following chapter we will therefore investigate the memory properties of a complex-oxide heterostructure composed of $\text{L2NO}_4/\text{LNO}_3$ bilayers.

Chapter 5

The top-bottom L2NO4/LNO3 heterostructure

Contents

5.1	The need for a functional electrode for the growth of oriented L2NO4	96
5.2	The bottom electrode layer: LNO3 films deposited by PiMOCVD	98
5.2.1	Optimization of the growth of LNO3 thin films on STO and LAO	98
5.2.2	Role of the impurities on the growth of LNO3 films on STO	103
5.3	Lanthanum-nickelate thin films deposited by PLD	106
5.3.1	Structural properties of LNO3 films deposited by PLD	107
5.3.2	Structural properties of L2NO4 films deposited by PLD	108
5.4	Comparison of LNO3 and L2NO4 single layers deposited by PiMOCVD and PLD	109
5.5	L2NO4/LNO3 bilayers	112
5.5.1	L2NO4/LNO3 bilayers deposited by PiMOCVD	112
5.5.2	L2NO4/LNO3 bilayers deposited by PLD	116
5.6	Resistance-change in Pt/LNO3/L2NO4/Pt heterostructures grown by PLD	117
5.6.1	The initialisation step	117
5.6.2	Analog-type bipolar resistance change in Pt/LNO3/L2NO4/Pt	119
5.6.3	Resistance relaxation	121
5.7	Summary	123

This final chapter tackles both the materials and device aspects of L2NO4/LNO3 memristive heterostructures. The first section is a general introduction on the structural and electrical properties of LNO3 reported in literature, and why it was chosen as functional electrode material for the growth of textured L2NO4. The second section covers the most important aspect of the deposition optimization and material properties of LNO3 thin films grown by PiMOCVD. The third section exposes briefly the structural properties of LNO3 and L2NO4 thin films deposited by a physical deposition method during an internship carried out in the Catalan Institute of Nanoscience and Nanotechnology (ICN2) located close to Barcelona in Spain. The electrical properties of the LNO3 and L2NO4 films grown by the two different deposition techniques are then compared in the fourth section. The fifth section reiterates the comparison between the two deposition techniques, but this time focusing on the material properties of L2NO4/LNO3 complex-oxide bilayers. The sixth section is dedicated to the more advanced electrical characterisation and memory capabilities of Pt/LNO3/L2NO4/Pt memristive devices prepared by PLD. A summary of the main results presented in this chapter is given in the final section.

5.1 The need for a functional electrode for the growth of oriented L2NO4

When aiming for an large scalability of the elementary memory components, the so-called “top-bottom” configuration of the electrodes is usually preferred over the planar architecture discussed in Chapter . This vertical electrode configuration suits well the ideal crossbar memory array type of architecture, presented in Figure 1.2a.

As has been discussed in Chapter 2, L2NO4 was chosen as a mixed ionic-electronic conductor with high oxygen mobility to understand and control the resistance-change phenomenon in VCMs. Nevertheless, as the oxygen mobility in L2NO4 is strongly affected by its crystallinity and crystal-orientation, the use of a functional template electrode is necessary and will answer a double purpose: on top of showing good electronic conductivity it should also ensure a good lattice match with L2NO4, controlling its crystallographic orientation through epitaxial considerations and thus, consequently, the ionic mobility in the final memristive heterostructure. The perovskite LNO3 satisfies these two requirements: a high electronic conductivity and a close lattice match with L2NO4. Furthermore, by measuring the changes in the cell parameters using *in-situ* XRD on samples exposed to different gas atmospheres, Moreno *et al.* demonstrated that L2NO4/LNO3 bilayers exchange oxygen at high temperatures ($T=600^{\circ}\text{C}$), both between each other and with the surrounding atmosphere [88].

Table 5.1 – Lattice parameters for rhombohedral LNO3 reported in literature. The pseudo-cubic lattice-parameter of LNO3 is used for the calculation of the lattice mismatch with STO and L2NO4 ($mismatch = \frac{a_{ref} - a_{LNO3}}{a_{ref}}$).

in hexagonal axes		pseudo-cubic	lattice mismatch (%)		ref
SG: R-3c (167)		lattice parameter	with STO [*]	with L2NO4 [◇]	
a (Å)	c (Å)	a (Å)	($a_{STO} = 3.905$ Å)	($a_{L2NO4} = 3.8617$ Å)	
5.4638	13.1445	3.863	1.06	-0.05	[49]
5.4561	13.1432	3.858	1.20	0.09	[140]
5.4573	13.1462	3.859	1.18	0.07	[43]
5.4397	13.192	3.846	1.50	0.39	[144]

^{*} ICDD: 00-035-1734, SG: Pm-3m (221), $a = b = c = 3.905$ Å

[◇] ICDD: 00-034-0314, SG: I4/mmm (139), $a = b = 3.8617$ Å, $c = 12.683$ Å

This capability makes this particular heterostructure an interesting playground for VCM applications.

This chapter is focused on the material properties of LNO3 thin films. The goal is to use this oxide as template electrode for the growth of c -oriented L2NO4 due to the excellent lattice match between the LNO3 perovskite structure and the layered L2NO4 Ruddlesden-Popper structure (see Table 5.1), itself composed of LNO3 perovskite layers alternating with LaO rock-salt type layers¹.

LNO3 has already been used as a template electrode layer in ferroelectric thin film devices [50, 80] due to a good lattice match with several state of the art ferroelectric perovskites such as Sr-doped PbTiO₃ and BaTiO₃ [61, 143]. LNO3 has metallic properties with a resistivity as low as 90 $\mu\Omega$.cm [36, 74, 144, 146] at room temperature and is thus a suitable candidate for a template bottom electrode material. It shows no metal to insulator transition (MIT) over the entire temperature range where the compound is stable. A MIT behaviour has only been reported for epitaxial films of only a few unit cells of LNO3 [74, 111, 112, 121].

LNO3 films have been grown using various solid [76, 106], liquid [58, 79] and vapour deposition methods [20, 25, 47]. On the other hand, to the best of our knowledge L2NO4/LNO3 bilayers have only been prepared using pulsed layer deposition (PLD) in [89].

The material properties of LNO3 thin films deposited by PiMOCVD are discussed in the following section.

¹The reader is redirected to Chapter 2: La₂NiO_{4+ δ} , a mixed ionic-electronic conductor for VCM applications for more details about the structural properties of L2NO4

5.2 The bottom electrode layer: LNO3 films deposited by PiMOCVD

The influence of the deposition conditions on the phase stability, the crystallinity and the composition of LNO3 thin films deposited on STO and LAO substrates by PiMOCVD is discussed in detail in Appendix B. These two single crystal substrates exert opposite strains on LNO3 (tensile for STO and compressive for LAO).

5.2.1 Optimization of the growth of LNO3 thin films on STO and LAO

This section summarizes the most important material aspects of the LNO3 thin films deposition optimization.

First, the La and Ni atomic concentration in the injected solution was optimized by fixing the precursor concentration to 0.02 mol/L, the temperature at $T = 750\text{ }^{\circ}\text{C}$ and using the following La/Ni atomic ratios in the injected solution: La/Ni = 2.00, 2.25, 2.50 and 2.75. Combining XRD and Electron-Probe Micro Analysis an optimized La/Ni precursor ratio of 2.38 was obtained. Next the temperature was varied between 550 and 750 $^{\circ}\text{C}$ using an initial precursor ratio La/Ni = 2.38 and 4000 pulses.

Figure 5.1.a and b show the θ - 2θ XRD patterns for films deposited on STO and LAO at temperatures between 550 and 750 $^{\circ}\text{C}$ using an initial precursor ratio La/Ni = 2.38 and 4000 pulses. The presence of predominant $h\ 0\ 0_{\text{LNO}_3}$ (h integer) is clearly observed over the entire temperature range, both for films on STO and on LAO. At 750 $^{\circ}\text{C}$ the higher order RP phases are present (dark blue dots, broad intensities around the $h\ 0\ 0_{\text{LNO}_3}$ diffraction peaks) as well as $h\ h\ 0_{\text{LNO}_3}$, L2NO4 and also a small amount of NiO impurities. When decreasing the temperature, the higher order RP phases quickly disappear. At 550 $^{\circ}\text{C}$, mainly $h\ 0\ 0_{\text{LNO}_3}$ reflections are present with a rather weak $2\ 0\ 0_{\text{NiO}}$ reflection for LNO3/STO suggesting that some NiO impurities are still present, while no NiO impurities are observed by XRD for the 550 $^{\circ}\text{C}$ film grown on LAO.

We finally note substrate-dependent effects in Figure 5.1.a and b: on the one hand the difference in the predominant orientation of NiO ($h\ 0\ 0_{\text{NiO}}$ on STO and $h\ h\ 0_{\text{NiO}}$ on LAO) and, on the other hand, the strong correlation between $h\ 0\ 0_{\text{NiO}}$ and $h\ h\ 0_{\text{LNO}_3, \text{L2NO}_4}$ in the films grown on STO, which will be detailed in the following section. The resistivity values for LNO3 thin films deposited both on STO and on LAO as a function of the deposition temperature are shown in Figure 5.2.

For LNO3 films deposited between 600 and 700 $^{\circ}\text{C}$, despite the lower intensity of NiO impurity peaks present in the XRD diffractograms for LNO3/LAO, the resistivity is higher than

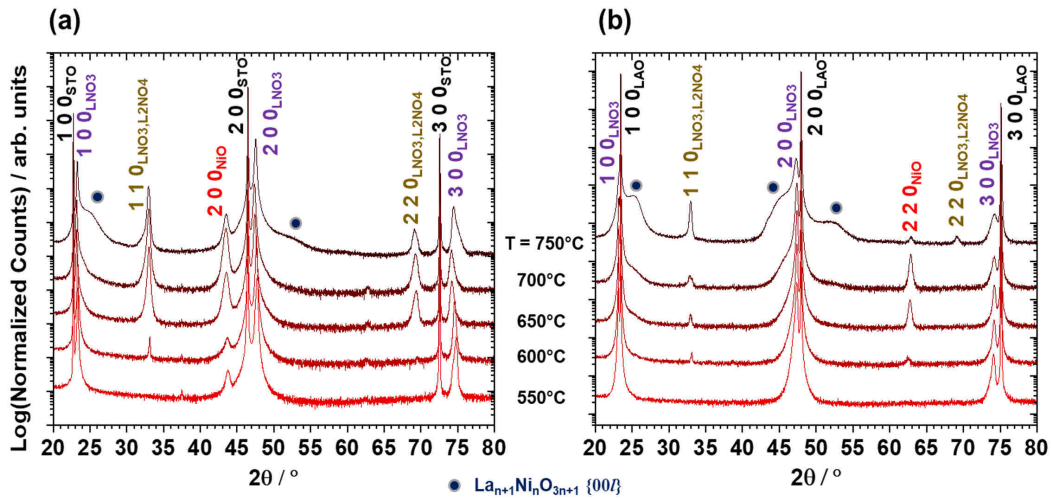


Figure 5.1 – θ - 2θ XRD patterns of (a) LNO3/STO and (b) LNO3/LAO thin film samples using a fixed La/Ni precursor ratio of 2.38 and increasing the deposition temperatures. All the films have a thickness ranging between 80 and 90 nm (4000 injected pulses). Bragg peaks for rhombohedral LAO and LNO3 are indexed in their pseudo-cubic lattice parameters.

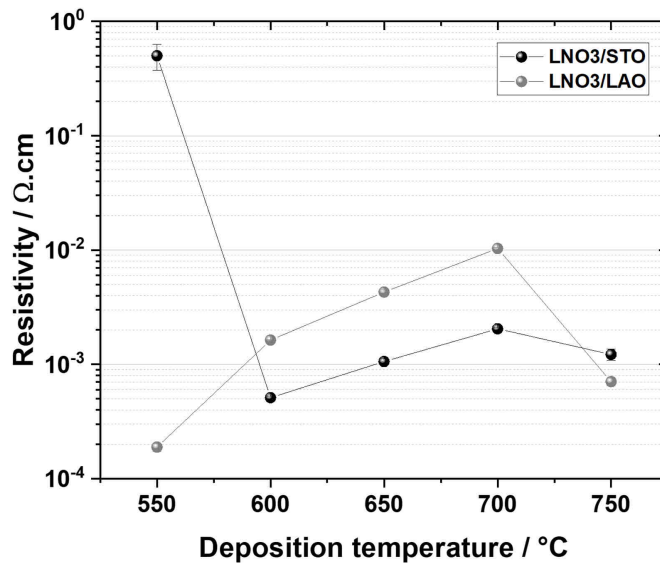


Figure 5.2 – Evolution of the LNO3 film resistivity as a function of the deposition temperature. Films were deposited simultaneously on STO and LAO single crystals using 4000 pulses (corresponding to a thickness of 85 ± 7 nm) of the precursor solution (only the deposition temperature was varied). The error bars were calculated using the standard deviation of five consecutive four probe resistivity measurements at different locations on the sample (they lie within the data points when not visible).

for LNO3 films grown on STO. When decreasing the deposition temperature from 750 °C to 600 °C, the resistivity goes through a maximum at 700 °C for both types of samples before reaching 1.6 mΩ.cm and 0.5 mΩ.cm at 600 °C for films on LAO and on STO, respectively. When decreasing down to 550 °C, the sample deposited on LAO reaches state of the art resistivity values of around 200 μΩ.cm. However, despite having been grown as part of the same batch under identical conditions, the resistivity measured for LNO3/STO deposited at the same temperature increases by several orders of magnitude up to 500 mΩ.cm. To understand the large resistivity difference for the films grown on different perovskite substrates, microscopic characterization of the microstructure of the films was carried out by TEM.

The TEM observations confirm the columnar growth of a dense, continuous and homogeneous crystalline LNO3 film when grown at 550 °C on top of STO (Figure 5.3.a). Each column corresponds to LNO3 in $[0\ 0\ 1]_{\text{LNO3}}//[0\ 0\ 1]_{\text{STO}}$, $[0\ 1\ 0]_{\text{LNO3}}//[0\ 1\ 0]_{\text{STO}}$ orientation relationship; it grows coherently (cube on cube) with the STO substrate. We could clearly identify the presence of NiO impurities which grow perpendicular to the LNO3 film. Figure 5.3.d shows a NiO impurity oriented in a $[0\ 0\ 1]_{\text{NiO}}//[0\ 0\ 1]_{\text{STO}}$, $[0\ 1\ 0]_{\text{NiO}}//[0\ 1\ 0]_{\text{STO}}$ orientation relationship, obtained by applying a mask on the $2\ 0\ 0_{\text{NiO}}$ spots on the FT (Fourier Transform) of the HRTEM image shown in Figure 5.3.c and doing the inverse FT. When measuring the in-plane resistivity of the films, these impurities would be crossing the path of the electrons and therefore their presence along the whole film thickness could be the reason of the large resistivity measured for these films submitted to tensile strain (on STO). When measuring the in-plane resistivity of the films, these impurities could hinder the flow of current, their presence along the whole film thickness could be the reason of the large resistivity measured for these tensily-strained LNO3 thin films.

The LNO3 film grown at 550°C on LAO observed by TEM (Figure 5.4.a) shows again a columnar-grown dense and uniform thin film. The film, which is now submitted to a compressive strain, has a much lower density of defects and a high epitaxial quality (Figure 5.4.d). A few localized $2\ 0\ 0_{\text{NiO}}$ impurities can be found at the film-substrate interface. Nevertheless as they are only a few unit cells thick they do not appear in the XRD patterns (Figure 5.1.b). Furthermore, as they are punctual and do not cross the film thickness they do not seem to affect the electrical properties of the sample. As previously shown (Figure 5.2) the resistivity measured for these reaches almost state of the art resistivity ($\sim 10^{-4}$ Ω.cm [74]), coherent with a good film quality. As will be shown in the following section, for films grown by PLD, which generally present a better crystalline quality (less impurities) such a low resistivity value is only achieved for LNO3 films of a thickness lower than 10 nm. Moreover, HRTEM images of LNO3/LAO films deposited at 650°C indicates that the increase in resistivity at this higher deposition temperature is probably related to the intergrowth of NiO grains across the entire

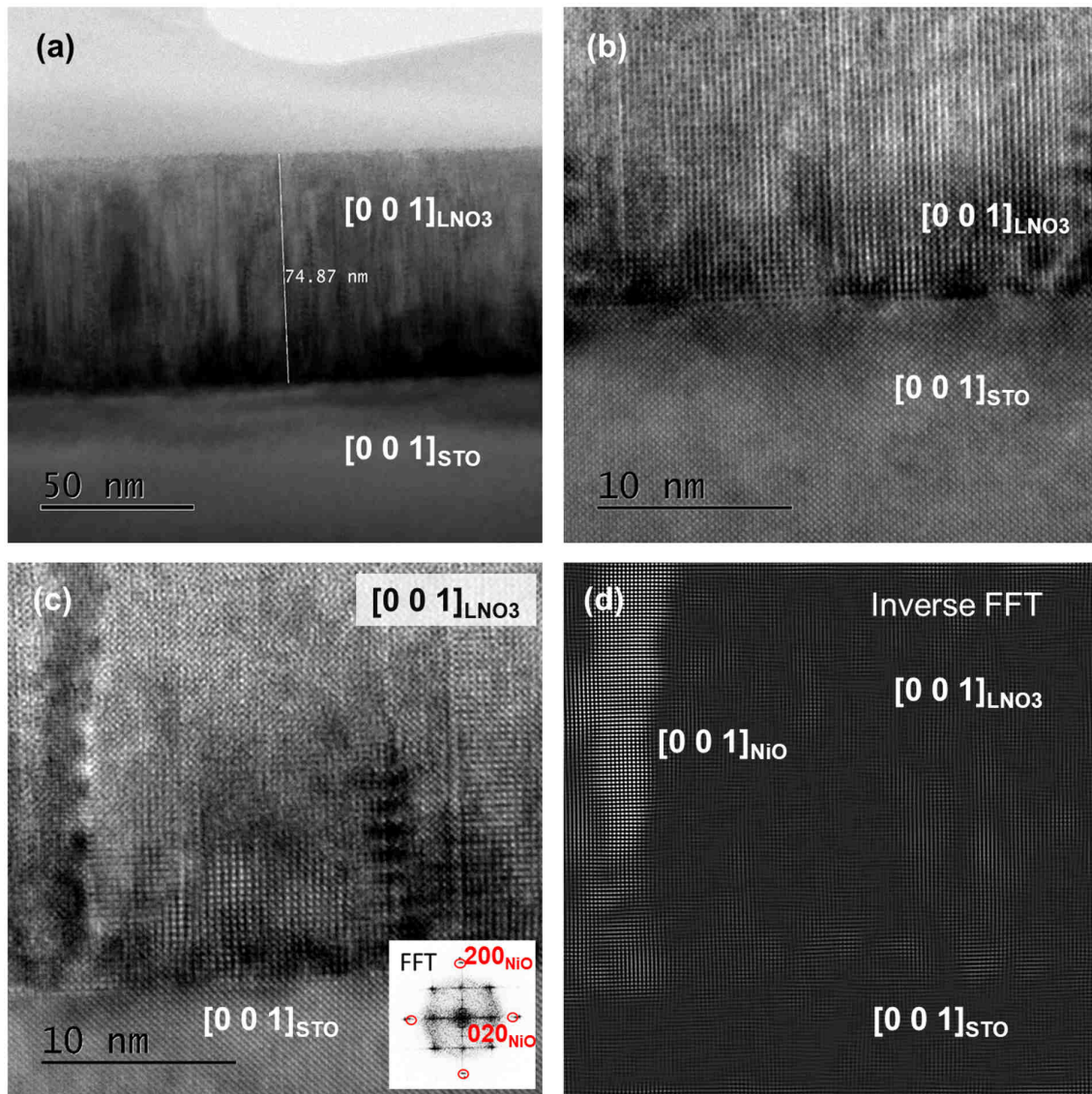


Figure 5.3 – (a) TEM cross-section presenting a general view of LNO3/STO obtained at 550 °C with La/Ni = 2.38 in the precursor solution (~75 nm thick films), (b-c) HRTEM images for different regions of LNO3/STO and (d) Filtered images showing the $[001]_{\text{NiO}}$ domains. The filtered image (d) was obtained by applying a FT to to the HRTEM image (c), followed by the use of a mask on the 200_{NiO} and 020_{NiO} spots in the Fourier space (red circles in inset) and doing the inverse FT.

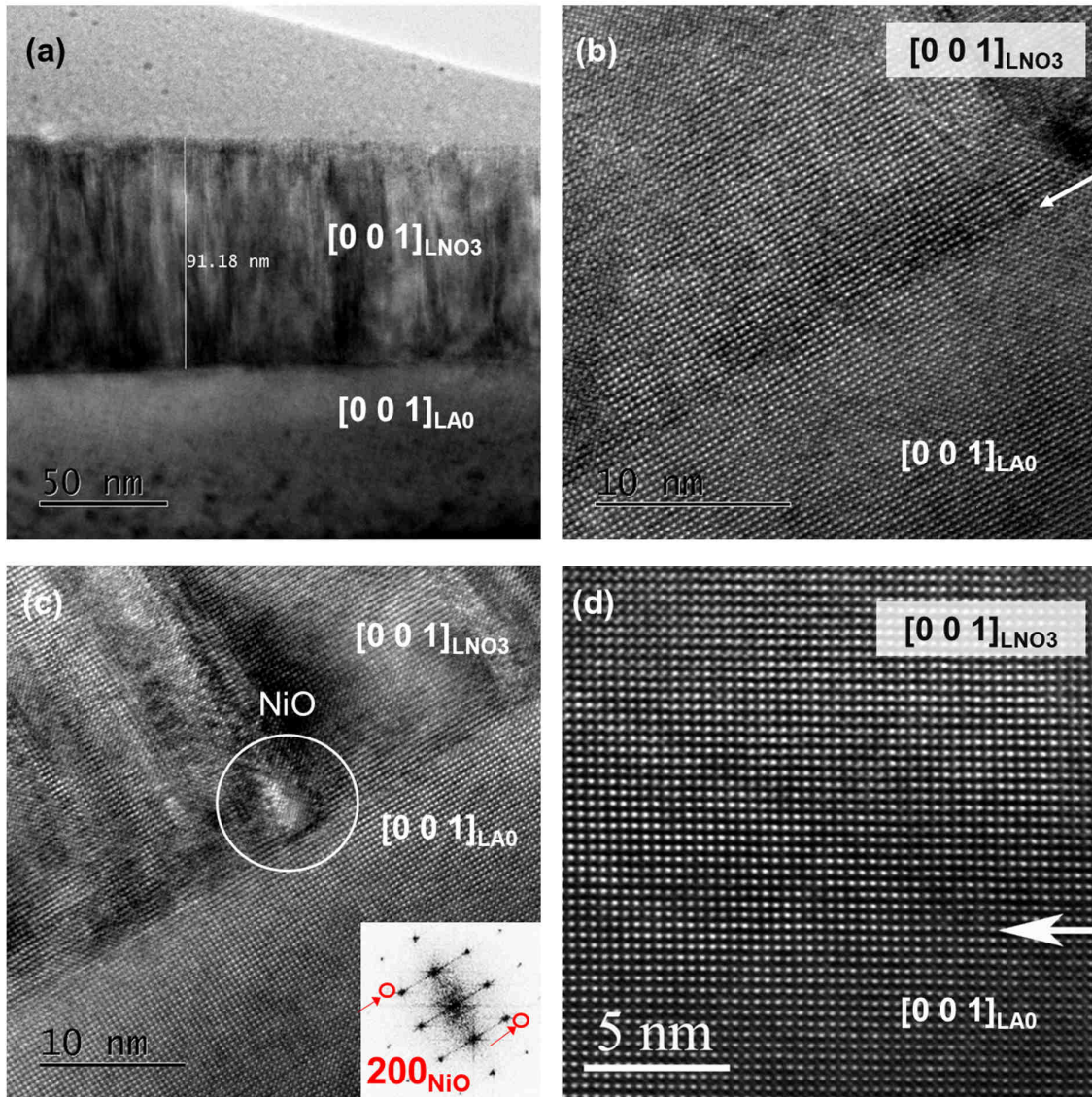


Figure 5.4 – (a) TEM cross-section presenting a general view of LNO₃/LAO obtained at 550 °C with La/N = 2.38 in the precursor solution (~90 nm thick films), (b-c) HRTEM images for different regions of LNO₃/LAO including electron diffraction pattern with the presence of 2 0 0_{NiO} spots marked with an arrow (inset) and (d) showing a magnified area with a very good epitaxial growth.

LNO3 film thickness which grow in a $[0\ 1\ -1]_{\text{NiO}}//[0\ 1\ 0]_{\text{LAO}}$ orientation relationship with the substrate (see Figure B.9 in Appendix B).

To summarize, we have observed that for the whole temperature range studied (550°C - 750°C) the crystalline quality of the films is better when grown on LAO (likely due to a lower lattice mismatch). When the impurity grains (NiO) cross the film from top to bottom, they lead to an important increase in resistivity, limiting the electronic conduction in the in-plane direction (parallel to the substrate surface). By the combination of XRD, TEM and electrical measurements can be concluded that the best deposition conditions achieved for LNO3 is highly substrate-dependent. For LNO3 films grown on STO, we found that the optimal deposition temperature is 600°C while for LAO it is slightly lower (550°C).

5.2.2 Role of the impurities on the growth of LNO3 films on STO

A common characteristic of all the LNO3 thin films deposited by MOCVD was the formation of NiO precipitates, which abundance and orientation depends strongly on the deposition parameters and substrate used. In this section, we will focus on the LNO3 films deposited on STO, only results obtained from samples prepared with an optimized La/Ni precursor ratio of 2.38 will be presented. More information on the material characterization carried out on LNO3/STO samples can be found in Appendix B.

Upon further analysis of the XRD patterns obtained from the temperature-optimization study presented in the previous section, a correlation between the peak intensities of the 2 0 0 reflection of NiO ($2\ 0\ 0_{\text{NiO}}$) and the 1 1 0 reflection of either LNO3 or L2NO4 ($1\ 1\ 0_{\text{LNO3, L2NO4}}$) can be observed, as shown in Figure 5.5.a (which is a magnification of Figure 5.1.a around $30^\circ \leq 2\theta \leq 50^\circ$). When plotting the integrated relative peak intensity of $1\ 1\ 0_{\text{LNO3, L2NO4}}$ as a function of $2\ 0\ 0_{\text{NiO}}$, it appears that more NiO leads to more L2NO4 and/or LNO3 domains oriented at 45° with respect to the STO substrate as shown in Figure 5.5.b. Understanding how (or if) the two impurities are correlated requires further investigation.

A thinner (1000 pulses) LNO3/STO sample grown at 650°C was prepared for TEM analysis to try to locate the NiO defects and $1\ 1\ 0_{\text{LNO3, L2NO4}}$ domains, as well as apprehending the overall film quality. Figure 5.6.a shows the cross section of the prepared LNO3/STO TEM lamella, showing a dense microstructure and a film thickness of ~14 nm. Figure 5.6.b is an electron diffraction image of the LNO3/STO interface region confirming the highly coherent growth of the film. The diffraction image does not contain powder rings and all the diffraction peaks could be indexed with only three different phases: $1\ 0\ 0_{\text{STO}}$, $1\ 0\ 0_{\text{LNO3}}$ and $1\ 0\ 0_{\text{NiO}}$ plus an extra LNO3 or in-plane L2NO4 domain rotated at 45°, coherent with the $1\ 1\ 0_{\text{LNO3, L2NO4}}$ domain indexed in the XRD patterns discussed previously. The indexation of all these different phases/domains is shown in Figure 5.6.c. From these results it can be seen that all the

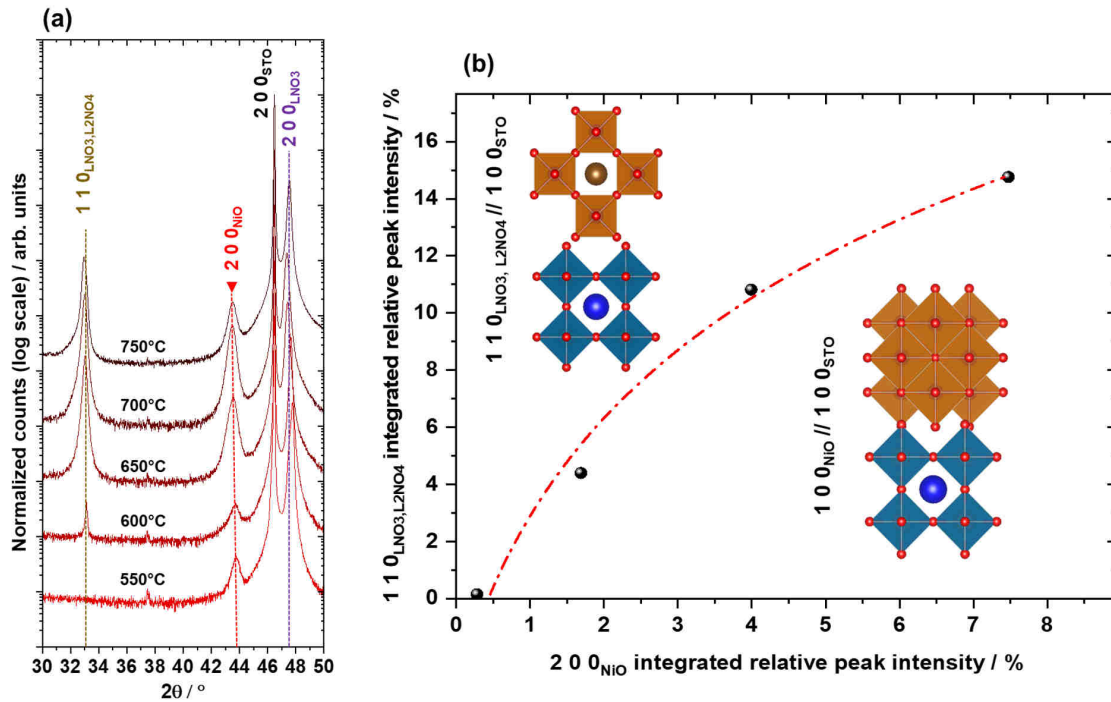


Figure 5.5 – (a) XRD patterns for LNO3/STO samples deposited at different temperatures. (b) Correlated evolution of the integrated relative peak intensities of $1\ 1\ 0_{\text{LNO}_3, \text{L2NO}_4}$ with $2\ 0\ 0_{\text{NiO}}$. The intensity for each phase was normalized to a percentage of the total integrated intensity of $2\ 0\ 0_{\text{LNO}_3}$, $1\ 1\ 0_{\text{LNO}_3, \text{L2NO}_4}$ and $2\ 0\ 0_{\text{NiO}}$. The dotted red curve is an empirical fit (exponential decay function).

reflections of the $1\ 0\ 0_{\text{LNO}_3}$ domain are aligned coherently with the STO substrate, showing that certain regions of LNO3 indeed grew epitaxially on STO. An important mosaicity of the $1\ 0\ 0_{\text{NiO}}$ domains is also observed (important spread of intensity perpendicular to the radial distance from the transmitted electron beam to the NiO reflection). Another interesting observation is the non-alignment of the $1\ 1\ 0_{\text{LNO}_3, \text{L2NO}_4}$ domain with the STO substrate. This suggests that these domains can grow freely and are not influenced by the substrate. They seem to grow coherently with certain $1\ 0\ 0_{\text{NiO}}$ domains that appeared within its mosaicity.

In order to control the film microstructure, structural and electrical properties it is useful to understand how all the phases are cohabiting and how they might influence each other. For this reason a HRTEM image has been acquired around an extended defect and is presented in Figure 5.7.a. By applying a Fast Fourier Transform (FFT) to this image, we obtain a complex image in the Fourier space (analogous to the reciprocal space used in crystallography). We can filter through all the signals constituting the total mathematical Fourier signal of the

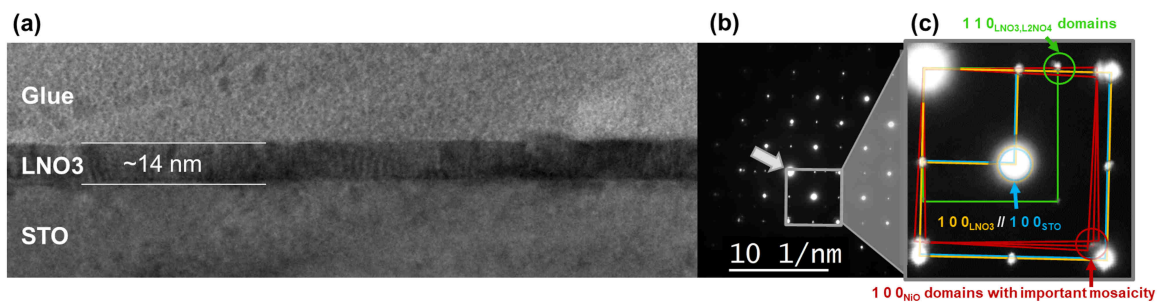


Figure 5.6 – (a) Low magnification TEM cross section image of a LNO3/STO sample deposited at 650 °C using 1000 pulses of a precursor solution with La/Ni = 2.38. (b) Electron diffraction image of the sample taken at LNO3/STO interface. The arrow shows the location of the transmitted electron beam. (c) Magnification of the electron diffraction image and partial phase indexation of the electron diffraction peaks.

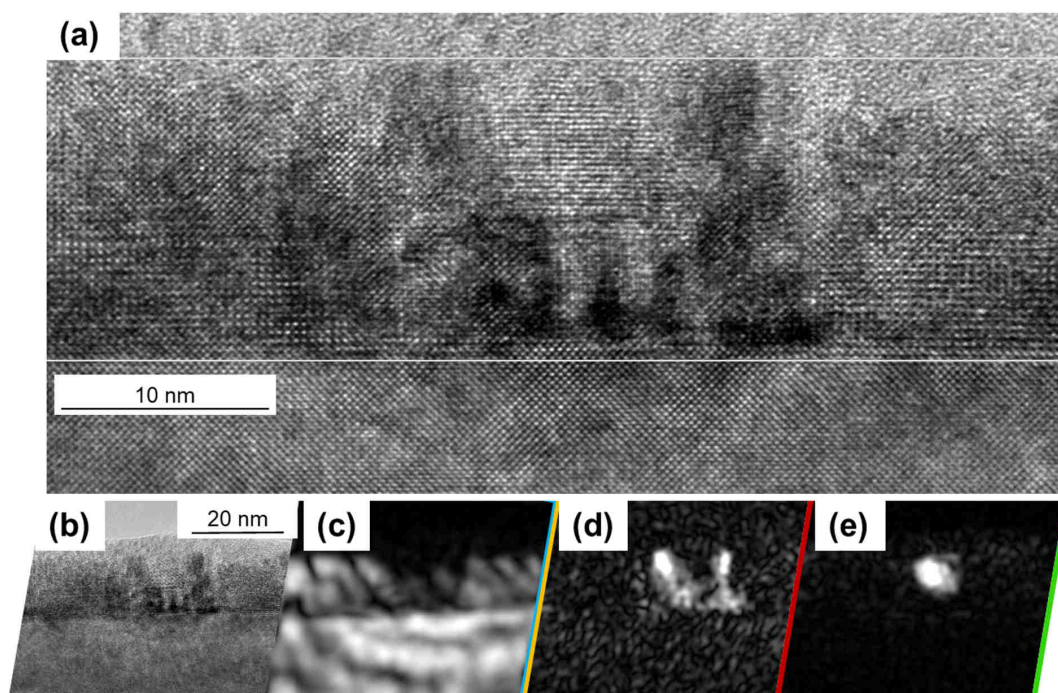


Figure 5.7 – (a) Cross-section HRTEM image of LNO3/STO taken around a NiO defect. (b) Unfiltered HRTEM image of the same area. (c-e) Filtered images showing the $1\ 0\ 0_{\text{LNO}_3} + 1\ 0\ 0_{\text{STO}}$, $1\ 0\ 0_{\text{NiO}}$ and $1\ 1\ 0_{\text{LNO}_3, \text{L}_2\text{NO}_4}$ domains, respectively. The filtered images were obtained by applying a FFT to (b), followed by an appropriate masking of the diffraction peaks of interest in the Fourier space followed by an FFT^{-1} to recover the amplitude information of the selected phase in direct space.

transformed image by masking the appropriate regions in Fourier space. The location in real space of the feature that was responsible for the signal in the Fourier space can be retrieved by applying the Inverse Fast Fourier Transform (FFT^{-1}) on the masked region. In essence, it is possible to locate a certain phase in a HRTEM image by masking one of its Bragg peaks in the reciprocal space and operating an FFT^{-1} on it. This is what was done in Figure 5.7.c-e where the amplitude information of the FFT^{-1} is displayed indicating which regions of the film have the highest contribution to the selected diffraction peak (or, more accurately, the mathematical Fourier signal for that Bragg peak). Each one of these images corresponds to the FFT^{-1} of the masked regions in Figure 5.6.c (coloured circles around the $1\ 0\ 0_{\text{LNO3}}$ / $1\ 0\ 0_{\text{STO}}$, $1\ 0\ 0_{\text{NiO}}$ and $1\ 1\ 0_{\text{LNO3, L2NO4}}$ diffraction peaks). The first filtered HRTEM image (Figure 5.7.c) corresponds to a filtered Bragg peak composed of the sum of $1\ 0\ 0_{\text{LNO3}}$ and $1\ 0\ 0_{\text{STO}}$ domains, showing the regions of the LNO3 film that have grown coherently on the STO substrate. The second filtered image (Figure 5.7.d) corresponds to the $1\ 0\ 0_{\text{NiO}}$ impurity phase, which had been found earlier using XRD. This image shows that the NiO phase is already formed close to the substrate from the beginning of the deposition and crosses the entire film thickness. It is not a relaxation mechanism that appears after having grown LNO3. This also explains why this NiO phase is highly textured due to epitaxial considerations with STO. Finally, the last image (Figure 5.7.e) shows a $1\ 1\ 0_{\text{LNO3, L2NO4}}$ domain that grew inside the NiO impurity. This supports the assumption that the presence of $1\ 1\ 0_{\text{LNO3, L2NO4}}$ domains is tightly linked to the presence of NiO. A preferential decomposition of LNO3 into L2NO4 + NiO, supported by the thermodynamic analysis of the La-Ni-O system carried out by Zinkevich *et al.* [147], could be the reason for the presence of the two phases in close proximity to each other.

To conclude this section on the optimization of LNO3 as bottom electrode for the growth of oriented L2NO4 by PiMOCVD, it appears that it is very difficult to eliminate the NiO impurities which grow from the very beginning of the deposition and can sometimes cross the entire thickness of the films. A deeper analysis of the XRD and TEM data suggests that the defects could act as nucleation points for other LNO3 or L2NO4 domains oriented at 45° (on STO substrates), lowering the overall film coherence. Controlling these NiO defects is desirable to improve the LNO3 film quality, both from an electrical and structural point of view.

5.3 Lanthanum-nickelate thin films deposited by PLD

In this section we will present how lanthanum-nickelate thin films could be successfully prepared using Pulsed Laser Deposition (PLD), a physical deposition method instead of the chemical method used until now. This deposition technique operates in vacuum (several mTorr)

and uses a high energy laser to ablate the surface of a ceramic target, transferring its chemical composition to a hot substrate. The number of laser pulses will determine the thickness of the film. Two batches of LNO₃ and L₂NO₄ thin films were prepared on STO substrates using this technique during a three-week internship carried out in the framework of a collaboration with the Catalan Institute of Nanoscience and Nanotechnology (ICN2) in Barcelona, in the Nanomaterials Growth unit. Each batch consists in three different samples with increasing film thickness, using respectively 200, 1000 and 3000 laser pulses to grow the LNO₃ and L₂NO₄ single layers. The deposition conditions are summarized in Table 5.2.

Table 5.2 – Deposition conditions used for the growth of LNO₃ and L₂NO₄ single layers by PLD.

Parameter	LaNiO ₃	La ₂ NiO ₄
Rotation of the target	15 RPM	
Distance target → substrate	55 mm	
Laser spot size	2x3 mm ²	
Laser fluency	1.1 J/cm ²	
Laser energy	66 mJ	
Number of pulses	200, 1000 and 3000	
Substrate temperature	600 °C	700 °C
pO ₂	70 mTorr	

In the following subsection the structural characteristics of these two batches of samples will be briefly described.

5.3.1 Structural properties of LNO₃ films deposited by PLD

X-ray diffractograms have been acquired for the first batch of three LNO₃/STO samples with increasing LNO₃ film thickness using a θ - 2θ measurement configuration around $2\ 0\ 0_{\text{STO}}$ ($2\theta \approx 46.5^\circ$), encompassing the 2θ range of both $2\ 0\ 0_{\text{LNO}_3}$ ($2\theta \approx 47.5^\circ$) and the possible NiO impurity peak discussed earlier in Section 5.2 (normally present around $2\theta \approx 43.5^\circ$). The resulting diffractograms are presented in Figure 5.8 and all show a single diffraction peak in addition to the substrate, which corresponds to $2\ 0\ 0_{\text{LNO}_3}$. The NiO impurity peak is no longer present in this sample grown by PLD. The increasing intensity and decreasing full-width at half maximum (FWHM) of the $2\ 0\ 0_{\text{LNO}_3}$ Bragg peak is coherent with a larger LNO₃ film thickness (from bottom to top). The clear thickness fringes present around $2\ 0\ 0_{\text{LNO}_3}$ are markers of a good LNO₃ thin film quality.

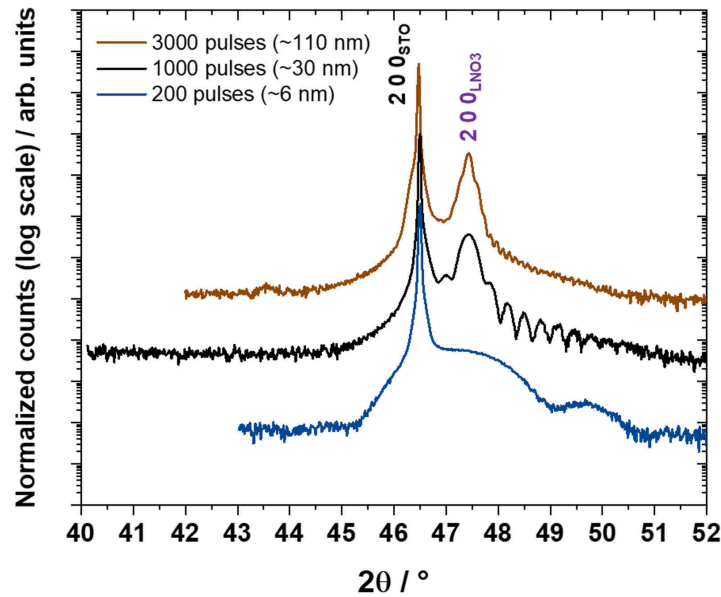


Figure 5.8 – XRD patterns of LNO3 thin films deposited on (100)STO by PLD at $T = 600\text{ }^{\circ}\text{C}$ and $p_{\text{O}_2} = 70\text{ mTorr}$. Only the number of laser pulses was varied to grow films with increasing thicknesses (from bottom to top: 6 nm, 30 nm and 110 nm-thick LNO3 films, respectively).

5.3.2 Structural properties of L2NO4 films deposited by PLD

Similar diffractograms have been acquired for the second batch of three L2NO4/STO samples with increasing L2NO4 film thickness. The results presented in Figure 5.9 provide very interesting information about the growth of L2NO4. Indeed, when increasing the film thickness from 5 nm to 30 nm, the XRD pattern shows only the $0\ 0\ 6_{\text{L2NO4}}$ ($2\theta \approx 43^{\circ}$), with a decrease of the peaks FWHM and an increase in the integrated intensity consistent with an increase in crystallite size and film thickness. However, when the thickness increases further to 80 nm, a new peak appears at $2\theta \approx 47^{\circ}$ coinciding with $2\ 0\ 0_{\text{L2NO4}}$. There is thus a certain “threshold thickness” (between 30 nm and 80 nm) where a -axis oriented L2NO4 is more stable than c -axis oriented L2NO4. Furthermore, if we consider the intensities of $0\ 0\ 6_{\text{L2NO4}}$ for the 30 nm and the 80 nm samples, we can see that it decreased for the thicker sample (the peak is also broader). This tells us that there are less c -oriented domains in the 80 nm sample than in the 30 nm sample, possibly meaning that once the a -axis domains are formed, they act as nucleation sites and scavenge the previously grown c -domains.

The reciprocal space maps (RSMs) presented in Figure 5.10 corroborate this hypothesis. Indeed, when looking at the in plane $-1\ 0\ 11_{\text{L2NO4}}$ reflection for the 30 nm-thick sample (Figure 5.10.a), we see a fully strained L2NO4 thin film while for the 80 nm thick L2NO4

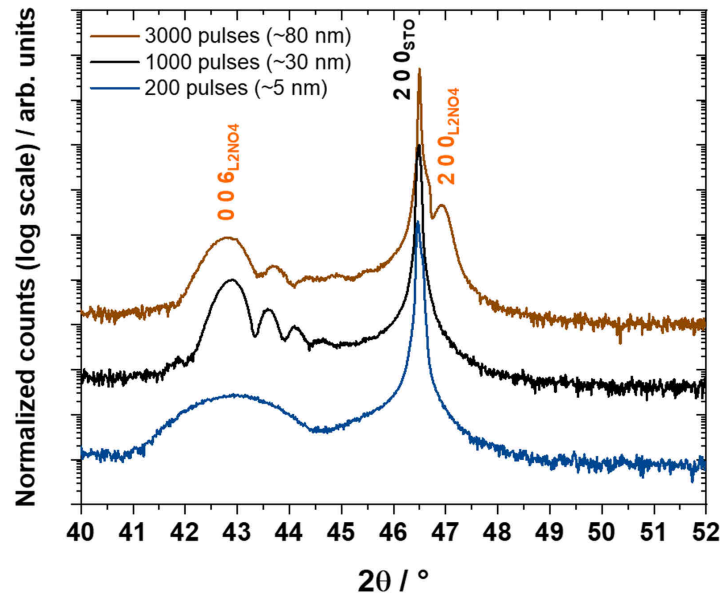


Figure 5.9 – XRD patterns of L2NO4 thin films deposited on (100)STO by PLD at $T = 700\text{ }^{\circ}\text{C}$ and $p_{\text{O}_2} = 70\text{ mTorr}$. Only the number of laser pulses was varied to grow films with increasing thicknesses (from bottom to top: 5 nm, 30 nm and 80 nm-thick LNO3 films, respectively).

film (Figure 5.10.b), the diffraction “spot” has a noticeably lower intensity and is more diffuse and isotropic, evidencing the loss of strain of the film. The lost intensity for $-1\ 0\ 11_{\text{L2NO}_4}$ is compensated by the appearance of the $-1\ -3\ 0_{\text{L2NO}_4}$ and $-3\ 0\ -3_{\text{L2NO}_4}$ reflections, corresponding to the in-plane a and b domains of L2NO4, respectively (see section C.2.2 in the appendix for more details on the different crystal orientations taken by L2NO4 when grown on (1 0 0)STO).

For now, it appears that the growth of high quality c -axis oriented L2NO4 can only be ensured for films having a thickness up to 30 nm, but a more complete study should be carried out to know more precisely when the “threshold thickness” for the appearance of a -domains is reached.

5.4 Comparison of LNO3 and L2NO4 single layers deposited by PiMOCVD and PLD

A systematic study on the influence of the LNO3 and L2NO4 film-thickness on their resistivity was carried out on the two batches of films prepared by PLD. The resistivity of the two materials is plotted against the film thickness in Figure 5.11 and compared with those depos-

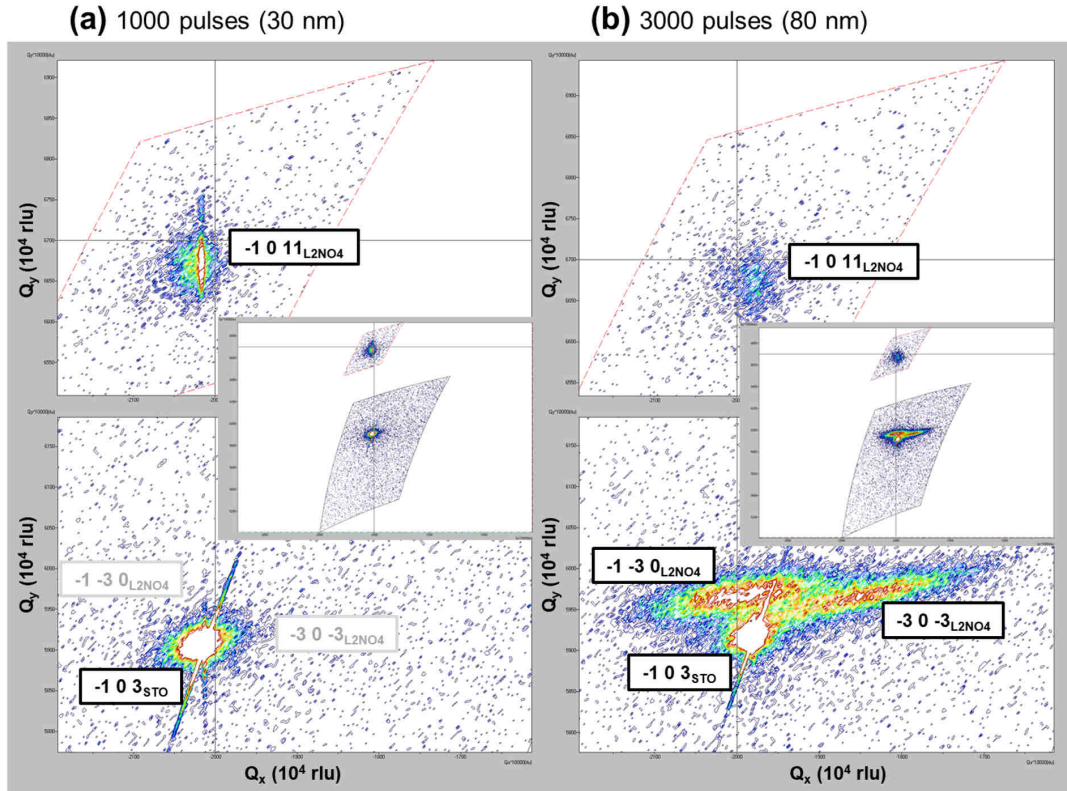


Figure 5.10 – RSMs (in reciprocal space values Q_x and Q_y) around the $-1\ -3\ 0_{L2NO4}$ and $-1\ 0\ 11_{L2NO4}$ reflections of L2NO4, which corresponds to the a and c -oriented domains of L2NO4, respectively. (a) 1000 laser pulses, corresponding to a 30 nm - thick L2NO4 film and (b) 3000 laser pulses, corresponding to a 80 nm film. The insets show the areas of the reciprocal space that were scanned for both samples. The intensity colour map is normalized to $-1\ 0\ 3_{STO}$, allowing for a qualitative comparison between samples. More details on the RSM measurements are given in appendix C.2.2.

ited by PiMOCVD, which deposition conditions are summarized in in Table 5.3. A major difference between the two deposition techniques is the working oxygen partial pressure (used as reactive gas during the deposition process), being 3.3 Torr against 70 mTorr for the chemical and the physical deposition method, respectively. The deposition temperature used for the growth of L2NO4 is also slightly lower for the CVD method (650 °C against 700 °C for PLD). A lower growth temperature was used to limit as much as possible a possible decomposition of LNO3 during the growth of L2NO4/LNO3 bilayers (presented in the following section). It can be noticed that for the thicker films ($30\text{ nm} < t < 110\text{ nm}$) there is roughly a two order of magnitude difference between the resistivity of LNO3 ($\sim 10^{-3}\ \Omega\cdot\text{cm}$) and L2NO4 ($\sim 10^{-1}\ \Omega\cdot\text{cm}$) thin films deposited by PLD. Interestingly, the resistivity values evolve in opposite directions for the low film thicknesses. For example, when $t = 5\text{ nm}$, the resistivity of LNO3 reaches a

Table 5.3 – Deposition conditions used for the growth of LNO₃ and L₂NO₄ single layers by PiMOCVD.

Parameter	LaNiO ₃	La ₂ NiO ₄
Precursors	La(TMHD) ₃ and Ni(TMHD) ₂	
La/Ni precursor ratio	2.38	5.00
Solution concentration	0.02 mol/L (solvent = m-xylene)	
Injection frequency	1 Hz	
Opening time	2 ms	
Number of injected droplets	1000, 2000 and 4000	4000
Evaporation temperature	220 °C - 280 °C (several heating stages)	
Substrate temperature	650 °C	650 °C
Carrier gas	34% Ar (218 sccm) + 66% O ₂ (418 sccm)	
Total pressure inside the reactor	5 Torr	

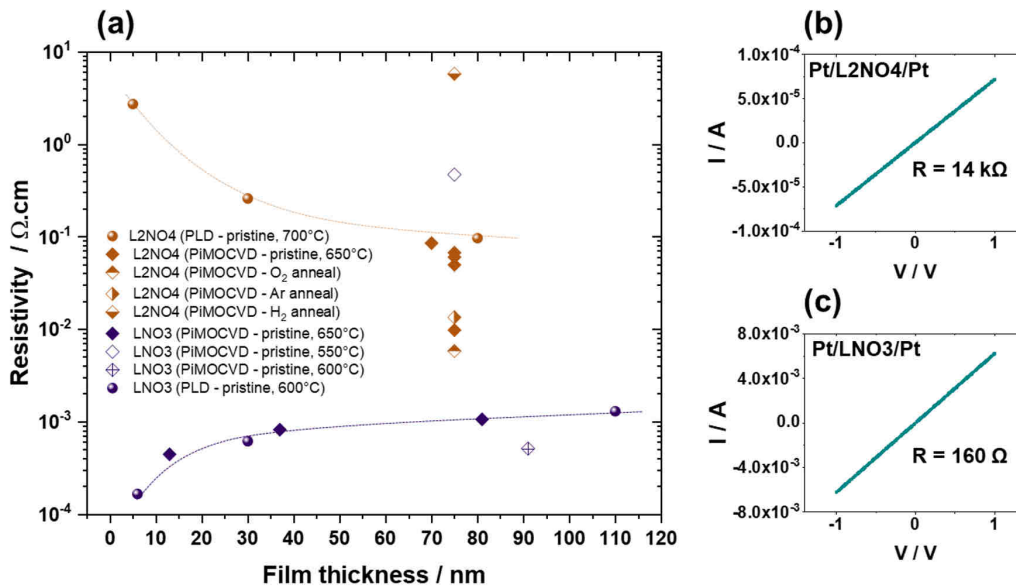


Figure 5.11 – (a) Resistivity as a function of film thickness for L₂NO₄/STO and LNO₃/STO samples deposited both by PiMOCVD (diamonds) and PLD (spheres). ‘O₂, Ar and H₂ anneal’ refers to pristine samples deposited by PiMOCVD having received a post annealing treatment in an oxygen, argon or H₂(6%)/Ar gas atmosphere (at T = 500 °C during 1 h). The resistivity of the samples has been measured with a 4-probe measurement setup. (b-c) I(V) characteristics of Pt/L₂NO₄/Pt and Pt/LNO₃/Pt heterostructures, respectively.

very low (state of the art) resistivity ($\sim 10^{-4}$ $\Omega\cdot\text{cm}$) while for L2NO4 it increases to ~ 3 $\Omega\cdot\text{cm}$, almost reaching the resistivity values of the highly reduced (hydrogen-annealed) samples prepared by PiMOCVD. The scatter in the resistivity values which have been obtained for L2NO4 samples deposited by PiMOCVD (both pristine or post-annealed) is displayed on the same plot (brown filled and half-filled diamonds, see legend in Figure 5.11 for more details) and shows the range of resistivity values which can be obtained with L2NO4. It should be noted that, except for highly reduced samples in $\text{H}_2(6\%)/\text{Ar}$, the resistivity of L2NO4 films deposited by PiMOCVD tends to be lower than the ones deposited by PLD (for a given film-thickness). This could be related to the larger oxygen partial pressure used in PiMOCVD when compared to the higher vacuum required in PLD systems. Conversely, the electrical resistivity of LNO3 thin films is similar for both deposition methods, despite having some impurities present in the LNO3 films grown by PiMOCVD (mainly in the form of NiO precipitates). On the other hand, the important dependence of the resistivity on the oxygen-stoichiometry of L2NO4 thin films could be much more affected by the deposition method due to the important difference in the operating oxygen partial pressure allowed by the deposition system (relatively high p_{O_2} for CVD methods and low for physical methods such as PLD). However, it is possible to mitigate this ‘operating p_{O_2} effect’ during deposition by using post-annealing treatments in controlled atmospheres, although this adds an extra processing step to the fabrication of the devices. An array of $\text{\O}200$ μm circular Pt electrodes has been deposited on L2NO4/STO and LNO3/STO samples prepared by PLD using e-beam evaporation through a shadow mask. A symmetric Pt/L2NO4/Pt heterostructure shows ohmic characteristics (Figure 5.11.b), consistent with the results already obtained for similar heterostructures deposited by PiMOCVD (see Section 3.2 in Chapter 3). Symmetric Pt/LNO3/Pt heterostructures also show ohmic characteristics (Figure 5.11.c) with a total resistance values of a few hundred Ohms (depending on the distance between electrodes).

These first electrical measurements show that the individual Pt/LNO3 and Pt/L2NO4 heterojunctions are not active from a memory point of view. Nevertheless, an extra junction has to be considered when working with a L2NO4/LNO3 bilayer sample: the L2NO4/LNO3 junction itself.

5.5 L2NO4/LNO3 bilayers

5.5.1 L2NO4/LNO3 bilayers deposited by PiMOCVD

L2NO4/LNO3 bilayers were grown for the first time by PiMOCVD on STO and LAO substrates using the conditions described in Table 5.4 (more details about this are available in

Table 5.4 – Deposition conditions used for the growth of L2NO4/LNO3 bilayers by PiMOCVD

Parameter	LaNiO ₃	La ₂ NiO ₄
Precursors	La(TMHD) ₃ and Ni(TMHD) ₂	
La/Ni precursor ratio	2.75	5.00
Solution concentration	0.02 mol/L (solvent = m-xylene)	
Injection frequency	1 Hz	
Opening time	2 ms	
Number of droplets	1000	5000*
Evaporation temperature	220 °C - 280 °C (several heating stages)	
Substrate temperature	600 °C	650 °C
Carrier gas	34% Ar (218 sccm) + 66% O ₂ (418 sccm)	
Total pressure inside the reactor	5 Torr	

* a stainless-steel shadow mask was used to control the areas where L2NO4 is deposited. The presence of this shadow mask might affect the film thickness: the measured L2NO4 film thickness of ~20 nm is much lower than would be expected with this amount of pulses (which should be >100 nm).

Appendix B.4). A deposition temperature of 600 °C was chosen for the deposition of LNO3 as a compromise (according to their resistivity values, see Figure 5.2) to grow the films simultaneously on both substrates and the La/Ni precursor ratio was exceptionally increased from 2.38 to 2.75 in order to reduce the remaining NiO impurities, but without success.

Figure 5.12.a and b show the XRD patterns of the L2NO4/LNO3 bilayer obtained by successive depositions of LNO3 (600 °C, 15 nm thick) and L2NO4 (650 °C, 20 nm thick) layers. They were acquired before the deposition (bare STO and LAO substrates), after the deposition of LNO3 and after the completion of the entire L2NO4/LNO3/STO or L2NO4/LNO3/LAO stack in order to better put in evidence the phases formed after each deposition step. The thickness fringes visible around $2\ 0\ 0_{\text{LNO3}}$ support a coherent growth of these films with a homogeneous thickness. The top L2NO4 layer has two preferential orientations corresponding to the *c*-axis oriented in-plane and out of plane respectively ($0\ 0\ 6_{\text{L2NO4}}$ and $2\ 0\ 0_{\text{L2NO4}}$ reflections in Figure 5.12.a and b). The orientation whis the *c*- axis of tetragonal L2NO4 oriented in plane has been observed previously when growing L2NO4/STO single layers both by PLD (section 5.3.2) and MOCVD techniques (section 2.3.1). It would be interesting to further investigate if this is an intrinsic relaxation mechanism in strained L2NO4 thin films and how the NiO impurities or $1\ 1\ 0_{\text{LNO3, L2NO4}}$ domains present in the LNO3 bottom electrode could help inducing this domain reorientation.

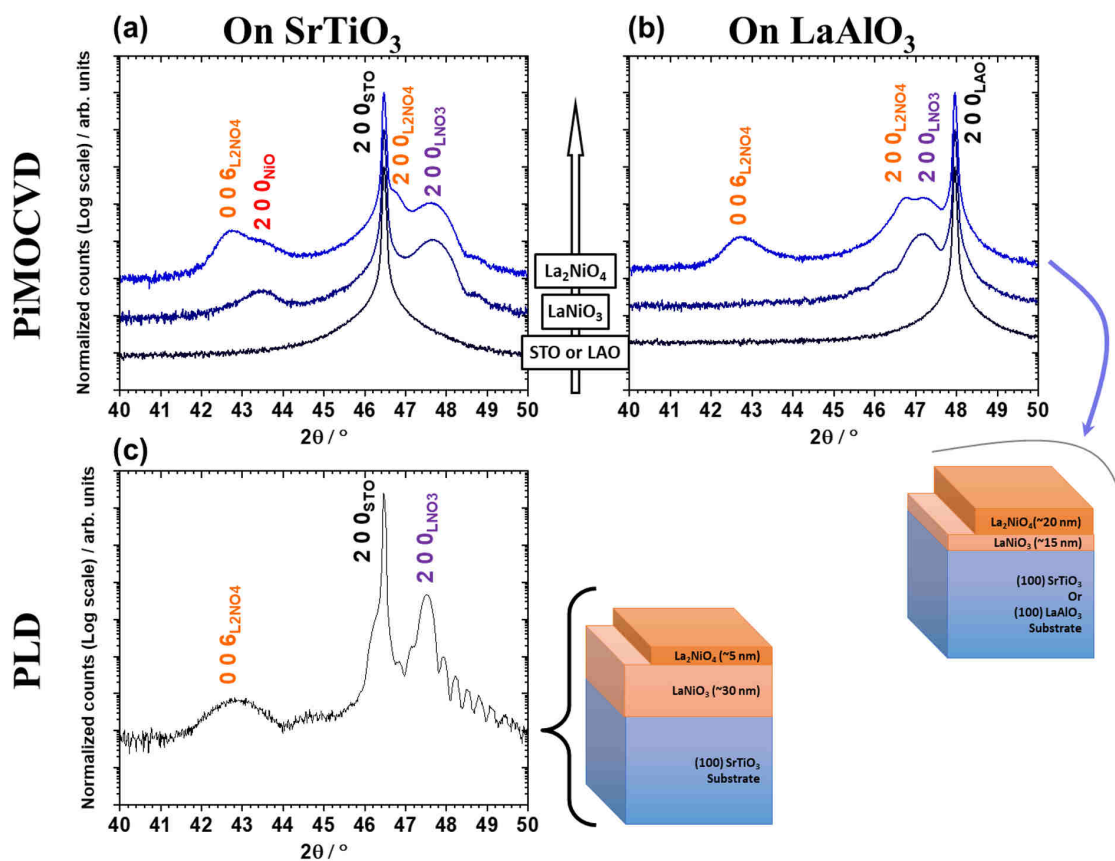


Figure 5.12 – XRD patterns (θ - 2θ scans) of (a) L2NO4/LNO3/STO and (b) L2NO4/LNO3/LAO samples. A new pattern was acquired at each step of the deposition process. Each new pattern has been manually offset with respect to the previous one to enhance readability. (c) XRD pattern of the final L2NO4/LNO3/STO heterostructure prepared by PLD. A schematic of the sample's structure and the different film thicknesses is shown for each deposition technique.

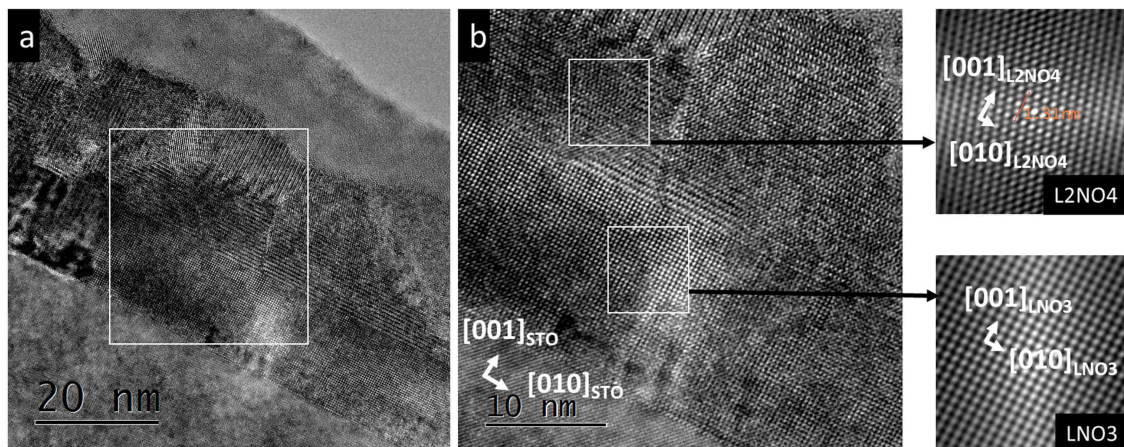


Figure 5.13 – HRTEM images of a L2NO4/LNO3/STO bilayer deposited by PiMOCVD. LNO3 and L2NO4 films were deposited at 600 °C and 650 °C using La/Ni ratios in the precursor solution of 2.75 and 5.00, respectively. The LNO3 and L2NO4 layers are 15 nm and 20 nm thick, respectively. (a) General view. (b) Enlarged area corresponding to the white square in (a). Magnified auto correlation images of selected regions in (b) are also included.

The two in-plane and out-of-plane orientations of L2NO4 are clearly observed in the cross-section HRTEM images of the L2NO4/LNO3/STO sample presented in Figure 5.13. The LNO3 layer directly on top of the STO substrate has a cube-on-cube orientation relationship ($[0\ 0\ 1]_{\text{LNO3}}//[0\ 0\ 1]_{\text{STO}}$, $[0\ 1\ 0]_{\text{LNO3}}//[0\ 1\ 0]_{\text{STO}}$). L2NO4 then grows on top of LNO3 with an $[0\ 0\ 1]_{\text{L2NO4}}//[0\ 0\ 1]_{\text{LNO3}}//[0\ 0\ 1]_{\text{STO}}$, $[0\ 1\ 0]_{\text{L2NO4}}//[0\ 1\ 0]_{\text{LNO3}}//[0\ 1\ 0]_{\text{STO}}$ orientation relationship (the basal plane of the tetragonal L2NO4 matching with the a-b plane of LNO3). Nevertheless, while this orientation seems favourable from an epitaxial point of view, other domains of L2NO4 tilted at 90°, corresponding to the $[0\ 1\ 0]_{\text{L2NO4}}//[0\ 0\ 1]_{\text{LNO3}}//[0\ 0\ 1]_{\text{STO}}$, $[0\ 0\ 1]_{\text{L2NO4}}//[0\ 1\ 0]_{\text{LNO3}}//[0\ 1\ 0]_{\text{STO}}$ orientation relationship are also present. This reorientation had been previously observed when growing L2NO4/STO single layers [124].

A difficulty encountered when carrying out the deposition of the bilayer by PiMOCVD was the fact that the stainless steel shadow mask used to cover certain regions of the sample when growing L2NO4 (to be able to access the LNO3 bottom electrode during electrical measurements) is not well adapted for the systems as it creates a gradient in the film thickness around it. Furthermore, the places where the mask locally contacts the film is subjected to higher temperatures (leading to film recrystallization) and possible contamination (for example from the iron present in the stainless steel mask) when compared to other non-contacted regions of the film. Other approaches will be used to grow bilayers by PiMOCVD in the future, for example with the use of sacrificial layers or by post-etching the L2NO4 film to uncover the LNO3 bottom electrode.

5.5.2 L2NO4/LNO3 bilayers deposited by PLD

To overcome the aforementioned difficulties when depositing the bilayers by PiMOCVD and to complement this work, L2NO4/LNO3 bilayers have also been deposited by PLD using the conditions detailed in Table 5.5.

Table 5.5 – Deposition conditions used for the growth of L2NO4/LNO3 bilayers by PLD.

Parameter	LaNiO ₃	La ₂ NiO ₄
Rotation of the target	15 RPM	
Distance target → substrate	55 mm	
Laser spot size	2x3 mm ²	
Laser fluency	1.1 J/cm ²	
Laser energy	66 mJ	
Number of pulses	1000	200
Substrate temperature	600 °C	700 °C
PO ₂	70 mTorr	

The L2NO4/LNO3 bilayer sample prepared by PLD (Figure 5.12.c) has a full sheet LNO3 bottom electrode grown epitaxially on STO (100). A very thin L2NO4 layer was then grown on top of LNO3. By taking advantage of the directional nature of the plasma plume in PLD, a simple blade put between the target and the substrate can serve as a mask to leave a region of the LNO3 film uncovered for electrical contacting. The L2NO4 and LNO3 films are 5 nm and 30 nm thick, respectively. The thicknesses of each film was carefully selected to avoid L2NO4 in-plane reorientation (which occurs for thicker films deposited by PLD) and to have a low enough sheet resistance of LNO3 for it to act as a bottom electrode. By choosing a 30 nm thick LNO3 bottom electrode layer and a 5 nm thick top L2NO4 layer, taking into consideration the three orders of magnitude difference in the resistivity of the two materials (Figure 5.11), the current is expected to take the shortest path through L2NO4 before flowing into LNO3 (thus choosing the path of least resistance and ensuring a ‘top-bottom’ biasing configuration).

The XRD diffraction pattern presented in Figure 5.12.c shows a L2NO4/LNO3/STO stack prepared by PLD using the (already optimized) deposition conditions presented in Table 5.5. Only the epitaxial LNO3 and L2NO4 domains are present, no NiO impurities nor phase reorientations could be observed in this sample. The clear thickness fringes visible around 200_{LNO3} support the coherent growth and phase homogeneity of the LNO3 bottom electrode.

The electrical properties of a Pt/LNO3/L2NO4/Pt multi-junction device is described in the

following section.

5.6 Resistance-change in Pt/LNO3/L2NO4/Pt heterostructures grown by PLD

An array of $\varnothing 200 \mu\text{m}$ circular Pt electrodes has been deposited on the L2NO4/LNO3/STO described in Figure 5.12.c using e-beam evaporation through a shadow mask, paying attention that Pt electrodes are present both on top of LNO3 and L2NO4. The measurement setup is better described in Figure 5.14

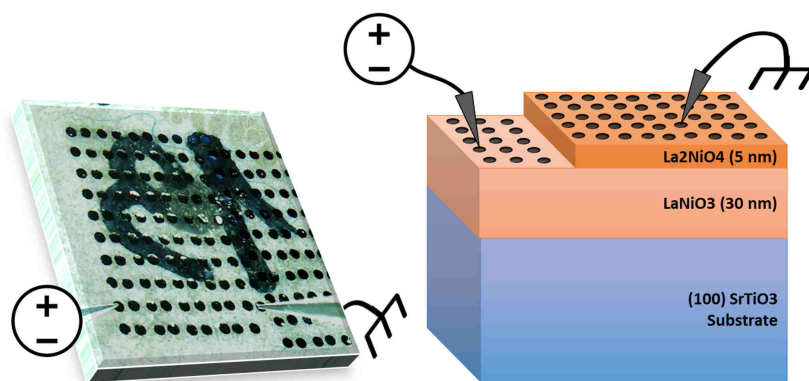


Figure 5.14 – Picture (left) and sketch (right) of the measuring configuration of a Pt/LNO3/L2NO4/Pt sample. Black circles are Pt electrodes (diameter of $200 \mu\text{m}$, thickness of 200 nm). The Pt electrode on the LNO3 side is biased while the Pt electrode on the L2NO4 side remains grounded.

In this section we will show that an initialisation step can trigger a reproducible analog and bipolar resistance-change behaviour. The initialised memory is volatile and shows interesting relaxation dynamics highly dependent on the previously programmed resistance state.

5.6.1 The initialisation step

Figure 5.15 shows the evolution of the $I(V)$ characteristics of a Pt/LNO3/L2NO4/Pt device when the maximum voltage amplitude is gradually increased from $\pm 1 \text{ V}$ to $\pm 10 \text{ V}$ by steps of 1 V every four sweeps. The IRS of the device when probed at relatively low voltages (for example $V = \pm 1 \text{ V}$ in Figure 5.15) shows a nonlinear behaviour in the $-0.5 \text{ V} \leq V \leq +0.5 \text{ V}$ region. Outside this region the electrical characteristics become ohmic. The ohmic characteristics are likely corresponding to an LNO3 electrode-limited conduction, but the nonlinearities

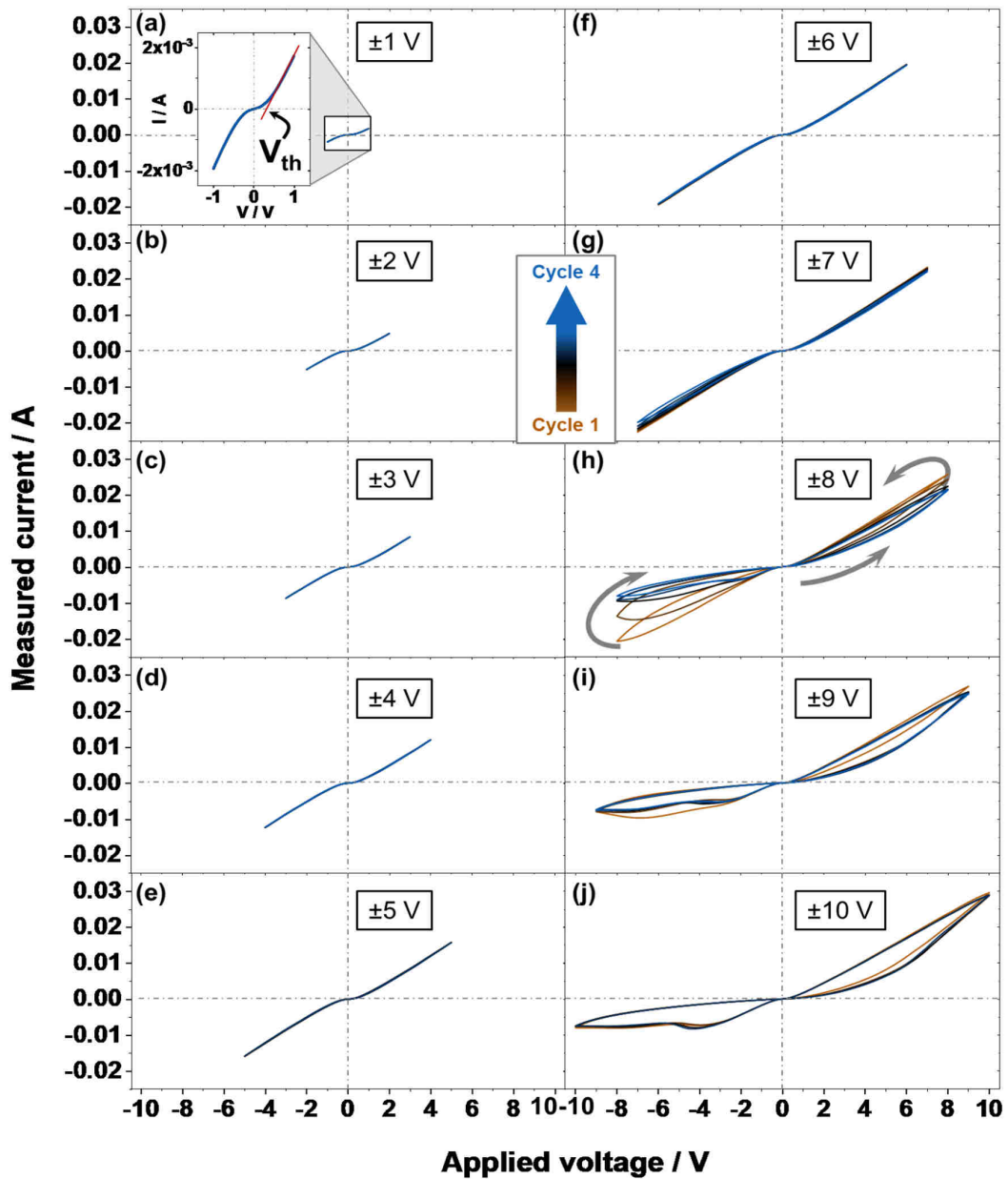


Figure 5.15 – (a-j) I-V characteristics showing the initialisation of a Pt/LNO₃/L₂NO₄/Pt memristive device prepared by PLD. Each panel shows four consecutive bipolar I(V) sweeps executed in the same biasing conditions (0 V → +V_{max} → 0 V → -V_{max} → 0 V). The maximum voltage amplitude (V_{max}) is increased from 1 V to 10 V with a step of 1 V in each new panel. The Pt electrode on the LNO₃ side was biased while the one on the L₂NO₄ film remained grounded throughout the experiment. The inset in (a) shows the small threshold voltage that needs to be overcome before observing an ohmic behaviour.

at very low voltages is an interesting and surprising phenomenon. Indeed, as has been previously measured, the individual Pt/LNO3 and Pt/L2NO4 junctions are ohmic (Figure 5.11.a and b), the nonlinearity in the measured I(V) characteristics of Pt/LNO3/L2NO4/Pt has been attributed to the LNO3/L2NO4 junction. The threshold voltage (V_{th} , the onset of the linear characteristics of the I(V) curve) is very low (~ 300 mV), meaning that the potential Schottky barrier existing at the LNO3/L2NO4 junction is very thin, explaining the rather symmetric I(V) characteristics with an almost absent rectification.

The electrical characteristics of Pt/LNO3/L2NO4/Pt show no hysteresis and are very reproducible up to ± 6 V, even when cycling several times the same voltage ranges. However, at ± 7 V the I(V) characteristics in the negative voltage region start changing and each new ± 7 V voltage cycle no longer exactly superimposes the previous one. This behaviour is drastically enhanced when increasing the voltage amplitude to ± 8 V and ± 9 V. A hysteresis is now clearly visible in the two voltage polarities, the shape of the I(V) curve in the IRS is still partially present in the I(V) characteristics but a new more resistive and rectifying resistance state is also present and closes the cycle between two well defined and reproducible resistance states. When sweeping the voltage between ± 10 V, the hysteretic memory behaviour is intensified further and becomes again highly reproducible after having completed the first cycle.

It is still unclear what exact physico-chemical processes occur at the interface during the initialisation. A likely scenario is that it triggers the drift and rearrangement of oxygen anions at the LNO3/L2NO4 interface, locally changing the amount of charge carriers and thus the junction properties. What is clear is that the device needs to exhibit both nonlinear and rectifying electrical characteristics to show a reproducible analog-type memory behaviour. More details on the memory characteristics of an initialized Pt/LNO3/L2NO4/Pt memristive device are given in the following section.

5.6.2 Analog-type bipolar resistance change in Pt/LNO3/L2NO4/Pt

The electrical characteristics of an initialised Pt/LNO3/L2NO4/Pt memristive device are detailed in Figure 5.16. Five ± 10 V cycles allow setting the device reproducibly in HRS and LRS. A positive voltage sweep changes the devices from HRS to LRS while a negative voltage sweeps resets it from LRS to HRS. It is interesting to notice that the first ± 10 V cycle (in orange) is not superimposing with the following four cycles, this is particularly visible in the positive voltage region. This is because this first 0 V \rightarrow $+10$ V \rightarrow 0 V sweep follows a 0 V \rightarrow -9 V \rightarrow 0 V sweep. The reset (at -9 V) was thus different than for the four following ± 10 V cycles and this translates into an offset in the set voltage. The smaller reset voltage of -9 V (instead of -10 V for the rest of the cycles) leads to a smaller set voltage needed to recover a lower resistance state, and thus a shift of the I(V) curve to the left in the positive voltage quad-

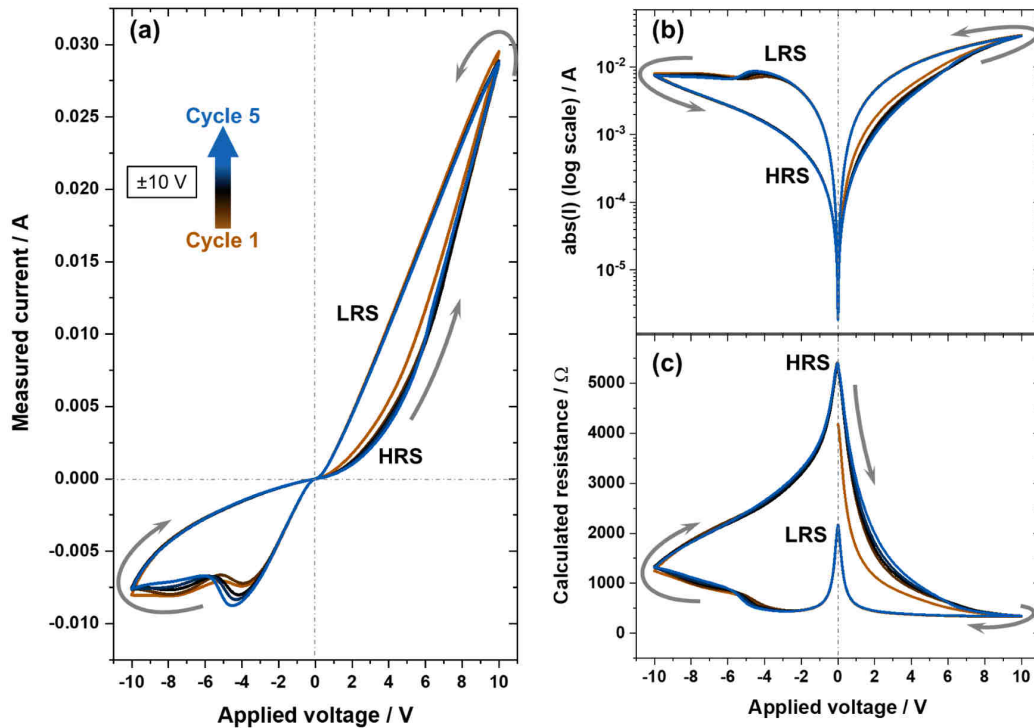


Figure 5.16 – (a) I-V characteristics of an initialised Pt/LNO3/L2NO4/Pt memristive device showing five consecutive analog-type resistance-change cycles. As depicted by the arrows, the cycle starts at 0 V in the HRS, is set in its LRS sweeping a positive bias up to +10 V and reset to HRS when sweeping a negative bias down to -10 V. The same biasing experiment is described in terms of $I(\log \text{ scale})$ -V and R-V characteristics in (b) and (c), respectively. The Pt electrode on the LNO3 side was biased while the one on the L2NO4 film remained grounded throughout the experiment.

rant (thus to smaller positive voltages). This is an important result as it shows that the biasing history of the device will determine its response to a new stimulus, showing its remarkable and intrinsic² memory properties. Not only the biasing conditions, but also the biasing *history* of the biasing influences the current memory state of the device.

As far as the memory window is concerned, Figure 5.16.c shows that the resistance of the device can be programmed between a HRS of $\sim 5200 \Omega$ and a LRS of $\sim 2200 \Omega$, corresponding to a $\frac{HRS}{LRS} = 2.4$ for $V_{\text{readout}} = 10 \text{ mV}$. Nevertheless, as the electrical characteristics are highly nonlinear at low voltages the resistance ratio can be ‘artificially’ increased by selecting a slightly larger readout voltage (for example $\frac{HRS}{LRS} = 5.2$ for $V_{\text{readout}} = 700 \text{ mV}$). A trade-off

²the word ‘intrinsic’ has been used here to highlight the fact that no additional software layer is required to program the memory properties of this device.

between a larger programming window and a lower readout voltage (which should remain non-destructive) might have to be made. Nevertheless, a large programming window is likely unnecessary for neuromorphic applications. Furthermore, the programmed resistance state of the Pt/LNO3/L2NO4/Pt memristive device has a certain degree of volatility, making it difficult to define an optimal and fixed programming window. The memory relaxation behaviour is discussed in more detail in the following section.

5.6.3 Resistance relaxation

A new pristine Pt/LNO3/L2NO4/Pt memristive device has been used to study the retention properties of such a system. Figure 5.17.a shows the resistance state of the device (using a readout voltage of $V_{\text{readout}} = +10$ mV) as a function of the experiment time (including dead times). The IRS of the device is first readout during 600 s showing a stable resistance state of $\sim 1900 \Omega$. The bottom left inset shows the highly nonlinear and slightly rectifying $R(V)$ characteristics of the IRS measured between ± 500 mV. The device is then initialised following the same procedure as has been described in subsection 5.6.1 (several bipolar voltage sweeps with increasing maximum voltage amplitude, from ± 1 V up to ± 10 V). The initialisation procedure sets the device in a HRS of $\sim 4200 \Omega$. The top right inset in Figure 5.17.a shows the highly reproducible analog-type resistance change behaviour already presented in Figure 5.16.c. Nevertheless, when the initialised HRS is readout during 600 s at a constant voltage of +10 mV, the resistance quickly relaxes back towards the IRS. The device lost nearly a third of its HRS in ten minutes (relaxation from $\sim 4200 \Omega$ to $\sim 2850 \Omega$). The partially relaxed $R(V)$ characteristics are shown in the middle-right inset in Figure 5.17.a and resembles the characteristics of the IRS with an additional vertical offset towards higher resistance values.

The second part of the experiment consisting in a series of stresses/relaxations applied to the sample is detailed in Figure 5.17.b. After the ten minutes-long relaxation from the initialised HRS, the sample is submitted to increasing and alternating positive and negative voltage levels. Each one of these 100 s long voltage stresses is followed by an equally long relaxation period during which the resistance state of the device is readout at +10 mV. Only the readouts are displayed in the figure. The first voltage stress consists in a 100 s long voltage level of $V = +1$ V. This positive stress significantly increased the relaxation rate of the device as can be seen from the ‘jump’ in resistance from $\sim 2850 \Omega$ to $\sim 2340 \Omega$, creating a discontinuity in the natural relaxation trend of the device (remember that the time scale is absolute: it also takes into account the dead times of the experiment, or for example in this case the duration of the voltage stress not represented in this figure). Nevertheless, the new resistance state did not reach the $\sim 1900 \Omega$ of the IRS, meaning that even though the HRS is volatile, it still has a certain stability as this first +1 V voltage stress did not manage to completely reset

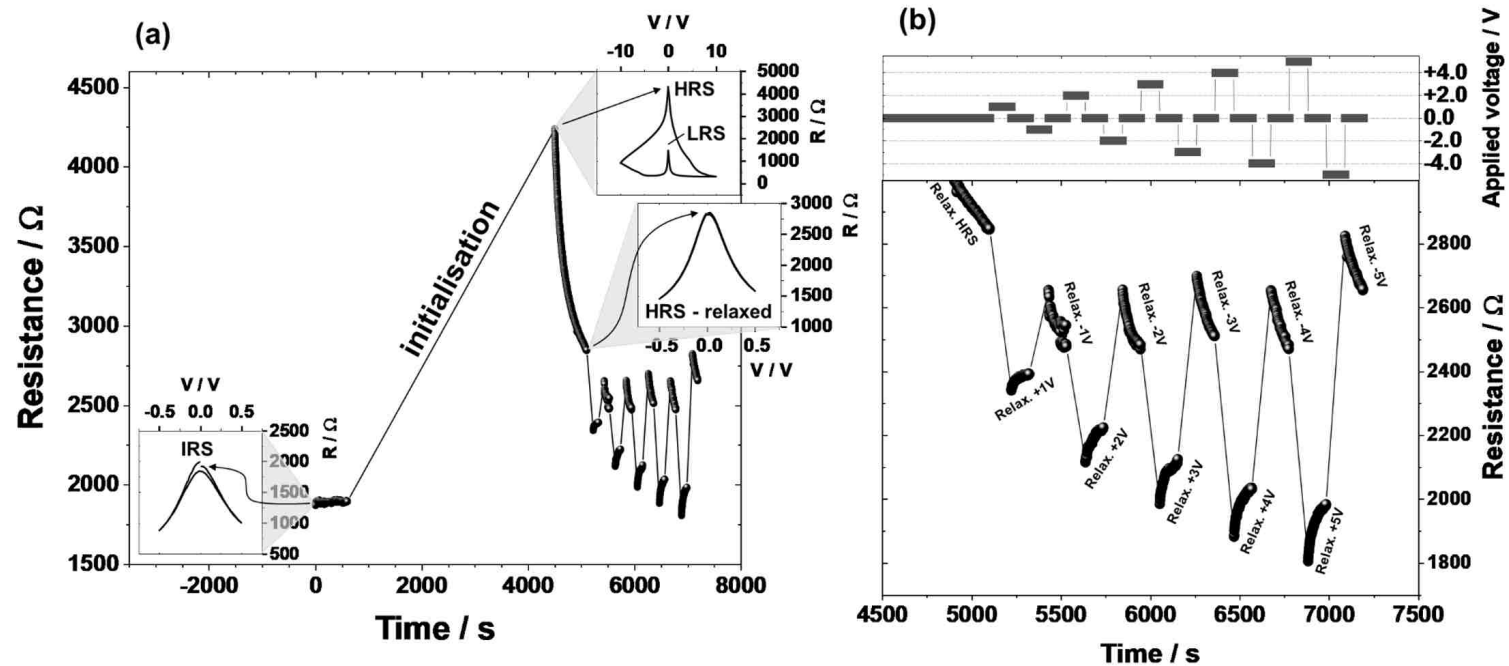


Figure 5.17 – (a) Evolution of the resistance over time of a Pt/LNO₃/L₂NO₄/Pt memristive device from its IRS to its initialised HRS, followed by the relaxation of the HRS and the relaxation of several programmed resistance states achieved by stressing the device with increasing and alternating positive and negative voltages. The insets show the R-V characteristics of the device in its IRS, HRS and after 600 s of relaxation from the HRS. (b) is a magnification of (a) between 4500 s and 7500 s during the stressing experiment. The end of the 600 s long relaxation from the initialised HRS is visible, followed by the 100 s long relaxations from the +1 V, -1 V, +2 V, -2 V, +3 V, -3 V, +4 V, -4 V, +5 V and -5 V voltage stresses (also 100 s). Only the readout voltage at +10 mV is shown in the two figures.

the device to its initial resistance value. Furthermore, and very surprisingly, the relaxation from this first ‘positive reset stress’ (indeed, positive voltages have been shown earlier to *reset* the Pt/LNO₃/L₂NO₄/Pt device from a HRS to a LRS) has a direction opposite to the previous relaxation: the device now spontaneously relaxes towards a *higher* resistance state. The opposite was true earlier as the HRS was decaying naturally to lower resistance values. After 100 s of relaxation, an opposite negative $V = -1$ V stress is then setting the device back to a higher resistance state of $\sim 2660 \Omega$. The following readout shows that the first natural relaxation from higher to lower resistance states could be retrieved, although the relaxation rate seems higher. The experiment is then continued and the same behaviour is measured: positive voltage stresses decrease the resistance state of the device, but the resistance increases back again during the relaxation period and the opposite is true for negative voltage stresses. Increasing the positive voltage amplitude increases the absolute change in resistance and also tends to increase the relaxation rate towards a higher resistance state, while increasing the opposite negative voltage amplitude also increases the change in resistance but has little effect on the relaxation rate towards lower resistance states. It can also be noticed that an increasingly lower resistance state can be reached when increasing the positive voltage stress, even to the point that after a voltage stress of $V = +4$ V or $+5$ V, the device finds itself temporally in a lower resistance state than its IRS, before spontaneously relaxing back towards a higher resistance state.

This complicated and highly intriguing device dynamics is surely related to the exchange and rearrangement of charges (electrons/holes) and/or ions (in the simple case, oxygen anions) across the interface or within the two lanthanum-nickelate films in the close proximity region. This type of electrical response offers a very versatile memory playground and is potentially highly interesting for neuromorphic hardware applications due to their inherent adaptability and analog response to a wide range of stimuli, proving that the current memory state of the memristive device is intricately linked to its entire biasing (and also *non-biased*) history.

5.7 Summary

The main points tackled in this chapter are summarized hereafter.

- The need for a template electrode for the growth of oriented L₂NO₄:
 - The perovskite compound LNO₃ is a suitable candidate for a template bottom electrode material due to its good electrical conductivity (resistivity values as low as $90 \mu\Omega\cdot\text{cm}$ have been reported in literature), as well as its good lattice match both

- with STO (< 1.70 %) used as substrate material and L2NO4 (< 0.50 %) grown on top;
- The chemical similarity between LNO3 and L2NO4 makes it easy to deposit one material or the other simply by changing the La/Ni ratio in the precursor solution when using a PiMOCVD system;
 - The exchange of oxygen between L2NO4 and LNO3 in L2NO4/LNO3 bilayers first reported by Moreno *et al.* [88] makes this system particularly interesting for VCM applications.
- Optimization of LNO3 as functional bottom electrode material by PiMOCVD:
 - The composition of the precursor solution ($2.00 \leq \text{La/Ni} \leq 2.75$) and the deposition temperature ($550 \text{ }^\circ\text{C} \leq T \leq 750 \text{ }^\circ\text{C}$) were varied to optimize the growth of LNO3 thin films on STO and LAO single crystal substrates. A substrate-dependence of the optimal growth conditions has been observed;
 - Resistivity values as low as 200 $\mu\text{ohm.cm}$ were obtained on LAO for $\text{La/Ni} = 2.38$ and $T = 550 \text{ }^\circ\text{C}$, while a resistivity of 500 $\text{m}\Omega.\text{cm}$ was measured for LNO3 deposited on STO (using the exact same deposition conditions). The important difference in the resistivity values has been attributed to a different microstructure, with a larger amount of percolating NiO precipitates in the LNO3/STO sample;
 - The effect of the persistent NiO impurities on the phase quality for LNO3 films deposited on STO has been studied in details by XRD and TEM, showing that these defects could be at the origin of some of the other defects observed in the films, such as LNO3 domain reorientations and/or L2NO4 precipitates.
 - Lanthanum-nickelate thin films deposited by PLD:
 - LNO3/STO and L2NO4/STO samples with different film thicknesses have been successfully prepared in the framework of a collaboration with ICN2 (Barcelona, Spain). XRD measurements carried out on the LNO3 thin films confirm the high crystal quality (single c out of plane orientation and thickness fringes) of these films throughout the entire 6-110 nm thickness range. Another orientation (c in-plane) of L2NO4 appears when $t > 30 \text{ nm}$;
 - The several orders of magnitude lower resistivity of the optimized LNO3 thin films when compared to L2NO4 (deposited either by PiMOCVD or PLD) validates its further use as bottom electrode for the growth of L2NO4/LNO3 bilayers. In particular, more than four orders of magnitude separate the resistivity of a 30 nm

thick LNO₃ film with that of a 5 nm L₂NO₄ film ($\rho \simeq 6 \cdot 10^{-4} \Omega \cdot \text{cm}$ and $3 \Omega \cdot \text{cm}$, respectively) when grown by PLD. Such a stack has been used to construct a Pt/LNO₃/L₂NO₄/Pt memristive device.

- L₂NO₄/LNO₃ bilayers:
 - L₂NO₄/LNO₃ complex oxide bilayers have been grown on STO both by PiMOCVD and PLD. However, the PiMOCVD-prepared bilayers still need further optimization to improve the epitaxial quality and the purity of the sample;
 - The L₂NO₄/LNO₃ bilayer sample prepared by PLD shows a high crystal quality, with the presence of the desired epitaxial LNO₃ and L₂NO₄ phases only.
- Resistance-change in Pt/LNO₃/L₂NO₄/Pt heterostructures grown by PLD:
 - The individual Pt/LNO₃ and Pt/L₂NO₄ junctions show ohmic characteristics and are inactive from a memory point of view. A slightly nonlinear Schottky characteristic has been measured for a Pt/LNO₃/L₂NO₄/Pt device and has been attributed to the LNO₃/L₂NO₄ junction;
 - A reproducible analog-type memristive behaviour has been obtained in an asymmetric Pt/LNO₃/L₂NO₄/Pt device after having carried out an initialisation step (consisting here in applying several bipolar voltage sweeps with increasing maximum voltage amplitude, from ± 1 V up to ± 10 V) necessary to SET the device in HRS. The initialization procedure could certainly be optimized by using a fixed voltage level, or repeating only one type of voltage sweep (*e.g.* ± 10 V, this has not been tested yet);
 - The programmed HRS exhibits a certain degree of volatility, which was probed using long samplings ($V = 10$ mV). The device loses one third of its HRS resistance value in ten minutes. However, the time it takes for the device to relax completely back to its IRS (or another low resistance state) was not measured.
 - 100 s long voltage stresses with opposite polarities could reversibly RESET and SET the device in a lower or higher resistance state (applying a positive or a negative voltage on the LNO₃ electrode side, respectively). A surprising relaxation behaviour has been measured where the device alternatively changes its resistance from lower to higher and from higher to lower values after applying a positive or a negative voltage stress, respectively;
 - Resistance states lying both higher and lower than the IRS of the device could be programmed. The current resistance state of the device and its response to a

new electric stimuli depends on a large part - if not entirely - on its programming history.

Although LNO3 has been selected as electrode material mainly due to its good electronic conductivity and lattice match with L2NO4 (needed for the growth of epitaxial L2NO4/LNO3 bilayers), the exact nature of the L2NO4/LNO3 junction still requires a lot of attention. Indeed, as the electrical properties of the two materials depend on their oxygen content, a range of electrical contacts from ohmic to highly Schottky could (in theory) be obtained. This, combined with the similar chemistry of the two materials, offers a huge playground for controlled oxygen storage/release (at least locally at the interface between the two materials) which is promising for interface-type VCM applications.

Concluding summary & perspectives

Valence-change memories (VCMs) are in essence electrochemical systems based on a metal oxide capacitor-like structure with electrodes of different oxygen affinity and/or work function and migrating defects. Their implementation in micro/nanoelectronic solid state devices relies on an electronic readout to measure the state of the device and to operate them, but their functionality highly depends on the chemical properties of the materials constituting the final device. Oxygen-ion motion and its subsequent oxidation/reduction reactions are key parameters that need to be controlled in order to improve the properties of this type of memories. This thesis has addressed the need for a rational design of interface-type VCMs by choosing a mixed ionic-electronic conducting material, as is the case of $\text{La}_2\text{NiO}_{4+\delta}$, as the functional layer around which the memristive device is constructed. The intrinsic bulk oxygen-ion conduction properties of $\text{La}_2\text{NiO}_{4+\delta}$, combined with the important range of oxygen overstoichiometry ($0 \leq \delta \leq 0.26$) it can accommodate within its structure without decomposing makes it an interesting playground for VCMs.

L2NO4 was successfully prepared in the form of highly textured thin films on perovskite single crystal substrates (STO, NGO and LAO) using pulsed-injection chemical vapour deposition ($T = 650 \text{ }^\circ\text{C}$, $p = 5 \text{ Torr}$, 63% O_2 /34% Ar gas mixture). The presence of 4 to 7 unit cells of LNO3 at the L2NO4/STO interface could be observed by HRTEM. The interlayer is absent when L2NO4 is grown on NGO or LAO substrates, meaning that the presence or absence of this interlayer could be attributed to a relaxation mechanism of the tensile strain induced by the clamping of L2NO4 on STO. A domain reorientation from $c_{L2NO4, \perp}$ (c -axis of tetragonal L2NO4 perpendicular to the substrates surface) to $c_{L2NO4, \parallel}$ (c -axis parallel) was shown when L2NO4 is grown on STO after a critical film thickness of $\sim 30 \text{ nm}$. The domain reorientation seems to be very favourable from an epitaxial point of view as it generates seemingly defect-free twin boundaries. An important effect of the oxygen content in $\text{La}_2\text{NiO}_{4+\delta}$ on its resistivity was measured ($\rho = 5.3 \times 10^{-3} \text{ } \Omega \cdot \text{cm}$, $1.1 \times 10^{-2} \text{ } \Omega \cdot \text{cm}$, $1.3 \times 10^{-2} \text{ } \Omega \cdot \text{cm}$ and $5.7 \text{ } \Omega \cdot \text{cm}$ for a δ overstoichiometry of approximately 0.08, 0.04, 0.03 and 0, respectively). The oxygen content was successfully tuned with post annealing treatments (1 h at $500 \text{ }^\circ\text{C}$ under O_2 , Ar or $\text{H}_2(6\%)/\text{Ar}$ gas atmospheres). The incorporation of oxygen in L2NO4 has a direct effect

on its structural lattice parameters (*e.g.* expansion of the *c*-axis). The increase in hole carriers through a self-doping mechanism was confirmed by measuring the work function of two L2NO4 films ($W_F = 4.1$ eV and 4.3 eV for pristine and oxygen-annealed L2NO4, respectively).

The optimized L2NO4 films have been used to prepare M/L2NO4/M heterostructures (M = Pt, Ag or Ti metallic electrodes prepared in cleanroom facilities by e-beam evaporation after a mild Ar-etch surface treatment). An ohmic contact is obtained when evaporating Pt (high work function) on L2NO4 while a slightly more resistive Schottky-like contact is obtained with Ag (low work function), consistent with a *p*-type Schottky contact model with L2NO4. Devices built with at least one Ti electrode also showed Schottky-like characteristics with an important increase in resistance. TLM experiments allowed calculating a relatively small Pt/L2NO4 contact resistance ($20 \Omega - 30 \Omega$), which is almost independent on the electrical properties of L2NO4. The transfer length (also extracted from the TLM) shows that lower resistivity values of L2NO4 are beneficial for a more homogeneous current injection throughout the Pt/L2NO4 junction (in the ‘top-top’ electrode configuration). The presence of an amorphous and likely oxygen-deficient TiO_x interlayer at the Ti/L2NO4 interface has been confirmed by HRTEM. This interlayer formed spontaneously when evaporating the Ti electrodes. Temperature measurements (in the 300 K-180 K range) showed that the conduction mechanism measured for the Pt/L2NO4 junction is almost temperature independent ($E_a \sim 10$ meV). However, the presence of a Ti contact highly affects the conduction mechanism and increases its temperature dependence. The activation energy increases ($E_a \sim 150$ meV) and depends on the temperature range that is considered (change of slope in the Arrhenius plot around 230 K). An evolution of the conduction mechanism from TAT at high temperature to direct tunnelling (when $T < 230$ K) has been proposed to explain this phenomenon. The newly formed TiO_x interlayer could act as the tunnelling barrier.

After having investigated the electrical properties of several M/L2NO4/M heterostructures, an asymmetric Pt/L2NO4/Ti was selected as a prototype to study the memory properties of L2NO4-based memristive device, as Ti is already known for its reactivity and oxygen storage capabilities. An initialisation step (application of a negative voltage on the Pt electrode) is required to trigger reproducible memristive characteristics. This initialisation step is, however, different from the more classical electroforming step, as the applied voltage does not need to be higher than the operation voltage. Highly reproducible analog-type $I(V)$ characteristics have been obtained after initialisation when cycling the device between ± 5 V. The LRS and HRS are separated by roughly one order of magnitude in resistance. Successive unipolar voltage sweeps ($0 \text{ V} \rightarrow -5 \text{ V} \rightarrow 0 \text{ V}$) can gradually increase the resistance state above the HRS until saturation. The presence of interstitial oxygen ions in L2NO4 are beneficial, and even neces-

sary to give rise to the memristive properties. A precise interplay between the TiO_x interlayer thickness, as well as its stoichiometry and homogeneity, and the oxygen content of L2NO4 are certainly crucial parameters that need to be controlled to tune the resistance-change and the retention characteristics of a Pt/L2NO4/Ti memristive device. Furthermore, highly multilevel and bipolar memory characteristics can be obtained when operating the device in pulsed-mode ($[-15 \text{ V}; 1 \text{ ms}]$ and $[+7 \text{ V}; 1 \text{ ms}]$ pulses to obtain a gradual SET or RESET of the device, respectively). A spontaneous relaxation (decrease of the resistance to LRS) has been measured when programming the device to a HRS, which is potentially interesting to study hardware-based and on-chip neuromorphic computation for real-time information processing. The gradual resistance-change behaviour (named here ‘GRC’) allows the device to transition from LRS to HRS and has been proposed as being an important marker of mass-transport limited redox-reactions, giving rise to the highly multilevel analog-type memory properties of the device. Reports on the mechanism leading to a GRC in literature can be roughly divided into two categories: ‘electrochemical’ and ‘charge trapping/detrapping’. We propose that these two mechanisms coexist, that the accumulation of oxygen ions at the $\text{Ti/TiO}_x/\text{L2NO4}$ junction play the role of the charge traps. The self-limiting nature of the GRC could be explained by mass transport-limited redox-reactions occurring at the metal/oxide interface.

The deposition optimization of metallic LNO3 thin films by PiMOCVD was carried out in order to prepare L2NO4/LNO3 bilayers for ‘top-bottom’ memristive architectures. The perovskite LNO3 is a suitable candidate for a template bottom electrode material due to its good electrical conductivity (resistivity values as low as $90 \mu\Omega\cdot\text{cm}$ have been reported in literature), as well as its good lattice match both with STO ($< 1.70 \%$) used as substrate material and L2NO4 ($< 0.50 \%$) grown on top, allowing the growth of highly-oriented L2NO4 films. Furthermore, the oxygen exchange between L2NO4 and LNO3 first reported by Moreno *et al.* [88] makes this system particularly interesting for VCM applications. LNO3 thin films with a high crystal quality were obtained on LAO for $\text{La/Ni} = 2.38$ in the precursor solution and $T = 550^\circ\text{C}$, with a film resistivity of $\sim 200 \mu\Omega\cdot\text{cm}$. A lower LNO3 film quality was obtained when grown on STO , due to the presence of (in some cases percolating) insulating NiO impurities. These impurities have been studied in detail by XRD and TEM, showing that they could be at the origin of some of the other defects observed in the films, such as LNO3 domain reorientations and/or L2NO4 precipitates. Pure (impurity-free) LNO3/STO samples were however successfully prepared in the framework of a collaboration with ICN2 in Barcelona (Spain). While L2NO4/LNO3 bilayers deposited by PiMOCVD require further optimization, the electrical properties of such complex-oxide heterostructures could be readily measured using samples prepared by PLD. An asymmetric Pt/LNO3/L2NO4/Pt memristive device in its IRS showed a small nonlinearity in the measured $I(V)$ characteristics. This nonlinearity at low voltage was

attributed to the LNO3/L2NO4 junction as Pt/LNO3 and Pt/L2NO4 both showed ohmic characteristics when measured in the same voltage range. A reproducible analog-type memristive behaviour was obtained in this asymmetric Pt/LNO3/L2NO4/Pt device after initialisation (setting the device in HRS). The programmed HRS is volatile. Voltage stresses with opposite polarities could reversibly RESET and SET the device in a lower or higher resistance state (applying a positive or a negative voltage on the LNO3 electrode side, respectively). The resistance state of the device and its response to a new electric stimuli highly depends on its programming history.

This thesis has showed that there is a large interest in studying complex-oxide materials, and mixed conductors in particular, for their use in VCM-based applications. An extensive and systematic device characterisation (varying for example the doping level, the film thickness, the surface preparation before electrode evaporation, etc) is still required to shine light on the very gradual analog-type resistance change characteristics measured in these L2NO4-based systems. It should be pointed out that our current understanding of the memory properties of L2NO4-based memristive devices is based only on strong experimental evidence. The further demonstration and completion of the model requires a complex simulation work, using for example a mobile dopant model to take into account the local self-doping induced by migrating oxygen interstitial ions in the L2NO4 lattice (and into the metallic electrode material).

While this idea was always present in the back of my mind, I did not find the time during this thesis to investigate the geopolitical and environmental aspects behind the extraction of rare-earth metals such as La. Although at this first stage L2NO4 was selected and studied as a prototypical memristive material due to its mixed ionic and electronic properties, if such a material were to become technologically viable these considerations should be receiving much more attention, in particular while no proper way of recycling the manufactured devices has been discovered. The toxicity of Ni should also be assessed.

Concerning the implications of hardware-based neuromorphic technologies briefly discussed in this thesis, while the field of artificial intelligence is fascinating and could highly improve our overall standard of living, too often social considerations are lacking behind the so-called ‘technological progress’. These aspects are, to my humble opinion, topics that should be receiving increased attention and should be discussed more openly and more often. Sometimes the conclusion should be drawn that the society is not yet ready for a certain technology, and pushing through that technology (usually for economical reasons) would just increase social inequities and tensions, leading to an unstable future. Throughout my studies, I realized that becoming a specialist in a certain discipline tends to make you relativize the implications of your research on society. As an illustration, specialists in the field of genetics might genuinely believe and already spread the idea that with the right tweaks to our genome,

we could for example eradicate all the diseases that have been and will ever be present on this planet. While this is a noble cause, as long as social inequities are present in our highly competitive societies, the likelihood of this type of human augmentation technology enabling a peaceful and ethical future seems uncertain to say the least. The same goes for artificial intelligence, and even more so *general* artificial intelligence. While it could potentially address beyond human-solvable problems such as climate-change, using it to create riches (or for military and war purposes) instead and further spread social inequities would also certainly render our future on this planet challenging. It is of the uppermost importance that these questions enter the political sphere as it is difficult to predict how fast these technologies will mature and become largely available without proper regulations.

References

- [1] W Román Acevedo, C Ferreyra, M J Sánchez, C Acha, R Gay, and D Rubi. 2018. Concurrent ionic migration and electronic effects at the memristive $\text{TiO}_x/\text{La}_{1/3}\text{Ca}_{2/3}\text{MnO}_{3-x}$ interface. *J. Phys. D. Appl. Phys.* 51, 12 (2018), 125304. <https://doi.org/10.1088/1361-6463/aaaed6> 50
- [2] Taner Akbay, Aleksandar Staykov, John Druce, Helena Téllez, Tatsumi Ishihara, and John A. Kilner. 2016. The interaction of molecular oxygen on LaO terminated surfaces of La_2NiO_4 . *J. Mater. Chem. A* 4, 34 (2016), 13113–13124. <https://doi.org/10.1039/C6TA02715F> 20
- [3] Yoshitaka Aoki, Carsten Wiemann, Vitaliy Feyer, Hong-Seok Kim, Claus Michael Schneider, Han Ill-Yoo, and Manfred Martin. 2014. Bulk mixed ion electron conduction in amorphous gallium oxide causes memristive behaviour. *Nat. Commun.* 5, 1 (dec 2014), 3473. <https://doi.org/10.1038/ncomms4473> 9
- [4] S. Asanuma, H. Akoh, H. Yamada, and A. Sawa. 2009. Relationship between resistive switching characteristics and band diagrams of $\text{Ti}/\text{Pr}_{1-x}\text{Ca}_x\text{MnO}_3$ junctions. *Phys. Rev. B* 80, 23 (2009), 235113. <https://doi.org/10.1103/PhysRevB.80.235113> 50
- [5] ASML. [n. d.]. webpage: the TWINSCAN NXE:3400B, accessing the 7 and 5 nm technology nodes. <https://www.asml.com/products/en/s46772?dfp{ }product{ }id=10850> 5
- [6] P. L. Bach, J. M. Vila-Funqueiriño, V. Leborán, Elías Ferreiro-Vila, B. Rodríguez-González, and F. Rivadulla. 2013. Strain-induced enhancement of the thermoelectric power in thin films of hole-doped $\text{La}_2\text{NiO}_{4+\delta}$. *APL Mater.* 1, 2 (aug 2013), 021101. <https://doi.org/10.1063/1.4818356> 30, 38
- [7] I.G. Baek, M.S. Lee, S. Sco, M.J. Lee, D.H. Seo, D.-S. Suh, J.C. Park, S.O. Park, H.S. Kim, I.K. Yoo, U.-I. Chung, and J.T. Moon. 2004. Highly scalable non-volatile resistive memory using simple binary oxide driven by asymmetric unipolar voltage

- pulses. *IEDM Tech. Dig. IEEE Int. Electron Devices Meet. 2004.* (2004), 587–590. <https://doi.org/10.1109/IEDM.2004.1419228> 8
- [8] Kyungjoon Baek, Sangsu Park, Jucheol Park, Young Min Kim, Hyunsang Hwang, and Sang Ho Oh. 2017. In situ TEM observation on the interface-type resistive switching by electrochemical redox reactions at a TiN/PCMO interface. *Nanoscale* 9, 2 (2017), 582–593. <https://doi.org/10.1039/c6nr06293h> 10
- [9] Christoph Baeumer, Christoph Schmitz, Amr H. H. Ramadan, Hongchu Du, Katharina Skaja, Vitaliy Feyer, Philipp Müller, Benedikt Arndt, Chun-Lin Jia, Joachim Mayer, Roger a. De Souza, Claus Michael Schneider, Rainer Waser, and Regina Dittmann. 2015. Spectromicroscopic insights for rational design of redox-based memristive devices. *Nat. Commun.* 6 (2015), 8610. <https://doi.org/10.1038/ncomms9610> 27
- [10] S. Bagdzevicius, K. Maas, M. Boudard, and M. Burriel. 2017. Interface-type resistive switching in perovskite materials. *J. Electroceramics* 39, 1-4 (dec 2017), 157–184. <https://doi.org/10.1007/s10832-017-0087-9> 7, 8, 42, 43
- [11] J Bassat. 2004. Anisotropic ionic transport properties in $\text{La}_2\text{NiO}_{4+\delta}$ single crystals. *Solid State Ionics* 167, 3-4 (feb 2004), 341–347. <https://doi.org/10.1016/j.ssi.2003.12.012> 20, 21, 22, 23, 26
- [12] J.M. Bassat, F. Gervais, P. Odier, and J.P. Loup. 1989. Anisotropic transport properties of La_2NiO_4 single crystals. *Mater. Sci. Eng. B* 3, 4 (sep 1989), 507–514. [https://doi.org/10.1016/0921-5107\(89\)90164-5](https://doi.org/10.1016/0921-5107(89)90164-5) 23, 25
- [13] J.M. Bassat, P. Odier, and J.P. Loup. 1994. The Semiconductor-to-Metal Transition in Question in $\text{La}_{2-x}\text{NiO}_{4+\delta}$ ($\delta > 0$ or $\delta < 0$). *J. Solid State Chem.* 110, 1 (may 1994), 124–135. <https://doi.org/10.1006/jssc.1994.1146> 25
- [14] J M Bassat, J P Loup, and P Odier. 1994. Progressive change with T from hopping to random phase propagation in $\text{La}_{2-x}\text{NiO}_{4-\delta}$ ($\delta > \text{or} = 0$). *J. Phys. Condens. Matter* 6, 40 (oct 1994), 8285–8293. <https://doi.org/10.1088/0953-8984/6/40/019> 25
- [15] Frances E. Bates and J.E. Eldridge. 1989. Normal modes of tetragonal La_2NiO_4 and La_2CuO_4 , isomorphs of the high T_c superconductor $\text{La}_{2-x}\text{Sr}_x\text{CuO}_4$. *Solid State Commun.* 72, 2 (oct 1989), 187–190. [https://doi.org/10.1016/0038-1098\(89\)90520-6](https://doi.org/10.1016/0038-1098(89)90520-6) 173
- [16] Radu Berdan, Eleni Vasilaki, Ali Khiat, Giacomo Indiveri, Alexandru Serb, and Themistoklis Prodromakis. 2015. Emulating short-term synaptic dynamics with

- memristive devices. *Sci. Rep.* 6, November 2015 (jul 2015), 18639. <https://doi.org/10.1038/srep18639> arXiv:1507.02066 85
- [17] R.N. Bhowmik and K. Venkata Siva. 2018. Non-equilibrium character of resistive switching and negative differential resistance in Ga-doped Cr₂O₃ system. *J. Magn. Mater.* 457 (2018), 17–29. <https://doi.org/10.1016/j.jmmm.2018.02.070> 86
- [18] E. Boehm, J. M. Bassat, P. Dordor, F. Mauvy, J. C. Grenier, and Ph Stevens. 2005. Oxygen diffusion and transport properties in non-stoichiometric Ln_{2-x}NiO_{4+δ} oxides. *Solid State Ionics* 176, 37-38 (nov 2005), 2717–2725. <https://doi.org/10.1016/j.ssi.2005.06.033> 21
- [19] Francesco Borgatti, Chanwoo Park, Anja Herpers, Francesco Offi, Ricardo Egoavil, Yoshiyuki Yamashita, Anli Yang, Masaaki Kobata, Keisuke Kobayashi, Jo Verbeeck, Giancarlo Panaccione, and Regina Dittmann. 2013. Chemical insight into electroforming of resistive switching manganite heterostructures. *Nanoscale* 5, 9 (2013), 3954–3960. <https://doi.org/10.1039/c3nr00106g> arXiv:_barata Materials and Techniques of polychrome wooden sculpture 50, 56
- [20] Mónica Burriel, Gemma Garcia, Marta D. Rossell, Albert Figueras, Gustaaf Van Tendeloo, and José Santiso. 2007. Enhanced High-Temperature Electronic Transport Properties in Nanostructured Epitaxial Thin Films of the Ln_{n+1}Ni_nO_{3n+1} Ruddlesden-Popper Series (n = 1, 2, 3, inf). *Chem. Mater.* 19, 16 (aug 2007), 4056–4062. <https://doi.org/10.1021/cm070804e> 16, 97
- [21] M Burriel, G Garcia, J Santiso, J A Kilner, R J Chater, and S J Skinner. 2008. Anisotropic oxygen diffusion properties in epitaxial thin films of La₂NiO_{4+δ}. *J. Mater. Chem.* 18, 4 (2008), 416–422. <https://doi.org/10.1039/b711341b> 21, 26
- [22] Mónica Burriel, Helena Téllez, Richard J. Chater, Rémi Castaing, Philippe Veber, Mustapha Zaghrioui, Tatsumi Ishihara, John A. Kilner, and Jean-Marc Bassat. 2016. Influence of Crystal Orientation and Annealing on the Oxygen Diffusion and Surface Exchange of La₂NiO_{4+δ}. *J. Phys. Chem. C* 120, 32 (aug 2016), 17927–17938. <https://doi.org/10.1021/acs.jpcc.6b05666> 21, 23
- [23] Mónica Burriel López. 2007. *Epitaxial thin films of lanthanum nikel oxides: deposition by PI-MOCVD, structural characterization and high temperature transport properties*. Ph.D. Dissertation. 155

- [24] Yunyu Cai, Qinglin Yuan, Yixing Ye, Jun Liu, and Changhao Liang. 2016. Coexistence of resistance switching and negative differential resistance in the α -Fe₂O₃ nanorod film. *Phys. Chem. Chem. Phys.* 18, 26 (2016), 17440–17445. <https://doi.org/10.1039/C6CP02192A> 87
- [25] N. Chaban, M. Weber, S. Pignard, and J. Kreisel. 2010. Phonon- @ -Raman scattering of perovskite LaNiO₃ thin films. *Appl. Phys. Lett.* 97, 3 (2010). <https://doi.org/10.1063/1.3464958> arXiv:1006.0103 97, 171
- [26] Yang Yin Chen, Ludovic Goux, Sergiu Clima, Bogdan Govoreanu, Robin Degraeve, Gouri Sankar Kar, Andrea Fantini, Guido Groeseneken, Dirk J Wouters, and Malgorzata Jurczak. 2013. Endurance/Retention Trade-off on HfO₂/Metal Cap1T1R Bipolar RRAM. *IEEE Trans. Electron Devices* 60, 3 (mar 2013), 1114–1121. <https://doi.org/10.1109/TED.2013.2241064> 10
- [27] Fu-chien Chiu. 2014. A Review on Conduction Mechanisms in Dielectric Films. *Adv. Mater. Sci. Eng.* 2014 (2014), 1–18. <https://doi.org/10.1155/2014/578168> 42, 193
- [28] F. C. Chou and D. C. Johnston. 1996. Phase separation and oxygen diffusion in electrochemically oxidized La₂CuO₄+d: A static magnetic susceptibility study. *Phys. Rev. B* 54, 1 (jul 1996), 572–583. <https://doi.org/10.1103/PhysRevB.54.572> 26
- [29] Alexander Chroneos, David Parfitt, John A. Kilner, and Robin W. Grimes. 2010. Anisotropic oxygen diffusion in tetragonal La₂NiO₄+ δ : molecular dynamics calculations. *J. Mater. Chem.* 20, 2 (2010), 266–270. <https://doi.org/10.1039/B917118E> 21, 24
- [30] L. Chua. 1971. Memristor-The missing circuit element. *IEEE Trans. Circuit Theory* 18, 5 (apr 1971), 507–519. <https://doi.org/10.1109/TCT.1971.1083337> arXiv:10.1109/TCT.1971.1083337 5
- [31] A.R. Cleave, J.A. Kilner, S.J. Skinner, S.T. Murphy, and R.W. Grimes. 2008. Atomistic computer simulation of oxygen ion conduction mechanisms in La₂NiO₄. *Solid State Ionics* 179, 21-26 (sep 2008), 823–826. <https://doi.org/10.1016/j.ssi.2008.04.013> 23
- [32] A de Andres, M T Fernandez-Diaz, J L Martinez, J Rodriguez-Carvajal, R Saez-Puche, and F Fernandez. 1991. Raman scattering of orthorhombic and tetragonal Ln₂NiO₄+ δ (Ln identical to La,Pr,Nd) oxides. *J. Phys. Condens. Matter* 3, 21 (may 1991), 3813–3823. <https://doi.org/10.1088/0953-8984/3/21/014> 173

- [33] Roger A. De Souza. 2017. Limits to the rate of oxygen transport in mixed-conducting oxides. *J. Mater. Chem. A* 5 (2017), 20334–20350. <https://doi.org/10.1039/C7TA04266C> 10, 12
- [34] A. Demourgues, P. Dordor, J.-P. Doumerc, J.-C. Grenier, E. Marquestaut, M. Pouchard, A. Villesuzanne, and A. Wattiaux. 1996. Transport and Magnetic Properties of $\text{La}_2\text{NiO}_{4+\delta}$ ($0 < \delta < 0.25$). *J. Solid State Chem.* 124, 2 (jul 1996), 199–204. <https://doi.org/10.1006/jssc.1996.0226> 25
- [35] Pan-Yue Deng and Vitaly A. Klyachko. 2011. The diverse functions of short-term plasticity components in synaptic computations. *Commun. Integr. Biol.* 4, 5 (sep 2011), 543–548. <https://doi.org/10.4161/cib.15870> 85
- [36] Y. Dobin, R. Nikolaev, N. Krivorotov, D. Dahlberg, M. Goldman, and M. Wentzcovitch. 2003. Electronic and crystal structure of fully strained LaNiO_3 films. *Phys. Rev. B - Condens. Matter Mater. Phys.* 68, 11 (2003), 3–7. <https://doi.org/10.1103/PhysRevB.68.113408> 97
- [37] J. Drennan, C.P. Tavares, and B.C.H. Steele. 1982. An electron microscope investigation of phases in the system La-Ni-O. *Mater. Res. Bull.* 17, 5 (may 1982), 621–626. [https://doi.org/10.1016/0025-5408\(82\)90044-7](https://doi.org/10.1016/0025-5408(82)90044-7) 177
- [38] Yuanmin Du, Hui Pan, Shijie Wang, Tom Wu, Yuan Ping Feng, Jisheng Pan, and Andrew Thye Shen Wee. 2012. Symmetrical negative differential resistance behavior of a resistive switching device. *ACS Nano* 6, 3 (2012), 2517–2523. <https://doi.org/10.1021/nn204907t> 86, 88
- [39] Christine Frayret, Antoine Villesuzanne, and Michel Pouchard. 2005. Application of density functional theory to the modeling of the mixed ionic and electronic conductor $\text{La}_2\text{NiO}_{4+\delta}$: Lattice relaxation, oxygen mobility, and energetics of Frenkel defects. *Chem. Mater.* 17, 26 (2005), 6538–6544. <https://doi.org/10.1021/cm050195f> 20
- [40] Ella Gale. 2011. The Memory-Conservation Theory of Memristance. (2011). arXiv:1106.3170 <http://arxiv.org/abs/1106.3170> 6
- [41] Xu Gao, Yidong Xia, Jianfeng Ji, Hanni Xu, Yi Su, Haitao Li, Chunjun Yang, Hongxuan Guo, Jiang Yin, and Zhiguo Liu. 2010. Effect of top electrode materials on bipolar resistive switching behavior of gallium oxide films. *Appl. Phys. Lett.* 97, 19 (nov 2010), 193501. <https://doi.org/10.1063/1.3501967> 13, 87

- [42] Gemma Garcia, Jaume Caro, José Santiso, José a. Pardo, Albert Figueras, and Adulfus Abrutis. 2003. Pulsed injection MOCVD of YSZ thin films onto dense and porous substrates. *Chem. Vap. Depos.* 9, 5 (2003), 279–284. <https://doi.org/10.1002/cvde.200306253> 155
- [43] J. L. García-Muñoz, J. Rodríguez-Carvajal, P. Lacorre, and J. B. Torrance. 1992. Neutron-diffraction study of RNiO₃ (R=La,Pr,Nd,Sm): Electronically induced structural changes across the metal-insulator transition. *Phys. Rev. B* 46, 8 (1992), 4414–4425. <https://doi.org/10.1103/PhysRevB.46.4414> 97
- [44] Gary A. Gibson. 2018. Designing Negative Differential Resistance Devices Based on Self-Heating. *Adv. Funct. Mater.* 28, 22 (2018), 1–9. <https://doi.org/10.1002/adfm.201704175> 85
- [45] J. B. Goodenough and S. Ramasesha. 1982. Further evidence for the coexistence of localized and itinerant 3d electrons in La₂NiO₄. *Mater. Res. Bull.* 17, 3 (1982), 383–390. [https://doi.org/10.1016/0025-5408\(82\)90089-7](https://doi.org/10.1016/0025-5408(82)90089-7) 60
- [46] P. Gopalan, M. W. McElfresh, Z. Kalškol, J. Spal/ek, and J. M. Honig. 1992. Influence of oxygen stoichiometry on the antiferromagnetic ordering of single crystals of La₂NiO_{4+d}. *Phys. Rev. B* 45, 1 (jan 1992), 249–255. <https://doi.org/10.1103/PhysRevB.45.249> 25
- [47] O.Yu Gorbenko and a.a Bosak. 1998. Growth of LaNiO₃ thin films on MgO by flash MOCVD. *J. Cryst. Growth* 186, 1-2 (1998), 181–188. [https://doi.org/10.1016/S0022-0248\(97\)00454-5](https://doi.org/10.1016/S0022-0248(97)00454-5) 97
- [48] Gaoyang Gou, Ilya Grinberg, Andrew M. Rappe, and James M. Rondinelli. 2011. Lattice normal modes and electronic properties of the correlated metal LaNiO₃. *Phys. Rev. B - Condens. Matter Mater. Phys.* 84, 14 (2011), 1–13. <https://doi.org/10.1103/PhysRevB.84.144101> arXiv:1105.0198 171
- [49] H. Guo, Z. W. Li, L. Zhao, Z. Hu, C. F. Chang, C. Y. Kuo, W. Schmidt, A. Piovano, T. W. Pi, O. Sobolev, D. I. Khomskii, L. H. Tjeng, and A. C. Komarek. 2017. Antiferromagnetic correlations in the metallic strongly correlated transition metal oxide LaNiO₃. *Nat. Commun.* 9, 1 (may 2017), 43. <https://doi.org/10.1038/s41467-017-02524-x> arXiv:1705.02589 97
- [50] H. Han, J. Zhong, S. Kotru, P. Padmini, X. Y. Song, and R. K. Pandey. 2006. Improved ferroelectric property of LaNiO₃/Pb(Zr_{0.2}Ti_{0.8})O₃/LaNiO₃ capacitors prepared by

- chemical solution deposition on platinized silicon. *Appl. Phys. Lett.* 88, 9 (2006), 092902. <https://doi.org/10.1063/1.2180878> 97
- [51] Musarrat Hasan, Rui Dong, H J Choi, D S Lee, M B Pyun, and Hyunsang Hwang. 2008. Uniform resistive switching with a thin reactive metal interface layer. *Appl. Phys. Lett.* 202102, 20 (2008), 202102. <https://doi.org/10.1063/1.2932148> 8
- [52] Akihiko Hayashi, Hiroyasu Tamura, and Yutaka Ueda. 1993. Successive structural phase transitions in stoichiometric La₂NiO₄ observed by X-ray diffraction. *Phys. C Supercond. its Appl.* 216, 1-2 (1993), 77–82. [https://doi.org/10.1016/0921-4534\(93\)90635-4](https://doi.org/10.1016/0921-4534(93)90635-4) 16
- [53] Anja Herpers, Christian Lenser, Chanwoo Park, Francesco Offi, Francesco Borgatti, Giancarlo Panaccione, Stephan Menzel, Rainer Waser, and Regina Dittmann. 2014. Spectroscopic proof of the correlation between redox-state and charge-carrier transport at the interface of resistively switching Ti/PCMO devices. *Adv. Mater.* 26, 17 (2014), 2730–2735. <https://doi.org/10.1002/adma.201304054> 50
- [54] T. W. Hickmott. 1962. Low-Frequency Negative Resistance in Thin Anodic Oxide Films. *J. Appl. Phys.* 33, 9 (sep 1962), 2669–2682. <https://doi.org/10.1063/1.1702530> 6
- [55] Zenji Hiroi, Takeshi Obata, Mikio Takano, Yoshichika Bando, Yasuo Takeda, and Osamu Yamamoto. 1990. Ordering of interstitial oxygen atoms in La₂NiO₄ observed by transmission electron microscopy. *Phys. Rev. B* 41, 16 (jun 1990), 11665–11668. <https://doi.org/10.1103/PhysRevB.41.11665> 20
- [56] LeVan Hong, TranDang Thanh, DaoNguyen Nam, NguyenChi Thuan, and NguyenXuan Phuc. 2008. Switching and Electrical Memory Effect in the Colossal Permittivity Material La₂NiO_{4+d}. *J. Korean Phys. Soc.* 53, 9(5) (nov 2008), 2582–2586. <https://doi.org/10.3938/jkps.53.2582> 85
- [57] M. Hücker, K. Chung, M. Chand, T. Vogt, J. M. Tranquada, and D. J. Buttrey. 2004. Oxygen and strontium codoping of La₂NiO₄: Room-temperature phase diagrams. *Phys. Rev. B* 70, 6 (aug 2004), 064105. <https://doi.org/10.1103/PhysRevB.70.064105> arXiv:cond-mat/0312421 18, 19
- [58] Kyu Seog Hwang, Seon Suk Min, and Yeong Joon Park. 2001. Formation of highly-oriented and polycrystalline lanthanum nickelate films by a spin coating-pyrolysis

- process. *Surf. Coatings Technol.* 137, 2-3 (2001), 205–208. [https://doi.org/10.1016/S0257-8972\(00\)01123-3](https://doi.org/10.1016/S0257-8972(00)01123-3) 97
- [59] Intel. [n. d.]. webpage: The Story of the Intel 4004, Intel's First Microprocessor (<https://www.intel.com/content/www/us/en/history/museum-story-of-intel-4004.html>, accessed 2018-11-19). <https://www.intel.com/content/www/us/en/history/museum-story-of-intel-4004.html> 4
- [60] K Ishikawa, W Shibata, K Watanabe, T Isonaga, M Hashimoto, and Y Suzuki. 1997. Metal - Semiconductor Transition of $\text{La}_2\text{NiO}_{4+\delta}$. *J. Solid State Chem.* 131, 2 (jul 1997), 275–281. <https://doi.org/10.1006/jssc.1997.7375> 25
- [61] M. Jain, N. K. Karan, J. Yoon, H. Wang, I. Usov, R. S. Katiyar, A. S. Bhalla, and Q. X. Jia. 2007. High tunability of lead strontium titanate thin films using a conductive LaNiO_3 as electrodes. *Appl. Phys. Lett.* 91, 7 (2007), 1–4. <https://doi.org/10.1063/1.2770962> 97
- [62] Moon Hyung Jang, Rahul Agarwal, Pavan Nukala, Dooho Choi, A. T. Charlie Johnson, I. Wei Chen, and Ritesh Agarwal. 2016. Observing Oxygen Vacancy Driven Electroforming in Pt-TiO₂-Pt Device via Strong Metal Support Interaction. *Nano Lett.* 16, 4 (apr 2016), 2139–2144. <https://doi.org/10.1021/acs.nanolett.5b02951> 66
- [63] Doo Seok Jeong, Byung Joon Choi, and Cheol Seong Hwang. 2016. Electroforming Processes in Metal Oxide Resistive-Switching Cells. In *Resist. Switch.* Wiley-VCH Verlag GmbH & Co. KGaA, Weinheim, Germany, 289–316. <https://doi.org/10.1002/9783527680870.ch10> 12, 13
- [64] Doo Seok Jeong, Herbert Schroeder, Uwe Breuer, and Rainer Waser. 2008. Characteristic electroforming behavior in Pt/TiO₂/Pt resistive switching cells depending on atmosphere. *J. Appl. Phys.* 104, 12 (2008). <https://doi.org/10.1063/1.3043879> 12, 86, 91
- [65] C. H. Jia, X. W. Sun, G. Q. Li, Y. H. Chen, and W. F. Zhang. 2014. Origin of attendant phenomena of bipolar resistive switching and negative differential resistance in $\text{SrTiO}_3\text{:Nb/ZnO}$ heterojunctions. *Appl. Phys. Lett.* 104, 4 (jan 2014), 043501. <https://doi.org/10.1063/1.4863505> 87
- [66] J. D. Jorgensen, B. Dabrowski, Shiyu Pei, D. G. Hinks, L. Soderholm, B. Morosin, J. E. Schirber, E. L. Venturini, and D. S. Ginley. 1988. Superconducting phase of $\text{La}_2\text{CuO}_{4+d}$. A superconducting composition resulting from phase separation. *Phys.*

- Rev. B* 38, 16 (dec 1988), 11337–11345. <https://doi.org/10.1103/PhysRevB.38.11337> 26
- [67] J. D. Jorgensen, B. Dabrowski, Shiyong Pei, D. R. Richards, and D. G. Hinks. 1989. Structure of the interstitial oxygen defect in $\text{La}_2\text{NiO}_{4+d}$. *Phys. Rev. B* 40, 4 (aug 1989), 2187–2199. <https://doi.org/10.1103/PhysRevB.40.2187> 16, 18, 20, 25, 26
- [68] J. Joshua Yang, Feng Miao, Matthew D. Pickett, Douglas A A Ohlberg, Duncan R. Stewart, Chun Ning Lau, and R. Stanley Williams. 2009. The mechanism of electroforming of metal oxide memristive switches. *Nanotechnology* 20, 21 (may 2009), 215201. <https://doi.org/10.1088/0957-4484/20/21/215201> 10, 12, 13
- [69] Woo-hwan Jung. 2013. Dielectric Relaxation and Hopping Conduction in $\text{La}_2\text{NiO}_{4+d}$. *J. Mater.* 2013 (feb 2013), 1–6. <https://doi.org/10.1155/2013/169528> 25
- [70] Vladislav V Kharton, Alexandre P Viskup, Eugene N Naumovich, and Fernando M B Marques. 1999. Oxygen ion transport in La_2NiO_4 -based ceramics. *J. Mater. Chem.* 9, 10 (1999), 2623–2629. <https://doi.org/10.1039/a903276b> 21, 25
- [71] John A. Kilner and Mónica Burriel. 2014. Materials for Intermediate-Temperature Solid-Oxide Fuel Cells. *Annu. Rev. Mater. Res.* 44, 1 (jul 2014), 365–393. <https://doi.org/10.1146/annurev-matsci-070813-113426> 27
- [72] Kuk-hwan Kim. 2011. *High Density Crossbar Structure for Memory Application*. Ph.D. Dissertation. 4
- [73] Sun Gil Kim, Ji Su Han, Hyojung Kim, Soo Young Kim, and Ho Won Jang. 2018. Recent Advances in Memristive Materials for Artificial Synapses. *Adv. Mater. Technol.* 1800457 (nov 2018), 1800457. <https://doi.org/10.1002/admt.201800457> 2, 3, 85
- [74] P D C King, H I Wei, Y F Nie, M Uchida, C Adamo, S Zhu, X He, I Bozovic, D G Schlom, and K M Shen. 2014. Atomic-scale control of competing electronic phases in ultrathin LaNiO_3 . *Nat. Nanotechnol.* 9, 6 (2014), 443–7. <https://doi.org/10.1038/nnano.2014.59> 97, 100
- [75] Dongkyu Lee and Ho Lee. 2017. Controlling Oxygen Mobility in Ruddlesden - Popper Oxides. *Materials (Basel)*. 10, 4 (mar 2017), 368. <https://doi.org/10.3390/ma10040368> 12
- [76] Hsin-Yi Lee, Tai-Bor Wu, and Jyh-Fu Lee. 1996. X-ray absorption spectroscopic studies of sputter-deposited LaNiO_3 thin films on Si substrate. *J. Appl. Phys.* 80, 4 (1996), 2175. <https://doi.org/10.1063/1.363109> 97

- [77] Jae Sung Lee, Shinbuhm Lee, and Tae Won Noh. 2015. Resistive switching phenomena: A review of statistical physics approaches. *Appl. Phys. Rev.* 2, 3 (sep 2015), 031303. <https://doi.org/10.1063/1.4929512> 10
- [78] Myoung-Jae Lee, Chang Bum Lee, Dongsoo Lee, Seung Ryul Lee, Man Chang, Ji Hyun Hur, Young-Bae Kim, Chang-Jung Kim, David H. Seo, Sunae Seo, U-In Chung, In-Kyeong Yoo, and Kinam Kim. 2011. A fast, high-endurance and scalable non-volatile memory device made from asymmetric Ta₂O_{5-x}/TaO_{2-x} bilayer structures. *Nat. Mater.* 10, 8 (aug 2011), 625–630. <https://doi.org/10.1038/nmat3070> 27
- [79] Aidong Li, Chuanzhen Ge, Peng Lü, and Naiben Ming. 1995. Preparation of perovskite conductive LaNiO₃ films by metalorganic decomposition. *Appl. Phys. Lett.* 1347, 1996 (1995), 1347. <https://doi.org/10.1063/1.115930> 97
- [80] Xin Li, Jiwei Zhai, and Haydn Chen. 2005. (Pb,La)(Zr,Sn,Ti)O₃ antiferroelectric thin films grown on LaNiO₃-buffered and Pt-buffered silicon substrates by sol-gel processing. *J. Appl. Phys.* 97, 2 (2005), 024102. <https://doi.org/10.1063/1.1834730> 97
- [81] Zhaoliang Liao, Peng Gao, Xuedong Bai, Dongmin Chen, and Jiandi Zhang. 2012. Evidence for electric-field-driven migration and diffusion of oxygen vacancies in Pr_{0.7}Ca_{0.3}MnO₃. *J. Appl. Phys.* 111, 11 (jun 2012), 114506. <https://doi.org/10.1063/1.4724333> 87
- [82] Zhaoliang Liao, Peng Gao, Yang Meng, Hongwu Zhao, Xuedong Bai, Jiandi Zhang, and Dongmin Chen. 2011. Electroforming and endurance behavior of Al/Pr_{0.7}Ca_{0.3}MnO₃/Pt devices. *Appl. Phys. Lett.* 99, 11 (sep 2011), 113506. <https://doi.org/10.1063/1.3638059> 56, 87
- [83] Ee Lim and Razali Ismail. 2015. Conduction Mechanism of Valence Change Resistive Switching Memory: A Survey. *Electronics* 4, 3 (sep 2015), 586–613. <https://doi.org/10.3390/electronics4030586> 193
- [84] X.J. Liu, X.M. Li, Q Wang, W.D. Yu, R Yang, X Cao, X.D. Gao, and L.D. Chen. 2010. Improved resistive switching properties in Ti/TiO_x/La_{0.7}Ca_{0.3}MnO₃ /Pt stacked structures. *Solid State Commun.* 150, 1-2 (jan 2010), 137–141. <https://doi.org/10.1016/j.ssc.2009.09.032> 50, 86
- [85] Veronika Metlenko, Amr H H Ramadan, Felix Gunkel, Hongchu Du, Henning Schraknepper, Susanne Hoffmann-Eifert, Regina Dittmann, Rainer Waser, and Roger a De Souza. 2014. Do dislocations act as atomic autobahns for oxygen in the

- perovskite oxide SrTiO₃ ? *Nanoscale* 6, 21 (aug 2014), 12864–12876. <https://doi.org/10.1039/C4NR04083J> 26
- [86] Licia Minervini, Robin W. Grimes, John A. Kilner, and Kurt E. Sickafus. 2000. Oxygen migration in La₂NiO_{4+δ}. *J. Mater. Chem.* 10, 10 (apr 2000), 2349–2354. <https://doi.org/10.1039/b004212i> 19, 22, 23
- [87] Gordon E. Moore. 1998. Cramming more components onto integrated circuits. *Proc. IEEE* 86, 1 (1998), 82–85. <https://doi.org/10.1109/JPROC.1998.658762> 4
- [88] Roberto Moreno, Pablo Garcia, James Zapata, Jaume Roqueta, Julienne Chaigneau, and José Santiso. 2013. Chemical strain kinetics induced by oxygen surface exchange in epitaxial films explored by time-resolved X-ray diffraction. *Chem. Mater.* 25, 18 (2013), 3640–3647. <https://doi.org/10.1021/cm401714d> 96, 124, 129, 208
- [89] R Moreno, J Zapata, J Roqueta, N Bagués, and J Santiso. 2014. Chemical Strain and Oxidation-Reduction Kinetics of Epitaxial Thin Films of Mixed Ionic-Electronic Conducting Oxides Determined by X-Ray Diffraction. *J. Electrochem. Soc.* 161, 11 (2014), F3046–F3051. <https://doi.org/10.1149/2.0091411jes> 97
- [90] Ruth Muenstermann, Tobias Menke, Regina Dittmann, and Rainer Waser. 2010. Coexistence of Filamentary and Homogeneous Resistive Switching in Fe-Doped SrTiO₃ Thin-Film Memristive Devices. *Adv. Mater.* 22, 43 (nov 2010), 4819–4822. <https://doi.org/10.1002/adma.201001872> 7
- [91] M. S. Munde, A. Mehonic, W. H. Ng, M. Buckwell, L. Montesi, M. Bosman, A. L. Shluger, and A. J. Kenyon. 2017. Intrinsic Resistance Switching in Amorphous Silicon Suboxides: The Role of Columnar Microstructure. *Sci. Rep.* 7, 1 (2017), 1–7. <https://doi.org/10.1038/s41598-017-09565-8> 13
- [92] V. Karthik Nagareddy, Matthew D. Barnes, Federico Zipoli, Khue T. Lai, Arseny M. Alexeev, Monica Felicia Craciun, and C. David Wright. 2017. Multilevel Ultrafast Flexible Nanoscale Nonvolatile Hybrid Graphene Oxide-Titanium Oxide Memories. *ACS Nano* 11, 3 (2017), 3010–3021. <https://doi.org/10.1021/acsnano.6b08668> 80
- [93] a. Navrotsky. 1994. Thermochemistry of Perovskite-related oxides with high oxidation states: Superconductors, sensors, fuel cell materials. *Pure Appl. Chem.* 66, 9 (jan 1994), 1759–1764. <https://doi.org/10.1351/pac199466091759> 19, 80
- [94] Viet Huong Nguyen, Ulrich Gottlieb, Anthony Valla, Delfina Muñoz, Daniel Bellet, and David Muñoz-Rojas. 2018. Electron tunneling through grain boundaries in transparent

- conductive oxides and implications for electrical conductivity: The case of ZnO:Al thin films. *Mater. Horizons* 5, 4 (2018), 715–726. <https://doi.org/10.1039/c8mh00402a> 60
- [95] S Nishiyama, D Sakaguchi, and T Hattori. 1995. Electrical conduction and thermoelectricity of $\text{La}_2\text{NiO}_{4+\delta}$ and $\text{La}_2(\text{Ni},\text{CO})\text{O}_{4+\delta}$. *Solid State Commun.* 94, 4 (apr 1995), 279–282. [https://doi.org/10.1016/0038-1098\(95\)00062-3](https://doi.org/10.1016/0038-1098(95)00062-3) 25
- [96] R. Ortega-Hernandez, M. Coll, J. Gonzalez-Rosillo, A. Palau, X. Obradors, E. Miranda, T. Puig, and J. Suñe. 2015. Resistive switching in $\text{CeO}_2/\text{La}_{0.8}\text{Sr}_{0.2}\text{MnO}_3$ bilayer for non-volatile memory applications. *Microelectron. Eng.* 147 (2015), 37–40. <https://doi.org/10.1016/j.mee.2015.04.042> 87
- [97] H Y Peng, G P Li, J Y Ye, Z P Wei, Z Zhang, D D Wang, G Z Xing, and T Wu. 2010. Electrode dependence of resistive switching in Mn-doped ZnO: Filamentary versus interfacial mechanisms. *Appl. Phys. Lett.* 96, 19 (may 2010), 192113. <https://doi.org/10.1063/1.3428365> 8, 27
- [98] H Y Peng, L Pu, J. C. Wu, D Cha, J H Hong, W N Lin, Y. Y. Li, J F Ding, A David, K Li, and T Wu. 2013. Effects of electrode material and configuration on the characteristics of planar resistive switching devices. *APL Mater.* 1, 5 (nov 2013), 052106. <https://doi.org/10.1063/1.4827597> 13
- [99] A. Perrichon, A. Piovano, M. Boehm, M. Zbiri, M. Johnson, H. Schober, M. Ceretti, and W. Paulus. 2015. Lattice Dynamics Modified by Excess Oxygen in $\text{Nd}_2\text{NiO}_{4+\delta}$: Triggering Low-Temperature Oxygen Diffusion. *J. Phys. Chem. C* 119, 3 (jan 2015), 1557–1564. <https://doi.org/10.1021/jp510392h> 23
- [100] R. A Mohan Ram, L. Ganapathi, P. Ganguly, and C. N R Rao. 1986. Evolution of three-dimensional character across the $\text{La}_{n+1}\text{Ni}_n\text{O}_{3n+1}$ homologous series with increase in n. *J. Solid State Chem.* 63, 2 (1986), 139–147. [https://doi.org/10.1016/0022-4596\(86\)90163-5](https://doi.org/10.1016/0022-4596(86)90163-5) 16, 18
- [101] C.N.R. Rao, D.J. Buttrey, N. Otsuka, P. Ganguly, H.R. Harrison, C.J. Sandberg, and J.M. Honig. 1984. Crystal structure and semiconductor-metal transition of the quasi-two-dimensional transition metal oxide, La_2NiO_4 . *J. Solid State Chem.* 51, 2 (feb 1984), 266–269. [https://doi.org/10.1016/0022-4596\(84\)90342-6](https://doi.org/10.1016/0022-4596(84)90342-6) 16, 18
- [102] D. E. Rice and D. J. Buttrey. 1993. An X-Ray diffraction Study of the Oxygen Content Phase Diagram of La_2NiO_4 . , 197–210 pages. <https://doi.org/10.1006/jssc.1993.1208> 16, 18, 19

- [103] J Rodriguez-Carvajal, M T Fernandez-Diaz, and J L Martinez. 1991. Neutron diffraction study on structural and magnetic properties of La_2NiO_4 . *J. Phys. Condens. Matter* 3, 19 (may 1991), 3215–3234. <https://doi.org/10.1088/0953-8984/3/19/002> 16, 18, 25
- [104] Aruppukottai M. Saranya, Dolores Pla, Alex Morata, Andrea Cavallaro, Jesús Canales-Vázquez, John A. Kilner, Mónica Burriel, and Albert Tarancón. 2015. Engineering Mixed Ionic Electronic Conduction in $\text{La}_{0.8}\text{Sr}_{0.2}\text{MnO}_{3+\delta}$ Nanostructures through Fast Grain Boundary Oxygen Diffusivity. *Adv. Energy Mater.* 5, 11 (jun 2015), 1500377. <https://doi.org/10.1002/aenm.201500377> 26
- [105] Saraswat. 1997. Metal/SC Ohmic contacts. (1997), 25. 51
- [106] K. M. Satyalakshmi, R. M. Mallya, K. V. Ramanathan, X. D. Wu, B. Brainard, D. C. Gautier, N. Y. Vasanthacharya, and M. S. Hegde. 1993. Epitaxial metallic LaNiO_3 thin films grown by pulsed laser deposition. *Appl. Phys. Lett.* 62, 11 (1993), 1233–1235. <https://doi.org/10.1063/1.109612> 97
- [107] A. Sawa, T. Fujii, M. Kawasaki, and Y. Tokura. 2004. Hysteretic current-voltage characteristics and resistance switching at a rectifying $\text{Ti}/\text{Pr}_{0.7}\text{Ca}_{0.3}\text{MnO}_3$ interface. *Appl. Phys. Lett.* 85, 18 (nov 2004), 4073–4075. <https://doi.org/10.1063/1.1812580> arXiv:arXiv:cond-mat/0409657v1 27, 50, 87
- [108] Akihito Sawa and Rene Meyer. 2016. Interface-Type Switching. In *Resist. Switch.* Wiley-VCH Verlag GmbH & Co. KGaA, Weinheim, Germany, 457–482. <https://doi.org/10.1002/9783527680870.ch16> 7
- [109] M. Sayer and P. Odier. 1987. Electrical properties and stoichiometry in La_2NiO_4 . *J. Solid State Chem.* 67, 1 (1987), 26–36. [https://doi.org/10.1016/0022-4596\(87\)90334-3](https://doi.org/10.1016/0022-4596(87)90334-3) 38, 80
- [110] R. Sayers, R. A. De Souza, J. A. Kilner, and S. J. Skinner. 2010. Low temperature diffusion and oxygen stoichiometry in lanthanum nickelate. *Solid State Ionics* 181, 8-10 (mar 2010), 386–391. <https://doi.org/10.1016/j.ssi.2010.01.016> 21
- [111] R. Scherwitzl, S. Gariglio, M. Gabay, P. Zubko, M. Gibert, and J. M. Triscone. 2011. Metal-insulator transition in ultrathin LaNiO_3 films. *Phys. Rev. Lett.* 106, 24 (2011), 3–6. <https://doi.org/10.1103/PhysRevLett.106.246403> arXiv:1101.5111 97
- [112] R. Scherwitzl, P. Zubko, C. Lichtensteiger, and J. M. Triscone. 2009. Electric-field tuning of the metal-insulator transition in ultrathin films of LaNiO_3 . *Appl. Phys. Lett.* 95, 22 (2009), 2007–2010. <https://doi.org/10.1063/1.3269591> 97

- [113] Herbert Schroeder, Victor V. Zhirnov, Ralph K. Cavin, and Rainer Waser. 2010. Voltage-time dilemma of pure electronic mechanisms in resistive switching memory cells. *J. Appl. Phys.* 107, 5 (2010), 1–9. <https://doi.org/10.1063/1.3319591> 12
- [114] Ivan K. Schuller, Rick Stevens, Robinson Pino, and Michael Pechan. 2015. *Neuromorphic Computing-From Materials Research to Systems Architecture Roundtable*. Technical Report. USDOE Office of Science (SC) (United States). <https://doi.org/10.2172/1283147> 1, 2, 3, 4
- [115] J-P. Sénateur, Catherine Dubourdieu, F Weiss, M Rosina, and A Abrutis. 2000. Pulsed injection MOCVD of functional electronic oxides. *Adv. Mater. Opt. Electron.* 10, 3-5 (may 2000), 155–161. [https://doi.org/10.1002/1099-0712\(200005/10\)10:3/5<155::AID-AMO406>3.0.CO;2-2](https://doi.org/10.1002/1099-0712(200005/10)10:3/5<155::AID-AMO406>3.0.CO;2-2) 151, 164
- [116] S U Sharath, J Kurian, P Komissinskiy, E Hildebrandt, T Bertaud, C Walczyk, P Calka, T. Schroeder, and L Alff. 2014. Thickness independent reduced forming voltage in oxygen engineered HfO₂ based resistive switching memories. *Appl. Phys. Lett.* 105, 7 (2014), 073505. <https://doi.org/10.1063/1.4893605> 27
- [117] Keiji Shono, Hiroyasu Kawano, Takeshi Yokota, and Manabu Gomi. 2008. Origin of negative differential resistance observed on bipolar resistance switching device with Ti/Pr_{0.7}Ca_{0.3}MnO₃/Pt structure. *Appl. Phys. Express* 1, 5 (apr 2008), 0550021–0550023. <https://doi.org/10.1143/APEX.1.055002> 50, 56
- [118] Hyunjun Sim, Hyejung Choi, Dongsoo Lee, Man Chang, Dooho Choi, Yunik Son, Eun-Hong Lee, Wonjoo Kim, Yoondong Park, In-Kyeong Yoo, and Hyunsang Hwang. 2005. Excellent resistance switching characteristics of Pt/SrTiO₃/Schottky junction for multi-bit nonvolatile memory application. *Electron Devices Meet. 2005. IEDM Tech. Dig. IEEE Int. 00, c* (2005), 758–761. <https://doi.org/10.1109/IEDM.2005.1609464> 8
- [119] Stephen J. Skinner. 2003. Characterisation of La₂NiO_{4+δ} using in-situ high temperature neutron powder diffraction. *Solid State Sci.* 5, 3 (2003), 419–426. [https://doi.org/10.1016/S1293-2558\(03\)00050-5](https://doi.org/10.1016/S1293-2558(03)00050-5) 16, 19, 24
- [120] S. J. Skinner and J. A. Kilner. 2000. Oxygen diffusion and surface exchange in La_{2-x}Sr_xNiO_{4+δ}. *Solid State Ionics* 135, 1-4 (2000), 709–712. [https://doi.org/10.1016/S0167-2738\(00\)00388-X](https://doi.org/10.1016/S0167-2738(00)00388-X) 21, 25
- [121] Junwoo Son, Pouya Moetakef, James M. LeBeau, Daniel Ouellette, Leon Balents, S. James Allen, and Susanne Stemmer. 2010. Low-dimensional Mott material: Trans-

- port in ultrathin epitaxial LaNiO₃ films. *Appl. Phys. Lett.* 96, 6 (feb 2010), 062114. <https://doi.org/10.1063/1.3309713> 97, 170, 173
- [122] Dmitri B. Strukov, Fabien Alibart, and R. Stanley Williams. 2012. Thermophoresis/diffusion as a plausible mechanism for unipolar resistive switching in metal-oxide-metal memristors. *Appl. Phys. A* 107, 3 (jun 2012), 509–518. <https://doi.org/10.1007/s00339-012-6902-x> 11
- [123] Dmitri B Strukov, Gregory S Snider, Duncan R Stewart, and R Stanley Williams. 2008. The missing memristor found. *Nature* 453, 7191 (2008), 80–3. <https://doi.org/10.1038/nature06932> arXiv:arXiv:0908.3162v1 6
- [124] D. Telesca, B.O. Wells, and B. Sinkovic. 2012. Structural reorientation of PLD grown La₂NiO₄ thin films. *Surf. Sci.* 606, 9-10 (may 2012), 865–871. <https://doi.org/10.1016/j.susc.2012.02.001> 33, 115, 180
- [125] Tran Dang Thanh, H. T. Van, D. T. A. Thu, L. V. Bau, Nguyen Van Dang, D. N. H. Nam, L. V. Hong, and Seong-cho Yu. 2017. Structure, Magnetic, and Electrical Properties of La₂NiO_{4+d} Compounds. *IEEE Trans. Magn.* 53, 11 (nov 2017), 1–4. <https://doi.org/10.1109/TMAG.2017.2703616> 85
- [126] Bobo Tian, Pavan Nukala, Mohamed Ben Hassine, Xiaolin Zhao, Xudong Wang, Hong Shen, Jianlu Wang, Shuo Sun, Tie Lin, Jinglan Sun, Jun Ge, Rong Huang, Chungang Duan, Thomas Reiss, Maria Varela, Brahim Dkhil, Xiangjian Meng, and Junhao Chu. 2017. Interfacial memristors in Al-LaNiO₃ heterostructures. *Phys. Chem. Chem. Phys.* 19, 26 (2017), 16960–16968. <https://doi.org/10.1039/C7CP02398G> 27
- [127] J. M. Tranquada, D. J. Buttrey, V. Sachan, and J. E. Lorenzo. 1994. Simultaneous ordering of holes and spins in La₂NiO_{4.125}. *Phys. Rev. Lett.* 73, 7 (aug 1994), 1003–1006. <https://doi.org/10.1103/PhysRevLett.73.1003> 20
- [128] J. M. Tranquada, Y. Kong, J. E. Lorenzo, D. J. Buttrey, D. E. Rice, and V. Sachan. 1994. Oxygen intercalation, stage ordering, and phase separation in La₂NiO_{4+d} with 0.05<d<0.11. *Phys. Rev. B* 50, 9 (sep 1994), 6340–6351. <https://doi.org/10.1103/PhysRevB.50.6340> 18, 19, 20, 25
- [129] Harry L. Tuller and Sean R. Bishop. 2011. Point Defects in Oxides: Tailoring Materials Through Defect Engineering. *Annu. Rev. Mater. Res.* 41, 1 (2011), 369–398. <https://doi.org/10.1146/annurev-matsci-062910-100442> 13

- [130] Raymond T Tung. 2014. The physics and chemistry of the Schottky barrier height. *Appl. Phys. Rev.* 1, 1 (mar 2014), 011304. <https://doi.org/10.1063/1.4858400> 43, 45, 77
- [131] Ilia Valov and Rainer Waser. 2016. 09 Physics and Chemistry of Nanoionic. In *Resist. Switch. From Fundam. Nanoionic Redox Process. to Memristive Device Appl.* 253–287. <https://doi.org/10.1002/9783527680870.ch9> 90
- [132] Sascha Vongehr. 2012. The Missing Memristor: Novel Nanotechnology or rather new Case Study for the Philosophy and Sociology of Science? *Adv. Sci. Lett.* 17, 1 (2012), 285–290. <https://doi.org/10.1166/asl.2012.4241> arXiv:arXiv:1205.6129v1 6
- [133] Zhongrui Wang, Saumil Joshi, Sergey E. Savel'ev, Hao Jiang, Rivu Midya, Peng Lin, Miao Hu, Ning Ge, John Paul Strachan, Zhiyong Li, Qing Wu, Mark Barnell, Geng-Lin Li, Huolin L. Xin, R. Stanley Williams, Qiangfei Xia, and J. Joshua Yang. 2016. Memristors with diffusive dynamics as synaptic emulators for neuromorphic computing. *Nat. Mater.* 16, September (2016). <https://doi.org/10.1038/nmat4756> 85
- [134] Zhiyong Wang, Laiyuan Wang, Masaru Nagai, Linghai Xie, Mingdong Yi, and Wei Huang. 2017. Nanoionics-Enabled Memristive Devices: Strategies and Materials for Neuromorphic Applications. *Adv. Electron. Mater.* 3, 7 (jul 2017), 1600510. <https://doi.org/10.1002/aelm.201600510> 2
- [135] Rainer Waser. 2012. Redox-Based Resistive Switching Memories. *J. Nanosci. Nanotechnol.* 12, 10 (2012), 7628–7640. <https://doi.org/10.1166/jnn.2012.6652> arXiv:Journal of Applied Physics vol. 97(2005):12, pp. 121301-121301-52 7, 9
- [136] M. C. Weber, M. Guennou, N. Dix, D. Pesquera, F. Sánchez, G. Herranz, J. Fontcuberta, L. López-Conesa, S. Estradé, F. Peiró, Jorge Iñiguez, and J. Kreisel. 2016. Multiple strain-induced phase transitions in LaNiO₃ thin films. *Phys. Rev. B* 94, 1 (jul 2016), 014118. <https://doi.org/10.1103/PhysRevB.94.014118> 172
- [137] Russell J Woolley, Benoit N Illy, Mary P. Ryan, and Stephen J Skinner. 2011. In situ determination of the nickel oxidation state in La₂NiO_{4+δ} and La₄Ni₃O_{10-δ} using X-ray absorption near-edge structure. *J. Mater. Chem.* 21, 46 (2011), 18592. <https://doi.org/10.1039/c1jm14320d> 196, 197
- [138] T. Yamamoto, R. Yasuhara, I. Ohkubo, H. Kumigashira, and M. Oshima. 2011. Formation of transition layers at metal perovskite oxide interfaces showing resistive switching behaviors. *J. Appl. Phys.* 110, 5 (2011). <https://doi.org/10.1063/1.3631821> 48, 56, 87

- [139] G. Yang, C. H. Jia, Y. H. Chen, X. Chen, and W. F. Zhang. 2014. Negative differential resistance and resistance switching behaviors in BaTiO₃ thin films. *J. Appl. Phys.* 115, 20 (may 2014), 204515. <https://doi.org/10.1063/1.4878236> 86
- [140] J. Yang. 2008. Structural analysis of perovskite LaCr_{1-x}Ni_xO₃ by Rietveld refinement of X-ray powder diffraction data. *Acta Crystallogr. Sect. B Struct. Sci.* 64, 3 (jun 2008), 281–286. <https://doi.org/10.1107/S0108768108005739> 97
- [141] J. Joshua Yang, Matthew D. Pickett, Xuema Li, Douglas A.A. Ohlberg, Duncan R. Stewart, and R. Stanley Williams. 2008. Memristive switching mechanism for metal/oxide/metal nanodevices. *Nat. Nanotechnol.* 3, 7 (2008), 429–433. <https://doi.org/10.1038/nnano.2008.160> 88
- [142] J. Joshua Yang, John Paul Strachan, Feng Miao, Min Xian Zhang, Matthew D. Pickett, Wei Yi, Douglas A A Ohlberg, G. Medeiros-Ribeiro, and R. Stanley Williams. 2011. Metal/TiO₂ interfaces for memristive switches. *Appl. Phys. A Mater. Sci. Process.* 102, 4 (2011), 785–789. <https://doi.org/10.1007/s00339-011-6265-8> 48, 50
- [143] Ki Hyun Yoon, Ji-Hoon Sohn, Byoung Duk Lee, and Dong Heon Kang. 2002. Effect of LaNiO₃ interlayer on dielectric properties of (Ba_{0.5}Sr_{0.5})TiO₃ thin films deposited on differently oriented Pt electrodes. *Appl. Phys. Lett.* 81, 26 (2002), 5012. <https://doi.org/10.1063/1.1531218> 97
- [144] Junjie Zhang, Hong Zheng, Yang Ren, and J. F. Mitchell. 2017. High-Pressure Floating-Zone Growth of Perovskite Nickelate LaNiO₃ Single Crystals. *Cryst. Growth Des.* 17, 5 (may 2017), 2730–2735. <https://doi.org/10.1021/acs.cgd.7b00205> arXiv:1705.00570 97
- [145] Zhengjun Zhang, Ye Zhao, and Minmin Zhu. 2006. NiO films consisting of vertically aligned cone-shaped NiO rods. *Appl. Phys. Lett.* 88, 3 (2006), 1–3. <https://doi.org/10.1063/1.2166479> 172
- [146] Mingwei Zhu, Philipp Komissinskiy, Aldin Radetinac, Mehran Vafaei, Zhanjie Wang, and Lambert Alff. 2013. Effect of composition and strain on the electrical properties of LaNiO₃ thin films. *Appl. Phys. Lett.* 103, 14 (2013), 141902. <https://doi.org/10.1063/1.4823697> 97
- [147] M. Zinkevich and F. Aldinger. 2004. Thermodynamic analysis of the ternary La-Ni-O system. *J. Alloys Compd.* 375, 1-2 (2004), 147–161. <https://doi.org/10.1016/j.jallcom.2003.11.138> 38, 106, 166, 167, 177

Appendix A

Lanthanum-nickelate thin film deposition and optimization using PiMOCVD

Contents

A.1 PiMOCVD: a chemical vapour deposition technique	151
A.1.1 Metal-Organic Chemical Vapour Deposition (MOCVD)	152
A.1.2 The particularities of PiMOCVD	155
A.1.3 Details on the substrate preparation and deposition procedure	155
A.1.4 Post annealing treatments	158
A.2 Role of the solvent on the structural properties of L2NO4 thin films deposited by PiMOCVD	158
A.3 The La/Ni ratio in the precursor solution	159

A.1 PiMOCVD: a chemical vapour deposition technique

The majority of the lanthanum-nickelate thin films presented in this thesis have been synthesized using Pulsed-injection Metal-Organic Chemical Vapour Deposition (PiMOCVD) [115], a chemical deposition technique based on the CVD process using metalorganic precursors in vapour phase, which are evaporated by injecting small drops of a solution containing the metals (in the form of metalorganic compounds) required to form, in this case, the ternary oxide. This technique allows to tune the film composition by varying the concentration of precursors in the solution. The aim of this section is to give a general idea about the theory behind this deposition method.

A.1.1 Metal-Organic Chemical Vapour Deposition (MOCVD)

MOCVD is a chemical deposition process in which one or more gaseous metal-organic precursors react on a solid surface in order to form a more or less dense layer depending on the deposition conditions (temperature, pressure, chemical nature and morphology of the substrate...). There are several key steps of the chemical reactions taking place in the vapour phase that should be taken into account in order to understand the process and thus have a better control over it:

- 1) Generation of active gases reactant species;
- 2) Transport of the gaseous precursors into the reaction chamber;
- 3) Gas phase reaction;
- 4) Adsorption of the reactive species onto the substrates surface;
- 5) Heterogeneous gas/solid reaction of the precursors catalysed by the heated substrate;
- 6) Desorption of the gaseous reaction by-products;
- 7) Transport of the by-products away from the surface.

Figure A.1 illustrates the PiMOCVD deposition process. Each of these steps is detailed hereafter.

1) Generation of active gases reactant species An important aspect of CVD is the need of having gaseous precursors at the reaction stage. Several types of precursors can be used, which can be either gaseous (e.g. silane, diborane, ammonia, etc), liquid or solid in their natural form. Common precursors include metal carbonyls ($\text{Ni}(\text{CO})_4$, $\text{Fe}_2(\text{CO})_9$...), metal hydrides (AlH_3 , BH_3 ...), halides (AgCl , LiCl ...) or metalorganic compounds ($\text{La}(\text{TMHD})_3$, $\text{Al}(\text{acac})_3$...) in the case of MOCVD. All of these chemicals are usually available in their solid form. In order to be able to use them for PiMOCVD they have to be dissolved in an appropriate solvent, typically monoglyme or m-xylene. The obtained mixture is then pulverized into tiny (but controlled) droplets with the help of high frequency piezoelectric elements or pulsed injection. After being formed, the droplets are injected into a circuit where a flow of inert carrier gas assures their transport to the reactor. Along the way, the droplets will be vaporized with the help of heating elements.

2) Transport of the gaseous precursors into the reaction chamber As far as the carrier gas is concerned, it does not necessarily have to be inert. Many oxide or nitride compounds can be deposited by MOCVD using a carrier gas containing oxygen or nitrogen, respectively. The flow rate of the gaseous precursor to the reaction chamber should be controlled to increase reproducibility. A high flow rate tends to favour a kinetically pseudo-stable phase whereas

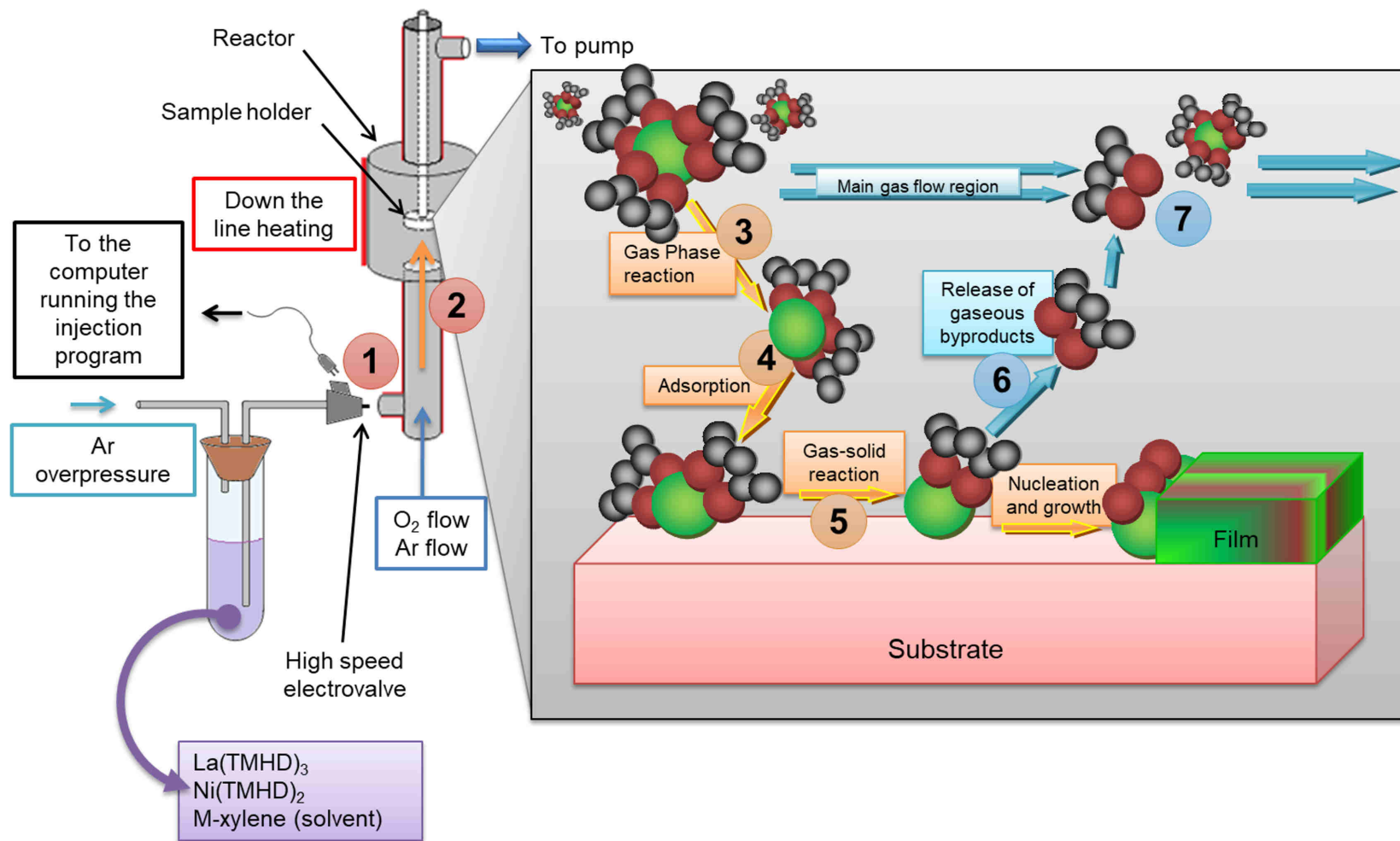


Figure A.1 – Detailed illustration of the PiMOCVD process. Steps 1-7 are described in the text.

a lower flow rate gives the system more time to achieve the thermodynamic stability. The deposition is slower when the flow rate decreases.

3) Gas phase reaction When the gaseous precursor reaches the reaction chamber, the high temperature usually leads to a preliminary gas phase reaction consisting in the partial breakdown of the precursor molecules. Part of the ionic-covalent bonds between the organic molecules and the metallic centres are broken, leading to an ‘activation’ of these molecules. The detached organic parts are evacuated away from the reaction chamber following the main gas flow.

4) Adsorption of the reactive species onto the substrates surface This part of the CVD process is crucial for obtaining a controlled deposition. In order to have this control, the substrate should act as a catalyst for the chemical reaction. In other words, the reactive species must not react among themselves before meeting the substrates surface. The pressure in the reaction chamber, the substrate temperature and chemical nature are typical parameters that have a strong influence on this reactivity. Low pressures (several Torr) tend to prevent undesired gas phase reactions and allow the deposition of more homogeneous films. This is because they favour the surface controlled deposition regime: the deposition is mainly controlled by the substrate temperature. At the opposite, high pressures coupled with high temperatures will favour the diffusion controlled regime: any molecule that arrives on the surface will react almost instantaneously. The kinetically limiting parameter is then determined by the time it takes the reacting species to diffuse from the gas phase to the surface. Too high substrate temperatures can be detrimental to the growth of the film since they can lead to fast desorption of the reacting molecules. There is always a temperature-related equilibrium between the adsorbing and the desorbing molecules that acts as a limiting factor for the growth of the film.

5) Heterogeneous gas/solid reaction of the precursors catalysed by the heated substrate Once the reactive gas molecules have adsorbed on the surface, a chemical reaction occurs at the gas/solid interface and launches the so called “nucleation step”. Small nuclei are formed and start to grow into bigger and bigger islands as long as there are reactants adsorbing on the surface. This chemical reaction transforms the previously activated molecules (during the gas phase reaction) into a deposit (the film) and by-products (the organic leftovers). The adsorbed molecules can diffuse along the heated substrate to find nuclei or other surface inhomogeneities (like crystallographic steps) that will make the reaction easier.

6-7) Desorption and transport of the gaseous reaction by-products away from the surface The gaseous by-products formed during the previous reactions (in the gas phase and at the gas/solid interface) can get adsorbed on the surface leading to film impurities. It is difficult to have a control over this phenomenon but high substrate temperatures and low partial pressures prove to be favourable towards the desorption of these molecules. In the particular case when oxide materials are grown, the presence of oxygen as reactive gas will help with the combustion of the organic ligands (when using for example metalorganic precursor molecules). The gaseous by-products are removed from the boundary layer through diffusion and/or convection and are then transported away from the deposition chamber with the rest of the gases (carrier gas and unreacted gaseous precursors).

A.1.2 The particularities of PiMOCVD

Pulsed-Injection MOCVD is a particular type of MOCVD that uses a high speed electro-valve to inject the precursor solution. This electro-valve makes it possible to form micro droplets of the precursor solution with a controlled volume (typically some microliters). The frequency of the pulses and the opening time of the valve are important parameters that will have a strong impact on the structure and the microstructure of the deposited material [42]. The main advantages of using PiMOCVD over regular MOCVD are listed below [23]:

- Precise control over the thickness and the stoichiometry of the deposited film;
- Use of unstable precursors since they are preserved under an inert atmosphere in the injector;
- Possibility to inject a multi-component solution allowing the growth of more complex films;
- It is also possible to use several injectors in parallel to obtain a multilayered structure;
- Finally, pulsed injection increases the reproducibility of the depositions.

A.1.3 Details on the substrate preparation and deposition procedure

The duration of the deposition itself can range from several minutes to several hours, depending on the thickness of the film that is targeted. Here, 70 minutes were needed to deposit an approximately 100 nm thick film. In the particular case of this study, the preparation of the substrates was done the day before the deposition. This preparation consists in the cleaning of

the substrates and their pasting on the substrate holder. All the substrates followed a mild 3-step cleaning process (acetone, isopropanol, deionized water) in an ultrasonicated bath. This cleaning step allows for the elimination of all the particles and impurities adsorbed on the surface (dust and other organic particles) and is an easy way to prevent big (μm) inhomogeneities in the deposited film. The substrates are then pasted on the sample holder. For this, silver paste is used allowing a good thermal conductivity between the sample and the sample holder. This paste makes it also possible to carry out depositions at high temperatures (up to $900\text{ }^\circ\text{C}$) without it losing its properties. Since the single crystal substrates used are rather small (1 cm^2), it was possible to paste several (up to four) on the same sample holder. This allows to deposit several films simultaneously and to compare the effect of different substrates on the deposited film, eliminating the small (uncontrolled) variations which can occur between two different experiments. The drying of the paste is rather long, this is why this first preparation step was usually carried out several hours before the deposition (usually the night before).

The precursor solution was prepared just before the deposition to limit its possible degradation over time. For reproducibility sake, the injector was cleaned before and after each deposition with cyclohexane (to limit the chances of it clogging) and kept in an argon overpressure whenever possible. In order to study the influence of the precursor solution on the composition of the deposited film, solutions with different La/Ni ratios were prepared, but the volume and total concentration were kept constant at 20 mL and 0.02 mol/L , respectively. The following chemicals were used for the growth of LaNO_3 and La_2NiO_4 thin films: organometallic precursors of Tris(2,2,6,6-tetramethyl-3,5-heptanedionato)lanthanum(III) ($\text{La}(\text{tmhd})_3$, 99%, 99.9%-La, CAS 1419-13-2 from Strem Chemicals) and Bis(2,2,6,6-tetramethyl-3,5-heptanedionato)-nickel(II), ($\text{Ni}(\text{tmhd})_2$, min. 98%, 99.9%-Ni, CAS 41749-92-2 from Strem Chemicals) dissolved in a meta-xylene organic solvent ($\text{C}_6\text{H}_4-(\text{CH}_3)_2$, 99%, CAS 108-38-3 from Alfa Aesar). The prepared precursor solution was ultrasonicated during ten minutes to dissolve the solid lanthanum and nickel precursors. Figure A.2 shows the structure of these metalorganic precursors.

The particular PiMOCVD frame which was used to prepare the samples presented in this thesis was home built at LMGP and is referred to as the "Bâti D11". It works in low pressure (several Torr) and can go up to $800\text{ }^\circ\text{C}$.

There is the possibility of work under argon, oxygen and nitrogen atmospheres, or a combination of these gases. Three injection entries allow connecting as many injectors to increase the deposition possibilities. The depositions were carried out at a pressure of 5 Torr in a mixed oxygen/argon atmosphere to obtain the desired oxides. Argon was also used as carrier gas during the heating and the cooling of the reactor. The injector head is connected to a software-controlled electrical casing which commands the injection parameters: the opening

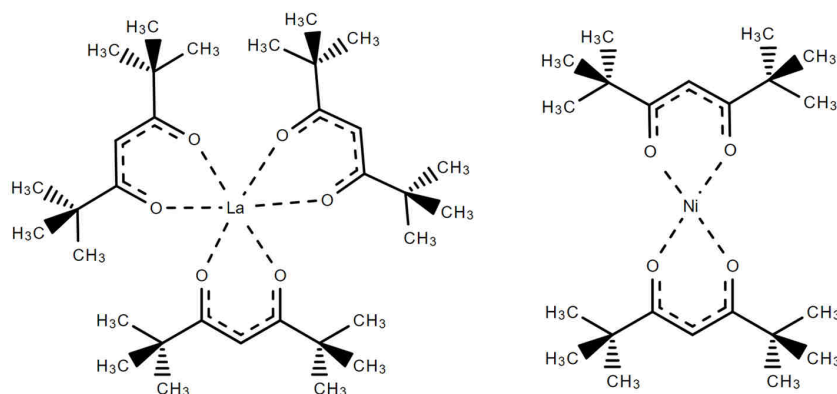


Figure A.2 – Metalorganic precursors used for the deposition of lanthanum-nickelate thin films by PiMOCVD (left: $\text{La}(\text{tmhd})_3$ and right: $\text{Ni}(\text{tmhd})_2$).

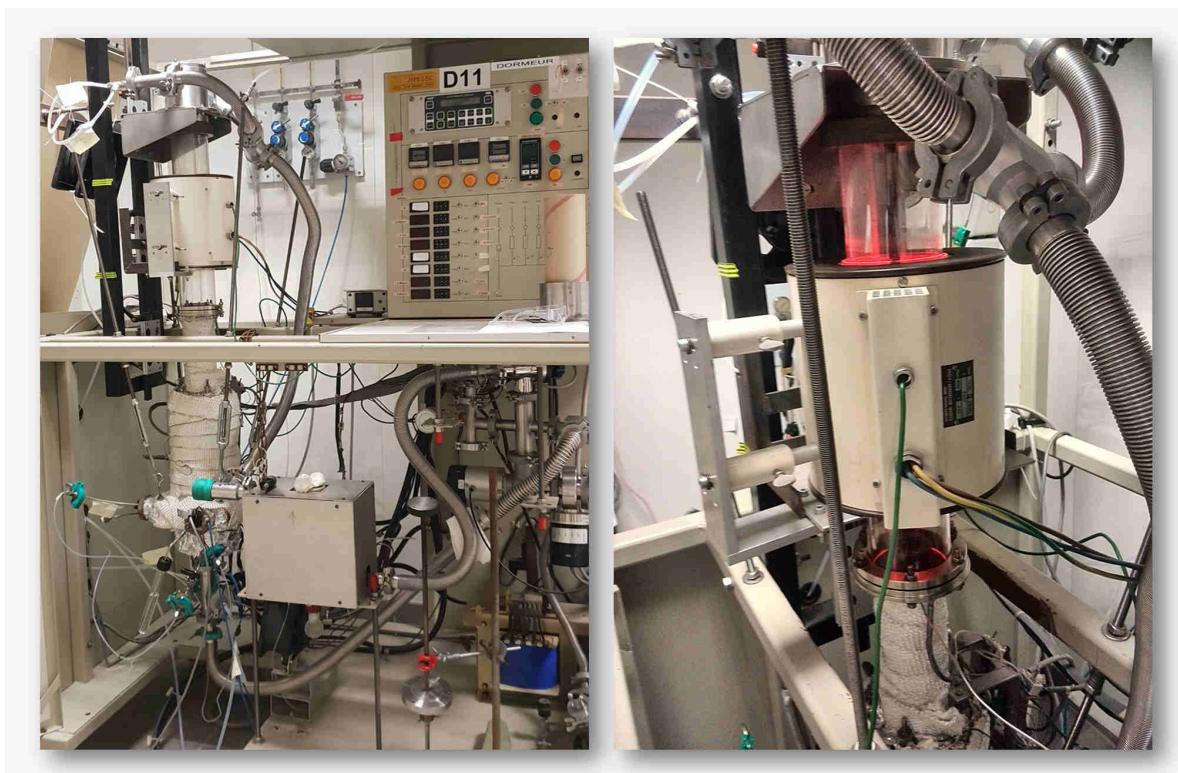


Figure A.3 – Pictures of the « Bâti D11 », the PiMOCVD reactor used for the deposition of lanthanum-nickelate thin films.

time (controlling the size of the injected droplets), the frequency of the pulses and their number. An opening time of 2 ms was used to inject droplets at a frequency of 1 droplet/s. These conditions allow depositing an approximately 100 nm thick film.

A.1.4 Post annealing treatments

Some of the prepared samples received an additional ex-situ post annealing treatment in a ceramic tubular furnace in order to tune the oxygen stoichiometry of the L2NO4 thin films (the structural and chemical results of these annealings are described in Section 2.3.2). A heating ramp of 10°C/min to 500°C with a 1 h dwell time and under 1 atm of either pure O₂, pure Ar or a H₂(6%)/Ar gas mixture was used. The furnace was then cooled down slowly to room temperature (without using any additional cooling system).

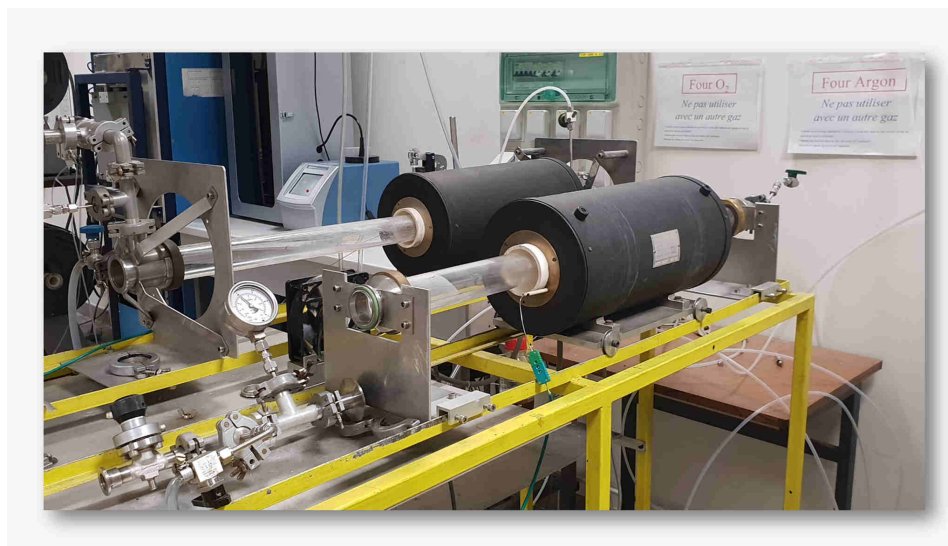


Figure A.4 – Picture of the tubular furnaces used for the post-annealing treatments.

A.2 Role of the solvent on the structural properties of L2NO4 thin films deposited by PiMOCVD

A monoglyme precursor was used initially to grow the lanthanum-nickelate thin films. This solvent was later replaced by the less-toxic m-xylene solvent.

Figure A.5 shows the XRD patterns of two sets of L2NO4/STO samples with different La/Ni precursor ratios in the injected solution: 4.75 (top) and 5 (bottom), using either

monoglyme (orange curves) or m-xylene (red curves) as the solvent. There is a striking difference between two samples deposited with two different solvents: in addition to the $00l_{L2NO4}$ (l even) reflections, new lanthanum-rich phases (La_2O_3) or $L2NO4$ phase with other orientations are present in the samples deposited with the monoglyme solvent, regardless of the La/Ni precursor ratio. There is also an overall increase in intensity (represented by the grey regions which correspond to the integrated intensity difference between the two XRD patterns) of the diffraction patterns acquired for the samples deposited with monoglyme, suggesting that more impurity phases could be present in these samples. This represented an additional reason for using m-xylene instead of monoglyme as the solvent for the further preparation of $LNO3$ and $L2NO4$ thin films.

A.3 The La/Ni ratio in the precursor solution

A systematic study on the effect of the La/Ni ratio in the precursor solution on the lanthanum-nickelate film structural properties deposited on STO substrates has been carried out. Only the composition of the injected solution was varied, increasing the La/Ni ratio from 2.00 to 2.75 and from 4.75 to 5.25 (four samples were prepared for each range) to find the optimal composition for the deposition of $LNO3$ (La/Ni in the film close to 1) and $L2NO4$ (La/Ni in the film close to 2) thin films, respectively. The deposition temperature was fixed at 750 °C, the number of pulses to 4000 and all the other deposition parameters were fixed to the standard ones (detailed in Table 2.1). Figure A.6 shows the La/Ni ratio in the film (measured by EPMA) against the one initially present in the precursor solution. A linear regression is satisfactory to fit the data, the slope of the linear fit of ~ 0.5 shows that the deposition yield of $Ni(TMHD)_2$ is almost twice the one of $La(TMHD)_3$.

As can be observed from the XRD results for the low La/Ni ratios (bottom XRD patterns), the desired $LNO3$ perovskite phase is present in all the samples grown on STO and a high texturization of the film can be observed in particular along the $[100]$ direction. The peak intensities for this phase orientation are rather high. Nonetheless, there are some key differences between these patterns. First, the films with the lowest La/Ni solution ratio (La/Ni of the solution of 2.00 and 2.25, corresponding to La/Ni ratio of the film of 0.87 and 0.96) present a narrow peak around 44° that can be attributed to the presence of a textured cubic NiO phase. This suggests that the precursor solution should be enriched even more in lanthanum. Furthermore, for these compositions, two narrow peaks around 33° and 69° are clear evidence of another orientation of the perovskite phase that, if the film is grown epitaxial, should not appear due to the imposed orientation of the substrate (along $[100]$). When the La/Ni ratio of the solution increases to 2.78 (1.28 in the film), the NiO peak disappears and two other

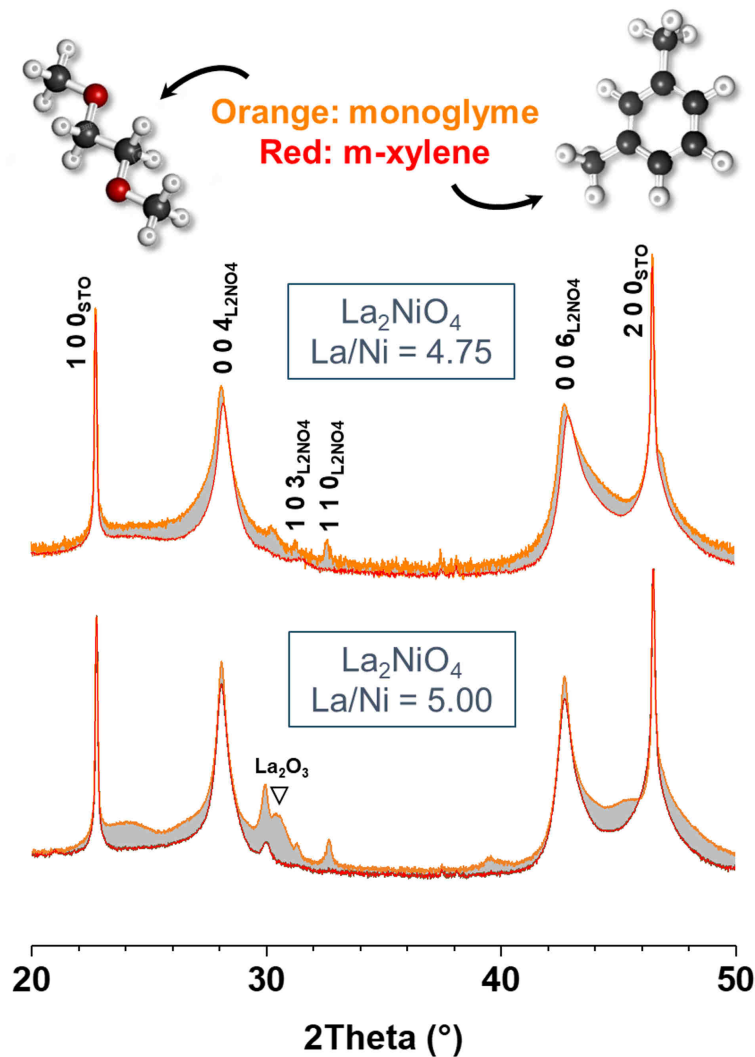


Figure A.5 – XRD patterns of L2NO4/STO samples (log scale) showing the role of the solvent on the quality of L2NO4 thin films. The films were deposited on STO at 750 °C using a precursor solution with a concentration of 0.02 mol/L and with two different La/Ni precursor ratios: 4.75 (top) and 5 (bottom), only the solvent was varied (either monoglyme or m-xylene has been used).

broader peaks appear around 26° and 54° corresponding to the oriented growth of a hexagonal La_2O_3 phase. Further details on the optimization of LNO3 are given in Appendix B. For the diffractograms corresponding to the high La/Ni ratios (top of Figure A.7), all the samples show a high texturization along $00l_{\text{L2NO}_4}$ (l even) phase as can be deduced by the five rather intense peaks around 14°, 28°, 43°, 58° and 75° corresponding to the 002 , 004 , 006 , 008 and 0010 planes of L2NO4, respectively. As the La/Ni solution ratio increases from 4.75 to

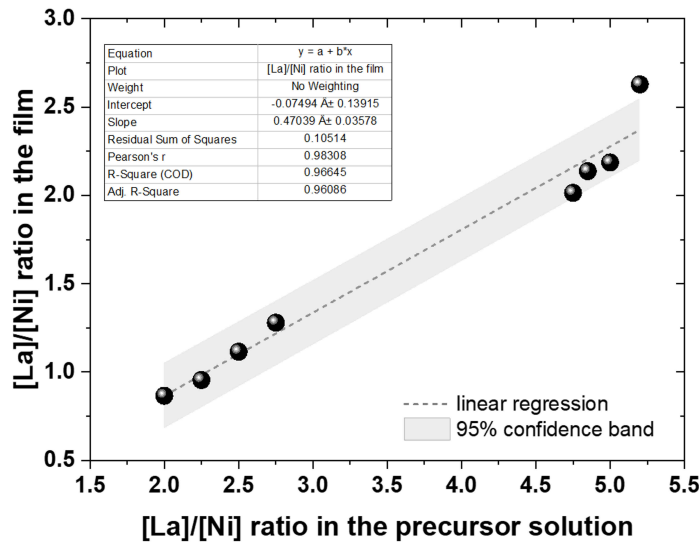


Figure A.6 – Correlation between the calculated La/Ni atomic ratio in the injected precursor solution and the effective composition (measured by EPMA) of the lanthanum-nickelate films deposited on STO deposited at 750 °C. LNO₃ is obtained for La/Ni ratios in the film close to 1 while L₂N₄O₄ is obtained for ratios close to 2.

5.20 (La/Ni film ratio from 2.01 to 2.63), the characteristic peaks of the L₂N₄O₄ phase gain in intensity. However, two small peaks situated at 30° and 62° appear when the La/Ni solution ratio reaches 5.20 (2.63 for the film) and can be attributed to the presence of oriented La₂O₃ in the film. This confirms that the precursor solution is too rich in lanthanum, leading to the precipitation of this lanthanum rich oxide phase. The La₂O₃ phase seems to be already present at a lower ratio of 5.00 (2.19 for the film), but in a very small quantity.

These XRD patterns, combined with the EPMA results (Figure A.6) show that a La/Ni solution ratio of 2.38 and of 5.00 are a good starting point for growing LNO₃ and L₂N₄O₄ thin films, respectively, with the highest phase purity (on STO substrates and at T = 750 °C). However, the deposition temperature of LNO₃ was lowered afterwards to 600 °C to further improve the film quality (details on the optimization procedure of LNO₃ thin films are presented in Appendix B). The deposition temperature of L₂N₄O₄ was also lowered (to 650 °C) as a compromise to prevent the decomposition of LNO₃ in view of the preparation of L₂N₄O₄/LNO₃ bilayers (discussed in Chapter 5).

The fact of having changed the deposition temperature would require an additional optimization of the La/Ni ratio. However, this second optimization was not carried out due to a lack of time, and because the films showed satisfactory structural and electrical properties for their use in a proof-of-concept of L₂N₄O₄-based memristive devices.

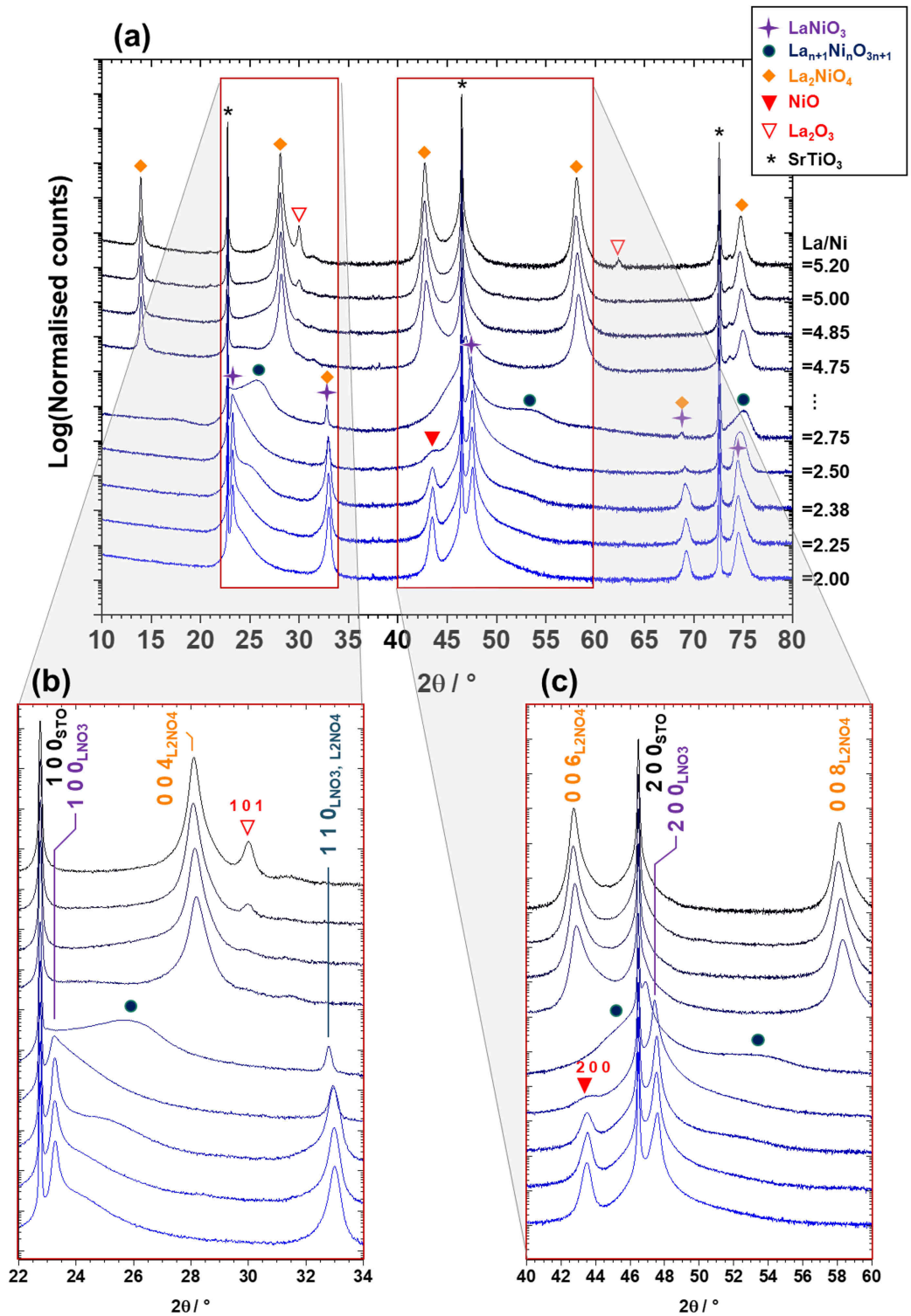


Figure A.7 – (a) θ - 2θ XRD patterns of lanthanum-nickelate thin films deposited on STO substrates with increasing La/Ni atomic ratios in the injected solution. (b) and (c) are magnifications of the areas inside the red rectangles drawn in (a). All the films were grown at $T = 750^\circ\text{C}$ with 4000 injected pulses of the different precursor solution.

Appendix B

LaNiO₃ thin film deposition and optimization by PiMOCVD

Contents

B.1 Experimental	163
B.1.1 Thin film deposition by PiMOCVD	163
B.1.2 Thin film characterization	165
B.2 LNO₃ deposition optimization using PiMOCVD	166
B.2.1 La and Ni atomic concentration in the injected solution	166
B.2.2 Temperature study	167
B.3 Film characterization	167
B.3.1 Electrical properties of the films	167
B.3.2 Strain effect in the epitaxial LNO ₃ /LAO and LNO ₃ /STO films	169
B.3.3 Microscopic Characterization of the microstructure: a TEM study	173
B.4 L₂N₂O₄/LNO₃ bilayers prepared by PiMOCVD	177
B.5 Conclusions	180

B.1 Experimental

B.1.1 Thin film deposition by PiMOCVD

LNO₃ thin films were deposited by PiMOCVD on STO (100) and LAO (100) perovskite single-crystal substrates (a pseudo-cubic setting was used for LAO). Silicon-based substrates

Parameter	Value
Substrate temperature	600-750°C
Evaporation temperature	280°C
Solution concentration	0.02 mol/L
Carrier gas	34% Ar (218 sccm) + 66% O ₂ (418 sccm)
Total pressure	5 Torr
Number of pulses	1000 – 4000

Table B.1 – Deposition conditions used for the growth of LNO₃ thin film by PiMOCVD

were also used for preliminary optimization tests. We used the PiMOCVD technique [115], based on the CVD process using vapours of metalorganics precursors that are evaporated by injecting small drops of a solution containing the cations. This technique allows to tune the film composition by varying the concentration of precursors in the solution. We used for this study Tris(2,2,6,6-tetramethyl-3,5-heptanedionato)lanthanum(III) (La(TMHD)₃, 99 %, 99.9 %-La, CAS 1419-13-2 from Strem Chemicals) and Bis(2,2,6,6-tetramethyl-3,5-heptanedionato)nickel(II), (Ni(TMHD)₂, min. 98 %, 99.9 %-Ni, CAS 41749-92-2 from Strem Chemicals) dissolved in a meta-xylene organic solvent (C₆H₄-(CH₃)₂, 99 %, CAS 108-38-3 from Alfa Aesar). The total precursor concentration was kept constant at 0.02 mol/L and the precursor ratio of La/Ni was around 2. The number of pulses was varied between 1000 and 4000 to obtain different film thicknesses. The standard deposition conditions are summarized in Table B.1. The composition of the injected solution and the deposition temperature were optimized to obtain highly oriented LNO₃ thin films on STO (LNO₃/STO) and LAO (LNO₃/LAO) and will be discussed in Section B.2.

The deposition optimization of L₂N₂O₄ by PiMOCVD was carried out in parallel and is detailed in Chapter 2. A preliminary study on the structural characteristics of two L₂N₂O₄/LNO₃ bilayers deposited on STO and on LAO, respectively, is presented at the end of the appendix where LNO₃ is used as a template for the growth of L₂N₂O₄. As these two lanthanum nickelate oxides show different thermodynamic stability ranges, a compromise in the deposition temperature was made. The optimal deposition temperature for L₂N₂O₄ (750°C) was lowered to 650°C to avoid the decomposition of the LNO₃ bottom layer. An optimized precursor ratio of La/Ni = 5.00 in the injected solution for the growth of L₂N₂O₄ was kept as a starting point for future optimization of these bilayers.

B.1.2 Thin film characterization

Phase identification, structural and crystallinity characterization of the samples were performed using X-ray diffraction (XRD) in θ - 2θ geometry (Bruker D8 Advance diffractometer) with monochromatic $\text{CuK}\alpha 1$ radiation ($\lambda = 1.5406 \text{ \AA}$). The presented XRD diffractograms were normalized in intensity and in position to the 2 0 0 substrate peak at 46.495° for LNO3 on STO and 47.960° for LNO3 on LAO. A PANalytical X'Pert MPD diffractometer was also used to acquire Grazing-Incidence XRD (GIXRD) diagrams for the films deposited on silicon during the preliminary tests. Grazing incidence was needed to reduce the important contribution of the substrate in the XRD diagrams. The morphology, chemical composition and thickness of the films were analysed using a scanning electron microscope (SEM) QUANTA 250 ESEM FEG. The overall atomic compositions and film thickness were determined by Electron-Probe Micro Analysis (EPMA) using a CAMECA SX50 spectrometer. Several areas were measured for each film at three different acceleration voltages in the range 10 to 20 keV. STRATAGEM software was used for data treatment. Film thickness, roughness and density were also determined by X-Ray Reflectivity (XRR) with a RIGAKU Smartlab diffractometer. Detailed structural characterizations of the films were carried out by transmission electron microscopy (TEM) with a JEOL 2010 microscope operated at 200 kV with a beam current of $110 \mu\text{A}$ (0.19 nm resolution) for high resolution TEM (HRTEM) studies. Scanning TEM (STEM) images were carried out with a JEOL 2100F microscope. For cross-section imaging, the samples were prepared with the MultiPrepTM system (Allied High Tech Products, Inc.), a semi-automated polishing tripod technique using diamond lapping films to achieve a sample thickness around $10 \mu\text{m}$. The final thinning of the TEM lamella was performed by a precision ion polishing system (PIPS, 691 model) with a milling angle of $\pm 7^\circ$ at 2.8 KeV and 500 eV to obtain a good electron-transparent area. Topography maps of the surface of the films were obtained using a Bruker Dimension 3100 Atomic Force Microscope (AFM) in tapping mode with an ARROW-NC tip from Nano-World (force constant of 42 N/m, resonance frequency of 285 kHz). The resistivity of the samples was obtained using a four probe measurement setup. Raman spectra were recorded at room temperature using a Horiba/Jobin Yvon LabRam spectrometer equipped with a liquid nitrogen cooled CCD detector. Experiments were conducted in the micro-Raman mode in a backscattering geometry using a 488 nm Ar^+ laser line for excitation. The laser light was focused with a x100 objective on a $1 \mu\text{m}^2$ spot at the sample surface and the laser power under the microscope was set to 1.3 mW to avoid laser heating effects. The Raman spectra were calibrated using a silicon reference spectrum (theoretical position at room temperature = 520.7 cm^{-1}).

B.2 LNO₃ deposition optimization using PiMOCVD

B.2.1 La and Ni atomic concentration in the injected solution

Prior to growing LNO₃ on perovskite single crystal substrates, preliminary investigations were carried out using films deposited at $T = 750^\circ\text{C}$ on a silicon-based substrate (Si(100) with a 300 nm thick SiN_x passivation layer) and the following La/Ni atomic ratios in the injected solution: La/Ni = 2.00, 2.25, 2.50 and 2.75. The corresponding GIXRD patterns (Figure B.1a.a) show the presence of a predominant polycrystalline LNO₃ phase (purple cross in the figure) coexisting with either a lanthanum rich phase (intermixed Ruddlesden Popper (RP) phases such as L₂NO₄ or La₄Ni₃O₁₀, dark blue dots in the figure) and/or a NiO phase (red triangle in the figure, cubic SG: Fm-3m (225), $a = 4.1771 \text{ \AA}$, ICDD: 00-047-1049). The amount of NiO is more important for the lowest La/Ni ratio whereas the quantity of RP phases is more important for high La/Ni ratios. This coexistence of LNO₃, Ni-rich and La-rich impurity phases is expected from thermodynamics [147] as low oxygen partial pressures (several Torr for PiMOCVD) and high temperatures favour the growth of higher order RP phases such as La₄Ni₃O₁₀, La₃Ni₂O₇ and L₂NO₄ rather than LNO₃. Figure B.1a.b shows XRD patterns corresponding to different La/Ni ratio in the injected solution for LNO₃/STO films. Note that the pseudocubic (resp. tetragonal I4/mmm) setting is used for the indexing scheme of LNO₃ (resp. L₂NO₄) and “h k l_{phase}” refers to the h k l Bragg reflection from any particular phase. For the three lowest La/Ni film ratios, highly textured LNO₃/STO films with h 0 0_{LNO₃} (purple label in the figure) are observed coexisting with NiO (red triangle in the figure) and RP or LNO₃ phases with [1 1 0]_{LNO₃, L₂NO₄} out of plane orientation (corresponding to the presence of 1 1 0_{LNO₃} and/or 1 1 0_{L₂NO₄} in the figure that will be indexed as 1 1 0_{LNO₃, L₂NO₄} in all the XRD diagrams). The observed coexistence of LNO₃, NiO and L₂NO₄ results from an instability of the LNO₃ at high temperature and low oxygen partial pressure [147]. Disordered RP phases (dark blue dots in the figure) become the majority phase for La/Ni = 2.75 in the solution whereas the NiO impurity is no longer present. The inset in Figure B.1a.b shows a linear dependence of the cationic ratio measured by EPMA in the films against the precursor ratios used in the injected solution for a deposition temperature of 750°C. An optimized La/Ni precursor ratio of 2.38 was extrapolated from this EPMA calibration curve to obtain films with the desired La/Ni = 1 ratio. It should be kept in mind that the optimal La/Ni film ratio is temperature dependent and that the coexistence of LNO₃, NiO and L₂NO₄ is observed even for the stoichiometric La/Ni = 1 ratio for the LNO₃ films obtained under the described deposition conditions. The presence of both Ni and La-rich impurities suggests that the deposition conditions are outside the thermodynamic stability zone for the growth of LNO₃ due to low oxygen partial pressure and high temperature used [147]. As this relatively low oxygen partial pressure is inherent

to the PiMOCVD technique, a study on the role of the deposition temperature on the phase stability was carried out and is presented in the next section.

B.2.2 Temperature study

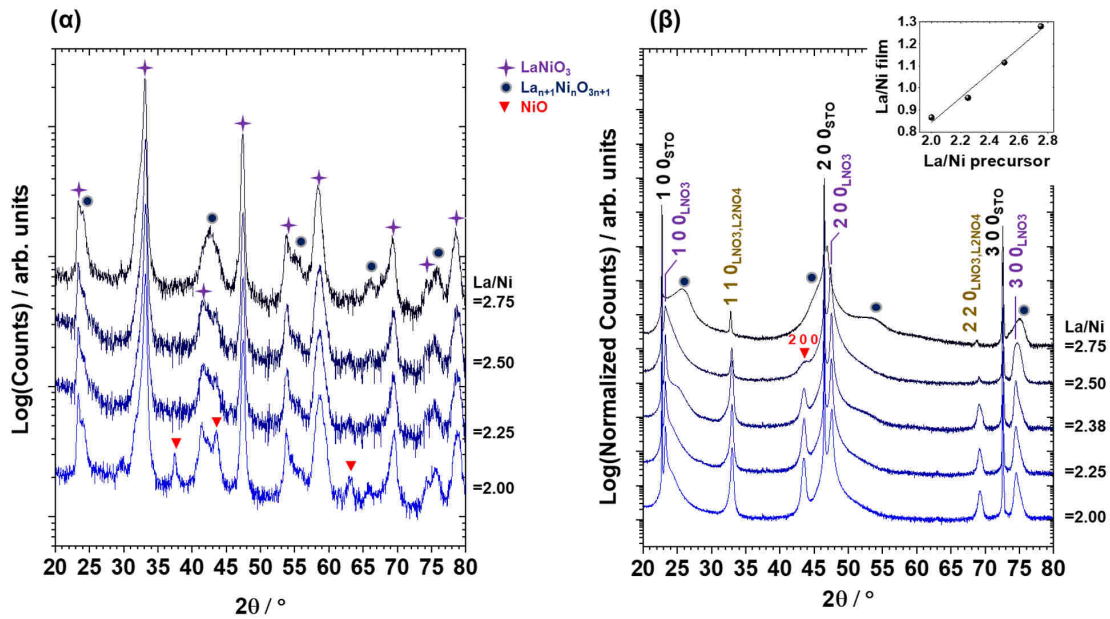
Two single crystal substrates with different lattice mismatch with respect to LNO₃ - STO, tensile strain of 1.79 % and LAO, compressive strain of -1.32 % - were used to study the effect of the deposition temperature on the phase stability and phase purity of the grown layer. Figure B.1b.α and β show the θ -2 θ XRD diagrams for films deposited on STO and LAO at temperatures between 550 and 750 °C using an initial precursor ratio La/Ni = 2.38 and 4000 pulses. The films thickness measured by XRR was between 78 and 92 nm (Figure B.2). The presence of predominant $h\ 0\ 0_{\text{LNO}_3}$ is clearly observed over the entire temperature range, both for films on STO and on LAO. At 750 °C the higher order RP phases are present (dark blue dots, broad intensities around $h\ 0\ 0_{\text{LNO}_3}$) as well as $h\ h\ 0_{\text{LNO}_3}$, L2NO₄ and also a small amount of NiO impurities. When decreasing the temperature, the higher order RP phases quickly disappear. At 550 °C, mainly $h\ 0\ 0_{\text{LNO}_3}$ are present with a rather weak $2\ 0\ 0_{\text{NiO}}$ reflection for LNO₃/STO suggesting that some NiO impurities are still present. This deposition temperature is coherent with the thermodynamic analysis carried out by Zinkevich *et al.* [147] when considering the operating oxygen partial pressure used in our PiMOCVD system (around 10^{-3} bar).

We finally note substrate-dependent effects in Figure B.1b.α and β: on the one hand the difference in the predominant orientation of NiO ($h\ 0\ 0_{\text{NiO}}$ on STO and $h\ h\ 0_{\text{NiO}}$ on LAO) and, on the other hand, the strong correlation between $h\ 0\ 0_{\text{NiO}}$ and $h\ h\ 0_{\text{LNO}_3, \text{L2NO}_4}$ in the films grown on STO. This points out a different microstructural accommodation of the NiO impurities together with the potential LNO₃ decomposition into L2NO₄ and NiO. The optimization procedure for L2NO₄ by PiMOCVD gave an optimal growing temperature around 750 °C. We therefore selected an intermediate temperature between 600-650 °C to grow LNO₃ on STO and LAO substrates in order to comply with these two conditions and minimize residual stress during the process.

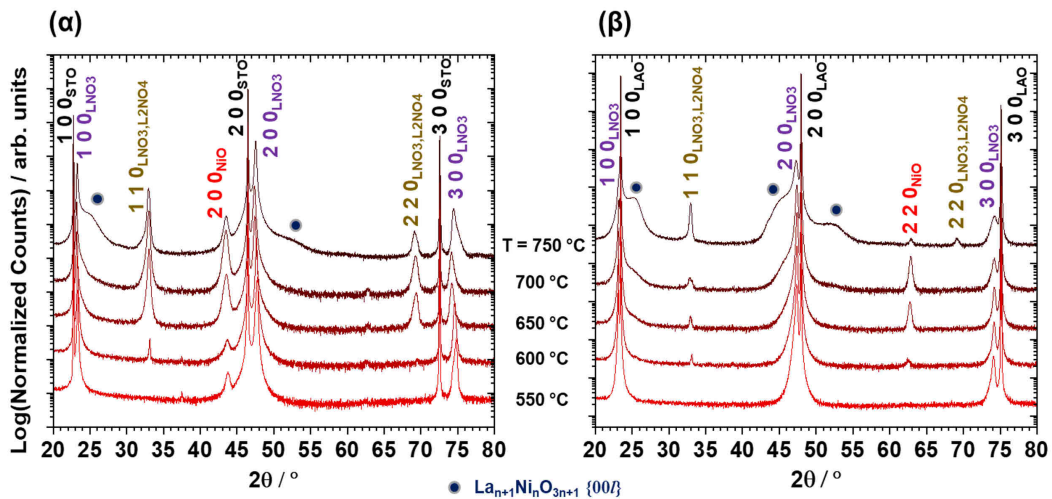
B.3 Film characterization

B.3.1 Electrical properties of the films

A relatively small influence of the La/Ni ratio on the resistivity is observed (Figure B.3a) as compared to the deposition temperature. Figure B.3b compiles the resistivity values for LNO₃ thin films deposited both on STO and on LAO as a function of the deposition temperature.



(a) (α) GIXRD patterns of LNO₃ thin films deposited on SiN_x with increasing La/Ni atomic ratios in the injected solution. (β) θ -2 θ XRD patterns of LNO₃ thin films deposited on STO substrates with increasing La/Ni atomic ratios in the injected solution. The inset shows the correlation between the calculated La/Ni atomic ratio in the injected precursor solution and the effective composition of the LNO₃ films deposited on STO as measured by EPMA. All the films were grown at T = 750 °C with 4000 injected pulses of the precursor solution at a frequency of 1 Hz.



(b) θ -2 θ XRD patterns of (α) LNO₃/STO and (β) LNO₃/LAO thin film samples using a fixed La/Ni precursor ratio of 2.38 and increasing the deposition temperatures. All the films have a thickness ranging between 80 and 90 nm (4000 pulses). Bragg peaks for rhombohedral LAO and LNO₃ are indexed in their pseudo-cubic lattice parameters.

Figure B.1 – Deposition optimization LNO₃ - XRD diagrams

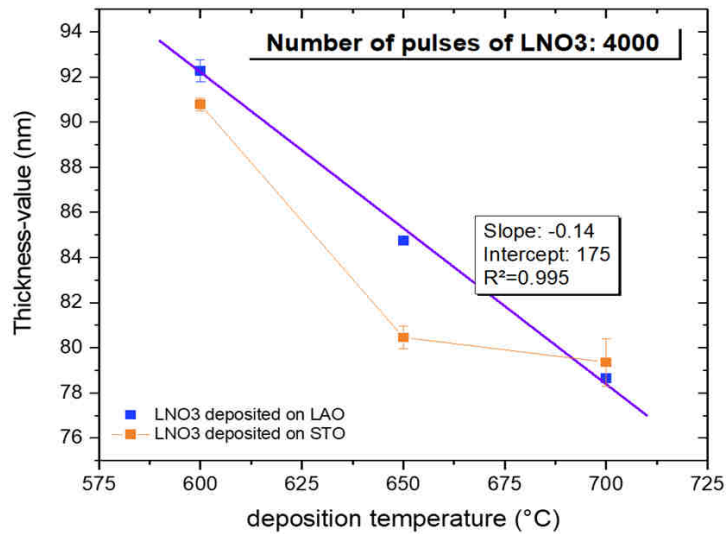
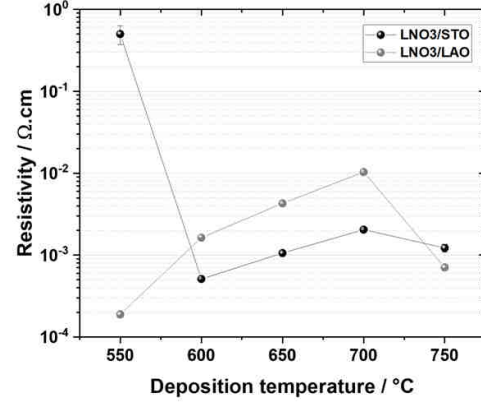
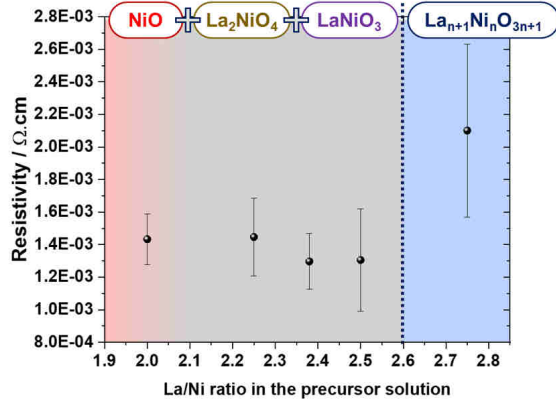


Figure B.2 – Correlation between the LNO3 film thickness as measured by XRR and the deposition temperature. The films were deposited both on STO (orange) and LAO (blue). The LAO dataset was best explained using a linear regression model (purple line) while the samples deposited on STO showed only a general tendency.

When decreasing the deposition temperature from 750 °C to 600 °C, the resistivity goes through a maximum at 700 °C for both types of samples before reaching 1.6 m Ω .cm and 0.5 m Ω .cm at 600 °C for films on LAO and on STO, respectively. When decreasing down to 550 °C, the sample deposited on LAO reaches state of the art resistivity values of around 200 $\mu\Omega$.cm. However, the resistivity measured for LNO3/STO deposited at the same temperature increases by several orders of magnitude up to 500 m Ω .cm. This is highly unexpected as the two samples were part of the same batch, thus deposited under identical conditions. A possible explanation could be a substrate-dependent percolation of insulating NiO impurities crossing the entire cross-section of the film (see Section 5.2.1 for more details).

B.3.2 Strain effect in the epitaxial LNO3/LAO and LNO3/STO films

To assess the clamping on the substrate and the resulting strain and modification of the structural properties of the films, LNO3 films with three different thicknesses have been deposited on STO and on LAO using the optimized deposition conditions discussed in the previous sections. The number of injected pulses was varied between 1000, 2000 and 4000 to obtain LNO3 films which correspond to thicknesses of around 15, 40 and 80 nm, respectively. The out of plane XRD patterns of the different samples are displayed in Figure B.4.a.



(a) Evolution of the LNO3 film resistivity as a function of La/Ni precursor ratio. All the films were deposited on STO single crystals at 750 °C using 4000 pulses (85±7 nm) of the precursor solution injected at 1 Hz with an opening time of 2 ms (only the La/Ni precursor ratio was varied). The error bars were calculated using the standard deviation of five consecutive 4-probe resistivity measurements done at different locations of the sample. Larger error bars thus represent samples having a larger inhomogeneity.

(b) Evolution of the LNO3 film resistivity as a function of the deposition temperature. Films were deposited simultaneously on STO and LAO single crystals using 4000 pulses (corresponding to a thickness of 85±7 nm) of the precursor solution (only the deposition temperature was varied). The error bars were calculated using the standard deviation of five consecutive four probe resistivity measurements at different locations on the sample (they lie within the data points when not visible).

Figure B.3 – Optimization of the LNO3 film resistivity.

Table B.2 – Out of plane lattice parameters of LNO3 films from Son *et al.*[121] are compared with our data on STO and LAO.

Substrate	Lattice parameter substrate (nm)	Lattice mismatch with LaNiO ₃ ($a_{\text{Substrate}} - a_{\text{LNO}_3, \text{bulk}} / a_{\text{Substrate}}$ in %)	LaNiO ₃ film thickness (nm)	Measured out of plane lattice parameter LaNiO ₃ (nm)	Reference
LaAlO ₃	*0.379	-1.32	10	0.3854	Son, J. et al. Low-dimensional Mott material: Transport in ultrathin epitaxial LaNiO ₃ films. Appl. Phys. Lett. 96, 062114 (2010).
LSAT	0.387	0.78	10	0.383	
DyScO ₃	0.394	2.54	10	0.384	
LaAlO ₃	0.379	-1.32	15	0.385	This work
SrTiO ₃	0.391	1.79	15	0.381	

*This value was corrected with respect to the one printed in the cited reference

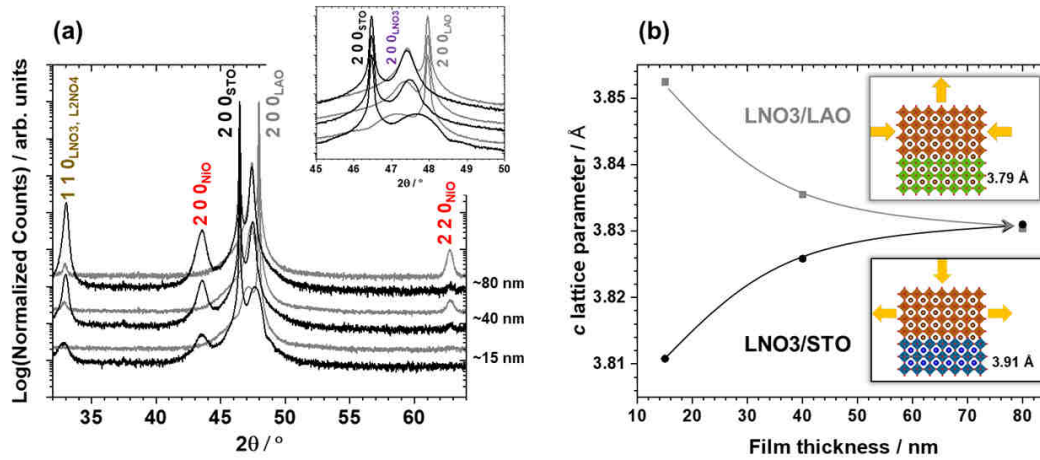


Figure B.4 – (a) XRD diagrams of LNO3/STO (black) and LNO3/LAO (grey) with increasing LNO3 film thickness. The inset is a magnification of the diagrams in the $46^\circ < 2\theta < 49^\circ$ region, encompassing the $2\ 0\ 0$ Bragg reflections of the STO and LAO substrates to better evidence the lattice relaxation of LNO3 when increasing the film thickness. (b) c lattice parameter relaxation with film thickness. The insets are sketches of the strain-induced lattice deformations of LNO3 grown on compressive LAO (top inset) and tensile STO (bottom inset). All the depositions were carried out at $650\ ^\circ\text{C}$ and with $\text{La/Ni} = 2.38$ in the precursor solution.

A clear peak displacement of $2\ 0\ 0_{\text{LNO}_3}$ is observed corresponding to a strain-induced lattice deformation of the perovskite structure and matches with a negative Poisson coefficient. Indeed, when grown on STO the basal plane of LNO3 experiences a tensile strain of 1.79 %, leading to a shortening of the perpendicular out of plane lattice parameter (see Table B.2 in supplementary information) as evidenced by a shift to higher 2θ values of the corresponding Bragg peak (inset in Figure B.4.a). The reverse situation is observed for the LNO3/LAO films where LNO3 experiences a compressive strain of -1.32 %. Both types of films grown on STO and on LAO relax to a common bulk pseudo-cubic out of plane lattice parameter of $c \approx 3.831\ \text{\AA}$ when increasing the film thickness from 15 to 80 nm as evidenced in Figure B.4.b. The schematics in this figure represent the strain state induced by clamping for both types of films. For LNO3/LAO films, a complementary analysis of the strain effect was investigated by Raman scattering experiments. A strong Raman scattering from STO precluded from recording Raman spectra of LNO3/STO films. According to the group theory, the Raman spectrum of LNO3 in its $R\text{-}3c$ rhombohedral structure is composed of five Raman-active modes ($A_{1g} + 4E_g$) [48] which have been observed for thin films [25]. As shown in Figure B.5, the five Raman-active modes are observed at 82, 153, 213, 401 and $447\ \text{cm}^{-1}$ for the 85 nm-thick LNO3 film. These values are very close to the positions obtained for a strain-free polycrystalline LNO3 film deposited on a Si substrate [25]. Due to the strong Raman lines of the LAO

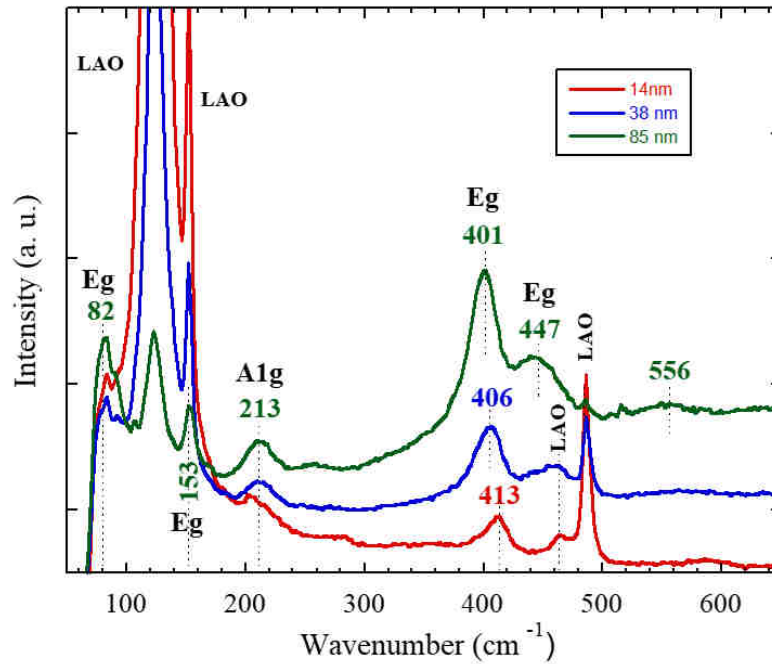


Figure B.5 – Raman spectra of LNO₃ films of different thicknesses (14, 38 and 85 nm). The films were deposited on LAO at 650 °C using an initial La/Ni ratio = 2.38 in the precursor solution. Lines are guides of for the eyes.

substrate in the thinnest film and to the proximity of several LAO and LNO₃ modes, only the positions of the E_g and A_{1g} modes respectively at 401 and 213 cm⁻¹ can be followed with decreasing film thickness. The most striking result concerns the shift of the E_g mode from 401 cm⁻¹ for the 85 nm-thick film to 413 cm⁻¹ for the 14 nm-thick film. This mode, attributed to a bending deformation of the oxygen octahedra [136], is directly related to the strain state of the film. This large shift towards high wavenumbers indicates a compressive strain in the film basal plane, which is in full agreement with the XRD results. No dependence on the film thickness is observed for the A_{1g} mode at 213 cm⁻¹, assigned to the [1 1 1] octahedral tilting vibration [136]. This is in agreement with previous observations [136] where strain relaxation mechanisms with thickness were interpreted as resulting from oxygen NiO₆ octahedron distortions rather than octahedron rotations (tilt).

Note that the additional mode observed at ~556 cm⁻¹ in the thickest film can be related to NiO detected in the LNO₃ XRD patterns [145] (see TEM discussion in the following subsection). As for the E_g mode at 447 cm⁻¹, its high intensity compared to the one usually observed could be explained by the presence of an additional mode at the same position, one possibility being the A_g mode at ~450 cm⁻¹ of L₂N₂O₄, which was detected by XRD in the

LNO₃ films [15, 32]. Raman and XRD results agree to indicate that the strain induced by the substrate is fully relaxed for the film thickness close to 80 nm. This value appears very large compared to that expected in high quality epitaxial films (usually relaxing the elastic stress due to the clamping on the substrate by dislocations) and questions about the relaxation mechanism which appears very complex in films thicker than 15 nm. It is certainly related to $1/2 \text{O}_{\text{LNO}_3, \text{L}_2\text{NO}_4}$ and additional NiO defects as clamping effects should rapidly become insignificant above a few nm. In particular, strain effects on the resistivity of LNO₃ films induced by clamping on the substrate should be negligible as they are usually reported for film thicknesses lower than 10 nm. For example Son *et al.* [121] showed that LNO₃ films deposited on LAO can have resistivity values at room temperature between 0.1 and 0.2 m Ω .cm for film thicknesses varying from 2.5 to 9 nm (with a metallic behaviour above 3 nm). Similar values are obtained for LNO₃/LSAT films where the resistivity at room temperature evolves from 10 to 1 m Ω .cm for 3, 4 and 5 nm thick films, respectively (LNO₃ shows a semiconducting behaviour below 4 nm). For thicker films (10-30 nm) the film resistivity is stable around 0.2 m Ω .cm. As the cubic lattice parameters of LSAT and STO are close, both should exert a tensile strain on LNO₃ (3.905 Å for STO compared to 3.87 Å for LSAT). This means that although the strain can affect the resistivity of LNO₃ over several orders of magnitude, it seems very unlikely to have an effect on films featuring a thickness above 10 nm. The variation in resistivity measured in our LNO₃/STO and LNO₃/LAO samples with increasing LNO₃ film thickness in the 13-85 nm range (Figure B.6) should thus be caused by a varying amount of impurity phases and/or a change of composition during the growth of LNO₃ (for example an increasing amount of oxygen vacancies).

More investigation about the relation between the microstructure and the film thickness has been undertaken using TEM and are presented in the next subsection.

B.3.3 Microscopic Characterization of the microstructure: a TEM study

Previous XRD results indicated that thin films (~15 nm) are dense and homogeneous with clear oscillations in the XRR patterns presented in Figure B.7.

The experimental density obtained from XRR is close to the expected theoretical value ($d = 7 \text{ g/cm}^3$) and the obtained thickness is $13.3 \pm 0.8 \text{ nm}$. This value is in good agreement with the thickness obtained from STEM (15 nm) in Figure B.8.a showing a cross section of a LNO₃/STO lamella with a dense microstructure. The contrast in the STEM images give evidence of the columnar-type growth of LNO₃, where the central column (one grain) is ~25 nm in diameter. Each column corresponds to LNO₃ in $[0\ 0\ 1]_{\text{LNO}_3} // [0\ 0\ 1]_{\text{STO}}$, $[0\ 1\ 0]_{\text{LNO}_3} // [0\ 1\ 0]_{\text{STO}}$ orientation relationship; it grows in a coherent way (cube on cube) with the STO substrate. This TEM observation corroborates the good microstructural qual-

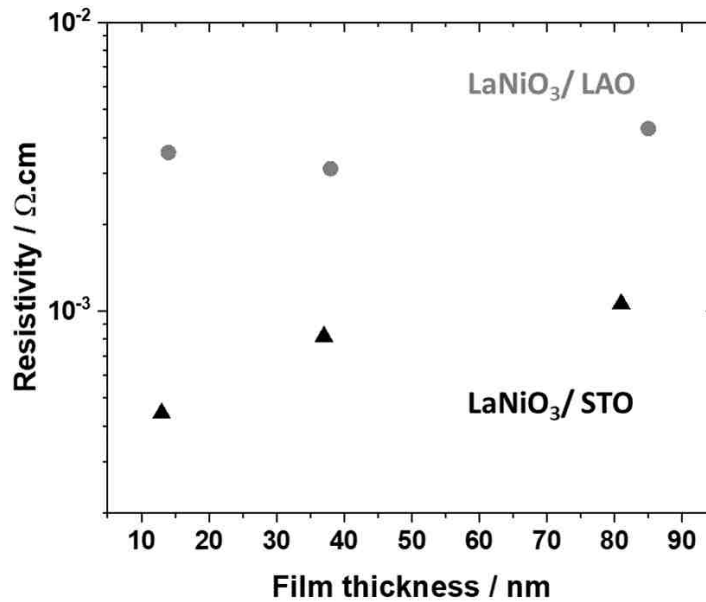
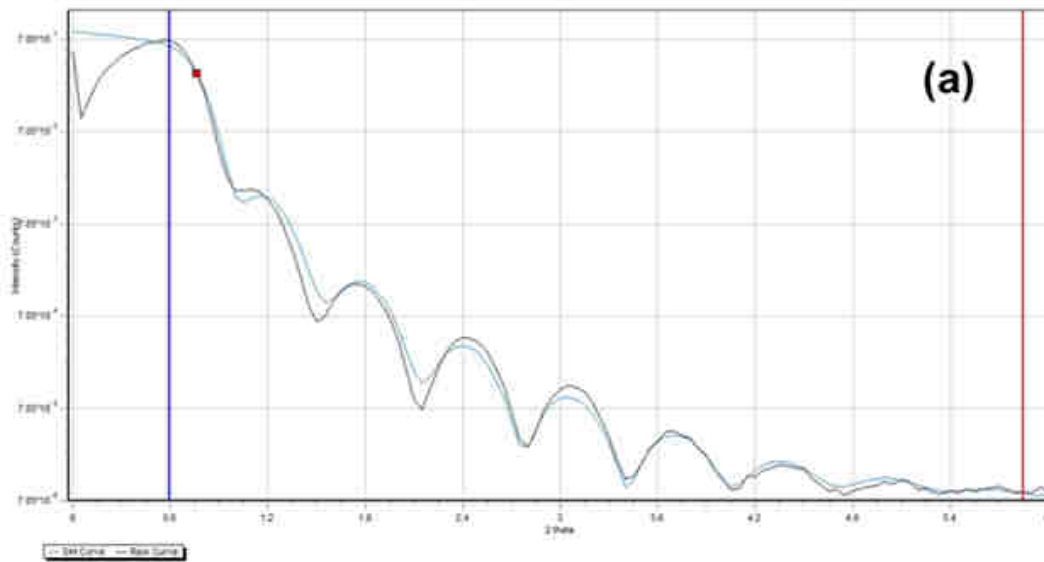


Figure B.6 – Resistivity of LNO₃ as a function of film thickness for films deposited on STO (triangles) and LAO (circles). All the films were deposited at 650 °C with La/Ni = 2.38 in the precursor solution.

ity of the sample as the measured thickness (~15 nm) matches with the correlation length calculated from the full width at half maximum of the $2\ 0\ 0_{\text{LNO}_3}$ diffraction peak, yielding a crystallite size of 14 nm.

Figure B.8.b shows a typical HRTEM image of the LNO₃/STO sample. Different contrasts are visible in the central region when compared to the lateral regions of the film (see autocorrelation images). These lateral regions present a contrast very similar to the substrate, corresponding to the cube-on-cube epitaxy of LNO₃ on STO. This observation is in good agreement with different orientations of the columns (Figure B.8.a) all corresponding to an orientation relationship of the type $[0\ 0\ 1]_{\text{LNO}_3} // [0\ 0\ 1]_{\text{STO}}$, $[0\ 1\ 0]_{\text{LNO}_3} // [0\ 1\ 0]_{\text{STO}}$. The columns with a different orientation grow coherently on STO and can retain strain due to clamping on the substrate. Despite the coherent growth of the LNO₃ epitaxial film, previous results on the resistivity and XRD indicate the presence of defects (depending on the thicknesses) in the form of NiO, La-rich phases and/or LNO₃ domains with a different orientation relationship than $[0\ 0\ 1]_{\text{LNO}_3} // [0\ 0\ 1]_{\text{STO}}$, $[0\ 1\ 0]_{\text{LNO}_3} // [0\ 1\ 0]_{\text{STO}}$. A deeper analysis of the HRTEM images (exemplified at the end of this subsection for LNO₃/LAO films) puts in evidence the presence of epitaxial NiO grown cube-on-cube on top of the STO substrate (with a $[0\ 0\ 1]_{\text{NiO}} // [0\ 0\ 1]_{\text{STO}}$, $[0\ 1\ 0]_{\text{NiO}} // [0\ 1\ 0]_{\text{STO}}$ orientation relationship). This is con-

N	R	Material	Cell input	Thickness	Roughness	Profile	Grading	Density I	Density B	Density N	SLPeriod
1	1	LaNiO3	density	13.2978	0.6485	No Gradient	10	7.79525	7.79525	7.086	13.2978
SUB	1	SrTiO3	density	0	0	No Gradient	0	5.117	5.117	5.117	0



N	R	Material	Cell input	Thickness	Roughness	Profile	Grading	Density I	Density B	Density N	SLPeriod
1	1	LaNiO3	density	13.8853	0.9018	No Gradient	10	6.62449	6.62449	7.086	13.8853
SUB	1	LaAlO3	density	0	0	No Gradient	0	5.5311	5.5311	5.5311	0

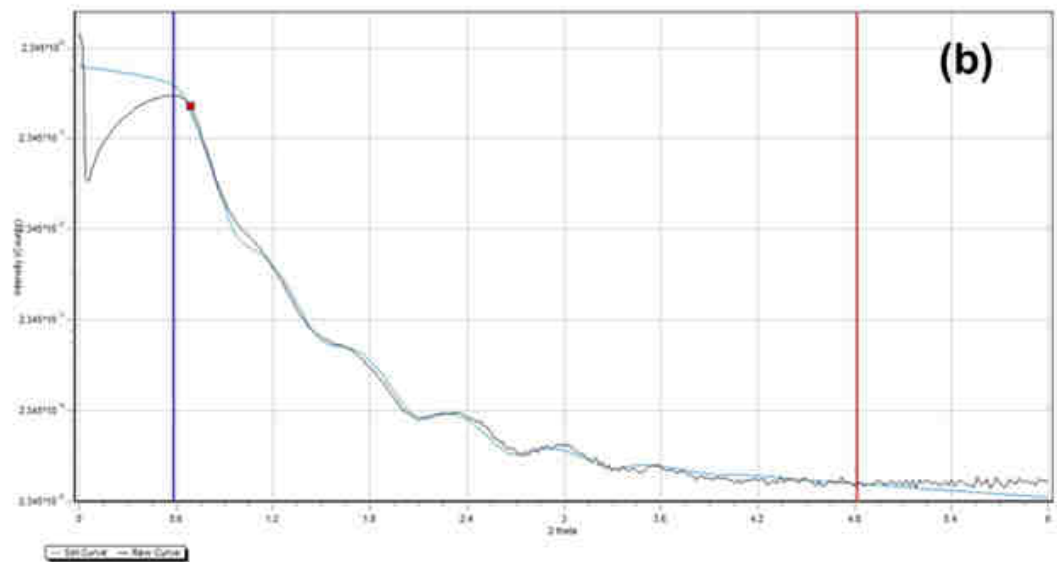


Figure B.7 – Measured and fitted XRR curves of LNO3 films obtained at 650 °C and with La/Ni = 2.38 in the precursor solution (~15 nm thick films). (a) LNO3/STO and (b) LNO3/LAO. Curve fitting was performed with LEPTOS software. The simulated layer density and thickness values are given in the tables displayed on top of each curve.

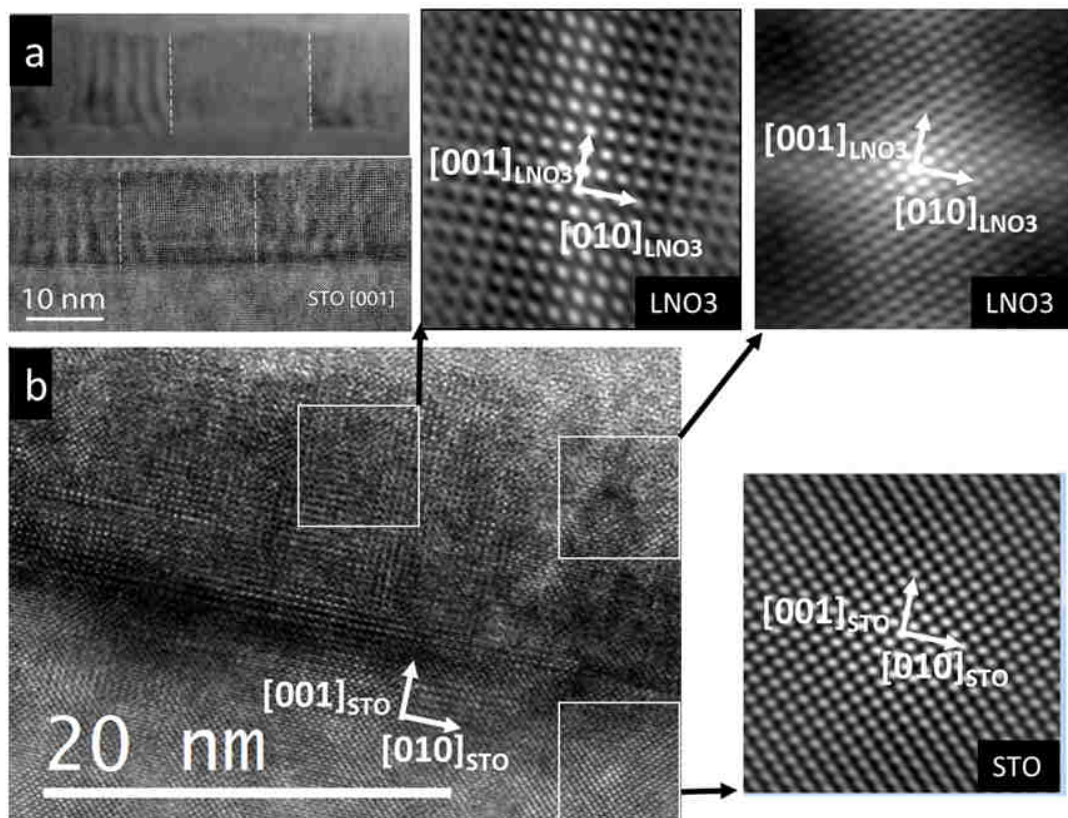


Figure B.8 – (a) STEM (top) and HRTEM (bottom) images presenting a general view of LNO3/STO obtained at 650 °C with La/Ni = 2.38 in the precursor solution (~15 nm thick films). (b) magnified HRTEM image for LNO3/STO. Enlarged auto correlation images of selected regions are included.

sistent with the previous XRD observations. This NiO phase surrounds another phase with a contrast compatible with L2NO4 with a $[1\ 1\ 0]_{\text{LNO4}}//[0\ 0\ 1]_{\text{STO}}$, $[0\ 0\ 1]_{\text{LNO4}}//[0\ 1\ 0]_{\text{STO}}$ orientation relationship. The situation is further complicated when considering the intricate thermodynamic stability of the La-Ni-O system and the different phases that can form (depending on the composition, temperature and oxygen partial pressure [147]). The existence of local intrinsic defects in the La-Ni-O system, for example in the form of RP-type of intergrowths, results in an important amount of discontinuities in the observed spacing between lattice fringes, and thus to additional reflections observed in the diffraction patterns [37]. Our HRTEM images show an important amount of these intergrowth-type defects, but an overall coherent growth of LNO3 is still achieved throughout the film. A rapid relaxation of the strain due to clamping on the substrate is thus expected even for the thinnest 15 nm-thick film. The lattice relaxation observed up to a thickness of ~80 nm probably finds its origin in another mechanism that should be consistent with the resistivity increase observed when increasing LNO3 film thickness on STO (Figure B.6).

A HRTEM image of the ~15 nm-thick LNO3 film grown on LAO shows that the film is dense and homogeneous (Figure B.9.a). The experimental density obtained from XRR is close to the expected theoretical value (6.6 instead of 7.1) and the fitted thickness is 13 ± 1.4 nm in agreement with the one obtained from HRTEM (15 nm). The dark contrast in Figure B.9.b corresponds to LNO3 whereas bright regions correspond to NiO and L2NO4 intergrowths. LNO3 and NiO are in $[0\ 0\ 1]_{\text{LNO3}}//[0\ 0\ 1]_{\text{LAO}}$, $[0\ 1\ 0]_{\text{LNO3}}//[0\ 1\ 0]_{\text{LAO}}$ and $[0\ 1\ 1]_{\text{NiO}}//[0\ 0\ 1]_{\text{LAO}}$, $[0\ 1\ -1]_{\text{NiO}}//[0\ 1\ 0]_{\text{LAO}}$ orientation relationships, respectively. They grow coherently on the substrate. A L2NO4-type phase is observed on top of the NiO phase and is better evidenced in the corresponding autocorrelation image. This phase has a $[0\ 1\ 0]_{\text{L2NO4}}//[0\ 0\ 1]_{\text{LAO}}$, $[0\ 0\ 1]_{\text{L2NO4}}//[0\ 1\ 0]_{\text{LAO}}$ orientation relationships.

B.4 L2NO4/LNO3 bilayers prepared by PiMOCVD

Figure B.10a shows the XRD patterns of a L2NO4/LNO3 bilayer obtained by PiMOCVD by successive depositions of LNO3 (600 °C, 15 nm thick) and L2NO4 (650 °C, 20 nm thick) layers. They were acquired before the deposition (bare STO and LAO substrates), after the deposition of LNO3 and after the completion of the entire L2NO4/LNO3/STO or L2NO4/LNO3/LAO stack in order to better evidence the phases formed after each deposition step. As almost no effect of La/Ni ratio is observed at 600 °C (Figure B.10b), the La/Ni precursor ratio was exceptionally increased from 2.38 to 2.75 in order to reduce the remaining NiO impurities but without success. The thickness fringes visible around the $2\ 0\ 0_{\text{LNO3}}$ support a coherent growth of these films with a homogeneous thickness. The L2NO4 layer has

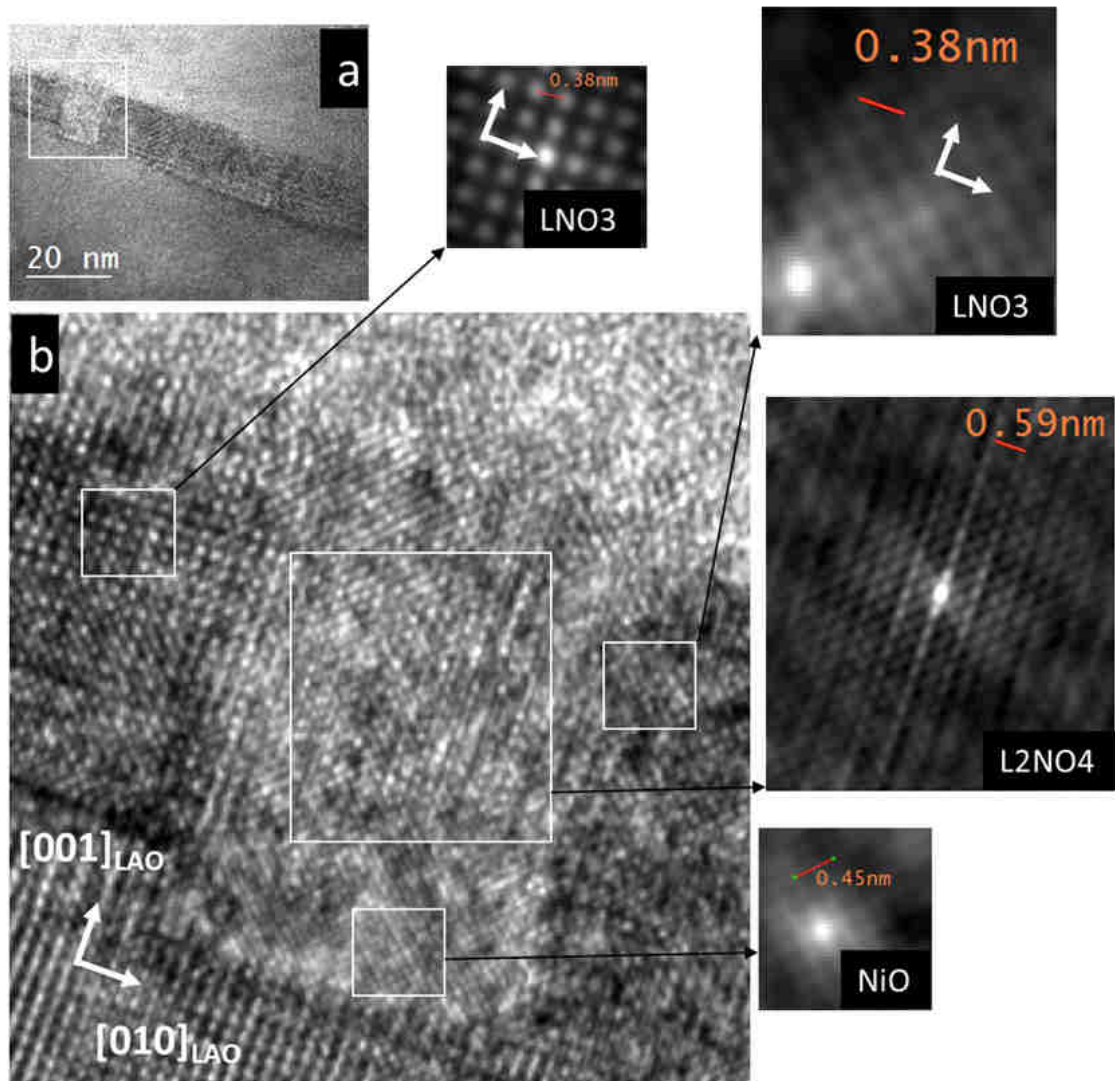
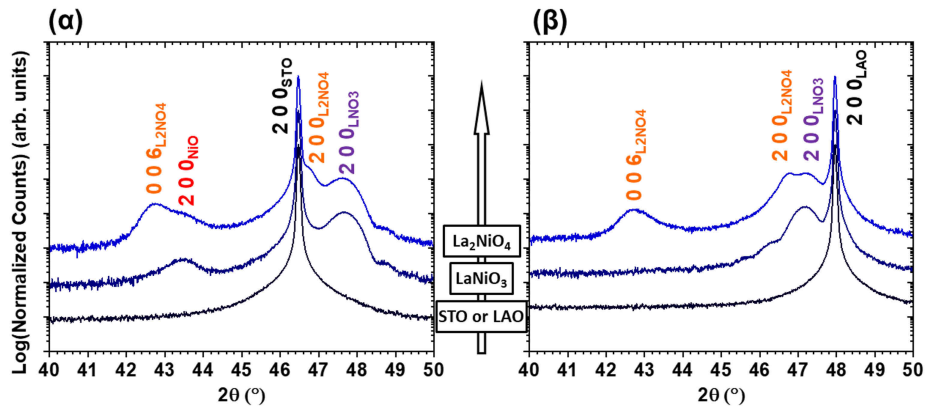
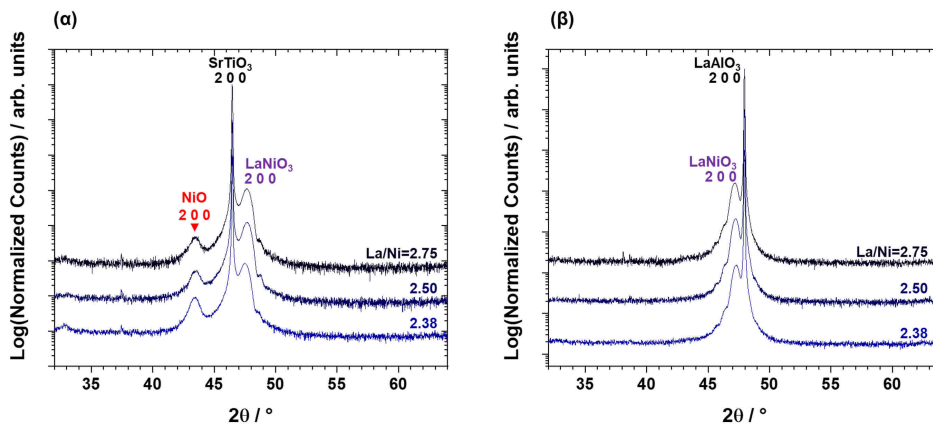


Figure B.9 – (a) HRTEM image of a LNO3/LAO film (~15 nm thick) deposited at 650 °C with La/Ni = 2.38 in the precursor solution. (b) magnification of (a) around the NiO/L2NO4 defect. Magnified auto correlation images of selected regions are also shown. The NiO phase is beneath the L2NO4 type phase.



(a) XRD patterns (θ - 2θ scans) of (α) L2NO4/LNO3/STO and (β) L2NO4/LNO3/LAO samples. A new pattern was acquired at each step of the deposition process (black line: substrate, dark blue LNO3/STO, lighter blue: L2NO4/LNO3/STO).



(b) Composition optimization carried out at 600 °C for (α) LNO3/STO and (β) LNO3/LAO samples. 1000 pulses ($f = 1$ Hz, opening time = 2 ms) were injected, corresponding to ~15 nm thick samples. The LNO3 films were deposited at the same time on both substrates using the same precursor solution.

Figure B.10 – XRD patterns of L2NO4/LNO3 bilayers and LNO3 single layers deposited on STO and LAO single-crystal substrates.

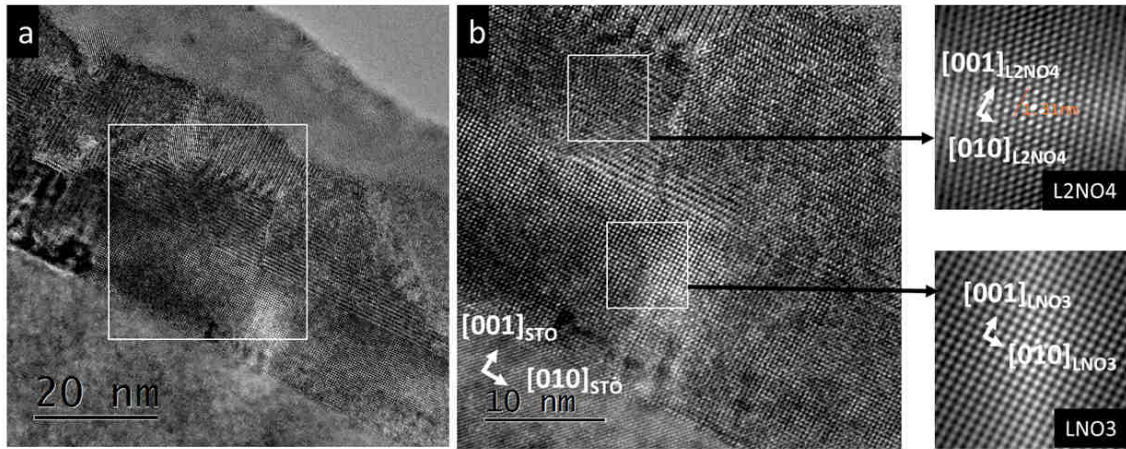


Figure B.11 – HRTEM images of a L2NO4/LNO3/STO bilayer. LNO3 (L2NO4) was deposited at 600 °C (650 °C) using a La/Ni ratio in the precursor solution of 2.75 (5.00). The LNO3 and L2NO4 layers are 15 nm and 20 nm thick, respectively. (a) General view. (b) Enlarged area corresponding to the white square in (a). Magnified auto correlation images of selected regions in (b) are also included.

two preferential orientations corresponding to the *c*-axis oriented in-plane and out of plane respectively (indexed as $0\ 0\ 6_{L2NO4}$ and $2\ 0\ 0_{L2NO4}$ reflections in Figure B.10a. α and β).

These two orientations are clearly evidenced in the cross-section HRTEM images of the L2NO4/LNO3/STO sample presented in Figure B.11. The LNO3 layer directly on top of the STO substrate has a cube-on-cube orientation relationship ($[0\ 0\ 1]_{LNO3} // [0\ 0\ 1]_{STO}$, $[0\ 1\ 0]_{LNO3} // [0\ 1\ 0]_{STO}$). L2NO4 then grows on top of LNO3 with the orientation relationship $[0\ 0\ 1]_{LNO3} // [0\ 0\ 1]_{L2NO4} // [0\ 0\ 1]_{STO}$, $[0\ 1\ 0]_{LNO3} // [0\ 1\ 0]_{L2NO4} // [0\ 1\ 0]_{STO}$ (the basal plane of the tetragonal L2NO4 matching with the *a*-*b* plane of LNO3). Nevertheless, while this orientation seems favourable from an epitaxial point of view, other domains of L2NO4 tilted at 90°, corresponding to the $[0\ 0\ 1]_{LNO3} // [0\ 1\ 0]_{L2NO4} // [0\ 0\ 1]_{STO}$, $[0\ 1\ 0]_{LNO3} // [0\ 0\ 1]_{L2NO4} // [0\ 1\ 0]_{STO}$ orientation relationships are also present. This reorientation had been previously observed when growing L2NO4/STO single layers [124].

B.5 Conclusions

The use of the PiMOCVD chemical deposition method allowed us to optimize the growth of LNO3 thin films with low resistivity for applications as bottom electrode and as template for growing L2NO4. In this study, the optimized parameters were the La/Ni precursor ratio and the deposition temperature. The set of optimal deposition conditions (La/Ni = 2.38, T = 600 °C) led to the growth of highly oriented LNO3 thin films both on SrTiO₃ and LaAlO₃

substrates with a reduced amount of coherent Ni and La-rich impurities. Resistivity values as low as $200 \mu\Omega\cdot\text{cm}$ validate further use of LNO3 as a template electrode for the growth of oriented LNO4 layers. Strain effects induced by the substrate were observed in LNO3/STO and LNO3/LAO films up to 80 nm of thickness, which are related to a complex microstructure of the films due to the coexistence of NiO, LNO3 and L2NO4 especially for the thickest films. Moreover, the first L2NO4/LNO3 bilayers were successfully grown using the PiMOCVD technique, although further optimization is still required to obtain higher epitaxial quality of the films with in particular less in-plane L2NO4 domain orientations.

Appendix C

Methods

Contents

C.1 Cleanroom microfabrication	183
C.2 Thin film characterization	185
C.2.1 X-Ray Diffraction	185
C.2.2 Reciprocal Space Maps of La_2NiO_4	185
C.2.3 Transmission Electron Microscopy	187
C.2.4 X-ray Photoemission Electron Microscopy (XPEEM)	188
C.2.5 Electron-Probe Micro-Analysis	189
C.2.6 Atomic-Probe Microscopy	190
C.2.7 Electrical Characterization	190
C.2.8 Raman Spectroscopy	190
C.3 Details on the Transmission Line Measurements (TLM) measurements	190
C.4 Conduction mechanisms in a metal/oxide/metal heterostructure	192

The details and instruments of the main microfabrication, structural, chemical and electrical characterization techniques used during this thesis are briefly described in this Appendix.

C.1 Cleanroom microfabrication

The microfabrication of Ag, Pt and Ti metallic contacts was carried out at the Plateforme de Technologie Amont (PTA) cleanroom facilities in Grenoble. The contacts were fabricated by e-beam induced metal evaporation (MEB550 from PLASSYS evaporator) at ambient temperature using a laser-assisted lithography process. A mild Ar^+ etch was used to prepare the

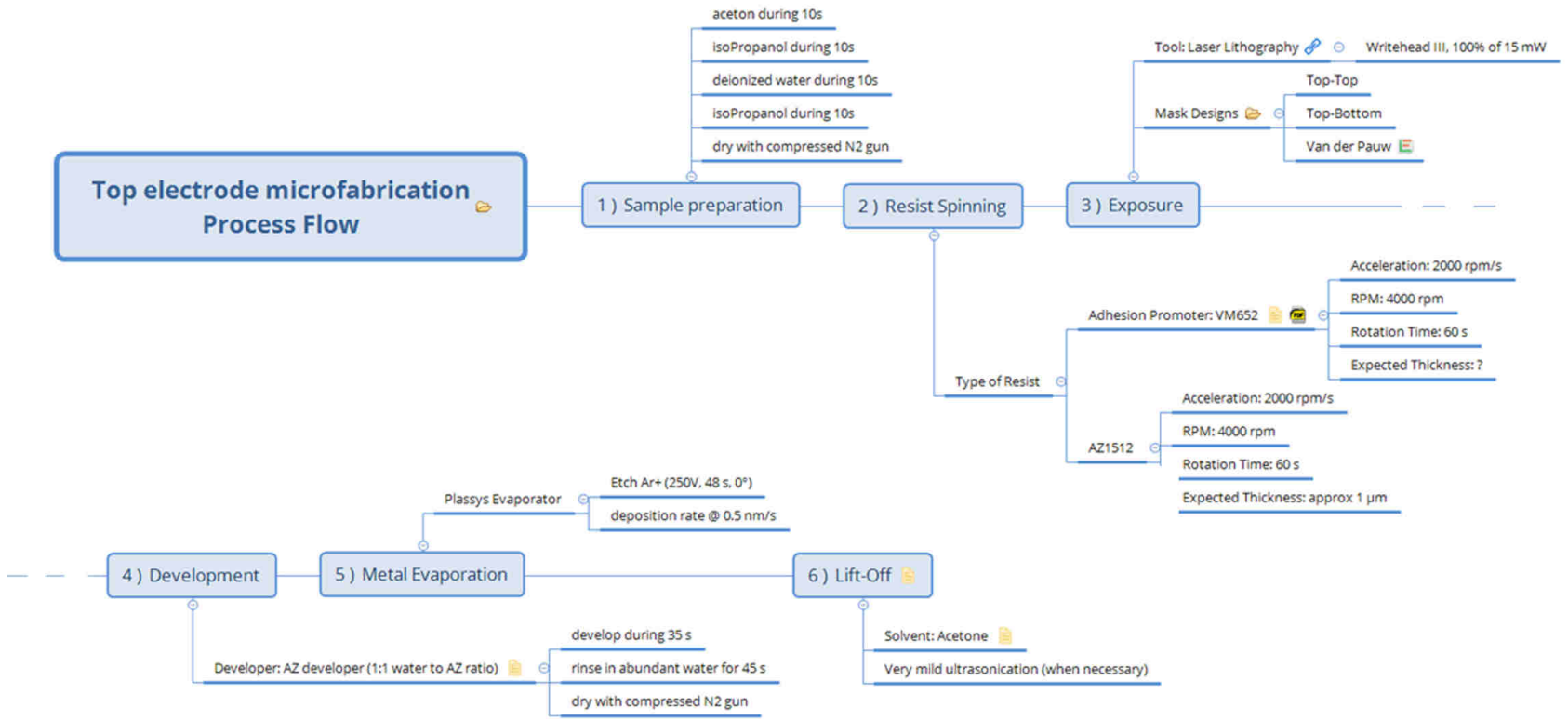


Figure C.1 – Process flow followed during the cleanroom microfabrication of metallic top electrodes.

exposed surface of the patterned sample and remove potential left-overs of the photoresist before metal evaporation. Figure C.1 shows the process flow followed for the preparation of the metallic top electrodes.

C.2 Thin film characterization

C.2.1 X-Ray Diffraction

Phase identification, structural and crystallinity characterization of the samples were performed using X-ray diffraction (XRD) in θ - 2θ geometry (Bruker D8 Advance diffractometer for the PiMOCVD films and PANalytical X'Pert Pro MRD diffractometer for the PLD films) with monochromatic $\text{CuK}_{\alpha 1}$ radiation ($\lambda = 1.5406 \text{ \AA}$). If not specified otherwise in the text, the presented XRD diffractograms have been normalized in intensity and in position to the 2 0 0 substrate peak at 46.495° for LNO3 on STO and 47.960° for LNO3 on LAO. A PANalytical X'Pert MPD diffractometer was also used to acquire Grazing-Incidence XRD (GIXRD) patterns. Grazing incidence was required (sporadically) to reduce the important contribution of the substrate (eg. on Si substrates) in the XRD diffractograms. The 'h k l_{phase}' writing convention has been used throughout the thesis to refer to the h k l Bragg reflection from any particular phase (e.g. 0 0 6_{L2NO4} refers to the 0 0 6 Bragg reflection of La_2NiO_4). Bragg peaks for rhombohedral LaAlO_3 and LaNiO_3 have been indexed in their pseudo-cubic lattice parameters.

Film thickness, roughness and density were also determined by X-Ray Reflectivity (XRR) with a RIGAKU Smartlab diffractometer.

C.2.2 Reciprocal Space Maps of La_2NiO_4

Figure C.2 illustrates the regions of the reciprocal space for L2NO4/STO samples deposited by PLD and measured using a PANalytical X'Pert Pro MRD lab diffractometer (ICN2, Barcelona) with a multichannel X-ray detector (PIXcel from Panalytical). It shows the indexed theoretical diffraction peaks which can be expected in these regions when considering a sample composed of three orthogonal orientations of the c -axis of tetragonal L2NO4 (ICDD: 00-034-0314, SG: I4/mmm (139), $a = b = 3.8617 \text{ \AA}$, $c = 12.683 \text{ \AA}$), consisting in one out of plane orientation (c -domains) and two in-plane orientations which are referred to as the a and b domains when the c -axis of L2NO4 lies along the a or the b -axis of the (1 0 0) SrTiO_3 single-crystal substrate (taken as reference). The results of the RSM measurements are shown in Section 5.3.2

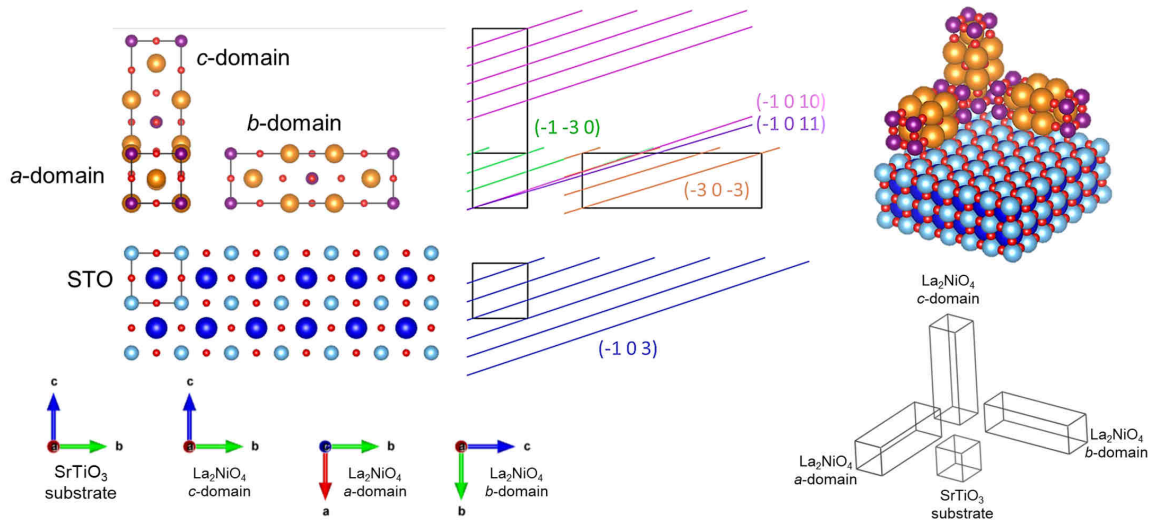


Figure C.3 – Schematic representation of the crystal orientation of tetragonal L2NO4 on top of STO and the position of the atomic planes responsible for the theoretical diffraction peaks shown in Figure C.2.

Figure C.3 illustrates the aforementioned crystal orientations of L2NO4 on top of the same (1 0 0) SrTiO₃ substrate, better showing the family of crystal planes responsible for the theoretical diffraction peaks shown in Figure C.2.

C.2.3 Transmission Electron Microscopy

Detailed structural characterization of the films was carried out by transmission electron microscopy (TEM) with a JEOL 2010 microscope operated at 200 kV with a beam current of 110 μ A (0.19 nm resolution) for high resolution TEM (HRTEM) studies. Scanning TEM (STEM) images were carried out with a JEOL 2100F microscope. For cross-section imaging, the samples were prepared with the MultiPrep™ system (Allied High Tech Products, Inc.), a semi-automated polishing tripod technique using diamond lapping films to achieve a sample thickness around 10 μ m. The final thinning of the TEM lamella was performed by a precision ion polishing system (PIPS, 691 model) with a milling angle of $\pm 7^\circ$ at 2.8 KeV and 500 eV to obtain a good electron-transparent area. In specific cases when a precise region of the sample needed to be imaged (for example below a specific electrode), cross-section lamellas were prepared with a focus ion beam (FIB) instead of the tripod technique.

For the specimens prepared by FIB (Figure 2.8 and Figure 3.8a-b), a FEI strata 400S equipped with a dual beam electron/Ga⁺ ions has been used. First an insulating layer is deposited inside the FIB chamber followed by a tungsten layer, to protect the surface of the sample.

A chunk of the sample is then extracted after milling it with Ga^+ ions accelerated at 30 kV. The chunk is placed on a TEM copper (Cu) grid with the help of a micromanipulator (from Omniprobe) and maintained in place with tungsten (deposited inside the FIB chamber). The regions of interest (ROI) to be analysed are thinned using Ga^+ ions with decreasing acceleration, from 16 kV to 2 kV in order to limit the amorphisation of the sample. The ROI is thinned to approximately 100 nm. High resolution STEM images have been acquired on a FEI TITAN Themis microscope with an electron acceleration of 200 kV.

Electron Energy Loss Spectroscopy (EELS) measurements EELS mapping has been carried out on a FEI Titan Themis microscope with an electron acceleration of 200 kV. The microscope is probe corrected, and is equipped with a Gatan Image Filter (GIF) Quantum with a CCD camera of 2048 pixels by 256 pixels allowing dual EELS and 2048 pixels-long spectras, this GIF is monitored by Gatan Microscope Suite 3 (GMS 3). The probe current has been fixed to 300 pA to maximize the intensity, at the same time increasing the signal to noise ratio but also avoiding damaging the sample with the electron beam. Similarly, the pixel size was set to 1.5 nm, offering a good spatial resolution and avoiding damaging the sample by the electron beam. The spectra are aligned with respect to the zero loss peak acquired simultaneously thanks to the dual EELS GIF. The element profiles have been obtained by integrating the area below the respective edges using a conventional GMS 3 data treatment.

C.2.4 X-ray Photoemission Electron Microscopy (XPEEM)

One L2NO4/STO $10 \times 10 \text{ mm}^2$ ‘as deposited’ (pristine) sample was cut in two pieces, one of which was annealed in flowing O_2 at 500 °C during one 1 h to increase its oxygen content and increase its hole carrier concentration by a self-doping process (see subsection: **Hole self-doping and electronic conductivity in L2NO4** in Chapter 2). The work function of the two samples was then measured using a XPEEM with a high transmission, aberration-compensated energy filter (double hemispherical analyser) and a focused monochromatic Al K source (1486.6 eV), the results are presented in Figure C.4. Both samples received a very mild argon-cluster etch (Ar^+2500 , 10 keV during 1 min) to remove possible surface contamination prior to the PEEM measurements.

The samples were stored in UHV (10^{-10} mbar) during 30 days after surface treatment and before the XPEEM measurements due to an issue with the measurement setup that needed to be fixed. A reduction of the L2NO4 films due to an equilibration of the sample with the atmosphere during that time period cannot be discarded, making it difficult to relate the measured work function directly with a precise oxygen content of the two samples. Nevertheless, relative differences between the pristine and the oxygen-annealed sample remain valid argu-

ments for the presumption that the additional oxygen ions (incorporated into the lattice after annealing the films in an oxidizing atmosphere) act as an acceptor dopants in L2NO_4 .

C.2.5 Electron-Probe Micro-Analysis

The morphology, chemical composition and thickness of the films were analysed using a scanning electron microscope (SEM) QUANTA 250 ESEM FEG. The overall atomic compositions and film thickness were determined by Electron-Probe Micro Analysis (EPMA) using a CAMECA SX50 spectrometer. Several areas were measured for each film at three different acceleration voltages in the range 10 to 20 keV. STRATAGEM software was used for data treatment.

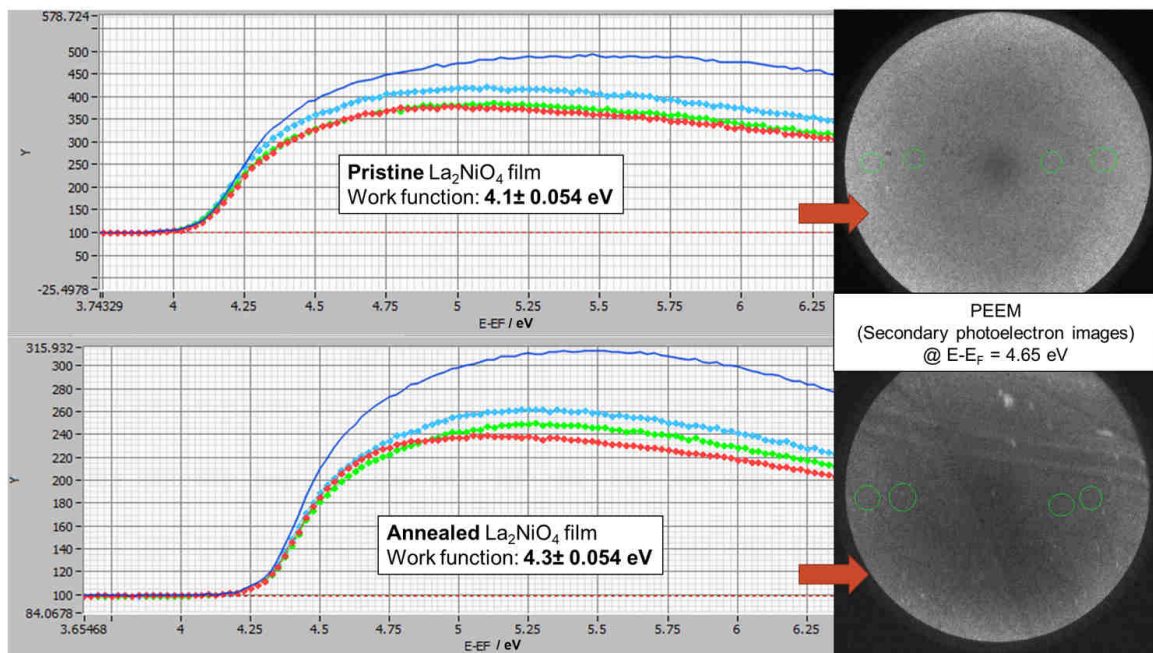


Figure C.4 – Secondary photoelectron energy spectrum ($E-E_f$) taken on two different $\text{L2NO}_4/\text{STO}$ samples. The first sample (top) is as deposited by PiMOCVD without further annealing post treatment (pristine), while the second one (bottom) is a piece of the same pristine sample but post-annealed in O_2 at 500°C during 1 h (with a heating ramp of $10^\circ\text{C}/\text{min}$). The corresponding secondary electron images taken at $E-E_f = 4.65\text{ eV}$ are displayed on the right side of each spectrum. Both samples received a very mild argon-cluster etch (Ar^+2500 , 10 keV during 1 min) to remove possible surface contamination before carrying out the XPEEM measurements.

C.2.6 Atomic-Probe Microscopy

Topography maps of the surface of the films were obtained using a Bruker Dimension 3100 Atomic Force Microscope (AFM) in tapping mode with an ARROW-NC tip from Nano-World (force constant of 42 N/m, resonance frequency of 285 kHz).

C.2.7 Electrical Characterization

The resistivity of the samples was obtained using a four probe measurement setup.

When not expressed otherwise, all measurements were carried out in ambient conditions. Current-Voltage (I-V) characteristics were obtained using a source-measurement unit (Agilent B1500) using two tungsten-carbide probes operated in a voltage-control mode in a Karl-Suss probe station. The devices were packaged when required, as in the case of the low temperature measurements carried out in vacuum. When not specified otherwise, the sweeps always start at zero bias and go as follows: 0 V \rightarrow +Vmax \rightarrow 0 V \rightarrow -Vmin \rightarrow 0 V. Current-time (I-t) characteristics when operated in “pulsed mode” consist in applying a voltage stress at higher voltages (≥ 1 V) to program the device to a higher or lower resistance state, applying either a positive or negative voltage, respectively. The remnant resistance state of the device is then readout after each programming pulse at a lower V = +10 mV bias to ensure that no ionic movement would be triggered by the electrical field.

C.2.8 Raman Spectroscopy

Raman spectra were recorded at room temperature using a Horiba/Jobin Yvon LabRam spectrometer equipped with a liquid nitrogen cooled CCD detector. Experiments were conducted in the micro-Raman mode in a backscattering geometry using a 488 nm Ar⁺ laser line for excitation. The laser light was focused with a x100 objective on a 1 μm^2 spot at the sample surface and the laser power under the microscope was set to 1.3 mW to avoid laser heating effects. The Raman spectra were calibrated using a silicon reference spectrum (theoretical position at room temperature = 520.7 cm^{-1}).

C.3 Details on the Transmission Line Measurements (TLM) measurements

As explained in Chapter 3, subsection 3.2.2, TLM measurements have been carried out on L2NO4/STO samples using bar-shaped platinum electrodes. The sketch and picture of the TLM test pattern are shown in Figure 3.6.

Here the derivation of Equation 3.3 and 3.4 used for the determination of the contact resistance, the sheet resistance and the transmission length after having carried out a TLM measurement (the equation is used for example in subsection 3.2.2) is detailed.

The total resistance measured in a passive metal/semiconductor/metal device can be expressed as follows:

$$R_T = R_{semi} + 2R_m + 2R_C \quad (C.1)$$

where R_T is the total resistance of the device, R_m is the resistance of the Pt electrode, R_C is the contact resistance between the metal and the semiconductor and R_{semi} is the resistance of the semiconductor. As a metal is a very good electronic conductor, its contribution to the total resistance is usually negligible compared to the resistance of the semiconductor, or even when compared to the contact resistance. Furthermore, the resistance of the semiconductor can be expressed as a function of its sheet resistance R_S :

$$R_{semi} = R_S \frac{L}{l} \quad (C.2)$$

where L is the length of semiconductor traversed by the current (distance between the electrodes used for the measurement), l is the length of the electrode. Equation C.1 now becomes:

$$R_T = \frac{R_S}{l}L + 2R_C \quad (C.3)$$

The contact resistance can also be expressed in terms of the specific contact resistivity ρ_C (expressed in $\Omega.cm^2$):

$$R_C = \frac{\rho_C}{L_T.l} \quad (C.4)$$

where L_T is the transfer length, or the average distance a charge carrier travels in the semiconductor beneath the contact before being injected in it. The transfer length can also be expressed as a function of the contact resistivity of the metal/semiconductor junction and the sheet resistance of the semiconductor (from equivalent circuit considerations) as follows:

$$L_T = \sqrt{\frac{\rho_C}{R_S}} \quad (C.5)$$

When taking into consideration Equations C.4 and C.5, Equation C.3 becomes:

$$\begin{aligned}
 R_T &= \frac{R_S}{l}L + 2R_C \\
 &= R_S \frac{L}{l} + 2 \frac{\rho_C}{L_T \cdot l} \\
 &= R_S \frac{L}{l} + 2 \frac{(R_S \cdot L_T^2)}{L_T \cdot l} \\
 &= \frac{R_S \cdot L}{l} + 2 \frac{R_S \cdot L_T}{l}
 \end{aligned}$$

and finally:

$$R_T = \frac{R_S}{l}(L + 2L_T) \quad (\text{C.6})$$

When plotting the measured resistance R_T for different pairs of identical electrodes with increasing distance between them, *i.e.* R_T vs L , and using a linear regression to fit the obtained curve, the sheet resistance can be retrieved from the slope of the linear regression line, the contact resistance and the transfer length can be obtained from the intercept of the linear regression line with the y-axis and the x-axis, respectively.

Once we have all these values, the contact resistivity can then be calculated as follows (using Equation C.4):

$$\rho_C = R_C \cdot L_T \cdot l$$

The contact resistivity is an intrinsic property of every metal-semiconductor couple (it will vary if one of the two is changed).

C.4 Conduction mechanisms in a metal/oxide/metal hetero-structure

Table C.1 shows the electric field and/or temperature dependence of the current density for the different conduction mechanisms illustrated in Figure 3.1 (Chapter 3).

Table C.1 – Equations expressing the field and temperature dependence of each of the conduction mechanisms presented in Figure 3.1 (from [27, 83]).

Conduction Mechanism	Current density dependence on electric field and temperature		Comments
	Complete expression	Simplified expression (A and B are constants)	
Interface limited conduction:			
(1) Schottky (Sch) emission	$J_{SchE} = A * T^2 \exp \left[\frac{-q \left(\phi_B - \sqrt{\frac{qE}{4\pi\epsilon}} \right)}{k_B T} \right]$	$J_{SchE} \propto T^2 \exp \left(A \frac{\sqrt{E}}{T} - B \right)$	Important at high T
(2) Fowler-Nordheim (FN) tunnelling	$J_{FN} = \frac{q^2}{8\pi\phi_B} E^2 \exp \left[\frac{-8\pi\sqrt{2qm^*} \phi_B^{3/2}}{3hE} \right]$	$J_{FN} \propto E^2 \exp \left(\frac{-A}{E} \right)$	Measured at low T
(3) Direct tunnelling	$J_{DT} \approx \exp \left[\frac{-8\pi\sqrt{2qm^*} \phi_B}{3h} \kappa t_{ox,eq} \right]$	$J_{DT} \propto \exp \left(-A \cdot \kappa t_{ox,eq} \right)$	Measured at low T, $t_{ox,eq} < 3 \text{ nm}$
Bulk limited conduction			
(4) Poole-Frenkel (PF) emission	$J_{PF} = q\mu N_C E \exp \left[\frac{-q(\phi_T - \sqrt{\frac{qE}{4\pi\epsilon}})}{k_B T} \right]$	$J_{PF} \propto E \exp \left(A \frac{\sqrt{E}}{T} - B \right)$	For high T and high E
(5) Ohmic conduction	$J_{Ohm} = \sigma E = q\mu N_C E \exp \left[\frac{-(E_C - E_F)}{k_B T} \right]$	$J_{Ohm} \propto E \exp \left(\frac{-A}{T} \right)$	Always present at very low E
(6) Space-charge limited conduction (SCLC)			
a. Ohmic region	$I \propto V$	$J \propto E$	Ohmic-like region at low E
b. Trap-unfilled region	$I \propto \frac{9}{8} \epsilon_i \mu \theta \frac{V^2}{d^3}$	$J_{SCLC} \propto E^2$	Child's square law region, in the case of a single discrete trap level
c. Trap-filled region	$I \propto V^n, n > 2$	$J_{SCLC} \propto E^n, n > 2$	Steep increase of current at high field

(7) Ionic conduction	$J_{ionic} \propto \frac{E}{T} \exp \left[\frac{-\Delta G^*}{k_B T} \right]$	$J_{ionic} \propto \frac{E}{T} \exp \left(\frac{-A}{T} \right)$	
(8) Hopping conduction			For low E
a. Nearest neighbour hopping (NNH)	$J_{NNH} = \sigma_0 E \exp \left(\frac{-T_0}{T} \right)$	$J_{NNH} \propto E \exp \left(\frac{-A}{T} \right)$	
b. Variable-range hopping (VRH)	$J_{VRH} = \sigma_0 E \exp \left(\frac{-T_0}{T} \right)^{1/4}$	$J_{VRH} \propto E \exp \left(\frac{-A}{T} \right)^{1/4}$	
(9) Trap-assisted tunnelling (TAT)	$J_{TAT} = A \exp \left[\frac{-8\pi\sqrt{2qm^*}}{3hE} \phi_T^{3/2} \right]$	$J_{TAT} \propto \exp \left(\frac{-A}{E} \right)$	Measured at low T

J is the current density, $A = \frac{4\pi m^* k_B^2}{h^3}$ is the Richardson constant, q is the electronic charge, m^* is the effective electron mass in the oxide, k_B is Boltzmann's constant, h is Planck's constant, T is the absolute temperature, $E = \frac{V}{d}$ is the electric field across the oxide, with V the applied voltage and d the oxide thickness, $\phi_B = q\phi_B$ is the Schottky barrier height energy, ϵ is the dielectric permittivity of the oxide, $\kappa = \frac{\epsilon}{\epsilon_0}$ is the relative dielectric permittivity of the oxide layer, $t_{ox,eq}$ is the equivalent oxide thickness, μ is the carrier mobility, N_C is the density of states in the conduction band, $\Phi_T = q\phi_T$ is the energy of the electron traps with respect to the conduction band edge, θ is the ratio of free and shallow trapped charge, ΔG^* is the free activation enthalpy, σ_0 is the electrical conductivity (at $T = T_0$), and finally E_C , E_F and E_V are the conduction band, Fermi and valence band energies, respectively.

Appendix D

Synchrotron-based experiments

Contents

D.1 X-Ray Absorption Near-Edge Spectroscopy (XANES)	195
D.2 Device in operation: microscopic aspects behind the resistance-change mechanism (in Pt/L2NO4/Ti)	198
D.2.1 Sample preparation	198
D.2.2 XRD in selected micro-patterned regions of the device	198
D.2.3 <i>Operando</i> Hard X-Ray Photoemission Spectroscopy (HAXPES)	200

Synchrotron experiments were carried out at the European Synchrotron Radiation Facility (ESRF) located in Grenoble, on beamline BM25 (SpLine). There are two branches on this bending magnet beamline, branch 'A' (BM25A) and branch 'B' (BM25B). BM25A is dedicated to X-Ray Absorption Spectroscopy (XAS) and High Resolution Powder Diffraction (HRPD) experiments, while BM25B is allocated to Hard X-Ray Photoemission Spectroscopy (HAXPES) and single-crystal X-Ray Diffraction experiments.

D.1 X-Ray Absorption Near-Edge Spectroscopy (XANES)

XANES measurements of the Ni-K edge were carried out in X-ray fluorescence mode due to the presence of a thick substrate. The counting times thus had to be increased (due to the lower intensities measured in fluorescence when compared to the direct transmission mode) to improve the signal to noise ratio and obtain absorption curves with enough intensity. Four scans were acquired and averaged for each measured energy edge to further improve the statistics.

The δ value of L2NO4/STO samples which had been subjected to different annealing treatments (in oxidizing or reducing atmospheres) to tune their oxygen content was estimated from

X-ray Absorption Near-Edge Structure (XANES) experiments, measuring the displacement of the Ni-K edge from which the Ni oxidation state was calibrated, and from there the oxygen content calculated by charge balance. Figure 2.11.c shows the shift of the Ni K-edge towards higher energies when the samples are treated in increasingly oxidizing atmospheres. A solid Ni foil was used as reference for the calibration of the curves. The edge position was obtained using the first/second derivative method.

The nickel oxidation state was determined with the help of a calibration curve constructed from the data provided by Woolley *et al.* [137]. In particular, three nickelate samples with a measured edge energy of 8333.0, 8345.2 and 8348.2 eV, corresponding to Ni(0), Ni(+II) and Ni(+III) oxidation states, respectively, have been used to plot the calibration curve. We have used a second order polynomial function to fit the data (see Figure D.1a). From this curve it was possible to estimate the Ni oxidation state in our films from the measured Ni-K edge positions (turquoise data points in Figure D.1a). The edge position was determined using the maximum of the first derivative of the XANES absorbance spectrum (first/second derivative method). A sufficient amount of significant digits is required for the coefficients obtained from the polynomial fit to obtain precision until the second decimal of the Ni oxidation state (we used 10 significant digits for the three coefficients extracted from the cubic fit as shown in the table inset of Figure D.1a). The oxidation state of Ni then allows the calculation of the oxygen off-stoichiometry δ through the following charge balance equation in $\text{La}_2\text{NiO}_{4+\delta}$:

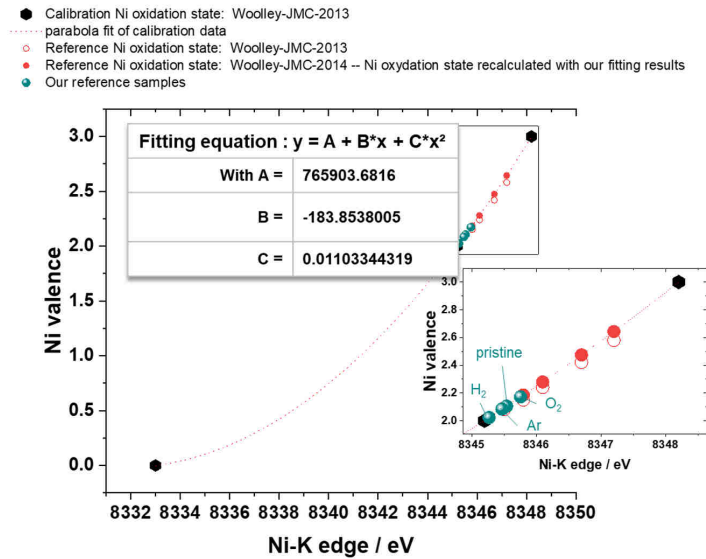
$$3 \times 2 + y + (4 + \delta) \times (-2) = 0$$

$$\delta = \frac{y - 2}{2}$$

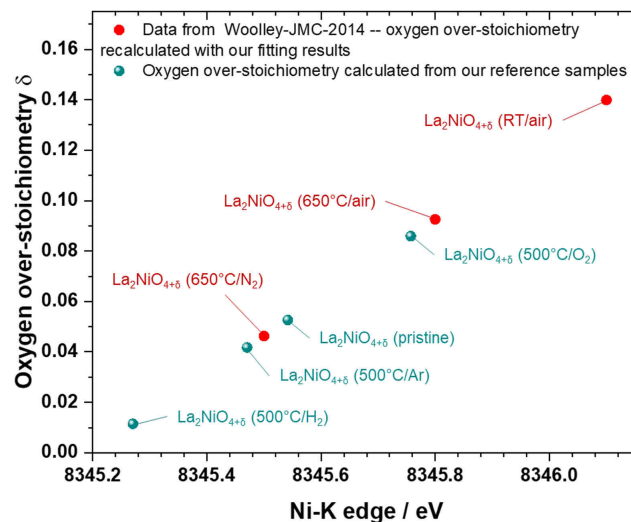
where δ is the oxygen off-stoichiometry and y is the oxidation state of Ni extracted from the position of the Ni-K edge and the calibration curve. If we use the Ni oxidation state determined from the calibration curve, it is then possible to link directly the oxygen over-stoichiometry to the Ni-K edge position:

$$\delta = \frac{y - 2}{2} = \frac{(765903.6816 - 183.8538005 \cdot E_{Ni_K} + 0.01103344319 \cdot E_{Ni_K}^2) - 2}{2}$$

where E_{Ni_K} is the measured energy of the Ni-K edge position. The resulting curve is shown in Figure D.1b. Our data (turquoise spheres) are compared to the data reported by Woolley *et al.* [137] (red circles), showing the important dependence of the oxygen over-stoichiometry in $\text{La}_2\text{NiO}_{4+\delta}$ on the preparation and atmospheric conditions during the XANES measurements.



(a) Calibration curve linking the Ni oxidation state to the Ni-K edge position measured by XANES. The black hexagons correspond to calibration data extracted from [137]. The empty red circles correspond to the Ni oxidation state calculated in [137] for a range of different nickelate samples with varying oxygen stoichiometry. We have recalculated (filled red circles) the Ni oxidation state for the same data using (slightly) different coefficients we obtained for the fitting of the same data calibration points. Finally, the turquoise spheres correspond to the calibrated Ni oxidation calculated from the Ni-K edge position measured for our samples.



(b) Relationship between the Ni-K edge position and the oxygen over-stoichiometry δ . Our data (turquoise spheres) from L2NO4/STO samples submitted to different annealing conditions (prior to the XANES measurement) is compared to the (recalculated) data reported by Woolley *et al.* [137] who measured the Ni-K edge position of L2NO4 pellets *in situ* under varying temperature and/or atmospheric conditions (red circles).

Figure D.1 – XANES calibration curves

D.2 Device in operation: microscopic aspects behind the resistance-change mechanism (in Pt/L2NO4/Ti)

D.2.1 Sample preparation

A new device was prepared specifically for XRD and *operando* HAXPES measurements in order to get a better insight in the microscopic mechanisms responsible for the resistance-change mechanism in Pt/L2NO4/Ti devices. However, for the standard characterization rather thick (200 nm) Pt and Ti top electrodes have been used for electrical contacting, mainly to ensure the mechanical stability when contacting them with the hard WC tips used in the probe station. As HAXPES is a surface technique, thinner electrodes were required to enable probing the metal/L2NO4 interface, and the bulk of L2NO4 below. A total thickness of 10 nm was used for both electrodes, with the particularity that an additional 5 nm-thick Pt layer was evaporated on top of the also 5 nm thick Ti electrode to protect the surface exposed to the atmosphere from oxidizing, while the Pt electrode was 10 nm thick.

The electrical characteristics of this new Pt/L2NO4/Ti sample were however ohmic and did not show memristive properties. An additional processing step was added, i.e. a mild Rapid Thermal Annealing (RTA) treatment consisting in a flash annealing (~30 s at 300 °C) of the sample in an inert Ar atmosphere in order to oxidise (at least partially) the Ti electrode from below (by giving some additional thermal energy to the oxygen ions in L2NO4 for them to diffuse into Ti). Figure D.2 shows how a large increase in resistance (from 1.4 to 9.5 k Ω measured at 10 mV) and nonlinear and slightly rectifying Schottky-like electrical characteristics could be obtained after this RTA treatment.

D.2.2 XRD in selected micro-patterned regions of the device

Advanced X-ray diffraction experiments were carried out at the BM25B SpLine beamline at ESRF. The X-ray beam ($E = 15$ keV) was focused down laterally to 250 μm , while the entire width of the sample (3 mm) was used, as required by the grazing incidence diffraction geometry used for these measurements. This meant that the initial 10x10 mm² sample had to be cut along the edges of the electrodes used for the measurements to control the areas which would be exposed to the synchrotron beam. Long rectangular-shaped electrodes were therefore evaporated to cover the entire electrode length (3000 μm) to maximize the thin film area exposed and therefore the diffracted intensity. The rectangular electrodes were connected by metallic stripes to larger squared electrodes (far from the measured region), which were electrically connected using clamps and then by cables to a Keithley2400 SourceMeter. A picture of the resulting sample is shown in Figure D.3.

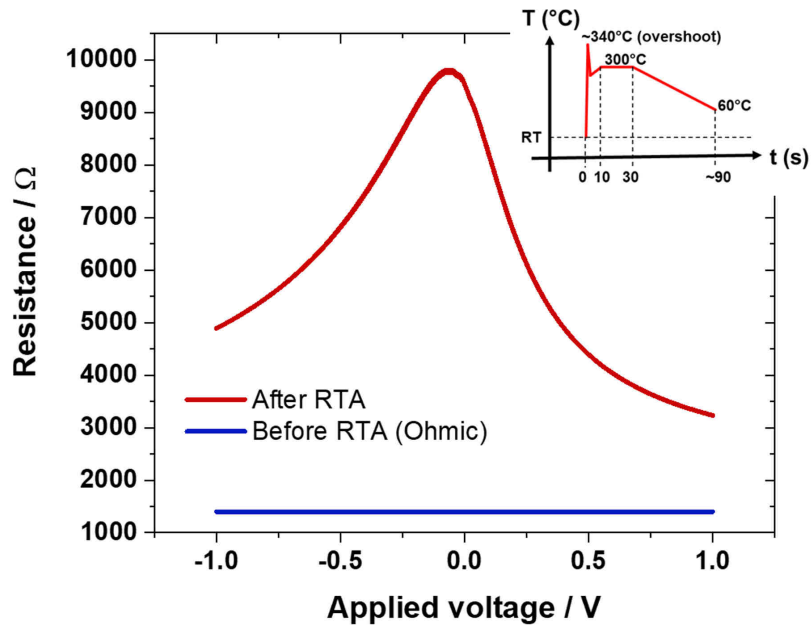


Figure D.2 – Electrical characteristics of a Pt/L2NO4/Ti/Pt device before and after the RTA treatment. The device initially shows ohmic characteristics and low resistance (1.4 kΩ), while an increase in resistance (to 9.5 kΩ) and a Schottky behaviour are obtained after RTA. The inset is an illustration showing the evolution of the temperature over time during the RTA process.

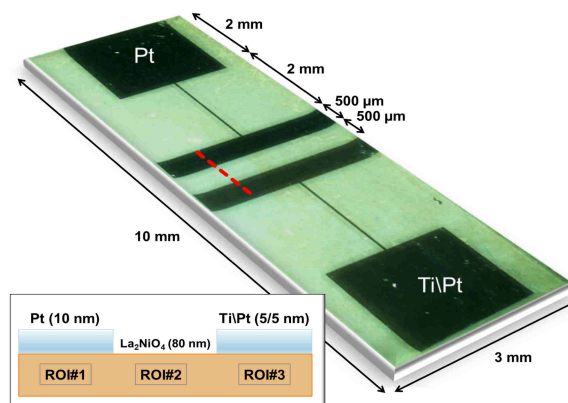


Figure D.3 – Picture of a Pt/L2NO4/Ti/Pt sample prepared for synchrotron measurements. A schematic at the bottom of the figure shows the cross-section of the sample (corresponding to the dashed red line in the picture).

Figure D.6.c shows the XRD patterns acquired in the three regions of interest (ROI): on the Pt electrode side (ROI#1), the bare L2NO4 film (ROI#2) and the Ti\Pt electrode side (ROI#3). The diffraction peak at $\Gamma \simeq 16^\circ$ belongs to polycrystalline Pt which is present in the two Pt and Ti\Pt electrodes, with a lower intensity in the later due to the lower thickness (10 nm against 5 nm, respectively). The absence of this diffraction peak in ROI#2 (bare L2NO4 film) confirms the proper alignment of the incident X-Ray beam (perpendicular to the sample). Interestingly, the two $0\ 0\ 6_{\text{L2NO4}}$ and $0\ 0\ 8_{\text{L2NO4}}$ reflections from the L2NO4 film ($\Gamma \simeq 17.5^\circ$ and 25° , respectively) have slightly different positions depending on the measured ROI. The difference is largest for ROI#3 (below the Ti electrode), showing a displacement of the two reflections towards higher Γ values (lower interplanar distance), consistent with a lower oxygen stoichiometry of L2NO4 (loss of interstitial oxygen ions). The corresponding out-of-plane c -lattice parameter of L2NO4 has been calculated using the position¹ of the $0\ 0\ 8_{\text{L2NO4}}$ peak. The resulting c parameter of L2NO4 for each ROI is shown in the upper part of Figure D.6.b (dotted light blue curve), confirming the important structural differences of L2NO4 depending on the measured region, and more particularly on the top electrode material. As said earlier, the low value of c measured in ROI#3 confirms the important oxygen scavenging capability of Ti, it was however unexpected that the *entire* L2NO4 film would be reduced below Ti, instead of only the first few nanometres at the surface in direct contact with the electrode. This can be attributed to the RTA process, which, even though it was done at relatively low temperatures (300 °C during 30 s), could strongly activate the oxygen diffusion in L2NO4 and make the scavenging process almost instantaneous. The complete reduction of L2NO4 below Ti might be the reason for the inferior memristive properties measured for this sample, suggesting that a precise oxygen stoichiometry (both in the TiO_x interlayer and in L2NO4) is required for optimal memory properties.

D.2.3 *Operando* Hard X-Ray Photoemission Spectroscopy (HAXPES)

Operando HAXPES measurements were carried out (also on BM25B) using an X-Ray beam focused down to $420 \times 3000\ \mu\text{m}^2$, covering almost the entire electrode and film regions (ROI#1, 2 and 3 in Figure D.3), to maximize the low intensities measured in photoelectron emission techniques (when compared to single crystal diffraction). Several core levels (for different elements) were measured ($\text{La}2p_{3/2}$, Ni1s, O1s, Ti1s, Pt3d_{5/2}) to probe possible changes in the binding energies characteristic of a reduction or an oxidation of for example Ti or Ni, but also to witness the possible oxygen motion throughout the material by measuring the evolution of the Ni1s or $\text{La}2p_{3/2}$ core levels during electrical biasing. Unfortunately, an issue with

¹The position was determined by fitting the diffraction peak with a pseudo-Voigt peak function

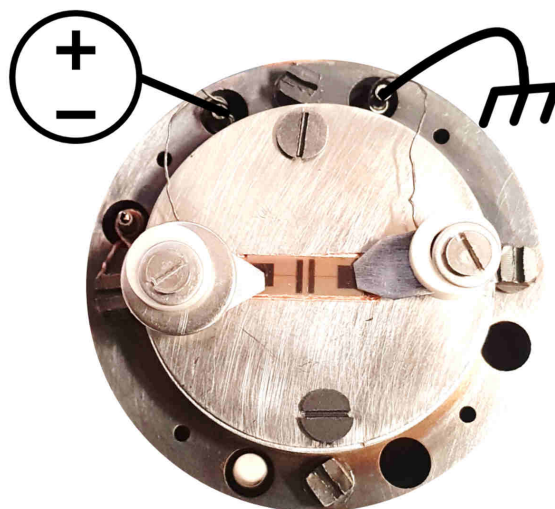


Figure D.4 – Measurement setup for the HAXPES *in-situ* biasing experiment.

the detecting system made it unstable when measuring high kinetic energies of the emitted photoelectrons (for $E_{\text{kin}} > 9000$ keV), which prevented from using data acquired for core levels with low binding energies (such as O1s). Figure D.4 shows the setup used for the *operando* HAXPES measurements. The sample holder allows contacting the sample with two clamps, the wires could then be passed through a feed-through compatible with the ultra high vacuum (10^{-9} Torr) required for this type of measurements. The sample could then conveniently be biased using a Keithley2400 SourceMeter directly from the control chamber.

Figure D.5 shows the Ti1s core level spectra² of the Pt/L2NO4/Ti/Pt memristive device in its initial (unbiased) resistance state, after having applied -30 V to the platinum electrode to SET the device in a higher resistance state and after having applied an opposite voltage (+20 V) to RESET the device in a lower resistance state. The SET voltage was applied for a substantial amount of time (more than 14 h) leading to a (small) increase of resistance from 10.8 k Ω to 13.9 k Ω . The RESET process (during which the bias was applied 'only' for 3 h) had a negligible effect on the final resistance of the device. The increased voltage amplitudes³ and durations required to trigger a (small) change in resistance are at least partially due to the device geometry. Indeed, these *operando* synchrotron measurements were subject to a trade-off: large electrodes were required to improve the statistics and obtain quantifiable pho-

²Five individual scans were averaged to obtain one single Ti1s scan with good statistics (for each biasing condition). A Shirley background was then removed from each averaged photoelectron emission spectrum. Finally, the intensity of each spectrum was normalized in integrated intensity (the area below the curve is the same for each spectrum). This allows comparing spectra acquired in different conditions (for example two measurements with different counting time).

³when compared for example to the ± 5 V sweeps described in Chapter 4 which were sufficient to trigger a memristive behaviour

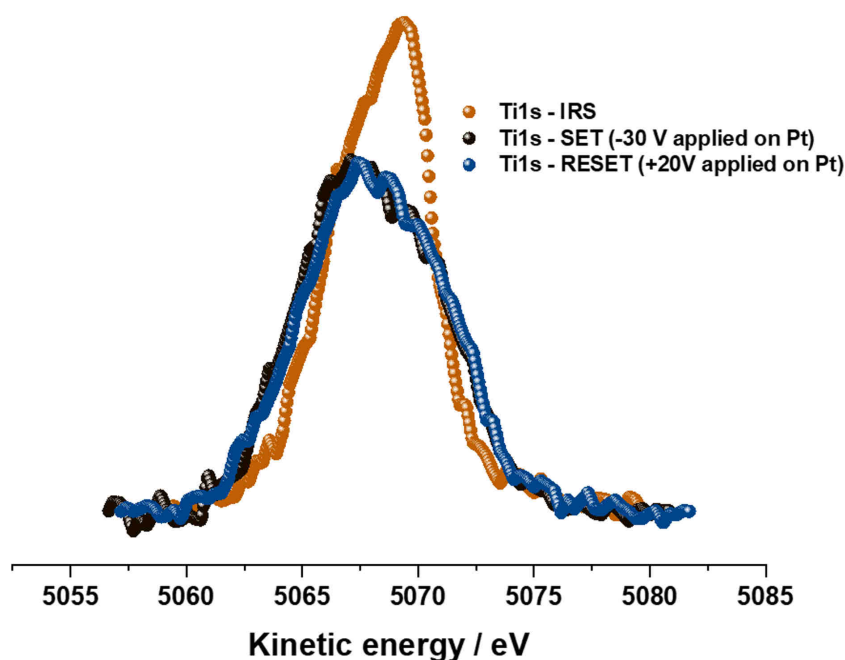


Figure D.5 – *Operando* HAXPES measurements of the Ti1s core level of the Ti top electrode when the Pt/L2NO4\Ti\Pt memristive device is in IRS (light brown), after SET (black) and after RESET (blue).

toemission spectra, but these large electrode areas (and the distance that separates them) leads to an important loss off electric power (small current densities and low electric fields), which might need to be higher to trigger oxygen ion motion and trigger the memristive response of the device. Furthermore, the failed attempt to RESET the device in a lower resistance state when applying +20 V could be linked to the ultra-high vacuum required for measurement, as similar (same type of device) *operando* XANES experiments (results not shown) carried out in atmospheric air did successfully obtain a change in resistance after the RESET biasing. Such a high vacuum could effectively act as a reducing atmosphere, once a sufficient amount of oxygen is removed from the sample, it could completely lose its memristive properties. Despite the relatively small changes in resistance, Figure D.5 shows that the Ti1s core level was subject to chemical changes during the biasing experiment. A clear decrease of the component at high kinetic energy around 5069 eV (low binding energy) is visible after having SET the device in HRS (when compared to the IRS - *i.e.* the black curve vs brown curve). The lower binding energies are usually related to metallic bounds, meaning that the amount of metallic Ti decreased after the SET process, which is coherent and confirms the oxidation of the Ti top

electrode in contact with L2NO4. This intensity loss is not restored after the RESET process as expected from the failed attempt to RESET the device to LRS discussed earlier, although a (small) loss of intensity on the left side of the blue curve (when compared to the black curve) is visible. This intensity loss of the high binding energy component in the photoemission spectrum could be the marker of a slight reduction of the sample. These results are however preliminary and require additional peak fitting to quantify the measured differences between spectra.

An interesting observation was made when measuring the La2p_{3/2} core level in different regions of the sample while applying the SET bias (-30 V). Figure D.6.a shows the photoemission spectrum of La2p_{3/2} in the IRS (brown curves) and *during* the SET process (blue curves) for each of the three measured regions of the sample (ROI#1, 2 and 3). While the La2p_{3/2} core level is similar for the three regions in their IRS, it is offset by several eV when applying the bias. The offset is expected, as applying a voltage shifts the electron energy levels to higher or lower values depending on the voltage polarity (for example, applying a negative voltage will make it easier to remove electrons from the sample due to coulomb repulsion, hence increasing their kinetic energy). Nevertheless, we did not expect to be able to locally probe the voltage drop across the sample this way. Indeed, even though all the La2p_{3/2} core levels are offset towards higher kinetic energy regardless of the ROI, the magnitude of the offset is different for each one of the three regions (21 eV in ROI#1, 18 eV in ROI#2 and 8 eV in ROI#3, see Figure D.6.a). As we are measuring a lanthanum core level⁴, we are sure that the measured voltage drop is across the L2NO4 film only (the Pt and Ti electrodes do not contain La). When plotting the voltage drop as a function of position (black arrows at the bottom of Figure D.6.b), we can see that it correlates well with the evolution of the out-of-plane *c*-lattice parameter of L2NO4 (dotted light-blue curve), which is related to the oxygen content of L2NO4. This means that the lower the oxygen content, the larger the voltage drop across L2NO4. The oxygen dependence of the resistivity of L2NO4 had already been measured *ex-situ* using samples annealed in different atmospheres (e.g. Figure 3.6 in Chapter 3). However, it has now been measured *in-situ*, being able to relate for the first time differences in the local oxygen stoichiometry of the L2NO4 film to resistivity changes within a single L2NO4 memristive device.

⁴The same is true for the Ni1s core level

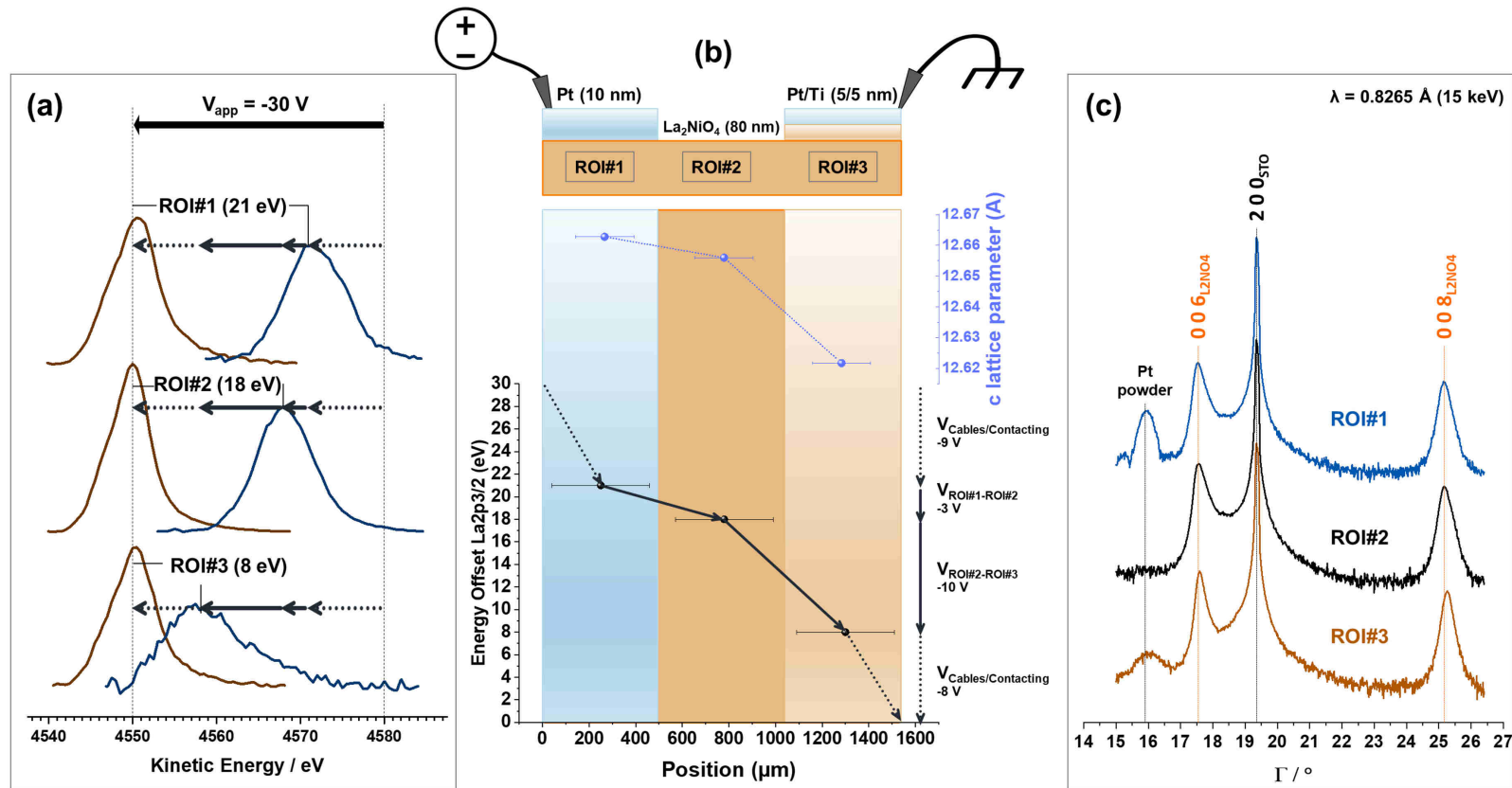


Figure D.6 – (a) *Operando* HAXPES experiment showing the energy shift of the La_{2p_{3/2}} core level in L₂NO₄ upon bias application for different locations on the Pt/L₂NO₄/Ti device depicted in (b). The peak around 4550 eV (brown) corresponds to the energy of La_{2p_{3/2}} in its pristine unbiased state measured: beneath the Pt electrode; for the exposed L₂NO₄ film and beneath the Pt/Ti electrode (from top to bottom). Upon the application of a strong negative bias (-30 V) on the Pt electrodes, the peak shifts towards higher kinetic energy (blue curves) with different magnitude depending on the measuring location on the sample (+21 eV, +18 eV and +8 eV shift measured at the Pt, Center or Ti location, respectively). (b) The graphic shows the values of energy shift extracted from (a) and the evolution of the *c* lattice parameter extracted from (c) as a function of the region of the Pt/L₂NO₄/Ti device that was measured. The horizontal error bars show the lateral size of the incident X-Ray beam. A cross-section schematic of the device showing the biasing conditions and the three regions of interest in the L₂NO₄ film is also shown on top of the graph. (c) Out of plane XRD patterns measured in the Pt, Center and Ti regions. The shift of the 0 0 6_{L₂NO₄} and 0 0 8_{L₂NO₄} Bragg reflections to higher Γ values when measuring beneath the Pt or the Pt/Ti electrode suggests a shortening of the out of plane *c* lattice parameter of L₂NO₄, consistent with a loss of interstitial oxygen.

Appendix E

Résumé de la thèse en Français

Les résultats présentés dans cette thèse s'inscrivent dans la recherche sur une nouvelle génération de mémoires basée sur le principe de la commutation résistive où l'application d'un champ électrique externe peut faire varier l'état de résistance du composant mémoire. Plus particulièrement, nous avons focalisé notre recherche sur les mémoires dites 'à changement de valence' (VCM), une sous catégorie de mémoire résistive où des réactions d'oxydoréduction sont à l'origine du changement de résistance du dispositif. Ce changement de résistance peut avoir lieu dans le volume du matériau actif (prenant par exemple la forme de filaments conducteurs) et/ou à l'interface avec l'une des deux électrodes utilisées en tant que matériau de contact et permettant d'opérer la mémoire électriquement. Lorsque le matériau actif est un oxyde, la dérive d'ions oxydes (O^{2-}) induite par l'application d'un champ électrique externe peut provoquer des réactions chimiques responsables du changement de résistance de la mémoire.

Nous avons choisi d'utiliser un oxyde complexe tel que $La_2NiO_{4+\delta}$ pour une conception rationnelle de VCMs. Ce matériau étant un conducteur mixte d'ions et d'électrons permettant de tirer parti de ses propriétés de conducteur d'ions O^{2-} dans le volume du matériau, nous avons voulu étudier si une amélioration du contrôle de la dérive/diffusion de ces ions améliore le contrôle de la mémoire en permettant entre autre une programmation multi-niveaux ouvrant la voie vers le calcul neuromorphique. $La_2NiO_{4+\delta}$ offre un terrain de jeu prometteur pour son utilisation dans les VCMs dans la mesure où, en plus d'être un conducteur ionique, il présente aussi une capacité de stockage d'oxygène sous la forme d'ions oxydes qu'il peut accommoder dans sa structure cristalline au sein de sites interstitiels tétraédriques sans se décomposer. Par ailleurs, étant aussi un bon conducteur électrique (semiconducteur type-p), il rend plus difficile la rupture diélectrique qui résulte bien souvent en un mécanisme de commutation résistive de type filamentaire plus stochastique par nature.

Nous avons pu préparer $La_2NiO_{4+\delta}$ sous la forme de films minces (~70 nm d'épaisseur)

sur des monocristaux de SrTiO_3 , NdGaO_3 et LaAlO_3 en utilisant un bâti de dépôt MOCVD à injection pulsée. Les conditions de dépôt optimales retenues sont : $T = 650\text{ }^\circ\text{C}$, $p = 5\text{ Torr}$ sous une atmosphère composée d'un mélange 63% O_2 /34% Ar . Des images HRTEM nous ont permis de constater la présence de 4 à 7 monocouches de LaNiO_3 à l'interface $\text{La}_2\text{NiO}_{4+\delta}/\text{SrTiO}_3$, ces couches ne sont pas présentes lors d'une croissance sur LaAlO_3 ou NdGaO_3 et suggère un mécanisme de relaxation de la mise en tension de $\text{La}_2\text{NiO}_{4+\delta}$ par SrTiO_3 (qui a un paramètre de maille plus grand). Une réorientation des domaines $c_{L2NO4,\perp}$ (axe c de $\text{La}_2\text{NiO}_{4+\delta}$ hors du plan, perpendiculaire au substrat) en $c_{L2NO4,\parallel}$ (dans le plan, parallèle au substrat) a été mise en évidence lorsque l'épaisseur du film dépasse les $\sim 30\text{ nm}$ (pour une croissance sur SrTiO_3).

Les propriétés électriques du $\text{La}_2\text{NiO}_{4+\delta}$ sont fortement liées à son contenu en oxygène. En effet, nous avons pu mesurer une évolution de la résistivité de ce matériau variant de $\rho = 5.3 \times 10^{-3}$ à $5.7\ \Omega\cdot\text{cm}$ pour une sur-stœchiométrie en oxygène (δ) allant de 0.08 à 0, respectivement. Nous avons fait varier le contenu en oxygène des échantillons en effectuant des recuits sous atmosphères contrôlées (oxydante O_2 ou réductrices Ar et/ou H_2). L'incorporation d'oxygène (lors d'un recuit sous oxygène par exemple) a un effet direct sur le paramètre de maille du $\text{La}_2\text{NiO}_{4+\delta}$. En particulier, nous avons pu mesurer l'expansion ou la contraction du paramètre de maille c en fonction de la valeur de δ .

Les films minces de $\text{La}_2\text{NiO}_{4+\delta}$ ont ensuite été utilisés dans la préparation d'hétérostructures métal/ $\text{La}_2\text{NiO}_{4+\delta}$ /métal. Le dépôt des contacts métalliques à été fait à l'aide d'un évaporateur par faisceau d'électrons en salle blanche, en utilisant des cibles de Pt, Ag ou Ti permettant d'obtenir différents types de contacts électriques. Nous mesurons par exemple un contact ohmique entre le Pt et le $\text{La}_2\text{NiO}_{4+\delta}$ alors qu'une non-linéarité est présente dans les caractéristiques électriques de la jonction Ag/ $\text{La}_2\text{NiO}_{4+\delta}$. Lorsque Ti est utilisé comme électrode, la résistance du dispositif est fortement accrue suite à la création spontanée d'une couche amorphe de TiO_x à l'interface Ti/ $\text{La}_2\text{NiO}_{4+\delta}$ que nous avons pu observer par microscopie électronique à transmission. Cette couche de $\sim 8\text{ nm}$ d'épaisseur a un rôle décisif sur les propriétés d'une mémoire résistive formée à partir de Pt/ $\text{La}_2\text{NiO}_{4+\delta}$ /Ti. Cette hétérostructure a été choisie en tant que premier prototype visant à étudier les propriétés memristives d'une VCM basée sur $\text{La}_2\text{NiO}_{4+\delta}$ puisque Ti est connu pour ces propriétés de stockage et d'affinité chimique pour l'oxygène. Une étape dite 'd'initialisation de la mémoire' est nécessaire en vue d'obtenir des propriétés memristives. Cette étape consiste en l'application d'une tension négative au niveau de l'électrode de Pt (tout en mettant la contre électrode de Ti à la masse) et diffère de l'électroformage plus classique en ce sens qu'il n'est pas nécessaire d'appliquer une tension supérieure à la tension d'opération de la mémoire, limitant donc les risques de rupture diélectrique irréversibles du composant. Des caractéristiques $I(V)$ de type analogique (transition graduelle entre l'état de haute et de basse résistance du dispositif) stables et largement reproductibles

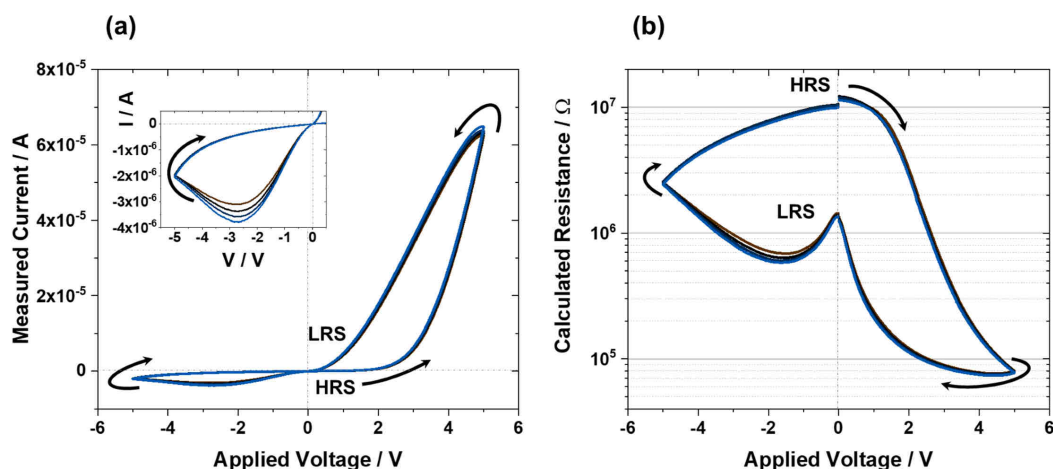


Figure E.1 – (a) Caractéristiques I(V) d’un composant Pt/L2NO4/Ti entre ± 5 V. (b) Caractéristiques R(V) du même composant calculées à partir du courant mesuré dans (a). HRS (pour ‘High Resistance State’) représente l’état du dispositif en haute résistance alors que LRS (Low Resistance State) représente son état basse résistance, il est possible de passer d’un état à l’autre en balayant la tension de 0 V à -5 V et de 0 V à +5 V, respectivement. La tension est appliquée sur l’électrode de Pt (Ti est à la masse).

ont été obtenues après initialisation de la mémoire. Un ordre de grandeur sépare l’état de haute et de basse résistance (nommés HRS et LRS, respectivement) lors d’un balayage entre ± 5 V. La présence d’oxygènes interstitiels dans le $\text{La}_2\text{NiO}_{4+\delta}$ est bénéfique sinon nécessaire à l’obtention d’un effet mémoire dans les dispositifs Pt/ $\text{La}_2\text{NiO}_{4+\delta}$ /Ti. Une interaction entre l’épaisseur et la composition de la couche de TiOx ainsi que la stœchiométrie en oxygène du $\text{La}_2\text{NiO}_{4+\delta}$ sont sûrement des paramètres cruciaux à prendre en compte pour l’optimisation des propriétés memristives de ces dispositifs. Nous avons observé un comportement largement multi-niveaux de la mémoire lorsqu’elle est programmée de manière pulsée (largeur de pulse d’une milliseconde pour une amplitude de -15 V). La mémoire est volatile en ce sens qu’elle relaxe spontanément d’un état HRS vers un état LRS. Cette volatilité offre néanmoins la possibilité d’implémenter une fonction d’oubli intéressante pour le calcul neuromorphique et l’intégration de réseaux de neurones artificiels au niveau hardware.

L’optimisation du dépôt de couches minces texturées de LaNiO_3 par PiMOCVD à aussi été effectué dans le cadre de cette thèse. Cette perovskite est un bon conducteur électrique (résistivité pouvant descendre jusqu’à $90 \mu\Omega.\text{cm}$) que nous avons voulu utiliser en tant qu’électrode pour la croissance de films orientés de $\text{La}_2\text{NiO}_{4+\delta}$, permettant une configuration dite ‘top-bottom’ des électrodes (au lieu de la configuration ‘top-top’ où les deux électrodes se trouve dans le plan à la surface du film que nous avons utilisé précédemment pour Pt/ $\text{La}_2\text{NiO}_{4+\delta}$ /Ti).

Par ailleurs, l'échange d'oxygène entre le $\text{La}_2\text{NiO}_{4+\delta}$ et le LaNiO_3 décrit par Moreno *et al.* [88] rend le système $\text{La}_2\text{NiO}_{4+\delta}/\text{LaNiO}_3$ très intéressant pour son utilisation en tant que VCM. Nous avons obtenu des couches minces de LaNiO_3 sur LaAlO_3 fortement texturées avec une résistivité de l'ordre de $\sim 200 \mu\Omega.\text{cm}$. La qualité cristalline des films est moins bonne (densité plus importante de défauts) lorsque le LaNiO_3 est crû sur un monocristal de SrTiO_3 dû au moins en partie à la présence d'impuretés de NiO (isolant) pouvant percoler sur toute l'épaisseur du film. Nous avons observé que le substrat utilisé pour la croissance a un rôle important sur la qualité cristalline et la résistivité des films de LaNiO_3 . Bien que nous ayons initié le dépôt de bi-couches $\text{La}_2\text{NiO}_{4+\delta}/\text{LaNiO}_3$ par PiMOCD, leur optimisation est encore nécessaire en vue de diminuer la densité de défauts (orientation mixtes, impuretés, ...) qu'ils contiennent et d'améliorer l'épitaxie. Ce type d'échantillon a cependant pu être préparé par PLD lors d'un stage effectué dans le cadre d'une collaboration avec l'ICN2 à Barcelone (au sein du groupe 'Nanomaterials Growth Unit'). Les résultats préliminaires issus des caractérisations électriques sur des dispositifs $\text{Pt}/\text{LaNiO}_3/\text{La}_2\text{NiO}_{4+\delta}/\text{Pt}$ ont montré qu'il est possible d'obtenir un comportement de mémoire analogique similaire à celui des dispositifs $\text{Pt}/\text{La}_2\text{NiO}_{4+\delta}/\text{Ti}$. La mémoire est volatile est relaxe progressivement d'un état HRS vers un état LRS. Nous avons pu observer que la réponse du composant à un stimulus électrique dépend fortement de son historique de programmation.

Cette thèse a démontré qu'il y a un fort intérêt à étudier l'utilisation d'oxydes complexes, avec en particulier les conducteurs mixtes ioniques-électroniques, pour leur utilisation dans les composants de type VCM et pour l'implémentation de réseaux de neurones artificiels au niveau hardware.

Abstract

This thesis is focused on the understanding and development of novel materials for *valence-change memories* (VCMs), a type of resistive switching memories in which the memory storage mechanism is based on internal redox reactions. VCMs are in essence electrochemical systems. Their implementation in integrated electronic circuits relies on a voltage (or current) to measure and operate the memory, but their functionality is highly dependent on the chemical properties of the materials constituting the memory. In this work we present how the mixed ionic-electronic conducting $\text{La}_2\text{NiO}_{4+\delta}$ compound offers an interesting playground for VCM applications due to its intrinsic bulk oxygen-ion conducting properties. We have successfully prepared $\text{La}_2\text{NiO}_{4+\delta}$ in the form of highly oriented thin films on SrTiO_3 single crystal substrates using pulsed-injection chemical vapour deposition (PiMOCVD). Post-annealing treatments in oxidizing/reducing atmospheres allow tuning the oxygen content and the *p*-type semiconducting properties of $\text{La}_2\text{NiO}_{4+\delta}$ due to a self-doping mechanism. The obtained oxygen over-stoichiometry in the $0 \leq \delta \leq 0.08$ range induced a variation of the film resistivity between $5.7 \Omega\cdot\text{cm}$ and $5.3 \times 10^{-3} \Omega\cdot\text{cm}$ for hydrogen or oxygen-annealed samples, respectively. The optimized $\text{La}_2\text{NiO}_{4+\delta}$ thin films have been used as a base for the microfabrication of metal/ $\text{La}_2\text{NiO}_{4+\delta}$ /metal heterostructures. The important role of the metal/oxide junction in interface-type VCMs is discussed in detail. In particular, an ohmic contact is obtained with $\text{La}_2\text{NiO}_{4+\delta}$ when using a high work function metal such as Pt, while rectifying contact properties are obtained when using Ti due to the presence of a spontaneously-formed TiO_x interlayer (~ 8 nm) at the Ti/ $\text{La}_2\text{NiO}_{4+\delta}$ interface. An asymmetric Pt/ $\text{La}_2\text{NiO}_{4+\delta}$ /Ti heterojunction has been selected as a first prototype to assess the memory capabilities of a $\text{La}_2\text{NiO}_{4+\delta}$ -based memristive device. A continuous bipolar analogue-type memory behaviour has been measured, together with strong multilevel programming capabilities when operated in pulsed mode. In addition, the promising results offered by this prototypical device have been extended for the first time to $\text{La}_2\text{NiO}_{4+\delta}/\text{LaNiO}_3$ bilayers, showing memory relaxation properties, which are potentially interesting for short-term memory and filtering applications in neuromorphic-based computational hardware.

Résumé de la thèse en français

Cette thèse porte sur la compréhension et le développement de matériaux innovants en tant que composant actif pour les mémoires résistives à changement de valence (VCM), qui constitue une sous-catégorie des mémoires résistives où des réactions d'oxydoréduction sont à l'origine du mécanisme de commutation résistive. Leur incorporation dans les circuits intégrés nécessite une tension (ou un courant) électrique pour lire et programmer la mémoire, cependant leurs fonctionnalités dépend essentiellement des propriétés chimiques des matériaux constituant la mémoire. Dans ce manuscrit nous étudions les propriétés du composé $\text{La}_2\text{NiO}_{4+\delta}$, un conducteur mixte d'ions et d'électrons qui de par sa conduction d'ions oxydes dans le volume du matériau offre un terrain de jeu prometteur pour les VCMs. Nous avons pu obtenir des films minces de $\text{La}_2\text{NiO}_{4+\delta}$ fortement texturés sur des substrats monocristallins de SrTiO_3 par dépôt chimique en phase vapeur à partir de l'injection pulsée de précurseurs métalorganiques (PiMOCVD). Des recuits sous atmosphère contrôlée ont permis de faire varier le contenu en oxygène et d'ajuster les propriétés semiconductrices-type *p* de $\text{La}_2\text{NiO}_{4+\delta}$ par un mécanisme d'auto-dopage. Une sur-stœchiométrie en oxygène dans la plage $0 \leq \delta \leq 0.08$ induit une variation de résistivité de $5.7 \Omega\cdot\text{cm}$ à $5.3 \times 10^{-3} \Omega\cdot\text{cm}$ pour un recuit sous hydrogène ou sous oxygène, respectivement. Les films minces de $\text{La}_2\text{NiO}_{4+\delta}$ ont ensuite été utilisés comme base dans la conception d'hétérostructures métal/ $\text{La}_2\text{NiO}_{4+\delta}$ /métal. Le rôle important de la jonction métal/oxyde sur les propriétés des VCMs de type interfaciales est discuté en détails. En particulier, un contact ohmique avec $\text{La}_2\text{NiO}_{4+\delta}$ est obtenu en utilisant un matériau d'électrode tel que le Pt ayant un travail de sortie élevé, alors qu'un contact rectifiant est obtenu avec Ti résultant de la présence d'une fine couche (~ 8 nm) de TiO_x formée de manière spontanée à l'interface Ti/ $\text{La}_2\text{NiO}_{4+\delta}$. Une hétérojonction asymétrique Pt/ $\text{La}_2\text{NiO}_{4+\delta}$ /Ti a été sélectionnée comme prototype afin d'évaluer les propriétés memristives de composants basés sur $\text{La}_2\text{NiO}_{4+\delta}$. Un changement de résistance bipolaire a été mesuré ainsi qu'une possibilité de programmation largement multi-niveaux lorsque la mémoire est stimulée de manière pulsée. Les résultats prometteurs obtenus par ce premier prototype sont ensuite étendus pour la première fois à un système plus complexe de bicouches $\text{La}_2\text{NiO}_{4+\delta}/\text{LaNiO}_3$. Des propriétés de relaxation ont été mesurées, rendant ces mémoires intéressantes pour leur utilisation en tant que mémoire volatile pour un filtrage dynamique dans des applications neuromorphiques.

